A Top Quark Mass Measurement Using the Stabilized R_{32} Variable with the ATLAS Detector

Dissertation

zur Erlangung des mathematisch-naturwissenschaftlichen
Doktorgrades
"Doctor rerum naturalium"
der Georg-August-Universität Göttingen

vorgelegt von

Stefan Guindon

aus

Cornwall, Ontario, Kanada

Göttingen, 2012

A Top Quark Mass Measurement Using the Stabilized R_{32} Variable with the ATLAS Detector

Dissertation

zur Erlangung des mathematisch-naturwissenschaftlichen
Doktorgrades
"Doctor rerum naturalium"
der Georg-August-Universität Göttingen

vorgelegt von

Stefan Guindon

aus

Cornwall, Ontario, Kanada

To My Wife, Lubka

"Much human ingenuity has gone into finding the ultimate Before. The current state of knowledge can be summarized thus:
In the beginning, there was nothing, which exploded."

– Terry Pratchett
Lords and Ladies

Fazit

Die vorliegende Arbeit beschreibt die erste Messung der Masse des Top-Quarks mit dem ATLAS-Experiment, einem von vier großen Experimenten am Large Hardon Collider, LHC. Das im Jahr 1995 an Experimenten am Tevatron entdeckte Teilchen ist das schwerste aller zur Zeit bekannten Elementarteilchen. Aufgrund seiner großen Masse – und damit starken Yukawa-Koppung an das Higgsfeld – spielt das Top-Quark eine besondere Rolle im elektroschwachen Sektor des Standardmodells der Elementarteilchenphysik.

Die Messung der Masse basiert auf der vollständigen Rekonstruktion des Endzustands, und damit des Top-Antitop-Quarkpaares. Dabei wird ein kinematischer Fit im Lepton + Jets-Kanal angewandt, welcher neben kinematischen Variablen auch Informationen über Algorithmen zur Identifikation von b-Quarks (*b-tagging*) verwendet. Der Lepton+Jets-Kanal hat ein großes Verzweigungsverhältnis, wenig Untergrund und lässt sich aufgrund des einen Neutrinos im Endzustand vollständig rekonstruieren. Die Rekonstruktionseffizienz mittels des kinematischen Fits ist dabei etwa 70%.

In jedem rekonstruierten Ereignis wird ein Schätzer für die Masse des Top-Quarks gebildet, das sogenannte R_{32}-Verhältnis. Dieses ist definiert als das Verhältnis der Masse des hadronisch zerfallenden Top-Quarks zu der rekonstruierten Masse des hadronisch zerfallenden W-Bosons. Der Vorteil dieser Variable ist eine verminderte Anfälligkeit des Schätzers auf Variationen in der Jet-Energie-Skala. Dessen Unsicherheit ist die dominierende Komponente in Messungen dieser Art. Desweiteren wurde die Ereignisselektion hinsichtlich der nächstgrößeren Quellen systematischer Unsicherheit optimiert, der Jet-Energie-Skala von b-Quarks und der Modellierung der Abstrahlung von Gluonen im Anfangs- und Endzustand der Top-Quark-Produktion.

Die Verteilung des R_{32}-Verhältnisses für Signal- und Untergrundprozesse wurde parametrisiert und sowohl die Normierungen als auch die Masse des Top-Quarks in einem Template-Fit an die Daten angepasst. Die Daten wurden in der ersten Hälfte 2011 mit dem ATLAS-Experiment gesammelt und entsprechen einer integrierten Luminosität von 1.04 fb^{-1}. Die Messung wurde im Elektron+Jets-Kanal und Muon+Jets-Kanal separat durchgeführt und die Resultate anschließend mittels der BLUE-Methode kombiniert. Die gemessene Masse des Top-Quarks ist:

$$m_{\text{top}}^{l+jets} = 174.4 \pm 0.9 \text{ (stat.)} \pm 2.5 \text{ (syst.) GeV/c}^2,$$

und stellt mit einer relativen Unsicherheit von etwa 1,5% einen erheblichen Erfolg der ATLAS-Kollaboration im Hinblick der Messungen mit ersten Daten dar.

Abstract

This thesis presents one of the first measurements of the top quark mass at the ATLAS experiment, one of the four large experiments located along the LHC. First discovered in 1995 at the Tevatron experiments CDF and DØ, the top quark is the heaviest of the known elementary particles. Due to its very large mass and large Yukawa coupling, it may yet play an unknown role in electroweak symmetry breaking. The large Yukawa coupling also means it has a strong connection to the Higgs field, and thus gives an indirect insight into the mass of the missing Higgs boson.

To measure the top quark mass, a kinematic reconstruction is performed using the KLFitter to properly reconstruct the decay products in the lepton + jets channel of a $t\bar{t}$ pair decay. The lepton + jets channel has a significant branching ratio and a moderate background. Using the kinematic information of the event, along with the b-tagging efficiency and rejection, the kinematic likelihood fitter obtains a reconstruction efficiency of about 70 % for each of the separate μ + jets and e + jets channels.

From the reconstructed event, a so-called R_{32} estimator is constructed, which is built from the hadronic hemisphere of the $t\bar{t}$ decay. The R_{32} is the ratio of the measured hadronic top mass and the reconstructed hadronic W mass. The ratio reduces the significant uncertainty due to the jet energy scale, the largest of the uncertainties on the top mass measurement. A further optimization of the estimator is performed to limit other systematics such as the bJES and initial and final state radiation effects. This is done with the use of the kinematic likelihood and larger p_T cuts.

A template fit is performed using a parametrization of the signal and background components of the R_{32} distribution. The method is cross checked using ensemble tests. The resulting mass is determined using 1.04 fb^{-1} of data collected during the 2011 ATLAS run. A large number of systematics are also quantified. The measurement is performed in both the e + jets and μ + jets channels separately and then combined into a single lepton + jets measurement using the best linear unbiased estimator (BLUE) method. The top mass is measured to be:

$$m_{\mathrm{top}}^{l+jets} = 174.4 \pm 0.9 \ (\mathrm{stat.}) \pm 2.5 \ (\mathrm{syst.}) \ \mathrm{GeV/c}^2,$$

with only a 1.5 % relative uncertainty on the top mass, a significant achievement for the early ATLAS data taking.

Contents

1. Introduction

The modern era of particle physics has pushed the technological and imagination boundaries to their limits. The search for the fundamental theory to describe the universe is no longer taking place in a one room office, but has brought us to the largest and arguably the most complex machine ever constructed: the Large Hadron Collider (LHC). This is the result of an evolution towards higher energies and search for new particles in a quest to discover the underlying theory of nature. This journey brings us full-circle, back to the moment immediately after the universe all began in the big bang, originally set into motion some 14 billion years ago.

The Standard Model of particle physics (SM), which now stands as a tested theory for our understanding of the fundamental interactions of nature, is the champion of our understanding of the universe. The SM is comprised of the interactions and interacting particles, such as the fermions and gauge bosons which combine to form a basis upon which all of particle physics is built. The Lagrangian formulation of the SM mathematically describes the interactions of particles, with the exception of interactions through gravity. The largest piece of this puzzle is the top quark, which is by far, the heaviest known particle. The partner to the top quark, the bottom quark, is approximately 35 times less its mass.

The top quark was first discovered at the Tevatron in 1995 by both the CDF and DØ collaborations [1, 2]. The Tevatron collider, the most advanced of its time, was built just outside of Chicago, Illinois, colliding protons and anti-protons at a centre-of-mass energy of 1.98 TeV. Running from 1989 until the end of September 2011, the Tevatron led physicists not only to the discovery of the top quark in 1995, but helped to make it the most precisely known quark in the SM [3]. With the shutdown of the Tevatron and the advent of collisions at energies 3.5 times that of the Tevatron, the Large Hadron Collider (LHC) now stands as the largest particle accelerator in the world.

Protons and neutrons, which make up the nuclei of atoms, consist of only up and down quarks. Neutrons consist of two down quarks and one up quark, while the proton is comprised of two up and one down quark. These two partner quarks make up the first generation of quarks. To date, there is no evidence of any other more fundamental substructure of the quark. The two extra generations, of which the top quark is a member, decay to the first generation found in nature.

The top quark is found in the third generation of quarks, along with its partner the bottom quark. The top quark was not discovered until 17 years ago, primarily due to its large mass. This uniquely large mass is also the reason for some of its other properties. One of the properties of the top quark is its very short lifetime. It decays rapidly into the bottom quark with the help of a weak gauge boson known as the W boson. This rapid decay is even ten times faster than the time necessary for hadronization: the process in which a quark and anti-quark pair bond into a hadron. The fact that hadronization does not occur for top quarks allows the properties of the quark to pass to its decay products.

Therefore, its properties such as mass, charge, and spin can be measured directly from its decay products.

The mass of the top quark can not only shed light on the properties of the quark itself, but also the SM, its interactions within electroweak theory, and the search for new physics beyond the SM (BSM). The top quark mass is a fundamental parameter of the SM and is connected to the theorized Higgs boson mass and W boson mass. Precision measurements of the top mass within the electroweak sector help to narrow the search of the Higgs boson within the SM. Due to its large mass, it also could have a connection to new particles not yet discovered or itself play a special role yet to be determined. Therefore, some searches for new physics BSM include the top quark.

The advent of the LHC has given the unique opportunity to further study the top quark and its properties such as its large mass and rapid decay via the weak force. With the large amount of data and a factor of 3.5 times the energy of its predecessor, the Tevatron, the top quark properties will only account for a fraction of the studies done on LHC data. There are still fundamental questions about the universe which could be answered at the LHC:

- Why are there three generations of leptons and quarks? The second and third generations of fermions are identical to their first generation in both charge and isospin, however are not stable and thus decay. What is the underlying reason for their existence?

- Is the Higgs boson responsible for the spontaneous breaking of the electroweak symmetry? If so, what is its mass? Could there be also non-SM Higgs bosons?

- Can we unify the three forces of our current Standard Model at higher energies, ($\Lambda_{GUT} \approx 10^{15}$ GeV), where the strengths of the three couplings of the Standard Model almost meet?

- Due to the Hierarchy problem from divergent loop diagram corrections to the Higgs mass, the SM is only valid up to a certain scale. Depending on the value of the Higgs mass, this scale could be as low as the order of 1 TeV, where the divergent diagrams would cancel with the supersymmetric partners. Is this question possibly answered by supersymmetry (SUSY) and the dark matter in our universe?

- Is it possible that the graviton particle, a theorized spin-2 particle responsible for mediating gravity, could be discovered at the LHC? Since the SM does not yet contain the theory of quantum interactions of gravity, is it possible that the particle mediating the force could be observed with high enough energies?

Some of these questions have the potential to be answered from studies performed at the LHC. The answers may also be linked to the top quark sector. This also includes the Higgs Boson, which if the existence within the current SM framework is true, would have a smaller mass than the top quark. This makes the precise top quark mass measurement essential to understanding our Standard Model of particle physics and all of the possible extensions which may come in this era of modern physics.

This work presents one of the first ever measurements of the top quark mass made at the LHC. The measurement focusses on a completely new technique to measure the top quark mass. This technique, which is referred to here as the R_{32} variable technique, uses the ratio of the reconstructed top quark mass and the W boson mass to make an event-by-event in-situ measurement of the top quark mass approximately canceling the

jet energy scale. The result is a large reduction of the jet energy scale at the expense of the precision of the measurement. For the early running of the LHC, the dependence on jet energy scale introduces the largest uncertainty of the top quark mass measurement. This measurement also uses a very sophisticated reconstruction algorithm, which uses a likelihood based on the decay products' kinematics. This measurement is the first of its kind used for the measurement of the top quark mass.

After the introduction in Chapter 1, Chapter 2 begins with a description of the Standard Model and how the top quark plays a very special role. The top quark production and decay will be described. In Chapter 3 the LHC and ATLAS detector are discussed. A full description of the ATLAS detector components and their purpose are shown. In Chapter 4 the full event selection and object reconstruction is explained. In Chapter 5 the final state of the top quark pair is illustrated as well as the signal and background Monte Carlo used to describe the data taken. The description of the data driven background estimation methods is also shown. In Chapter 6 a comparison of MC to data is made for the events used to estimate the top quark mass. Chapter 7 describes the reconstruction algorithm used to recreate the top quark pair. A kinematic likelihood estimator is used to properly select the jet ordering. In Chapter 8 the R_{32} estimator is described and built. The stabilization against the jet energy scale is also shown. Chapter 9 describes the template method used to measure the top mass. In Chapter 10, a validation of the template method is performed. In Chapter 11, the list of systematic uncertainties are described. In Chapter 12, the top mass measurement is made and the systematic uncertainties of the method are evaluated. The final chapter contains a summary of the work as well as a comparison of the method to the world average top quark mass and other top mass measurements.

2. Physics

2.1. Standard Model of Particle Physics

The Standard Model of Particle Physics (SM) combines the three forces, electromagnetic, weak, and strong into one mathematical theory. This theory describes the symmetries of the universe. The principle of symmetries, first described by Emmy Noether [4], declares that for every continuous symmetry of a system, there must be a conservation law. The conservation of energy or angular momentum are based on this principle. The same is true for the SM, where interactions of particles are confined by these symmetries. To conserve local symmetries, gauge fields are introduced which model the interactions of the particles. The SM describes the gauge fields which make up the three forces.

Beginning in the 1960's, the ideas of unification of forces under one fundamental theory had taken strong roots. At this time, the idea of quarks were proposed by Murray Gell-Mann and Georg Zweig [5]. This gave a natural ordering to the vast number of particles which had been recently discovered, by their quark composition. By the end of the decade, the first evidence of quarks were found through deep inelastic scattering experiments. At the time, only the up (u), down (d), and strange (s) quarks had been observed, and the hadrons (baryons and mesons) could be arranged by a simple classification of the type of quarks of which they constituted. This laid the foundation for the formulation of what would later be called the Standard Model of Particle Physics.

The SM is a theory developed in the early 1970's to unify the forces and associated particles under one complete theory [6–8]. The unification which was first theorized by Steven Weinberg, Sheldon Glashow, and Abdus Salam in 1967, which later won them the Nobel Prize for Physics, accounting for all observed phenomena.

With the discovery of the J/Ψ particle [9,10], composed of a charm (c) and anti-charm ($\bar{c}$), it was clear that fermions, spin-1/2 particles, could be arranged by generations. It also showed a very nice symmetry between quarks and leptons. At the time, the first two generations had been noted as: (ν_e , e) with (u , d) and (ν_μ , μ) with (c , s). The lepton section of each generation, for example: (ν_e , e), consists of one electrically neutral neutrino, with weak isospin $+1/2$, and one negatively charged lepton (-1) with a weak isospin $-1/2$. For the quark section, the generations are split by electric charges of $-1/3$ and $+2/3$ and isospin $\pm 1/2$ as with the leptons. The generations are identical in charge and isospin, however differ in mass and stability. The only stable generation is the first.

Following the surprising evidence of the tau lepton (τ) at SLAC in 1975 [11], the generation symmetry between leptons and quarks of the model was broken. As a result, three new particles had to be discovered to keep the symmetry: one extra neutrino and two quarks, forming a complete third generation. It was not too long a wait to find the Υ meson, which was observed in 1977 [12,13], leading to the fifth quark: the bottom quark (b). This left two yet-to-be discovered particles: the partner to the τ, the tau-neutrino (ν_τ), which was discovered in 2000 [14] and the partner quark to the b, the top quark

(t), discovered in 1995. The complete list of fermions, ordered by generation, is shown in Table 2.1.

$$\text{Quarks:} \quad \begin{pmatrix} u \\ d \end{pmatrix} \quad \begin{pmatrix} c \\ s \end{pmatrix} \quad \begin{pmatrix} t \\ b \end{pmatrix}$$

$$\text{Leptons:} \quad \begin{pmatrix} \nu_e \\ e \end{pmatrix} \quad \begin{pmatrix} \nu_\mu \\ \mu \end{pmatrix} \quad \begin{pmatrix} \nu_\tau \\ \tau \end{pmatrix}$$

Table 2.1.: List of particles described within the SM. The quarks and leptons are ordered horizontally by generation and vertically by isospin, where each bracket contains a $+1/2$ and $-1/2$ weak isospin T_3 component in such an order.

The model making up the SM is comprised of vector bosons which mediate the forces. These vector bosons contain integer spin values and thus obey Bose-Einstein statistics, whereas the fermions obey Fermi-Dirac statistics. The missing gauge boson, the Higgs boson is a scalar boson and has yet to be observed. The forces of the SM, along with their gauge bosons and properties are listed in Table 2.2.

Force	Relative Strength	Gauge Bosons	Theory
Strong	1	8 gluons	QCD
Electromagnetic	10^{-2}	γ	QED
Weak	10^{-6}	Z^0 and $W^\pm$	QFD
Gravitation	$< 10^{-40}$	Gravitons	General Theory of Relativity

Table 2.2.: Overview of the four known forces along with their properties. The gravitational force is added to show a comparison of all fundamental forces, even though the graviton has yet to be observed, and is currently not part of the SM.

In cases where the Lagrangian is required to be invariant under local transformations, a gauge field is necessary to conserve the symmetry. This is the case for the SM, where the Lagrangian must be invariant under a group of local transformations. Local transformations are transformations which are performed at different space-time points.

The quanta of the gauge groups within the SM are the gauge bosons previously mentioned. The gauge bosons are the quanta which mediate the forces. The local gauge theory describing the SM can be written as the combination of two special unitary groups and one unitary group:

$$SU(3)_C \times SU(2)_L \times U(1)_Y. \tag{2.1}$$

The C, L, and Y indices denote the colour quantum number for quarks in the strong force, the third isospin component of left-handed particles, and hyper-charge, respectively.

The Lagrangian describing the SM is comprised of a term for the strong interactions $\mathcal{L}_{QCD}$, a term for electroweak interactions $\mathcal{L}_{EW}$, a term for the Higgs mechanism $\mathcal{L}_{Higgs}$, and a term for the Yukawa coupling $\mathcal{L}_{Yukawa}$. The components are described in the following sections.

2.1.1. Electromagnetic Force

The electromagnetic force is mediated by the photon (γ). The gauge theory representing this force is described by quantum electrodynamics (QED). The theory is based on the unitary group $U(1)_Q$, where Q represents the charge. The mediating photon has zero mass and is responsible for interactions made by the electromagnetic force. The coupling of charged fermion fields Ψ to the photon field A_μ is described by the Lagrangian density:

$$\mathcal{L}_{QED} = \Psi^\dagger(i\gamma^\mu D_\mu - m_f)\Psi - \frac{1}{4}F_{\mu\nu}F^{\mu\mu}, \tag{2.2}$$

where the field strength and covariant derivative are given respectively by:

$$
\begin{aligned}
F_{\mu\nu} &= \delta_\mu A_\nu - \delta_\nu A_\mu \text{ and} \tag{2.3}\\
D_\mu &= \delta_\mu - ieA_\mu. \tag{2.4}
\end{aligned}
$$

The γ^μ are the Dirac matrices and e is the electric charge. The photon field, A_μ, is massless and non self-interacting. As a result, photons are massless and do not interact with one another.

2.1.2. Electroweak Force

The electroweak force is the combination of the electromagnetic and weak forces at energies above approximately 100 GeV. The fields can be represented by left handed and right handed components. They are produced as a result of applying the chiral operators:

$$
\begin{aligned}
O_L &= \frac{1-\gamma_5}{2} \text{ (left handed projector)} \tag{2.5}\\
O_R &= \frac{1+\gamma_5}{2} \text{ (right handed projector)} \tag{2.6}
\end{aligned}
$$

The γ_5 is a Dirac spinor with a left handed eigenvalue of -1 and right handed eigenvalue of + 1. Electroweak theory is represented by the combination of the two unitary groups $SU(2)_L$ and $U(1)_Y$ into a $SU(2) \otimes U(1)$ symmetry group. For the $SU(2)_L$, the third component of the weak isospin I$_3$ is conserved and for the $U(1)_Y$, the hypercharge (Y). They are related to the electric charge by:

$$Q = \frac{Y}{2} + I_3. \tag{2.7}$$

Weak isospin is either $+1/2$ or $-1/2$, and each fermion is given a weak isospin value. The left handed fermions are only found in doublets, with $\pm 1/2$ isospin. The right handed fermions contain isospin of 0. As a result, right handed fermions are invariant under $SU(2)_L$ and treated as singlets. $SU(2)_L$ is also non-Abelian, therefore the gauge bosons of the weak force may be self-interacting, however the electromagnetic component does not allow such self-interactions. Therefore the two components will have separate gauge fields for $SU(2)_L$ and $U(1)_Y$. They are: W$_{\mu\nu}$ and B$_\mu$, respectively.

The Lagrangian for electroweak model can be written as:

$$\mathcal{L}_{EW} = \Psi_L^\dagger\gamma^\mu D_L^\mu\Psi_L + \Psi_R^\dagger\gamma^\mu D_R^\mu\Psi_R - \frac{1}{4}W_{\mu\nu}W^{\mu\nu} - \frac{1}{4}B_{\mu\nu}B^{\mu\nu}, \tag{2.8}$$

where the covariant derivative for left handed fermions is given by :

$$D_L^\mu = i\partial^\mu - g\frac{\tau}{2}W_{mu}^i - \frac{g'}{2}YB^\mu,\qquad(2.9)$$

and for right handed fermions:

$$D_R^\mu = i\partial^\mu - \frac{g'Y}{B^\mu}.\qquad(2.10)$$

The Lagrangian contains four terms, the first of which describes the interactions of left handed particles, the second describes right handed particle interactions, and the last two terms describe the interactions between the gauge fields themselves.

The g and g' are the coupling constants of the weak and electromagnetic interactions, respectively. They are related to the electroweak mixing angle[1] by:

$$\sin\theta_W = \frac{g'}{\sqrt{g^2 + g'^2}}.\qquad(2.11)$$

This angle is not predicted by the Standard Model and can only be verified by experiment. It has been experimentally determined to be 0.23116(13) [15].

The electroweak model gives rise to four fields: the neutral photon and Z boson, and the charged $W^\pm$ bosons. They can be written as combinations of gauge fields and the electroweak mixing angle:

$$
\begin{aligned}
A_\mu &= W_\mu^3\sin\theta_W + B_\mu\cos\theta_W \quad\text{(photon)}, & (2.12)\\
Z_\mu &= W_\mu^3\cos\theta_W - B_\mu\sin\theta_W \quad (Z), & (2.13)\\
W_\mu^\pm &= \frac{1}{\sqrt{2}}(W_\mu^1 \mp iW_\mu^2) \quad (W^\pm). & (2.14)
\end{aligned}
$$

The three linear combinations represent the photon, Z and $W^\pm$ bosons respectively. In electroweak theory, the gauge bosons themselves should all be massless. This is the case for the photon, however, the massive $W^\pm$ [16,17] and Z bosons [18,19] were discovered in the 1980's at CERN in Geneva, Switzerland at the UA1 and UA2 experiments. Therefore there needs to be a theory to account for the mass of the weak gauge bosons. The arguably simplest and most widely accepted is the Higgs mechanism described in the following section.

Another aspect of electroweak theory arises from the fact that the mass and weak eigenstates of the quarks are not identical. Since the $W^\pm$ gauge bosons are electrically charged, they allow for flavour changing within the quark sector. The weak eigenstates are described by the CKM (Cabibbo-Kobayashi-Maskawa) matrix [20, 21]. The largest coupling is given by quarks of the same generation, but off diagonal elements have non-zero values [15]. These non-zero off diagonal values are the magnitude of the flavour changing in the quark sector. The CKM matrix values are not predicted by the SM, however they have been measured through experimental means.

---

[1]Also called the Weinberg angle

2.1.3. The Higgs Mechanism

The electroweak theory thus far does not allow for mass terms of the gauge bosons. Since this is not the case, a theory which still contains the gauge invariance while adding masses to the weak bosons must be introduced. To do so, the Higgs mechanism [22–24] which is achieved through spontaneous symmetry breaking is needed.

The Higgs potential is found in Figure 2.1. At the centre of the system, an unstable maximum exists. An object sitting on the top of this maximum will remain at rest. However, if an external force is applied to the system, the object must choose a direction as it moves towards the stable minima located at the bottom of the potential. This "choice" is spontaneous symmetry breaking and is represented by the Higgs mechanism.

The Higgs mechanism introduces a new scalar field (Φ) which is given as:

$$\Phi = \begin{pmatrix} \phi_1 \\ \phi_2 \end{pmatrix}, \tag{2.15}$$

where the Lagrangian for the Higgs is written as:

$$\mathcal{L}_{Higgs} = (D^\mu \Phi)^\dagger (D_\mu \Phi) - V(\Phi), \tag{2.16}$$

where,

$$V(\Phi) = \mu^2 |\Phi|^2 + \lambda |\Phi|^4. \tag{2.17}$$

The covariant derivative is the same as the electroweak covariant derivative in Eq. 2.9. Taking the minimum of the scalar potential to be non-zero and degenerate ($\lambda > 0$), in order to have a potential minimum not at zero, the resulting μ^2 must be negative. The resulting shape of the potential of such a Higgs fields is found in Figure 2.1.
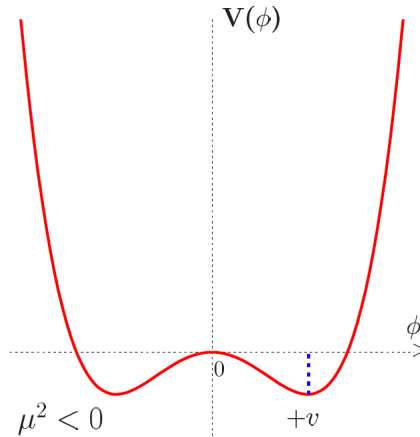

Figure 2.1.: The Higgs potential V for the scalar field ϕ for values of $\mu^2 < 0$. The figure is taken from [25].

The minimum of this potential is therefore non zero, but determined to be:

$$|\Phi|^2 = -\frac{\mu^2}{2\lambda} \equiv \frac{\nu^2}{2} \tag{2.18}$$

where ν is the vacuum expectation potential. The vacuum expectation potential has been measured to be $\nu = 246$ GeV, which is also verified by the relation of ν to the gauge bosons through the eigenstates by:

$$m_\gamma = 0 \tag{2.19}$$

$$m_W = \frac{g\nu}{2} \tag{2.20}$$

$$m_Z = \frac{\nu}{2}\sqrt{g^2 + g'^2} \tag{2.21}$$

The non-zero potential of this field results in the creation of a Higgs boson. This boson, is expected to have spin zero and mass equal to $m_H = \sqrt{2}\mu$. μ however is not predicted by the SM, as a result neither is the Higgs boson mass. Therefore ongoing searches for the Higgs boson continue over a wide range of energy.

The Higgs mechanism is not only responsible for giving mass to the gauge bosons, but also the mass of all the fermions. The mass terms for fermions are added to the SM Lagrangian, $\mathcal{L}_{SM}$, by hand through the coupling to the Higgs field. The Yukawa Lagrangian is written as:

$$\mathcal{L}_{Yukawa} = -i\sum_f \lambda_f \Psi_f^\dagger \Phi \Psi_f, \tag{2.22}$$

where the sum is given over all fermions f. This coupling of the fermion to the Higgs field is called the Yukawa coupling (λ_f). The resulting mass is related to the vacuum expectation value from the Higgs potential and the Yukawa coupling of the fermion to the Higgs field. The Yukawa couplings for most leptons are very small, however the Yukawa coupling for the top quark is given by:

$$\lambda_t = \frac{\sqrt{2}m_{\text{top}}}{\nu} \approx 1. \tag{2.23}$$

Due to the large Yukawa coupling, the top quark, via loop-corrections, has the largest coupling to the Higgs field and can help determine the Higgs boson mass along with the precision measurement of the W boson.

The fact that the Yukawa coupling of the top mass is so large, and the single loop diagrams for the corrections to the Higgs mass are divergent; there needs to be a fine-tuning such that the Higgs boson is in the range it is currently expected. Thus, a cut-off scale is introduced as an upper limit to which the SM is valid. A simple way to solve this problem is to introduce symmetrical particles, which only contain spin-1/2 differences to each other. As a result, the loop diagrams will cancel and thus no fine-tuning is required to obtain a Higgs mass with an order ≈ 200 GeV. This solution is the basis for most supersymmetric models, which are being searched for at the LHC.

The list of particles described within the SM, along with their measured masses is found in Figure 2.2. The only unknown on the plot is the mass of the Higgs boson, which has a lower limit of 114 GeV from direct searches at LEP [26]. Limits from the Tevatron, ATLAS and CMS have also narrowed the search for the Higgs Boson [27–29], which have narrowed the allowed range of the Higgs boson mass to $115.5 < m_H < 127$ GeV. ATLAS and CMS experiments both show hints of excess data at about 125 GeV.
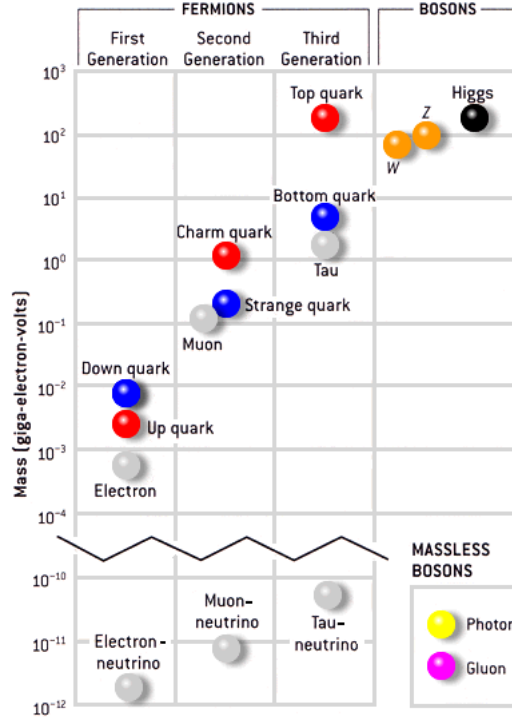
Figure 2.2.: The relative masses of all particles within the SM. The only unknown is the expected Higgs Boson mass. Figure taken from [30].

2.1.4. Strong Force

The final force currently described within the SM is the strong force [31–33]. The strong force is described by Quantum Chromodynamics (QCD). QCD is described by the non-Abelian local gauge symmetry group SU(3). The quantum numbers of the strong force are the three colours (red,green,blue). The SU(3) group has nine eigenstates, eight of which are linear combinations of the three colours and the ninth is a colour singlet. The eight linear combinations are the eight gluons [34], which are the mediating gauge bosons in the strong interaction. The colour singlet state is not realized in nature. The strong force has several properties which make it unique in comparison to the other forces:

Asymptotic Freedom : At very low energies the strong force is large compared to the other forces (such as the weak force). However, when the energy of the interaction is very large, the force is much weaker. Quarks act as free particles in this energy range. David Gross, David Politzer, and Frank Wilczek were awarded the Nobel Prize in Physics in 2004 for this discovery.

Confinement : Free quarks cannot exist as observable entities. Quarks combine to form *colour neutral* objects such as mesons or baryons (two quark or three quark objects). They cannot be broken into single quarks since the force required to separate them grows larger than the potential to create two new quarks. Thus, nature chooses to create the additional pair of quarks, creating two pairs, instead of allowing two free quarks.

Similarly to the electroweak interactions, the generators of the $SU(3)$ group are the eight so-called Gell-Mann matrices (λ_a). The Lagrangian can be written as:

$$\mathcal{L}_{QCD} = \sum_q \Psi^\dagger_{q,c}(i\gamma^\mu D_\mu - m)\Psi_{q,c} - \frac{1}{4}G^a_{\mu\nu}G^{\mu\nu}_a, \qquad (2.24)$$

where the covariant derivative is given by:

$$D_\mu = \partial_\mu + ig_s t_c \mathcal{A}^c_\mu. \qquad (2.25)$$

The gluon field strength tensors are denoted by G^a_μ, the $\mathcal{A}^a_\mu$ are the gluon fields running over all possible colour eigenstates. The coupling constant of the strong interaction is given by g_s. This constant of the strong interaction is related to the coupling constant (α_s) as:

$$\alpha_s = \frac{g_s^2}{4\pi}. \qquad (2.26)$$

However, both g_s and α_s are not constant. α_s is shown in Figure 2.3. The strength of the coupling changes based on the the energy scale. At high energies, α_s becomes very small, this is one of the results of asymptotic freedom. The quarks then can be considered as free objects. Also to note, α_s depends on which scale is chosen.
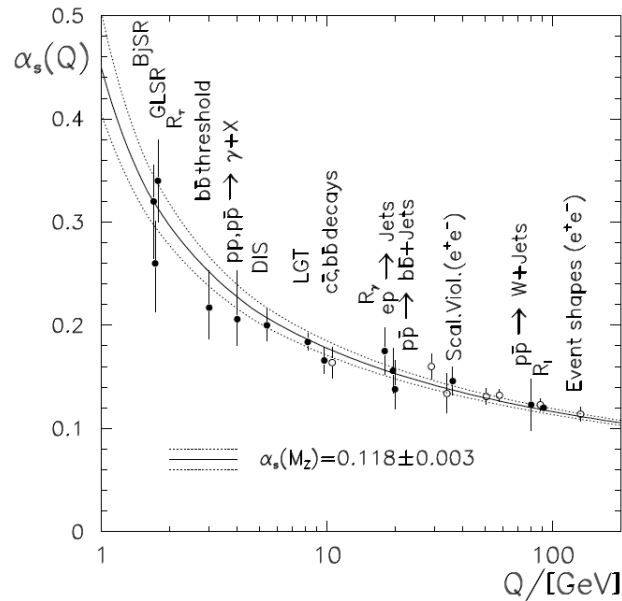

Figure 2.3.: The coupling constant, α_s, of the strong force. α_s is energy dependent, diverging at low energies and becoming very small at high energies. Due to this property, quarks are considered free at high energies, or small distances. The size of the constant is also dependent on the scale chosen, in this case, the mass of the Z boson is taken for reference. The figure is taken from [35].

2.1.5. Lagrangian of the Standard Model

The Lagrangian for the SM $\mathcal{L}_{SM}$ can now be organized by the Higgs component, fermion component, gauge components, and Yukawa component.

$$\mathcal{L}_{SM} = \mathcal{L}_{gauge} + \mathcal{L}_{Yukawa} + \mathcal{L}_{Higgs} + \mathcal{L}_{fermion} \tag{2.27}$$

where the components are given by:

$$\mathcal{L}_{gauge} = -\frac{1}{4}F^{\mu\nu}F_{\mu\nu} \tag{2.28}$$

$$\mathcal{L}_{Yukawa} = -i\sum_f \lambda_f \Psi_f^\dagger \Phi \Psi_f \tag{2.29}$$

$$\mathcal{L}_{Higgs} = (D^\mu\Phi)^\dagger(D_\mu\Phi) - V(\Phi) \tag{2.30}$$

$$\mathcal{L}_{fermion} = i\sum_f \Psi_f^\dagger \gamma^\mu D_\mu \Psi_f \tag{2.31}$$

In this way, the separate parts of the Lagrangian are responsible for several properties of nature. The gauge term is responsible for the gauge boson interactions (W, B and G), the Yukawa creates the mass terms due to the particle interaction with the Higgs scalar field (Ψ), the Higgs potential is created by the Higgs component and the fermion component is responsible for fermion interactions within the SM.

2.2. The Top Quark

The top quark has a special role within the SM due to its unique properties. The top quark is the heaviest known particle within the SM. From electroweak precision fits, it is expected to be larger than the SM Higgs boson. Since it takes a large amount of energy to create top quarks it took physicists almost 20 years from the discovery of bottom quark to confirm its existence. As a result, the top quark was only discovered at the Tevatron proton anti-proton collider. Direct searches at LEP could not discover the top quark in the e^+e^- collider [36, 37] due to insufficient centre-of-mass energy. The only other place where the top quark has been seen experimentally is at the LHC [38]. At the LHC, due to high luminosities and high energies, top quarks are produced abundantly.

The top quark is a very good probe of SM physics. Since the top quark is so much heavier than the bottom and W boson combined, the two particles to which it decays, it can decay very rapidly, even quicker than hadronization. This results in a top quark which passes on its properties, such as its spin and helicity, directly to its decay products. The CKM matrix entry for V_{tb} is almost 100 %. The value from the PDG is [15]:

$$V_{tb} = 0.999152^{+0.000030}_{-0.000045}. \tag{2.32}$$

Furthermore, because the coupling of fermions to fields is given by the Yukawa coupling, the strength of which is proportional to the mass, the top quark may give the first hints into physics beyond the SM. Therefore precise measurements of the top quark properties are important to test the SM and to which extent it is valid. The LHC will help shed light on these properties since a significant number of top quarks are produced. The properties of the top quark are described in the following sections.

2.3. Top Quark Production

Top quarks can be produced one of two ways at the LHC. Either top quarks can be produced in pairs ($pp \to t\bar{t}$) through the strong interaction, or they are produced as single quarks due to electroweak processes. The $t\bar{t}$ pairs are produced significantly more than the single top processes, which will be discussed in the following section.

The process which describes $t\bar{t}$ production is Quantum Chromodynamics (QCD). Two protons are rotated in opposite directions where they are made to collide with one another. At very small energies, proton collisions would resemble two point-like objects. However, it is known that at higher energies the proton can be broken down into further objects: quarks and gluons. It is the collision between the quarks and gluons from the opposite turning protons which create the $t\bar{t}$ pairs.

In the Leading Order (LO) scenario, two incoming particles produce two outgoing top quarks. The cross section (σ) for such a $2 \to 2$ process is given by:

$$\sigma_{pp \to X} = \sum_{i,j} \int dx_i dx_j f_{p_1}(x_1, Q^2) f_{p_2}(x_2, Q^2) \hat{\sigma}_{i,j}(x_1, x_2, \alpha_s) \tag{2.33}$$

where x_a represents the momentum fraction of the two colliding partons, $\hat{\sigma}_{a,b}$ stands for the partonic cross section and Q^2 is the scale at which the process takes place. The indexes i, j sum over quarks, anti-quarks and gluons. The f_{p_i} are the parton distribution functions (PDFs) which describe the constituents of the proton and the probability to which partons carry a certain amount of the proton momentum. This model is known as factorization and is shown schematically in Figure 2.4.
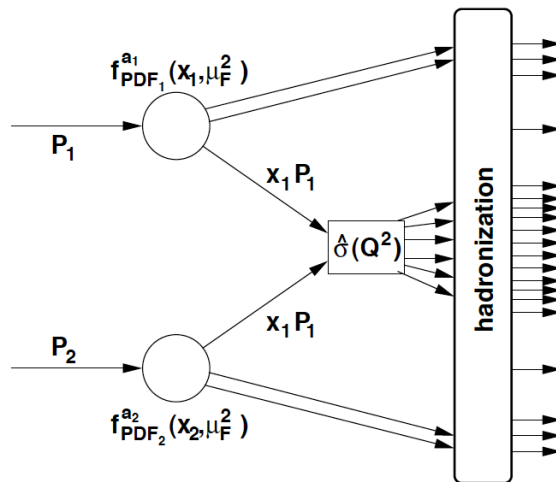

Figure 2.4.: Factorization model for a hard scattering process which describes two constituents of the incoming protons which collide together. The resulting hard scattering process and hadronization is displayed. Taken from [39].

It is known through deep inelastic scattering experiments, that protons are not point-like objects. A proton is comprised of three valence quarks: two up quarks and one down

quark. However, at higher energies, those of the LHC, due to the non-Abelian nature of SU(3) and also the asymptotic freedom behaviour of QCD, the proton is filled with a large number of quarks and gluons. At smaller distances, the proton is filled with self-interacting gluons and so-called sea-quarks, produced in quark anti-quark pairs from gluons. With higher energies, these gluons and sea quarks will carry enough energy to produce top quarks at the LHC when the two constituents of the protons collide. The PDF used in CTEQ6 is found in Figure 2.5.
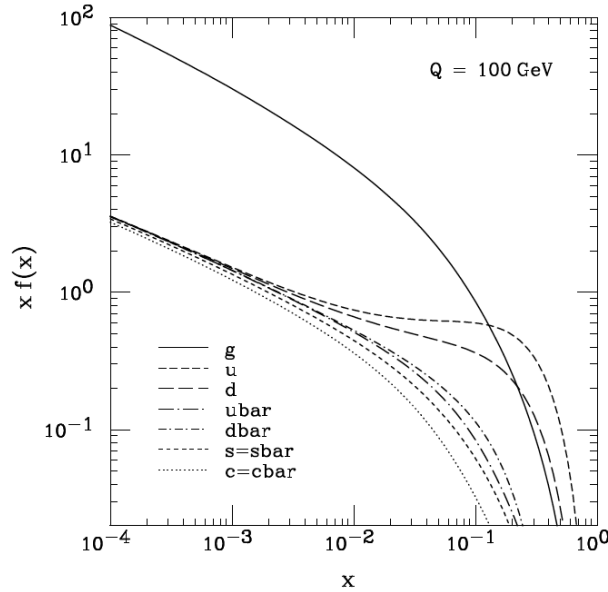

Figure 2.5.: Proton density function (xf) as a function of the proton momentum fraction (x) from CTEQ6M [40]. The majority of the momentum is carried by the three valence quarks: two up and one down quark. When a proton carries a relatively small amount of energy, most of the $t\bar{t}$ pairs will be created by these valence quarks since they contain enough momentum and energy to create $t\bar{t}$ pairs. However, as the energy of the proton is increased, a larger number and fraction of gluons and sea quarks carry a sufficient amount of the fraction of the proton energy.

At leading order, to create a $t\bar{t}$ pair, either a quark anti-quark pair of opposite type need to annihilate, or two gluons need to fuse together. The two possible production scenarios are depicted in Figure 2.6. Though these are the same production mechanisms as the Tevatron, the rates for the individual processes have changed. At the Tevatron with $\sqrt{s} = 2$ TeV, $q\bar{q}$ annihilation was the predominant mechanism in creating $t\bar{t}$ pairs ($\approx 90\%$). At the LHC, at $\sqrt{s} = 7$ TeV, gg fusion is more likely to produce $t\bar{t}$ pairs ($\approx 80\%$).

The reason of such a reversal from the Tevatron to the LHC in likely production mechanisms for $t\bar{t}$ pairs comes from two different sources: the LHC is a pp instead of $p\bar{p}$ collider and the larger centre-of-mass energy. Since the LHC is a pp collider, there are no valence anti-quarks. All the valence quarks are of u and d type. As a result, for a $q\bar{q}$ collision to occur, at least one of the two quarks needs to be a sea quark, which is carrying significantly less momentum than a valence quark.
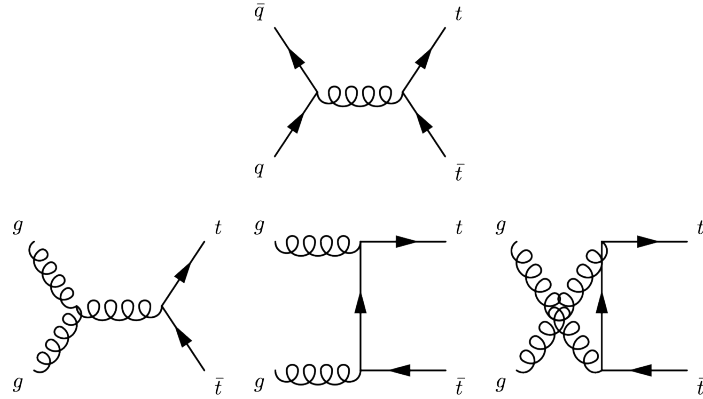
Figure 2.6.: Leading order Feynman diagrams for $t\bar{t}$ production. (Top): Quark - antiquark annihilation, where a valence quark and sea quark annihilate or two sea quarks annihilate. (Bottom): Gluon fusion. There are three separate indistinguishable LO gluon fusion production possibilities.

The second reason for the reversal in expected production mechanisms comes from the higher energy at the LHC. With higher energy, gluons and sea quarks will contain a larger proton momentum and energy. As a result, they will be able to produce $t\bar{t}$ pairs more significantly. Since there is a larger number of gluons than sea quarks in the proton at high energies, and the fraction of momentum needed to create $t\bar{t}$ pairs is smaller, gluon fusion is the predominant $t\bar{t}$ production mechanism at the LHC.

Using a classical example, the energy needed of the two proton constituents to create a $t\bar{t}$ pair has to be at least the mass of the two top quarks (≈ 350 GeV). Therefore, if two identical objects carrying each the same amount of energy collide, the minimum fractional energy of the constituent is given by the following expression:

$$x_{t\bar{t}} = \frac{E_{t\bar{t}}}{E_{\sqrt{s}}}. \tag{2.34}$$

At the LHC, using $E_{\sqrt{s}} = 7$ TeV, the proton fraction momentum required to create a $t\bar{t}$ pair is only $x_{t\bar{t}} = 0.05$, compared to at the Tevatron where it was $x_{t\bar{t}} = 0.18$. At proton momenta of the $t\bar{t}$ production threshold, gluons are predominant in the proton, as seen in Figure 2.5, and result in gluon fusion being the predominant process.

The overall cross section for the production of $t\bar{t}$ events increases significantly when moving from Tevatron to the LHC. In fact, at $\sqrt{s} = 7$ TeV, the cross section is over ten times higher than at the Tevatron during Run II. The cross section of different physics events is shown in Figure 2.7 for the Tevatron and LHC at energies of 7, 10 and 14 TeV.

The figure shows the rise in $t\bar{t}$ cross section as one goes to higher energies. It also highlights the challenges in obtaining a $t\bar{t}$ event from all of the events produced by LHC collisions. At 7 TeV, there is approximately a nine order of magnitude difference between the total cross section σ_{tot} and σ_{t}. That requires on average an order of 10^9 collisions for every 1 top event. For observing Higgs events, the ratio is at least an order of magnitude larger. As a result, the LHC needed to move to higher luminosities than those at the Tevatron in order to have a chance to observe the Higgs and to produce a significant amount of $t\bar{t}$ pair events with only several years of LHC running. This also produces a
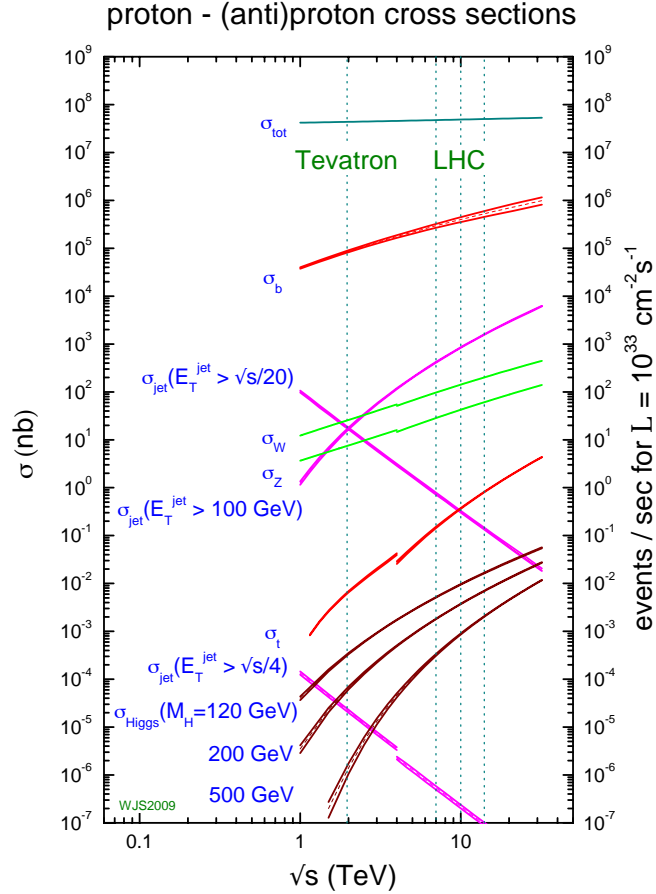
proton - (anti)proton cross sections

Figure 2.7.: Theoretical cross section for several physics processes at the Tevatron and LHC. The two energies ($\sqrt{s} = 7$ TeV and 14 TeV) for the LHC operating points are highlighted. This figure shows two important concepts: firstly, the large increase in the order of magnitude for the top cross section (σ_t) and the large total cross section (σ_{tot}) from which top events need to be chosen. This figure is taken from [41].

larger challenge to select the physics events from the large amount of total events. Also, more sophisticated detectors and trigger streams to select interesting events are needed.

One of the theoretical $t\bar{t}$ cross sections in pp collisions calculated at the approximate NNLO level by [42], using a top quark mass of 173 GeV and PDF set MSTW [43] is:

$$\sigma_{t\bar{t}}^{\text{theo.}} = 163 \, {}^{+7}_{-5} \, (\text{scale}) \, \pm \, 9 \, (\text{PDF}) \text{ pb}. \tag{2.35}$$

The first cross section measurement at $\sqrt{s} = 7$ TeV at ATLAS using a profile likelihood on the first 35 pb^{-1} collected during the 2010 ATLAS run found a $t\bar{t}$ cross section of [44]:

$$\sigma_{t\bar{t}}^{ATLAS} = 187 \pm 11 \, (\text{stat.}) \, {}^{+18}_{-17} \, (\text{syst.}) \pm 6 \, (\text{lumi.}) \text{ pb}, \tag{2.36}$$

and is one of the most precise published measurements ever made on the $t\bar{t}$ cross section.

2.4. Single Top

Top quarks can not only be produced in pairs, but also via electroweak single top quark production. Single top production occurs via the weak interaction. Single top was first observed at the Tevatron at both CDF and DØ experiments [45, 46]. Measurements give a direct handle on the V_{tb} entry in the CKM matrix and a look at the electroweak coupling. There are three separate processes which can result in single top events. The three processes in the production of single top quarks, listed in order of highest to lowest cross section are:

t-channel space-like single top production through a virtual W boson. The production occurs with a light quark,

Wt-channel associate Wt production from a heavy b quark. Along with the top, a W boson is radiated,

s-channel time-like production through a W boson decaying to a top and b quark.

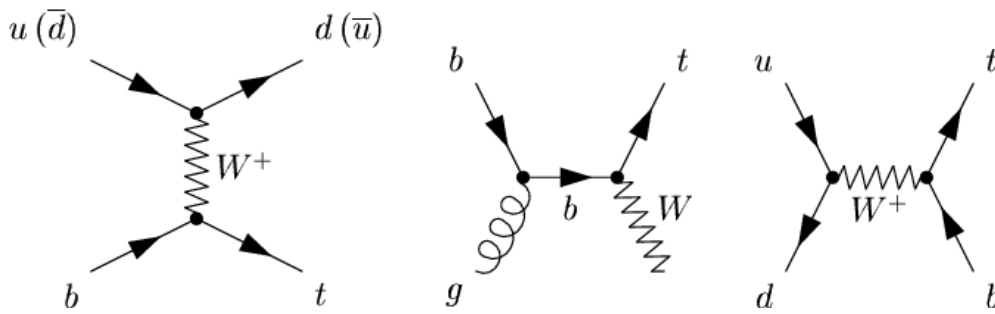The LO Feynman diagrams for the three separate processes are visualized in Figure 2.8.

Figure 2.8.: Feynman diagrams depicting the production of single top events at the LHC. (Left): t-channel production with a virtual W and b. This decay channel is dominant at the LHC. (Middle): Associate Wt production of a top quark, and (Right): s-channel production of a single top. Single top decays are treated as signal in this analysis due to their dependence on top mass. Feynman diagrams are taken from [47].

These processes account for only a small amount of top quark production [48–50], using a top mass of 172.5 GeV, the cross sections are:

$$\sigma_t = 64.57 \pm 1.33 \text{ (scale)} \, ^{+1.38}_{-0.68} \text{ (PDF) pb (t)}, \tag{2.37}$$

$$\sigma_t = 15.74 \pm 0.40 \text{ (scale)} \, ^{+0.66}_{-0.68} \text{ (PDF) pb (Wt)}, \tag{2.38}$$

$$\sigma_t = 4.63 \pm 0.07 \text{ (scale)} \, ^{+0.12}_{-0.10} \text{ (PDF) pb (s)}. \tag{2.39}$$

Since single top cross sections are large enough at the LHC, the t-channel observation [51] and cross section measurement [52] at ATLAS has already taken place using only the first 200 pb^{-1} and 0.7 fb^{-1} respectively. It is also important to note that the single top quark production cross sections for t and $\bar{t}$ are not the same ($\sigma_t \neq \sigma_{\bar{t}}$).

2.5. Top Quark Decay

Once top quarks are produced, they decay rapidly via the weak force. The decay of the top quark within the SM, is via a $W^{\pm}$ boson to either one of the down, strange, or bottom quarks. The probability for a given quark from the top decay is described by the CKM matrix. The CKM matrix is theorized to contain a V_{tb}, which when squared, gives the probability of a top decaying to a bottom through the W boson. The value of $|V_{tb}|^2$ is found to be almost 1; the exact value is shown in Eq. 2.32. This means that almost all of the top decays are to a bottom quark.

Using the two properties of the top quark: that the mass is large and that the V_{tb} entry of the CKM matrix is almost unity, it is possible to calculate the lifetime of the top quark. Using only exclusive $t \to Wb$ decays ($|V_{tb}|^2 = 1$), one can calculate the expected top width given a certain top mass, assuming $m_b = 0$ and $m_t = 170$ GeV/c^2 and $m_W = 80.4$ GeV/c^2 [53,54]:

$$\Gamma_t = \frac{G_F \, m_t^3}{8\pi\sqrt{2}} \times |V_{tb}|^2 \left(1 - \frac{m_W^2}{m_t^2}\right)^2 \left(1 + 2\frac{m_W^2}{m_t^2}\right) \left[1 - \frac{2\alpha_s}{3\pi}\left(\frac{2\pi^2}{3} - \frac{5}{2}\right)\right] \approx 1.5 \text{ GeV/c}^2.$$

$$(2.40)$$

In the equation, G_F denotes the Fermi coupling constant. The top width of 1.5 GeV/c^2 corresponds to a top lifetime of about $5 \cdot 10^{-25}$ s. Since this means:

$$\Gamma_t > \Lambda_{QCD} \approx 200 \text{ MeV/c}^2, \qquad (2.41)$$

the top quark decays before hadronizing. The hadronization time scale is of the order of 10^{-24} s: an order of magnitude longer than the lifetime of the top quark. This makes the top quark of special interest to study. It does not hadronize with a second quark and is therefore a "bare" quark.

With top quarks decaying exclusively via $t \to Wb$, the classification of a t decay is solely based on the decay of the W boson. The W boson has the possibility of either decaying hadronically or leptonically: $W \to q\bar{q}$ or $W \to l\nu_l$. Also to note, the two quarks to which the W can decay hadronically are not of the same type since the pairs total charge must be equal to the original ± 1 of the original W. Taking the $t\bar{t}$ decay to be:

$$t\bar{t} \to W^+W^-b\bar{b}, \qquad (2.42)$$

along with the two W bosons, there will always be two bottom quarks in all possible $t\bar{t}$ decay channels. The probability for a W boson to decay hadronically is 2/3 compared to the possibility of decaying into a charged lepton and neutrino, which is only 1/3. In the first scenario, there are six possible outcomes compared to only three in the leptonic decay. From the decay of the two W bosons, the decay can be classified as:

alljets : both W bosons decay into two quarks each, leaving 6 jets in the final $t\bar{t}$ decay, two of which are b jets,

lepton + jets : one W boson decays into two quarks and the other into a charged lepton and neutrino, resulting in two b quarks, two light quarks and a lepton and neutrino. In this case, the W decay to tau is only partially considered since the tau will decay furthermore. Only the tau final states containing an electron or muon are considered, or

dilepton : both W bosons decay into a charged lepton and neutrino separately resulting in two b quarks, two charged leptons and two neutrinos.

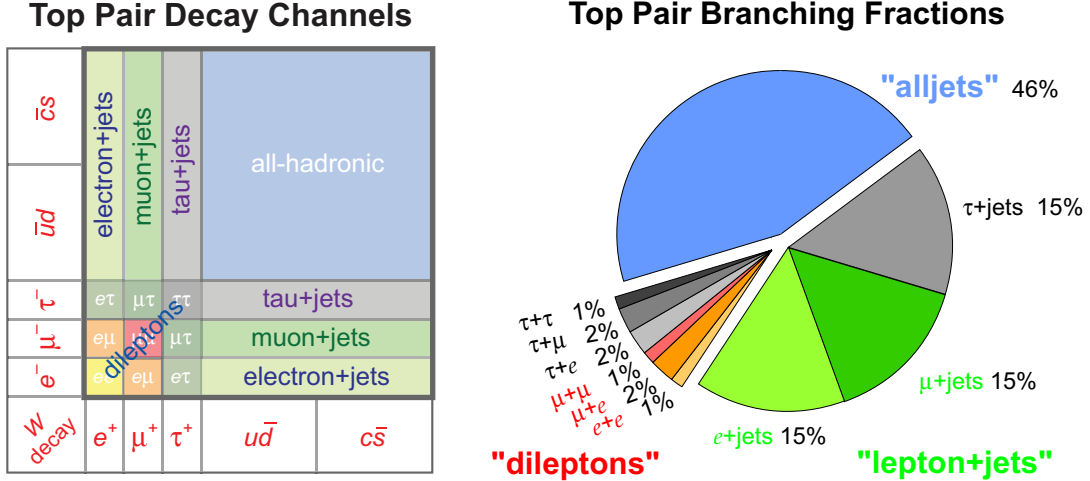The detailed decay possibilities along with the branching ratios are shown in Figure 2.9.

Figure 2.9.: $t\bar{t}$ decay modes and their branching rations. The $t\bar{t}$ decay only depends on the possible decays of the two W bosons. The decay is limited to three general categories: alljets, lepton+jets, or dilepton. Figures taken from [55].

It is possible to measure the top mass in all three channels of decay, each having its own advantages and disadvantages. The resulting topology of the events from each channel are slightly different. In the alljets channel, the two b quarks are among a six quark jet final state. This channel has a large branching fraction ($\approx 46\%$) and no missing transverse energy ($\not{E}_T$) from an escaping neutrino. Even though this channel is very susceptible to variations in the Jet Energy Scale (JES), it allows the possibility to measure two W boson masses to obtain a handle on the scale. The alljets channel however has a very large background contribution from QCD multijets, events which are very difficult to model and must be understood from data.

The dilepton channel is the other extreme. In this scenario, two charged leptons with their neutrino pairs are created alongside the two b quarks. There is a very small branching fraction of $t\bar{t}$ decays in this channel, only about 9%. There is also a large $\not{E}_T$ component and limited kinematic knowledge as the system is under-constrained. The dilepton channel however has a very clean signature. As a negative, the channel has no handle on the JES as both W bosons decay to leptons only.

The last channel, lepton + jets or single lepton, is a mixture of the two extremes. In the lepton + jets channel one W decays leptonically and the other hadronically, resulting in two light quarks, one charged lepton and one neutrino alongside the two b quarks. The branching fraction is still quite large, even when only the τ + jets decays where the tau decays leptonically are considered. The signature is also clean, comprising of two light jets, two b jets, a charged lepton and some $\not{E}_T$. The channel suffers from effects due to variations in the JES, but still contains a hadronically decaying W boson in order to

measure the scale. The JES, however, is still one of the largest challenges to properly determine the top mass in this channel. The lepton + jets decay channel is shown in Figure 2.10.
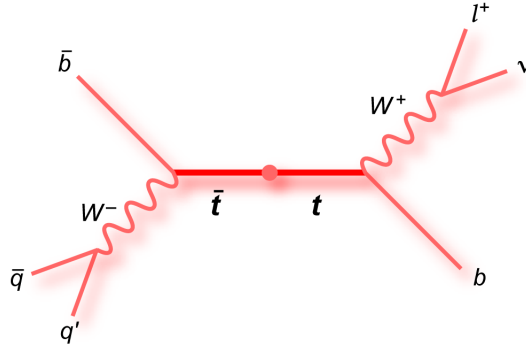

Figure 2.10.: Diagram of the $t\bar{t}$ decay into the lepton + jets channel. In this decay scenario, one W decays into two light quarks whereas the second W decays into a charged lepton and a neutrino. The original two b quarks from the $t \to Wb$ highlight the signature. This Figure is taken from [55].

A candidate $t\bar{t}$ event at ATLAS, decaying into the lepton + jets channel where the reconstructed lepton is an electron, is found in Figure 2.11. The decay contains four jets, one electron and a significant amount of missing energy from the neutrino.
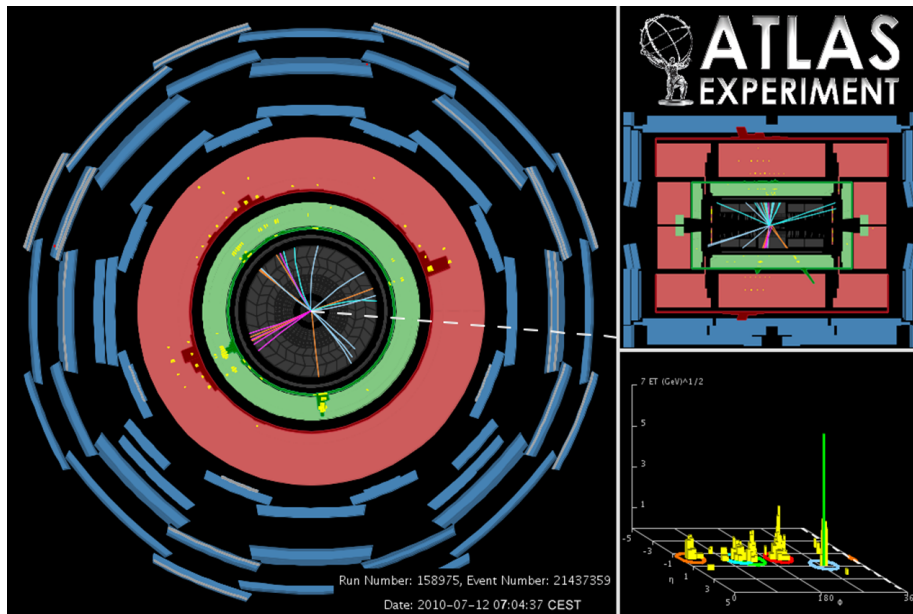

Figure 2.11.: Candidate $t\bar{t}$ decay into the lepton + jets channel at ATLAS. Four jets are reconstructed along with the electron, which contains a single track. The dashed line shows the direction of the missing energy in the transverse direction, representing the neutrino. Figure is taken from [56].

2.6. Four Jet Inclusive Final State

The final state containing four jets and one charged lepton is not unique to the $t\bar{t}$ pair decay in the lepton + jets channel. Several other physics processes contain a similar signature. This signature can either occur due to four jets and a real lepton or as the result of a misidentification of a lepton. The following processes are separated by either real charged lepton or a misidentified lepton.

2.6.1. Real Charged Lepton

The largest physical background in the $t\bar{t}$ decay to lepton + jets channel is from W + jets events. This is a process which contains a real charged lepton + neutrino and jets. With larger energies, this physics process occurs significantly in the four jet inclusive signature[2]. The significant contribution is the result of the production of a W through the weak force and at least four jets due to QCD multijet production from the strong force. In some occasions, though only with a small probability, a gluon can produce a $b\bar{b}$ pair similar to the two b quarks in the $t\bar{t}$ decay[3]. Therefore b-tagging, the process via which a jet is determined to have come from a b quark, can significantly help reduce this large background, however cannot completely eliminate it. The background process is realized in Figure 2.12.

In addition to $Wb\bar{b}$ + jets heavy quark production, it is possible to produce $c\bar{c}$ pairs which are also treated differently from the light quark pairs, since they are also *heavy* with respect to the light pairs. The final heavy quark production can also be the result of Wc + jets. In this scenario, however, one of the quarks from the W must be improperly reconstructed as a lepton. This process is considered, but does not have a significant contribution to the total W + jets background.
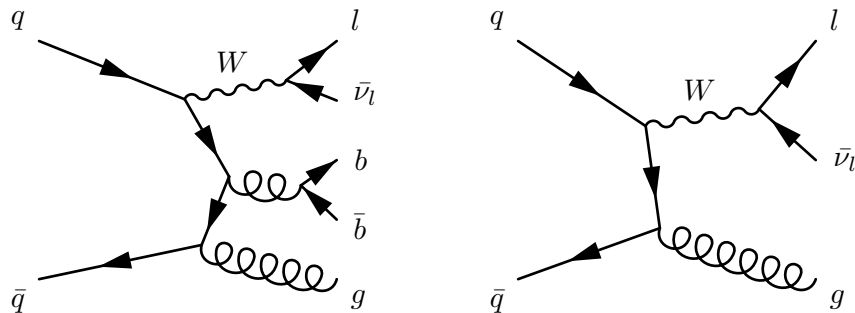

Figure 2.12.: W + jets background processes. (Left): $Wb\bar{b}$ + jets event where a gluon splits into a $b\bar{b}$ and the W decays into a charged lepton and neutrino. There is no misidentification in this process as it contains the same final state as a single lepton $t\bar{t}$ decay with two b quarks. (Right): W + jets event where a light quark is improperly tagged as a b jet.

The second process which contains a real lepton is in the Z + jets channel. Similar to the W + jets, the Z + jets channel contains a Z produced from the weak interaction of

---

[2]Four or more jets in the final state.
[3]Heavy quark production is denoted by $Wb\bar{b}$ + jets.

quarks. The extra jets are produced via QCD. In this process, a gluon splitting into a $b\bar{b}$ pair can produce real heavy jets in this signature. This process is denoted by $Zb\bar{b}$ + jets. The same is true for $Zc\bar{c}$ + jets, similar to the W + jets process.

In the Z + jets signature, the Z decays into a $l\bar{l}$ pair, in which one of the leptons is not reconstructed. The result is a real lepton, missing energy and jets. The Z + jets Feynman diagram is found in Figure 2.13.
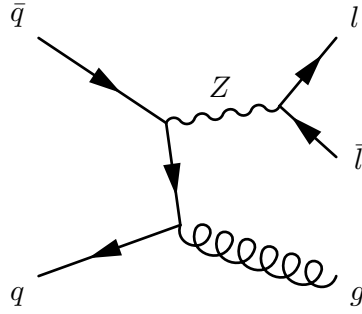

Figure 2.13.: Z + jets background signature. One of the leptons from the $Z \to l\bar{l}$ decay is not reconstructed. The Z is produced via the weak interaction whereas the addition jets arise via the nature of the strong force.

The third process which may result in a four jet inclusive final state with a real charged lepton comes from single top decay, described in Section 2.4. Single top's most dominant decay channel at the LHC is the t-channel, where a space-like W and b result in a top quark. Since this final state is top mass dependent, it is taken as a signal contribution for the analysis. This leaves the background mass independent. The three possible decay signatures for single top at the LHC are shown in Figure 2.14. In all three possible scenarios, a real charged lepton and neutrino result from a $t \to Wb$ decay. Due to the strong force, QCD multijets appear as the other jets in the signature.
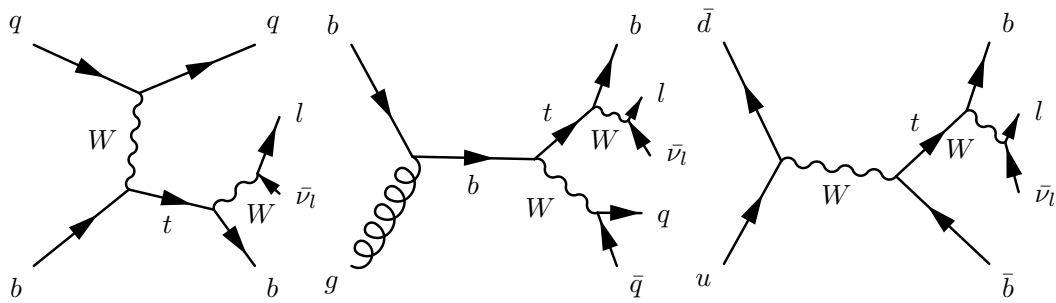

Figure 2.14.: (Left): t-channel, (middle): Wt associate production channel, and (right): s-channel single top production along with the decay signature. In all three contributions, a real charged lepton and neutrino appear in the final state. The resulting extra quarks are produced by the strong interaction. Some of these quarks may be b quarks. This signature is also top mass dependent.

The last background process described is the diboson production. In this case, two bosons, either: WW, WZ, or ZZ are produced simultaneously. The resulting decay produces a real lepton. The WW channel will have a resulting charged lepton and jets similar to the two W bosons decaying in the lepton + jets decay. The same signature is true in the WZ diboson scenario, where the W boson decays leptonically and the Z boson into two quarks. In the ZZ channel, two quarks and two charged leptons are produced, one of the leptons is not be reconstructed. The decay signature of the three diboson processes are found in Figure 2.15.
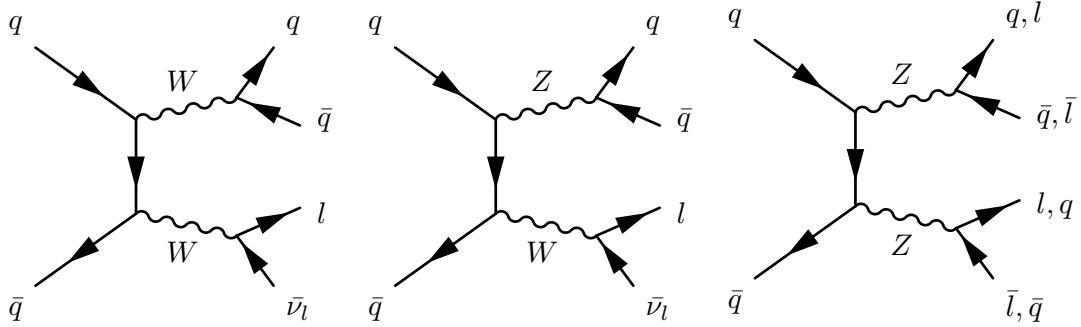

Figure 2.15.: Diboson production and decay signature. (Left): WW decay into $q\bar{q}$ pair and a charged lepton and neutrino. (Middle): WZ decay similar to the WW decay signature and (right): ZZ decay where one Z decays into a $q\bar{q}$ pair and the other Z boson decays into two leptons, where one of the leptons is missed.

2.6.2. Misidentified Lepton

The following set of background events arise from a misidentification of the charged lepton. This misidentification occurs in both the e + jets and μ + jets channels as a result of several different reasons. In the e + jets channel, a jet can be misidentified as an electron. This occurs as a result of the signature in the detector which are similar for jets and electrons. In the μ + jets channel, a b jet may decay semi-leptonically, resulting in a μ. This μ is expected to be reconstructed inside the jet[4], in this case however it is reconstructed outside the jet and is therefore taken as a signal lepton from a W decay and not from a b jet.

QCD multijets is a background in the four jet inclusive channel as a result of a misidentified lepton. QCD multijets production occurs via the strong force. In this scenario, jets are produced due to the nature of the strong interaction. As a result, in a significant portion of events, the event will only contain jets. Due to misidentifications of the jets, it is possible that a jet is improperly reconstructed as a lepton in both channels. The resulting QCD multijets production will then appear as $t\bar{t}$ background. The signature of this process in both channels is found in Figure 2.16. This background is significantly reduced through the identification of a b jet.

---

[4]A μ reconstructed within the jet is denoted as *non-isolated*; a μ outside of a jet: *isolated.*
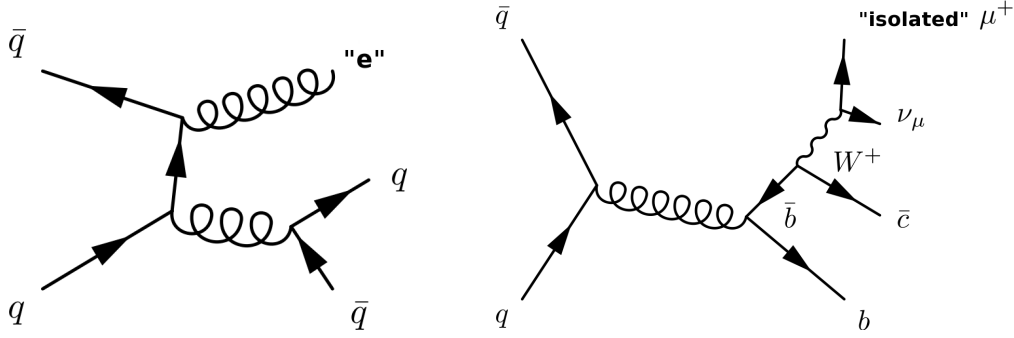
Figure 2.16.: (Left): QCD multijets event where a jet is misidentified as an electron and (right): QCD multijets event where a semi-leptonically decaying b quark produces a muon inside the jet. However, the muon is reconstructed as isolated instead of non-isolated.

2.7. Properties of the Top Quark

The top quark is very unique with respect to the other quarks. Studying quarks is quite difficult due to the effects of hadronization. Quarks hadronize due to the nature of Quantum Chromodynamics (QCD) and its properties. As a result, the quarks have hadronized before they decay, thus their properties contain an interference term due to the bound state. This is however not the case for the top quark. The top quark in fact is completely unaltered before the decay; leaving the information of its pole mass, spin and charge directly to the decay products. Measurements of these properties can verify several expected phenomena of the SM:

- The charge of the top quark. Similar isospin quarks have the charge $+2/3$ e, however there is no reason other than symmetry as to why this is also the top quark charge. It is possible that the top quark charge is instead an exotic $-4/3$ e. Therefore the charge of the top quark is verified experimentally.

- The $V - A$ structure of the Wtb coupling, where V and A are the vector and axial vector contributions to the vertex. This is a fundamental principle of the weak force. Measurements of the W helicity are made from the W boson offspring of the top quark, checking for longitudinally polarized and left-handedly polarized components. It is expected that there are no right-handedly polarized W bosons decaying from top quarks in the SM.

- If the top mass is the same as its anti-matter partner: the anti-top ($\bar{t}$). This would verify CPT symmetry in the top sector.

- The spin of the top quark. Since the decay is so quick, the spin correlations of the top and anti-top quark can be measured directly by the angular distributions of the resulting decay products.

Such studies have yet to show any deviation from SM expected phenomena [57–60]. One of the most exciting properties of the top quark is its uniquely large mass.

2.7.1. Relationship to the Higgs Boson

As was stated, the top mass is linked to the Higgs boson mass. The Higgs mechanism breaks the electroweak symmetry at low energies. Each particle has a different coupling strength to this field. For example, a "massive" neutrino has a very small coupling to the Higgs field (the mass of the neutrino is very small), whereas the top couples very strongly. The top quark mass is the only fermion close to the electroweak scale, Λ_{QCD}. Due to this large mass, it indirectly limits the search for the Higgs boson. The coupling to the Higgs boson is shown in the Feynman diagrams in Figure 2.17.
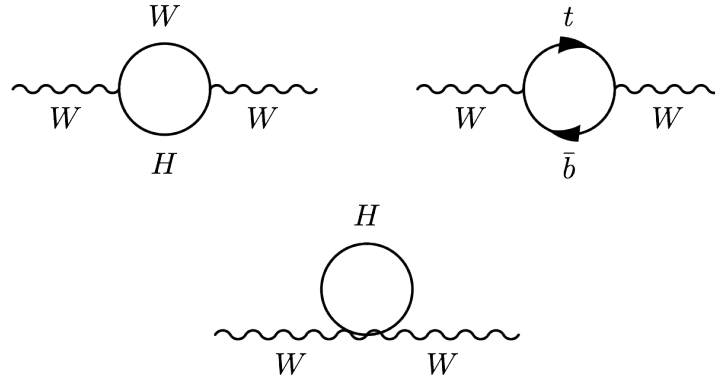
Figure 2.17.: Lowest order Feynman diagrams for corrections of the Higgs boson mass based on the top quark and W masses. These link the W boson mass, top quark mass and Higgs Boson mass.

The direct measurements of the top mass and W boson mass are the best handle on the indirect search for the Higgs boson. Every massive particle adds some virtual correction via loop diagrams to the Higgs boson mass. Fitting all the components of the observed electroweak variables can give an indirect limit on the SM Higgs boson. Taking the electroweak quantities, which include the masses and couplings of the weak bosons; they depend only on five of the 28 independent parameters in the SM. Three of the independent parameters are the Z boson mass [61], the Fermi coupling constant G_F, measured by the μ lifetime [62] and the electromagnetic coupling constant α [63]. Precision electroweak measurements help to determine these three independent SM parameters. The W mass is related to the Z mass and to the top quark mass due to radiative corrections given in [64]:

$$M_W^2 = \frac{\pi\alpha}{\sqrt{2}\mathrm{G_F}} \cdot \frac{(1 + \Delta r/2)}{\sin^2\theta_\mathrm{W}}, \tag{2.43}$$

where $\sin^2\theta_\mathrm{W}$ is the Weinberg angle defined as:

$$\sin^2\theta_\mathrm{W} \equiv \frac{\mathrm{M_W^2}}{\mathrm{M_Z^2}}; \tag{2.44}$$

the ratio squared of the mass of the W boson divided by the Z boson mass. The two extra corrections to the W mass come from the term Δr and are shown via loop diagrams. The W boson mass dependence on top quark mass is quadratic whereas the dependence on the

Higgs boson mass is logarithmic. The correction terms for the Higgs and the top quark are:

$$\Delta r_t \quad \approx \quad -\frac{3G_F}{8\sqrt{2}\pi^2 \tan^2\theta_{\mathrm{W}}} \cdot m_t^2 \tag{2.45}$$

$$\Delta r_H \quad \approx \quad \frac{3G_F M_W^2}{8\sqrt{2}\pi^2} \left(\ln\frac{\mathrm{m}_H^2}{\mathrm{M}_Z^2} - \frac{5}{6} \right) \tag{2.46}$$

As a result, the Higgs boson mass is sensitive to the top quark mass. The better the precision on the measurement of the top quark mass, the narrower the possible range for the SM Higgs boson. Using the combination of all the free parameters of the SM which contribute to the Higgs mass, including the masses of all known particles, a χ^2 fit of the electroweak SM is performed. The fit uses the measurements made previously at LEP and by SLD, CDF, and DØ collaborations. In this fit, the Higgs boson mass is a free parameter. The minimization of this fit is shown in Figure 2.18. Alongside this fit, the dependence of the top quark mass and W boson mass on the Higgs boson mass can be seen. Also highlighted are the boundaries for the direct search which is performed at the Tevatron and LEP. LHC results are not yet included in the combined fit, only in the direct exclusion limit setting seen by the shaded region of the figure.
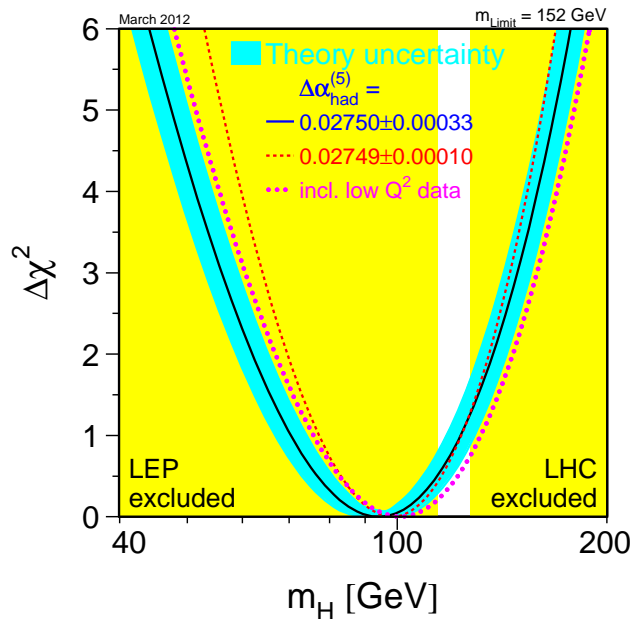

Figure 2.18.: Fit of the Electroweak data using a free Higgs boson mass. The minimum of the χ^2 fit shows the expected to Higgs boson mass. The yellow region is excluded by direct searches at the Tevatron, the LHC, and LEP. Updated in March 2012 with the new most precise mass measurement of the W Boson. Figure taken from [65].

It can be seen that the SM prefers a small Higgs mass, of 92 GeV with an experimental uncertainty of $+34$ and -26 GeV/c^2 at the 68 % Confidence Level (C.L.) [65]. The fit

corresponds to an upper bound on the SM Higgs boson mass, at 95 % C.L., of 161 GeV/c^2. From the 2-dimensional plot in Figure 2.19, the region where the Higgs boson is expected, highlighted by the green oval, leaves only a small overlapping area with the gray, which indicates the remaining possible Higgs boson mass range from direct searches at the LHC, Tevatron and LEP.
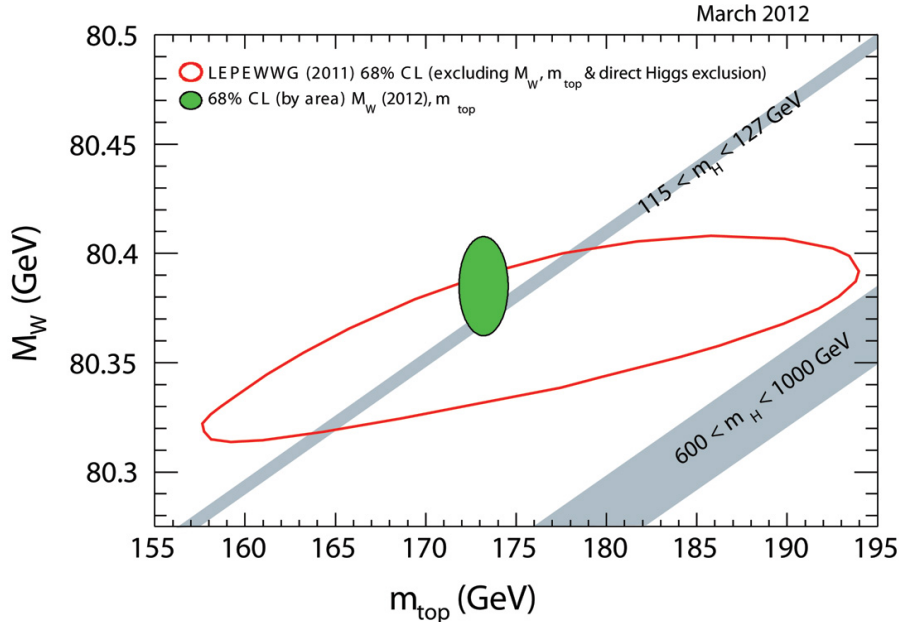

Figure 2.19.: Expected region of the Higgs boson mass due to direct measurements of the top quark and W boson masses, m_t and m_W respectively. The 2-dimensional plot gives the green 68 % C.L. contour from the electroweak fit using the latest top and W boson mass measurements. The remaining possible Higgs boson mass given by direct searches is shown in the gray region. This figure uses the latest electroweak combination [65].

2.7.2. Top Quark Beyond the SM

The large mass of the top quark not only sheds light on the search for the Higgs boson, but also possible extensions to the SM. The Higgs boson mass can be calculated using the corrections due to the top mass (its Yukawa coupling strength) and the W boson. These two corrections are the largest corrections to the Higgs boson mass due to the quadratic dependence on the mass.

$$m_H^2 = m_{H,0}^2 + \delta m_H, \tag{2.47}$$

where $m_{H,0}$ is the first order Higgs mass and δm_H is given by [66]:

$$\delta m_H = \frac{3\lambda_{UV}^2}{8\pi^2 \nu^2} \cdot (-4m_t^2 + 2m_W^2 + m_Z^2 + m_H^2). \tag{2.48}$$

The correction term to the Higgs boson mass (δm_H) is proportional to the squared mass couplings. ν represents the vacuum expectation energy at about 246 GeV. The unanswered

question is to the value of the SM cut-off: λ_{UV}. This cut-off represents the value up to which the SM is valid. If this cut-off is the Planck scale:

$$\lambda_{UV} = 10^{19} \text{ GeV} \tag{2.49}$$

then the terms in the Higgs boson mass correction are divergent and require fine-tuning in order to obtain a Higgs boson mass $\mathcal{O}(100 \text{ GeV/c}^2)$.

A possible solution to this fine-tuning (or Hierarchy) problem is the addition of new particles which can cancel the divergent loop corrections to the Higgs mass. These particles appear in super-symmetric models as the partners to all fermions and bosons, which contain the opposite statistics. As a result, fermions have bosonic super-symmetric partners and vise-versa. In the correction to the Higgs mass, these terms cancel one another due to the change in sign. The λ_{UV} may then be of the order of a few TeV and the mass of the Higgs may be naturally small. The understanding of the top mass and its value is key to verify the SM and possible extensions. Due to its large mass, the top quark mass and Yukawa coupling may still play a special yet to be determined role in the SM or future extensions.

2.7.3. Top Quark Mass Definition

There are several different top quark mass definitions. The top mass presented thus far has been the mass used in the electroweak fit. This mass is denoted as $M_{\overline{MS}}$ which is used in the $\overline{MS}$ renormalization scheme. This mass is calculated to be 10 GeV/c^2 smaller than the pole mass M_{pole}, which is the top mass calculated in the electroweak fit for $t\bar{t}$ production [67–69]. For a mass measured from the cross section, renormalization is used and therefore such a mass is calculated.

Direct measurements of the top quark mass are made using a calibration given by the MC. The mass within the MC generator is given as M_{MC}. The top quark pole mass can be calculated from the MC top mass to the first order by [70]:

$$M_{pole} = M_{MC} + Q(\alpha_s(Q)c), \tag{2.50}$$

It is expected that the coefficients (c) and scale (Q) are of the order 1 GeV/c^2. They are given by the MC parton showering and the cutoff for radiation [71]. As a result, the M_{MC} is expected to have a difference of $\mathcal{O}(1 \text{ GeV/c}^2)$ to the pole mass. For all direct measurements, the MC top quark mass is used. This is also the case for the measurement described in this thesis.

2.7.4. Previous Measurements of the Top Quark Mass

Since its discovery in 1995, the top quark mass has been measured using a variety of different techniques. With the understanding of detector performance and over 20 years of run time, the top quark mass became the most well known mass of any quark. The precision of the mass is of the order of 0.5% from the latest Tevatron combination [3]. Top quark mass measurements have either been made from direct or indirect evidence. Some of the different types of measurements are described in the following list:

Distribution Fitting Methods: where the use of a distribution which is significantly dependent on top quark mass is utilized to extract the top quark mass in data. The signal and background distributions, $S(x_i|m_t, \epsilon)$ and $B(x_i|m_t, \epsilon)$ respectively, are templates of a given distribution which depends on m_t. Therefore, a dependence against the mass can be measured by a fit of these distributions against data. Using the example of the binned likelihood, $L(m_t, \epsilon, f_s)$, a fit is made which is dependent on the signal fraction f_s and on signal and background distributions which are dependent on the top quark mass and nuisance variables (ϵ) such as the JES.

$$L(m_t, \epsilon, f_s) = \sum_{i=1}^{N} [f_s S(x_i|m_t, \epsilon) + (1 - f_s) B(x_i|m_t, \epsilon)]. \qquad (2.51)$$

Extensions to the simple 1-d model employ the dependence of the signal and background distributions ($S(x_i|m_t, \epsilon)$ and $B(x_i|m_t, \epsilon)$ respectively) on a nuisance parameter, such as the JES. This improves the sensitivity to the top quark mass by adding an extra dimension to the fit for the JES. The most precise alljets measurement was performed at CDF using this method [72]:

$$m_{top}^{alljets} = 172.5 \pm 1.4 \text{ (stat.)} \pm 1.5 \text{ (syst.) GeV/c}^2. \qquad (2.52)$$

Templates were created for variations in top mass and JES and a 2-dimensional fit was performed. Another powerful extension to this method is the so-called "ideogram method" which uses the event-by-event top mass resolution. Such a method is performed at DØ. The resulting top mass from this method performed at DØ in the lepton + jets channel is [73]:

$$m_{top}^{ideogram} = 173.7 \pm 4.4 \text{ (stat. + JES)} \,_{-2.0}^{+2.1} \text{ (syst.) GeV/c}^2. \qquad (2.53)$$

The ideogram method has also been used by the CMS collaboration in the μ + jets channel using a reconstruction similar to what has been previously performed at DØ [74]. The resulting mass measurement uses the full 2011 dataset of 4.7 fb^{-1}, and results in a top mass value of [75]:

$$m_{top}^{CMS \ ideogram} = 172.6 \pm 0.6 \text{ (stat. + JES)} \pm 1.2 \text{ (syst.) GeV/c}^2. \qquad (2.54)$$

The uncertainty is slightly underestimated as underlying event and colour reconnection systematic uncertainties were not evaluated. As a result, the analysis is still only preliminary and expected to have slightly larger uncertainties. To date, this is the most precise LHC top mass measurement.

Neutrino Re-Weighting Methods: involve analyzing a kinematically under-constrained system due to the two missing neutrinos. Integration over the neutrino rapidity is performed. Since the JES is not able to be calibrated in the dilepton channel, a correction may be taken from the $t\bar{t} \rightarrow$ l+jets events. This allows the correction for the JES in dilepton events. The most recent measurement at DØ gives a top quark mass of [76]:

$$m_{top}^{dilepton} = 174.0 \pm 2.4 \text{ (stat.)} \pm 1.4 \text{ (syst.) GeV/c}^2, \qquad (2.55)$$

when using a correction obtained from lepton + jets events. This is the most precise measurement in the dilepton channel.

Integration Methods: better known as Matrix Element Methods (MEM), which use integration over the parton-level quantities. The method was introduced by DØ in 2004 [77]. It is especially powerful when only limited data is available since it is very CPU intensive as integration is made over several quantities per event and is non-trivial. The probability of observing x per event is given as:

$$P(x|a) = \frac{1}{\sigma_i(a)} \cdot \frac{d\sigma_i(x|a)}{dx}, \tag{2.56}$$

where $\sigma_i(a)$ is the cross section of the process, x are the observables and a are the set of parameters. This method has given the most precise measurement ever made of the top quark mass [78].

$$m_{top}^{l+jets} = 173.0 \pm 1.2 \text{ GeV/c}^2 \tag{2.57}$$

Its DØ counterpart is found at [79]. The method is one of the most precise methods to measure the top mass. Essentially the events are fit within a χ^2 minimization, where distributions of detector transfer functions and event modeling are considered. This results in a significantly improved estimator. The drawback to such an analysis is the required understanding of the detector and modeling of signal density functions. Also the minimization may be non-trivial and a significant amount of CPU time is required. As a result, this method has not yet been applied on LHC data.

Indirect via the Cross Section: which uses the measured $t\bar{t}$ cross section to indirectly calculate the top quark mass. This method assumes the SM theoretical description of the mass dependence to the cross section and higher order corrections to the theoretical cross section. It has been performed at the Tevatron in [80,81]. The correlation between mass and cross section can be seen in Figure 2.20, where several different approximate NNLO cross section calculations are given with their intersection at different possible mass values.
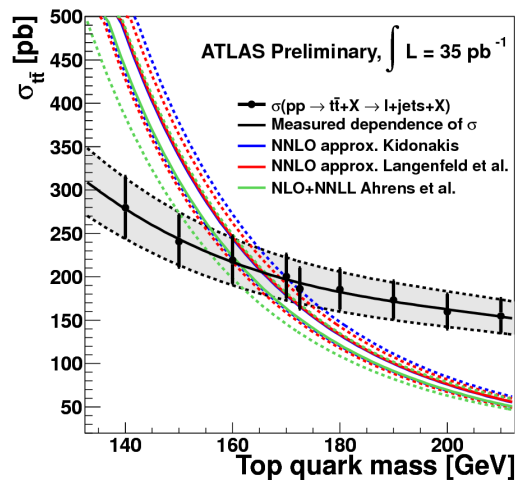

Figure 2.20.: Relationship of several NNLO theoretical cross sections to the t quark mass in pp collisions at $\sqrt{s} = 7$ TeV. Figure taken from [82].

Using the measured ATLAS $t\bar{t}$ cross section value, and the *Kidonakis et. al.* calculation, the top quark mass was calculated to be at ATLAS [82]:

$$m_t^{\sigma_{t\bar{t}}} = 166.2 \; ^{+7.8}_{-7.2} \text{ GeV.} \qquad (2.58)$$

However, this mass is different from the M_{MC} mentioned in the other measurements of the top quark mass as it uses a renormalization scale.

These measurements, along with many others, have all played a roll in the evolution of the top mass shown in Figure 2.21. Depicted are the measurements of the top mass and the increase in precision over time, beginning with indirect searches at e^+e^- colliders and evidence from electroweak fits up until the year 1995. Afterwards, the numbers begin to converge at approximately 175 GeV/c^2 after the first measurement at the two experiments at the Tevatron. All of this culminates with a very precise direct top quark mass measurement. The final points on the graph show the first produced analyses from ATLAS and CMS, which are measurements performed on data collected in 2010 and 2011 [83, 84].
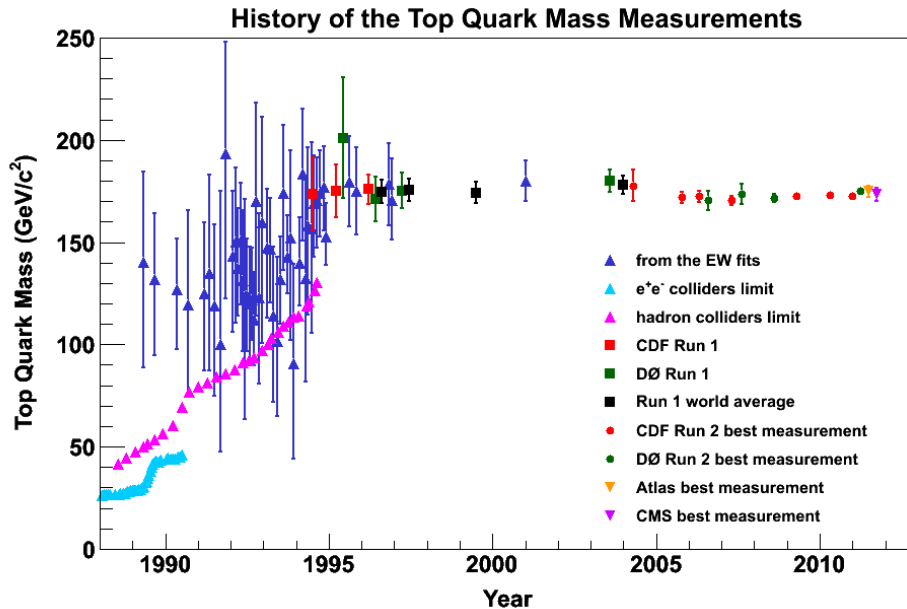
Figure 2.21.: Evolution of the top mass measurement as a result of direct and indirect searches over the past 20 years. Updated in 2012.

The current top mass measurement precision is dominated by the Tevatron. At present, there is no top mass measurements made at the LHC in the world average calculation. The current world average of the top quark mass, calculated in 2011 [3], is:

$$173.2 \pm 0.6 \text{ (stat.)} \pm 0.8 \text{ (syst.) GeV/c}^2 \qquad (2.59)$$

Several of the measurements performed at both DØ and CDF are highlighted by channel and experiment in Figure 2.22. Many analyses are used in the calculation of the top quark mass world average, from several channels at both the Tevatron experiments.
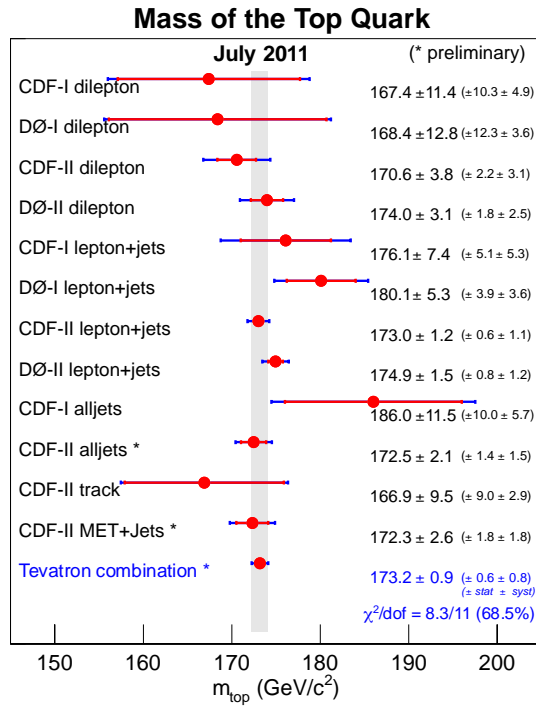
Figure 2.22.: Current world average of the top quark mass. The combination uses Tevatron results only. The measurements from all decay channels in both experiments are used to maximize the knowledge of the top quark mass. Figure taken from [3].

3. Experimental Setup

3.1. The LHC

The Large Hadron Collider (LHC) is the largest particle accelerator in the world. The accelerator itself is located on the border between Switzerland and France, at CERN, the European Organization for Nuclear Research [85]. The tunnel, which contains the particle accelerator, is a total of 27 km in circumference. There are a total of six experiments which can be found at the LHC. The four largest experiments are housed at several different locations along the beam line, they include: ATLAS [86], CMS [87], ALICE [88] and LHCb [89].
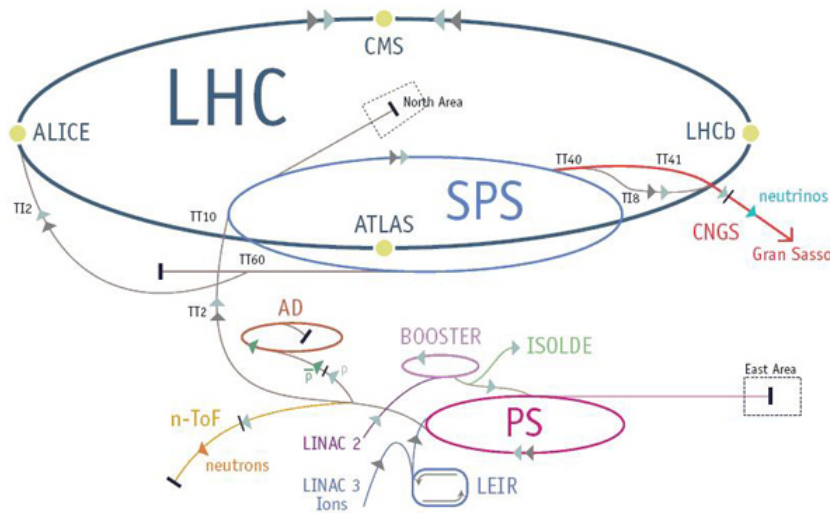
Figure 3.1.: The CERN accelerator complex, which houses more than 30 km of tunnel. The drawing shows the journey of the protons from the LINAC to the LHC where they are made to collide within one of the four detector halls located around the LHC ring. Figure taken from [90].

The accelerator within the tunnel was rebuilt and converted from an electron-positron collider following the LEP shutdown in 1999, to a complex proton-proton collider. The protons begin their journey in a canister of hydrogen gas. The hydrogen atoms are stripped of their electrons, leaving only the protons, and are accelerated in the Linear Accelerator known as LINAC. From the LINAC, the protons are brought into the PS Booster where they reach a nominal energy of 1.4 GeV. After they leave the booster, the protons are brought to the first of three large rings: the Proton-Synchrotron (PS). The PS has a circumference of 630 m, increasing the stored energy of the protons up to 25 GeV. Once

they have reached this energy, the protons are sent to the SPS, a 6.9 km ring where they reach an energy of 450 GeV. This is the last phase before the protons enter the LHC.

Once the protons enter the LHC, they are split into two groups, one rotating clockwise and the other rotating counter-clockwise. The protons are then ramped to the colliding energy of 3.5 TeV per beam. After the protons have reached their nominal energy within the LHC, of 3.5 TeV, they are made to collide inside one of the four detectors. The resulting centre-of-mass energy ($\sqrt{s}$) is 7 TeV[1]. This process can be visualized in the collider complex at CERN found in Figure 3.1.

To allow the protons to reach an energy of 3.5 GeV, the accelerator is cooled to a temperature of $-271\ ^oC$ or 1.7 K. At this temperature, the magnets are superconducting. To keep the protons aligned in the beam, magnetic dipoles and quadruples are used. The protons are found grouped together in bunches, and are kept together at a defined energy using a radio frequency (RF) technique. The LHC is designed to store up to 2808 bunches at time differences between bunches of 25 ns.

The four large detectors at the LHC are focused on several different areas. The ALICE experiment studies the quark-gluon plasma which was the state of the universe moments after the big bang. This is done by colliding lead ions (Pb) instead of protons. LHCb is trying to locate rare b-hadron decays in the search for CP-violation which would explain the resulting triumph of matter over anti-matter in our early universe. ATLAS and CMS are multi-purpose detectors built to find the Higgs boson and other new particles which may be created at high energies. In addition to the four large experiments, there are also two smaller experiments along the LHC ring. The first is TOTEM [91], measuring protons from deep inelastic scattering at very high η regions and LHCf [92], which uses the forward particles to create the effects of cosmic rays.

3.2. The ATLAS Detector

The ATLAS (**A T**oroidal **L**HC **A**pparatu**S**) Experiment is one of the four large detector experiments located on the LHC ring. It is housed about 100 m underground in a cavern at point 1 along the LHC. The ATLAS detector has a height of 25 m and a length of 44 m and weighs approximately 7 000 tons. The detector has an onion shell structure with six main components: inner detector, calorimeters, muon spectrometer, and trigger system.

The ATLAS detector, along with its main components, is shown in Figure 3.2. The ATLAS collaboration is the largest physics collaboration in the world, upwards of 3 000 scientists are involved from about 40 countries from around the world. All of the detector components are described in the following sections.

3.2.1. Measurements at the ATLAS Detector

When measuring position at ATLAS, a right-handed set of coordinates is used. The z-axis of a cartesian plane denotes the beam line. The centre of the detector is the origin, (0,0,0) position, of the 3-d plane. The x-axis points towards the centre of the LHC ring, which leaves the y-axis pointing upwards in direction.

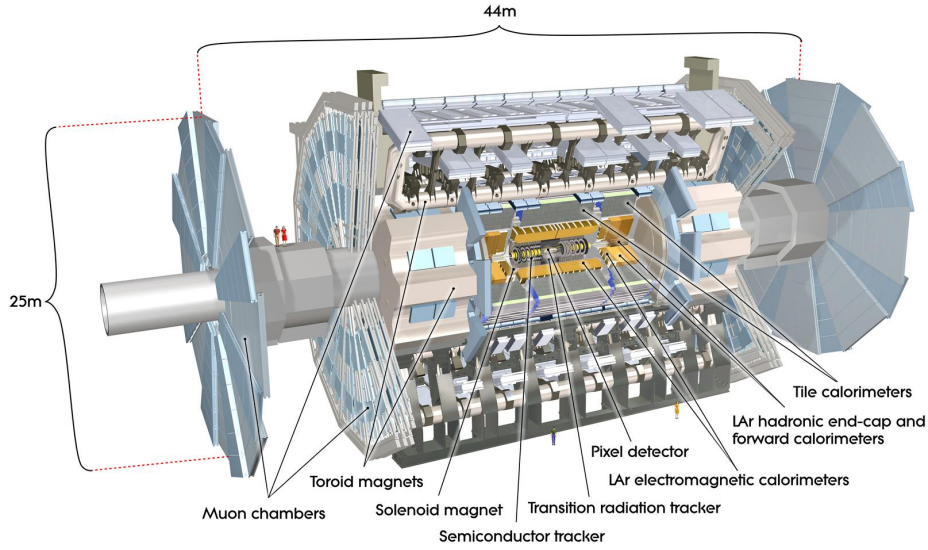[1]The original design $\sqrt{s}$ is 14 TeV, which will be reached after an upgrade shutdown in 2013.

Figure 3.2.: The ATLAS Detector. Highlighted are the main components of the onion structured detector. The whole apparatus has a total length of about 44 m and a height of 25 m, weighing in total 7 000 tons. Figure taken from [93].

To measure the angle from the beam line (θ), a relativistic quantity referred to as the pseudorapidity is used (η). Pseudorapidity is given by the formula:

$$\eta = -\ln\left[\tan\left(\frac{\theta}{2}\right)\right]. \tag{3.1}$$

A cross-section of the ATLAS Inner detector in units of η is shown in Figure 3.3. Pseudorapidity is used as a variable in relativistic hadron colliders due to the fact that a shift in pseudorapidity is Lorentz invariant. This means the expected QCD multijet particle rate per shift in pseudorapidity ($\Delta\eta$) is constant. The second variable used at ATLAS is the azimuthal angle, denoted by ϕ.

The final variables used at ATLAS are the transverse components of momentum (p_T) and energy (E_T). Since the collider uses protons, which contain multiple quarks and gluons traveling at various fractions of the proton's momentum, the initial longitudinal energies and momenta are unknown for the colliding particles. As a result, the transverse components are used since the total initial transverse energy and momenta are zero. The resulting imbalance in transverse momenta allows for undetectable particles, such as neutrinos, to be quantified by the missing transverse energy ($\not{E}_T$).

3.2.2. Inner Detector

The first section of the ATLAS detector, and closest to the interaction point, is the Inner detector [94]. The inner detector is designed to perform precision tracking and vertex measurements for charged particles, up to a precision of 5 cm on the vertex position. The section itself is subdivided into several components: the pixel detector, the semiconductor tracker (SCT), and the transition radiation tracker (TRT). The three components are
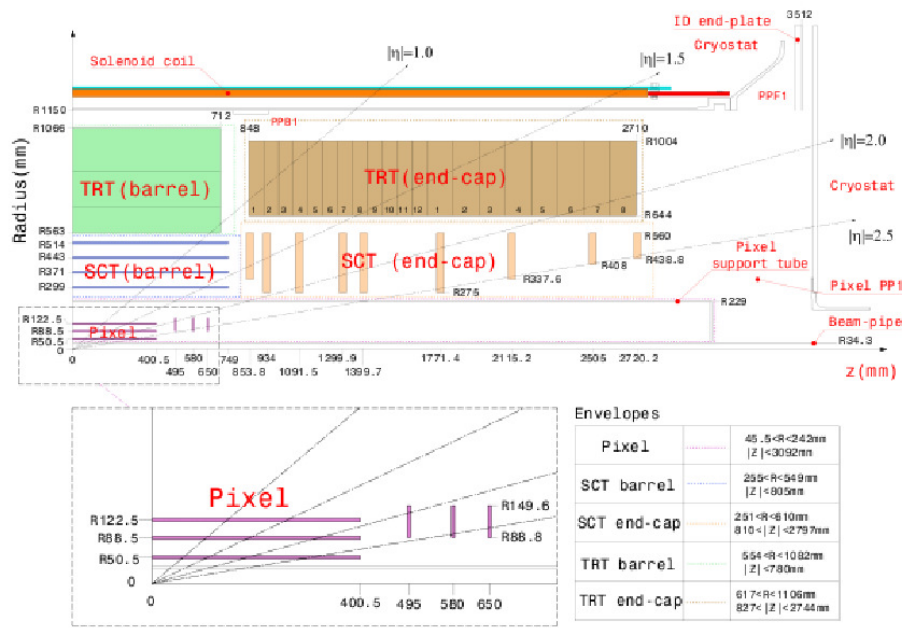
Figure 3.3.: The ATLAS inner detector denoted by sections of pseudorapidity (η). The variable η begins at 0 for an upwards trajectory and continues to ∞ when pointing horizontally. The useful region for object reconstruction within the detector extends to an $|\eta| \approx 2.5$. Figure taken from [93].

shown in Figure 3.4. The three components of the inner detector each contain a barrel and end-cap region. A computer generated image shows the relative distances of each subsection of the inner detector to the beam of protons in Figure 3.5.
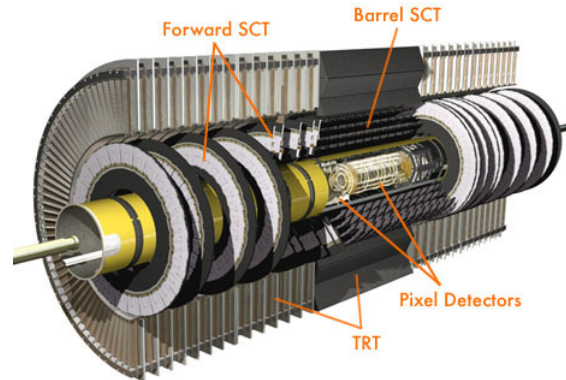
Figure 3.4.: The ATLAS inner detector and its main components. The innermost component is the pixel detector made of silicon pixel sensors. The second component, moving outwards from the interaction point, is the silicon strip detector. Finally, located at the outermost section of the inner detector are the transition radiation tracker tubes. Figure taken from [93].
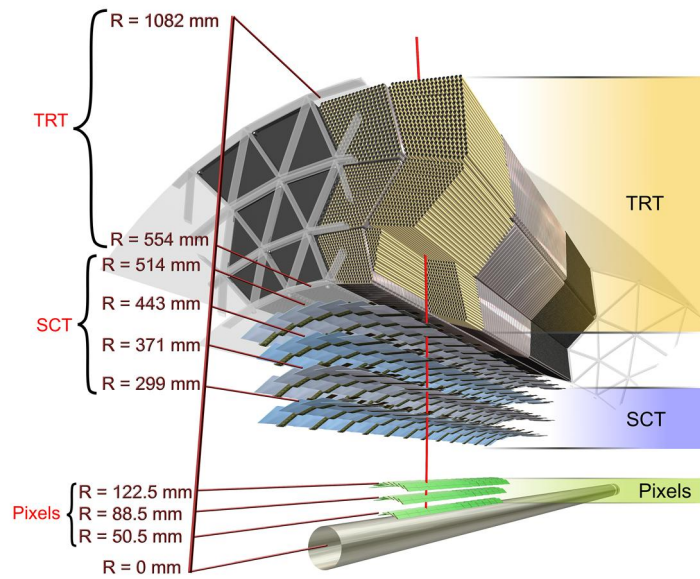
Figure 3.5.: A computer generated image of the inner detector and the three subsections'
distances from the beam. The Inner detector has three components which
lie at certain distances away from the beam in order to get a precise position
measurement of the particle interaction vertex and the direction and charge
of the outgoing charged particles. Figure taken from [93].

The pixel detector is composed of tiny pixel sensors ($50 \times 400 \ \mu m^2$). The sensors are
made of silicon, which is a semiconductor detector, where timing and position is read-out.
The pixel detector has three cylindrical layers which lie between 50 mm and 123 mm from
the centre of the beam axis. The detector extends to an η range of 2.6. In total, there are
over 80 million read-out channels. The resolution of the pixel detector is up to 12 μm.

The second component is the silicon strip detector. The SCT is similarly made of silicon
semiconductors, however instead of pixel sensors, long strips are built to cover a larger
region. The strips themselves are aligned with a 40 mrad angle to one another in order to
reduce ghost hits when multiple charged particles hit the same strips. A single strip covers
an area of 80 μm by 12.6 cm. The SCT is setup in four double-layer sections, totaling
over 6.2 million read-out channels. The resolution of the SCT detector is up to 17 μm.

The final component of the inner detector is the transition radiation tracker. The TRT
is comprised of about 400 000 Xenon gas filled straw tubes. Each straw tube has a radius
of 2 mm and a length of 7 m. The gas is comprised of 70 % Xe, 27 % CO_2 and 3 % O_2.
At the centre of each tube is a tungsten anode wire. The outside of the tube acts as a
cathode. The straw tubes are placed from about 55 cm to 110 cm away from the beam.
The TRT is used to differentiate between charged particles, especially electrons, which can
be distinguished from heavier charged particles due to the different amounts of radiation
they produce inside the tube. Different materials with differing dielectric constants are
placed around the straws. As the charged particles traverse the material, they produce

transition radiation. The resolution of the TRT is up to 130 μm.

All charged particles will leave tracks within the inner detector. It is important that the tracks can be properly reconstructed and that they can be traced back to the vertex. The reconstructed track efficiency and impact parameter (d_0) are shown in Figure 3.6 for minimum bias $\sqrt{s} = 7$ TeV collision events. The reconstructed track efficiency is calculated by the number of matched tracks divided by the number of generated tracks in a certain p_T and η bin. It can be seen that the track efficiency is dependent on p_T, and that the efficiency reaches a plateau of about 80% at track p_T of about 1 GeV. Therefore, tracks can be reconstructed in the inner detector beginning at about a p_T of 1 GeV. The same plateau is seen as a function of η. The best reconstruction efficiency, about 80%, can be seen in the barrel region of the inner detector. The transverse impact parameter, denoted by d_0, is very important for selecting b-jets decaying from $t\bar{t}$ events. This impact parameter is calculated by the transverse displacement of a reconstructed track compared to the jet axis, to which the track belongs. The d_0 is signed positive if the track crosses the jet axis in front of the primary vertex and negative if it crosses behind the primary vertex. This will be explained in further detain in Section 4.1.3, where it is described in the context of b-jet identification. The performance of the inner detector in data is shown to be as expected by MC simulations. The performance of the inner detector also depends on the magnet system at ATLAS, which helps identify charged particles. The magnet system is described in Section 3.2.5.
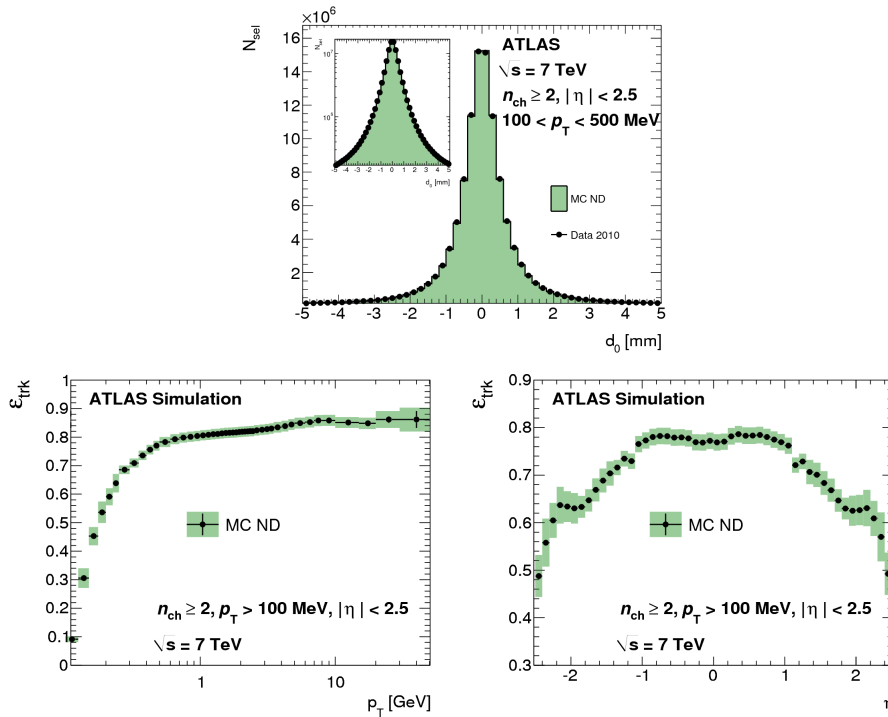
Figure 3.6.: (Top): Impact parameter (d_0), (left): track efficiency in bins of p_T and, (right): track efficiency in bins of η of reconstructed tracks from minimum bias events from $\sqrt{s} = 7$ TeV collision events. The plots show very good MC to data agreement for reconstructed track efficiency and d_0 displacement. Figures taken from [95].

3.2.3. Calorimeter System

The ATLAS detector's second main component is its calorimeter system: the electromagnetic calorimeter and the hadronic calorimeter [96]. The two calorimeters are used to measure the deposited energy of the particles through the interaction with the detector material. The reason for splitting the calorimeter into two separate components is due to having two types of particles which have different properties pertaining to energy deposition. The particles which decay in the calorimeter system at ATLAS, do so via particle showering. The material of the calorimeter causes incoming particles to shower in the calorimeter, depositing the resulting energy in the absorber material of the detector. The first type of particle are particles which shower in the electromagnetic part of the calorimeter. The resulting energy deposition is in the form of photon emission or electron-positron creation. The second type of particles which are created at hadron colliders and decay within the calorimeter are jets. These are hadrons such as pions or Kaons, which have a much larger particle shower than electrons. The ATLAS calorimeter system, and its two sections, are shown in Figure 3.7.
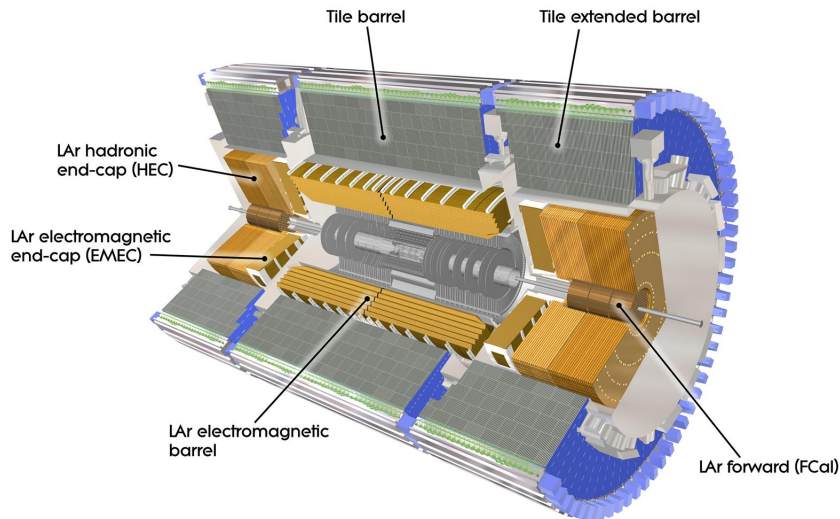
Figure 3.7.: The calorimeter component of the ATLAS detector, comprising of the electromagnetic and hadronic components. The electromagnetic component is made of liquid Argon (LAr), in both the barrel and end-cap regions. The hadronic component is a tile calorimeter in the barrel region and LAr region on the two end-caps. There is also a LAr forward calorimeter very close to the beam pipe at both ends of the detector. Figure taken from [93].

The electromagnetic calorimeter, which is found directly after the inner detector, is divided into three parts. The three parts of the electromagnetic calorimeter are the barrel component ($|\eta| < 1.475$) and two end-cap components ($1.385 < |\eta| < 3.2$). The calorimeter is comprised of liquid Argon (LAr) which is used to absorb the energy of the charged particles [97]. The detector is build with accordion shaped electrodes and lead absorber plated. The liquid Argon is kept at 87 K and absorbs the energy of the charged particles. The LAr material has also radiation hardness and good energy resolution. The electro-

magnetic section of the calorimeter system is much more finely sectioned as compared to the hadronic calorimeter. The granularity of the electromagnetic calorimeter in the (η, ϕ) - plane is $\Delta\eta = 0.025$ and $\Delta\phi = 0.025$ for both the barrel and end-cap regions. To account for energy loss of particles before reaching the calorimeter, a pre-sampler is located in front of the electromagnetic calorimeter, in the barrel region.
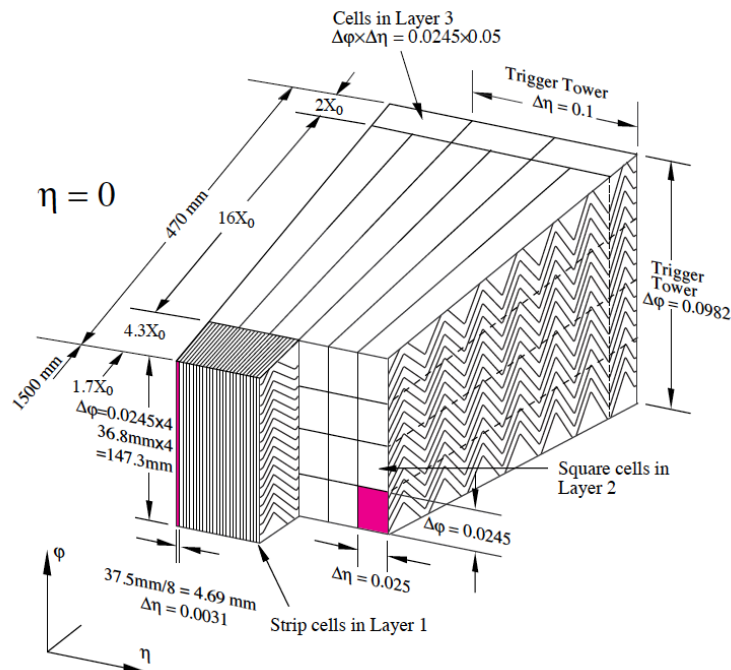

Figure 3.8.: A schematic of the LAr electromagnetic calorimeter. The accordian-shaped electrodes and placement of the LAr is shown with respect to the incoming particles. The figure is taken from [93].

The calorimeter size, denoted in radiation lengths (X_0), is over 24 X_0. One radiation length denotes the distance for a relativistic particle to lose all but $1/e$ of its original energy. Therefore, a length of 24 X_0 is enough so that almost all of the electron's or photon's energy is deposited. In the end-cap region, the length exceeds 26 X_0. The energy resolution of the electromagnetic calorimeter consists of a constant noise term and a dependence of $1/\sqrt{E}$. The expected resolution of the electromagnetic calorimeter is shown in Figure 3.9 for several different electron energies and positions in the detector.

The hadronic calorimeter at ATLAS is built in three sections: the tile calorimeter, the LAr hadronic end-cap region and the LAr forward region. The tile component is comprised of a section of scintillators. The scintillators measure light due to incoming particles with the help of wavelength shifting fibers [98]. The active medium is made of absorber plates, as in the LAr calorimeter, and scintillating tiles. The tile section of the hadronic calorimeter extends to an $|\eta|$ of 1.8, which consists of both the barrel and extended barrel regions. Since hadrons have a much larger radiation length, the charged hadrons begin decaying in the electromagnetic calorimeter and continue into the hadronic calorimeter. The majority of energy is deposited in the latter. The deposited energy creates scintillating light, which is detectable by the tile calorimeter. The tile placement
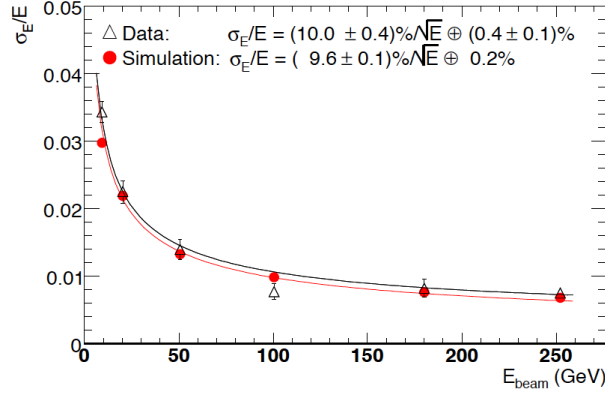
Figure 3.9.: The expected calorimeter energy resolution for given electrons with different energies and $|\eta|$ positions. The figure is taken from [93].

is such that it is parallel to the particle direction. This allows the read-out cables to be placed at the end of the calorimeter, minimizing effects due to dead material.

The energy resolution of the tile calorimeter is given by the same terms as the liquid Argon calorimeter plus an extra term which goes as $1/E$. The performance is much coarser than the LAr calorimeter. On the end-cap regions, there is no Tile calorimeter component, instead a LAr calorimeter is used for the hadronic calorimeter. The entire calorimeter extends to an $|\eta|$ of 4.9. The LAr hadronic components are similar to the electromagnetic section of the calorimeter system, however copper is used as opposed to lead. The total size of the calorimeters, both electromagnetic and hadronic are shown in Figure 3.10.
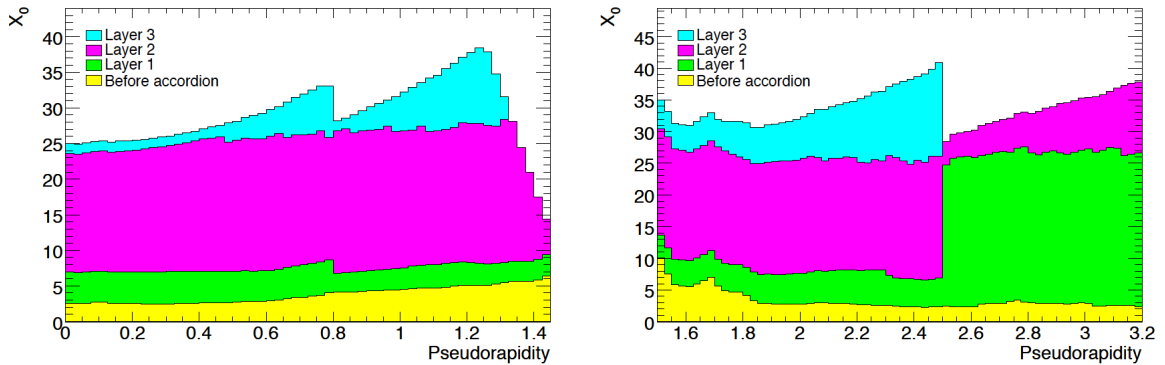
Figure 3.10.: (Left): Electromagnetic and (right): hadronic sections of the calorimeter system for various regions in η. The hadronic section is much larger than the electromagnetic section of the calorimeter system. The figures show the different layers of the calorimeter as well as the amount of interaction material in front of the detector. The figures are taken from [93].

3.2.4. Muon Spectrometer

The muon spectrometer at ATLAS is the largest component of the detector and the outermost from the beam [99]. The muon detector is used to measure muons which originate from the proton-proton collision. Since muons are minimum ionizing particles at energies of the order of 1-100 GeV [15], they traverse through the calorimeters without depositing much of their energy, and can be measured in the muon spectrometer.

The muon spectrometer is split into four separate components: the muon drift tubes (MDT), the resistive plate chambers (RPC), the thin gap chambers (TGC), and the cathode strip chambers (CSC). Three of the four components of the muon spectrometer are shown for both the barrel and the end-cap regions in Figure 3.11. The CSC is a very tiny chamber located very close to the beam pipe in the inner station, which is subjected to high levels of particle radiation. The purpose of these four components is to measure the position, momentum, charge as well as to trigger on muons from the collision event.
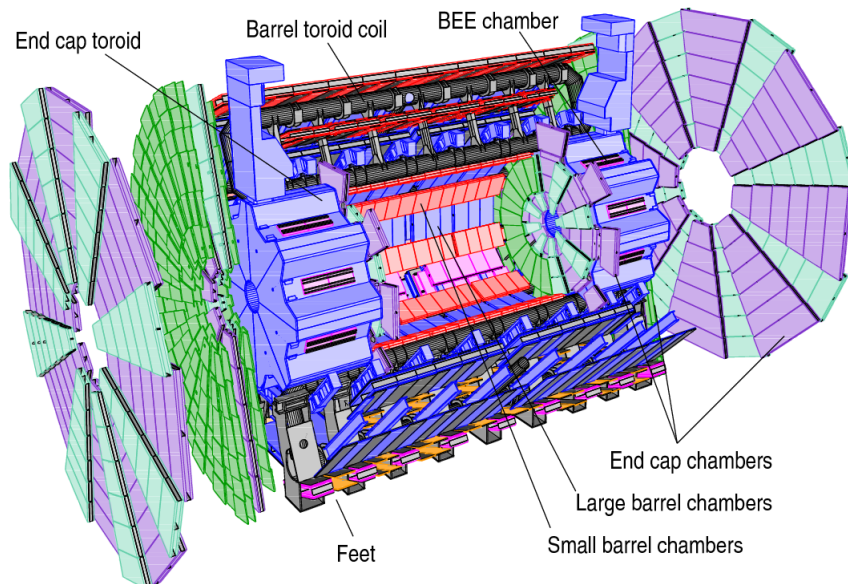
Figure 3.11.: The muon spectrometer of the ATLAS Detector. It is comprised of four components: the MDT, the RPC, the TGC, and the CSC (not shown in Figure). The spectrometer measures muons from the collision which pass through the detector without depositing all of their energy. They ionize the gases of the MDT and are triggered on by the RPC and TPC. Figure is taken from [100].

The MDT measures the traversing charged muon due to its ionization of the gas. The gas within the tube is comprised of 93 % Ar and 7 % CO_2. The centre of the tube contains an Aluminum wire. The ionization of the gas creates electrons and ions which drift according to the electric field. Using many tubes, the position, momentum and charge of the muon can be measured precisely. The MDT contains 1 088 chambers, containing a total of 339 000 read-out channels covering an area of 5 500 m^2. The barrel region of the MDT measures out to an $|\eta|$ of 1. MDT chambers are also located on the end-cap region.

The RPC is used to trigger for muons. It also aides in measuring the position of a muon traversing through the detector. The RPC is located in the barrel region and contains 544 chambers with 359 000 read-out channels and covering a total area of 3 650 m^2. Its end-cap counterpart is the TGC which triggers for muons in the end-cap region. The TGC contains 3 588 chambers with 318 000 read-out channels and covering an area of 2 900 m^2.

The smallest component of the muon system at ATLAS is the CSC. The CSC measures the position of muons at very high η. Due to its position close to the beam pipe, it is subjected to high levels of radiation. The CSC only contains 32 chambers with 30 700 read-out channels covering an area of only 27 m^2.

The muon chambers combine to measure muon momenta resolution up to 3 % for muons with energies between 10 - 200 GeV. For higher momentum muons, up to 1 TeV, the resolution is approximately 10 %. A majority of the muons which decay from a single lepton $t\bar{t}$ decay are within the range 10-200 GeV. The muon resolution for data and MC is found in Figure 3.12, studied in muons from $\sqrt{s} = 7$ TeV collision events with reconstructed muons in the barrel and end-cap regions of the detector. In both cases, the detector performance is worse than the expected MC performance, more so in the end-cap regions of the detector.
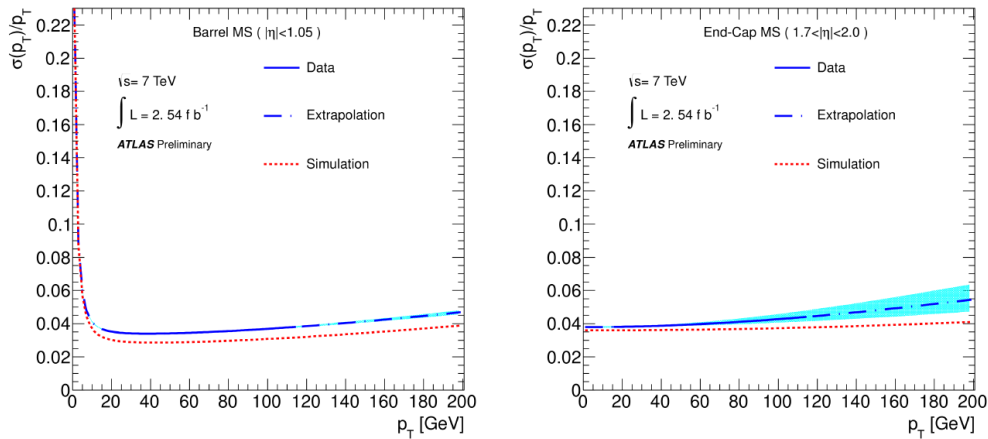
Figure 3.12.: (Left): Barrel, and (right): end-cap region muon resolution measurements. In both cases, the data has a worse resolution than the MC. The largest difference occurs in the end-cap region. Figures are taken from [101].

3.2.5. Magnet System

The ATLAS detector is significantly different from the other multi-purpose LHC detector, CMS, due to its non-uniform magnetic field. Within the ATLAS detector, there are two separate magnetic fields: a solenoid field and a toroidal field. The structure which creates the solenoid and toroidal magnetic fields is found in Figure 3.13. The entire magnetic field is non-uniform, and contains a transition region, where the effective magnetic field is very small.

The inner magnetic field, which encompasses the inner detector, is a solenoid field. The solenoid magnetic field is a constant 2 T within the inner detector, bending the
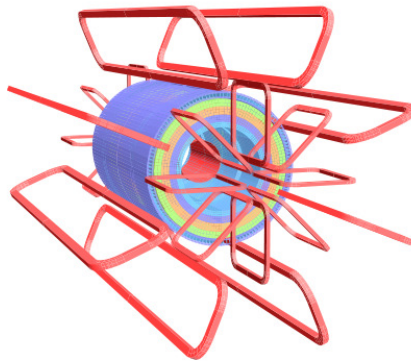
Figure 3.13.: The magnet system at ATLAS. Construction of the magnet system show-
ing both the inner magnet, depicted as the cylindrical region in the inner
part of the detector. The large red rectangular shaped magnets in the
outer part of the detector is the toroidal magnet. The figure is taken
from [93].

charged particles. The same effect occurs in the non-uniform toroidal field within the
muon spectrometer. The average magnetic field due to the toroid magnet is 0.5 T. This
allows the muon momentum and charge to be precisely measured in both the solenoid and
toroid regions of the magnetic field. The resulting resolution on the muon p_T contains a
constant term and a term dependent on the muon p_T.

3.2.6. Trigger

At the LHC, *pp* collisions create an overwhelming amount of primary interactions. As a
result, a trigger system is designed to significantly reduce the number of recorded events
to only the events which are of interest for physics [102]. The trigger itself is divided into
three sections:

Level 1 uses only the muon chambers and calorimeter to make a decision on the event.
The maximum pass rate is 75 kHz and the decision time, or latency, is 2 μs. The
trigger uses the information from the muon chambers such as momentum of the
muon, while information such as missing transverse energy and energy deposited in
certain regions of the calorimeter are taken into account when making the decision.

Level 2 then takes the information from the Level 1 trigger and so called Regions of
Interest (ROIs) to make a decision. The calorimeter, muon and tracking sections
are pipelined and still only individually looked at by the trigger. The pass rate is of
the order of 1 kHz and the latency is between 1 and 10 ms depending on the event.

Event Filter is the final section of the trigger and uses offline reconstruction in order
to determine the pass or failure of an event. At this stage, the three pipelines are
combined into one event, allowing information such as tracking and jet reconstruction
to be used in the decision making process. Full-event buffers store the information
and the event filter rate allows a rate of approximately 200 Hz.

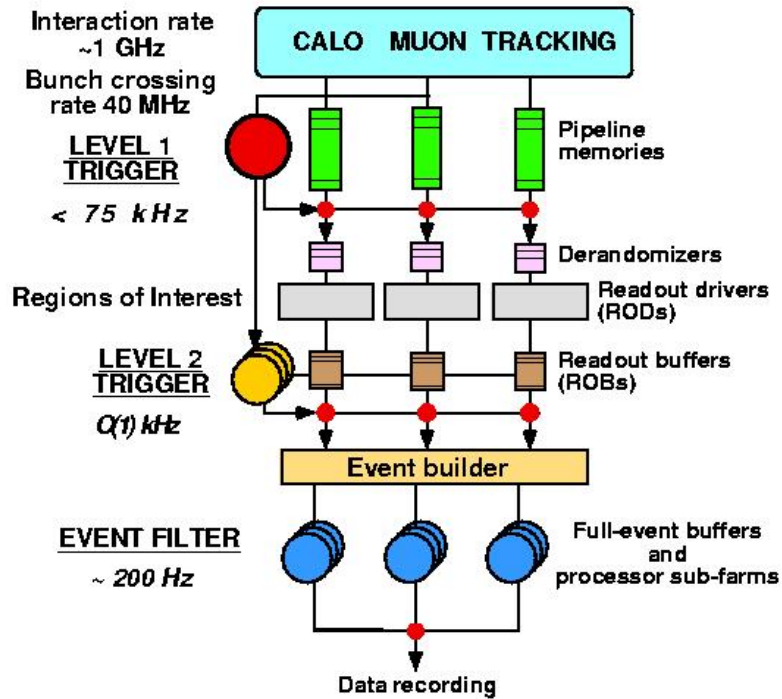The schematic of the trigger decision is shown in Figure 3.14.

Figure 3.14.: The ATLAS trigger system. Information is stored in three pipelines: calorimeter, muon and tracking systems. In the Level 1 trigger decision, information from the calorimeter and muon detectors is used to decide upon keeping the event. In Level 2, ROI are declared and analyzed along with the Level 1 decision. Finally, the event is reconstructed and looked at as a whole in the Event Filter trigger. The trigger is used to only store data which can be used for physics. Figure taken from [102].

4. Event and Object Reconstruction

4.1. Object Definition

To measure the top quark mass, it is necessary to identify the objects which result from the $t\bar{t}$ decay. In the lepton + jets channel, those objects are jets (both b and light), leptons and neutrinos which result in missing transverse energy ($\not{E}_T$). Using these objects, a candidate $t\bar{t}$ event is reconstructed and selected.

4.1.1. Jets

Jets are reconstructed objects originating either from quarks or gluons in the hard process or by soft radiated gluons. A jet is the result of QCD, where quarks and gluons are combined forming multiple pairs of mesons and baryons. These objects form a particle jet. The resulting mesons and baryons shower in the calorimeter and are found in clusters of energy mostly within the hadronic calorimeter. A schematic of a jet is visualized in Figure 4.1.
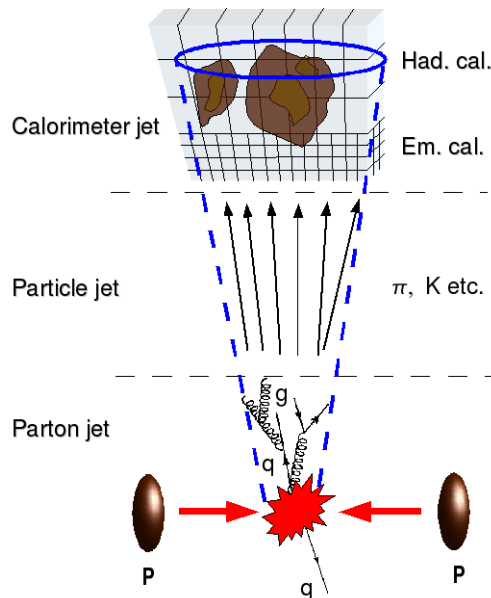
Figure 4.1.: Schematic of a jet originating from a hard scattering process evolving to its deposit in the calorimeter of the ATLAS detector. Highlighted are the different stages of jet production at hadron colliders and the resulting response in the inner detector and calorimeters. Figure taken from [103].

Jets are reconstructed primarily as clusters in the hadronic and electromagnetic segments of the calorimeter. A jet also results in many charged tracks within the inner detector. Therefore the performance of the inner detector and calorimeter are crucial in reconstructing jets.

Since QCD is collinear and infrared divergent, jet algorithms should also be collinear and infrared safe. The algorithm then must be required to use no seeds in the determination of the shape of the energy cluster, as is done with standard cone jets. As a result topological clusters using the anti-k_T algorithm are used [104, 105]. Anti-k_T jets are formed from cells above a given threshold. These cells then begin the clustering of other cells in the surrounding region. In several steps, cells are clustered to the primary cell if they follow a certain threshold criterion based on the distance from the original primary cell. With this algorithm, if there are several cells above the threshold constituting a primary cell, the cluster is split: forming two separate jets. If however the distance between the two objects, in (η, ϕ)-space, is less than the jet size (0.4 in this case) the extra object may be removed and combined into a single cluster. The distance in (η, ϕ)-space is denoted by ΔR[1]. The distance measurement used to make this decision between object i and j is given by:

$$d_{i,j} = \min \left[\frac{1}{p_{T,i}^2}, \frac{1}{p_{T,j}^2} \right] \cdot \frac{\Delta\eta_{ij}^2 + \Delta\phi_{ij}^2}{R}, \tag{4.1}$$

where R is the jet size of 0.4. The disadvantage to using the anti-k_T model compared to a cone jet algorithm is that it is more likely to include soft jets due to pileup [106]. The cone based algorithm is however not collinear or infrared safe. The anti-k_T jet algorithm can be seen in Figure 4.2. The resulting jet shape in the calorimeter is very much cone-like and symmetrically round, more so for harder jets.
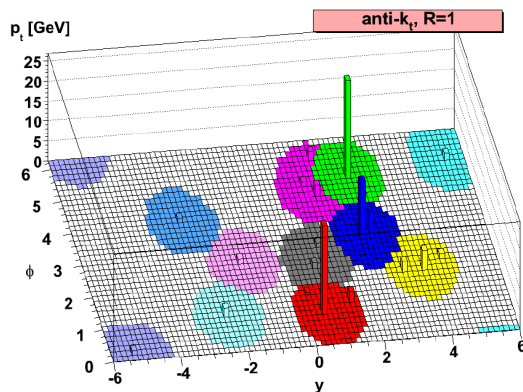
Figure 4.2.: Anti-k_T jet algorithm where different jets are represented by the different colours. Using this model, the jets are infrared and collinear safe, creating a "cone-like" shape around each maximum deposit of energy in the calorimeter. Figure taken from [107].

---

[1]Where the distance of two points is given by $\Delta R = \sqrt{(\Delta\eta)^2 + (\Delta\phi)^2}$

4.1.2. Jet Calibration

Of importance in a top quark mass measurement is the understanding of the jet energy scale (JES). The JES is the response difference between the original objects and the energy determined in the detector. This translation in energy returns the energy of the measured object back to its particle level. Jet calibration is performed to account for either dead material of the detector, or the different responses in the hadronic and electromagnetic calorimeter. A calibration referred to as EM+JES is performed. The calibration is determined from a scheme at the electromagnetic scale with jet energy scale calibration [108, 109]. The scale uses only the electromagnetic corrections of cells and corrects the jets based on their p_T and η. The material and difference between hadronic to electromagnetic response is also taken into account. The different components of the JES are:

Calorimeter Response

The calorimeter response is a result of the measured response of the individual particles contained within a jet. Each individual particle is compared to the deposition in the calorimeter cell. The response is based on η and p_T of the jet. This has been measured in MC and verified in 2010 data. The uncertainty on the response is found to be between 1.5 % and 4 %. For high p_T jets ($p_T > 100$ GeV/c), this term dominates the total JES.

Underlying Event

The underlying event in the default PYTHIA MC is changed to the PERUGIA2010 modeling, which has been previously derived at the Tevatron. The differences in JES of the underlying event to the nominal underlying event used in PYTHIA are taken as the uncertainties.

η-Intercalibration

An η-intercalibration is performed over the complete η range of the detector to obtain a uniform response. The response for different detector regions is not uniform due to effects such as dead material and differing amounts of detector materials. To measure the uncertainty in calorimeter response, dijet events in which one of the two jets is found in the central η range are studied. The central η range is well understood and thus the second jet acts as a probe of the not-well understood detector range. Comparisons of data to MC response allow the determination of an uncertainty of the JES. This component dominates the JES uncertainty at low p_T regions ($p_T < 50$ GeV) and forward detector regions.

Parton Shower Model

The default PYTHIA MC is exchanged with a differing shower model. The shower model used as a variation is ALPGEN with HERWIG and JIMMY models. The difference is taken as the uncertainty.

Close-by Jets

Events at the high luminosity of the LHC contain many jets, some of which are overlapping. Close-by jets may result in the degradation of the calorimeter response to a nearby jet. As a result, an additional JES uncertainty term is added to account for this effect. This effect was studied in QCD MC events and compared to data. The total effect is found to be less than 3 % [110].

Noise Thresholds

In the creation of jets through topological cluster algorithms, a noise over threshold is used on calorimeter cells. Variations in the noise may effect the jet shape, as it has an effect on the topological clustering. The response is checked in data and MC and the differences in the response are taken as systematic. The effect is limited to low p_T jets and found to be of minimal effect on the total JES.

Flavour Composition

Due to the differences in jet shape, an additional uncertainty is the result of the quark-gluon composition of the sample. To account for the differences in jet flavour, measurements are made of the response in the calorimeter from gluon or quark dominated samples. For background samples, a 50:50 composition sample is used and for signal samples a more quark dominated sample is used for the JES.

Pileup

Due to the increase in luminosity in data collected in 2011, the effect of pileup on the MC is not properly modeled. An additional uncertainty is added to the MC to account for the underestimation of pileup on the calorimeter response. The pileup component has an additional uncertainty of up to 5 to 7 % depending on the detector region, within $|\eta| < 2.5$. The pileup component of the JES is found in Table 4.1. It is added in quadrature to the other components.

Uncertainty [%]	$|\eta| < 2.1$	$|\eta| > 2.1$
$p_T < 50$ GeV	5 %	7 %
$50 < p_T < 100$ GeV	2 %	3 %
$p_T > 100$ GeV	0 %	0 %

Table 4.1.: JES uncertainty component due to pileup. The additional uncertainty is added in quadrature to the other components. The largest uncertainties are found at forward jet regions and low p_T jets.

To quantify the calibration for jets used at the EM scale, the jet response is plotted along with the total JES in Figure 4.3. The JES is split into the various components and the combination of the uncorrelated terms are added together and shown as a function of the jet p_T.
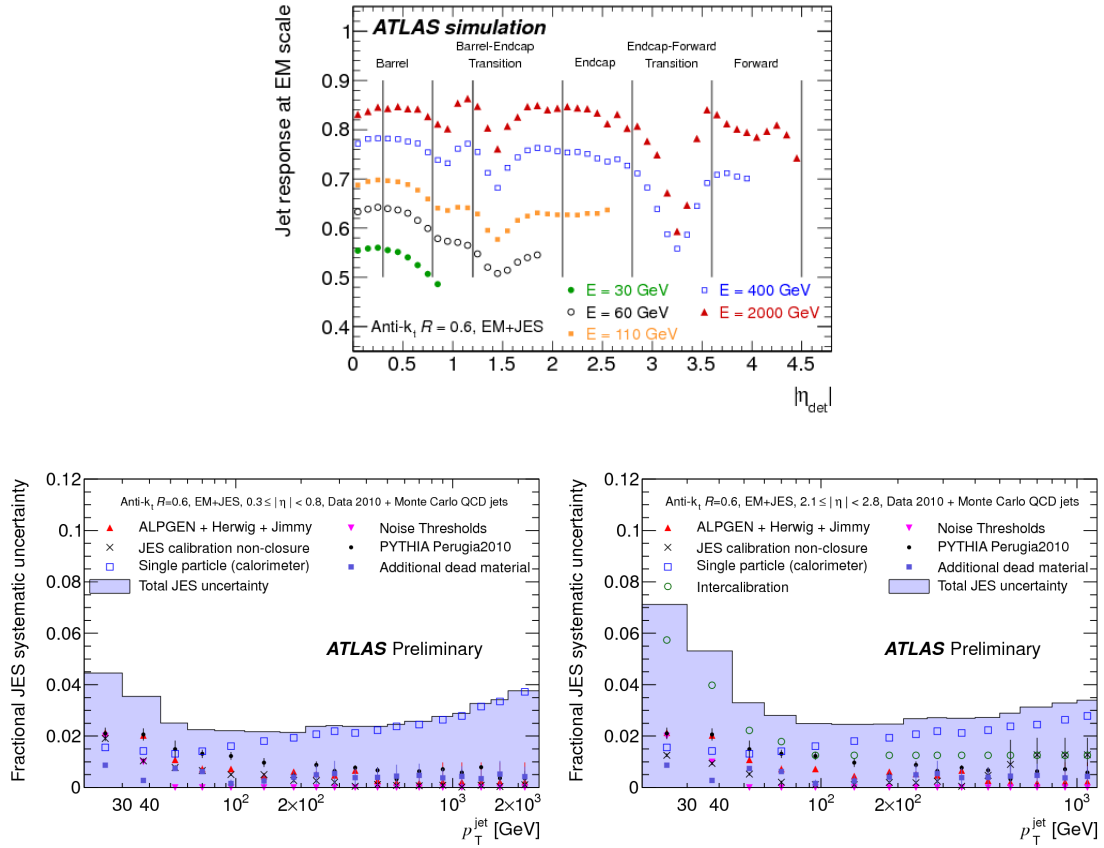
Figure 4.3.: (Top): Jet Response at EM Scale for different regions of the detector. Different energies are highlighted. The transition regions show a large drop in response and are thus excluded from reconstructing objects. (Bottom left): JES breakdown in the barrel region from several MC and detector components. The largest JES component is the calorimeter response, which at high p_T, almost completely accounts for the total uncertainty. (Bottom right): JES breakdown in the forward region, $|\eta| > 2.1$. Figures taken from [111].

The jet response at EM scale is plotted for different η regions of the detector. These η segments are also used for the JES determination. The response is quite similar through all ranges of the detector for a given energy, except in the transition regions such as $1.37 < |\eta| < 1.52$. This region will also be excluded for calorimeter reconstructed objects. The JES uncertainty is shown against the jet p_T. The different contributions to the JES are also shown. It can be seen that the largest uncertainty, especially at high p_T, is due to the calorimeter response. At low p_T, the JES is dominated by the η-intercalibration. The dependence on pile-up is not shown in the total JES calculation, however it does also account for a significant portion of the JES on top of the plotted values. The additional JES due to pile-up is up to 7 % in forward regions ($|\eta| > 2.1$) and 5 % in the central region. The total JES uncertainty ranges from 2.5 % to 8 % in total. In addition to the JES, an additional bJES of up to 2.5 % is added in quadrature to true b-jets due to the fragmentation of b-hadrons.

4.1.3. b Jet Identification

In $t\bar{t}$ decays, b jet identification is vital. The better the identification of b jets, the more pure the $t\bar{t}$ signal sample is. Most backgrounds to $t\bar{t}$ contain only light jets, or very few number of events with true b jets. Jets which are improperly tagged are referred to as "mis-tagged". As a result of the low frequency of b jets in $t\bar{t}$ background, it is important to have a good b-tagger which has a high rejection of light jets.

b jets have a unique property as they decay in-flight. The b meson which is created lives a sufficiently long time (≈ 1.5 ps) allowing it to travel away from the original primary vertex before decaying. This results in a secondary vertex, displaced from the original one. The resulting secondary decay will create many displaced tracks with respect to the original primary vertex. These displaced tracks will also, on average, cross the original flight path of the jet in front of the primary vertex, resulting in a larger number of positively signed impact parameters (d_0). This can be seen in Figure 4.4. The second unique property of b jets is their decay. On occasion, the b meson will decay semi-leptonically, resulting in a muon. Since muons escape the calorimeter and are measured at the muon chambers, they are easily identified. Therefore finding a non-isolated muon inside of a jet is also a good discriminant for b jets.
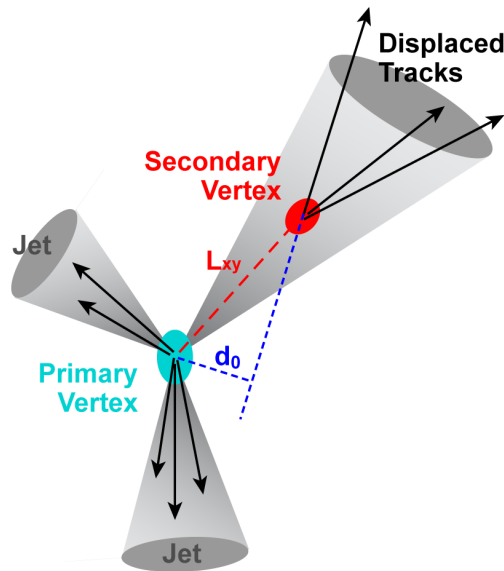
Figure 4.4.: The resulting secondary vertex as a result of the long living b meson. The displaced tracks from this b meson decay can recreate a secondary vertex which can determine the probability of an original b quark. Tracks assigned to a jet are reconstructed back to the primary vertex. If the track crosses the original jet axis in front of the primary vertex, the impact parameter (d_0) is signed positive. b-jets will on average have a larger number of positively signed d_0 as opposed to light jets. Figure taken from [112]

To identify b quarks a b-tagger is used. The b-tagger used for this analysis is an advanced tagger known as JetFitterCombNN. The algorithm uses a combination of two separate fits. The first fit comes from the IP3D algorithm and the second from the JetFitter algorithm.

The IP3D algorithm [113] uses both the longitudinal and transverse impact parameters to determine if there is a secondary vertex. The distributions which are used to determine the likelihood ratio fit of the IP3D algorithm are two-dimensional histograms of the signed transverse impact parameter significance and the longitudinal impact parameter significance. The correlation between these two variables is also taken into consideration. The d_0 and its significance are shown for different jet types in Figure 4.5. The impact parameter significance is given by the d_0 divided by its error, σ_{d_0}:

$$S_{d_0} = \frac{d_0}{\sigma_{d_0}} \tag{4.2}$$

This signed impact parameter and its significance are very good discriminants for the different types of jets.
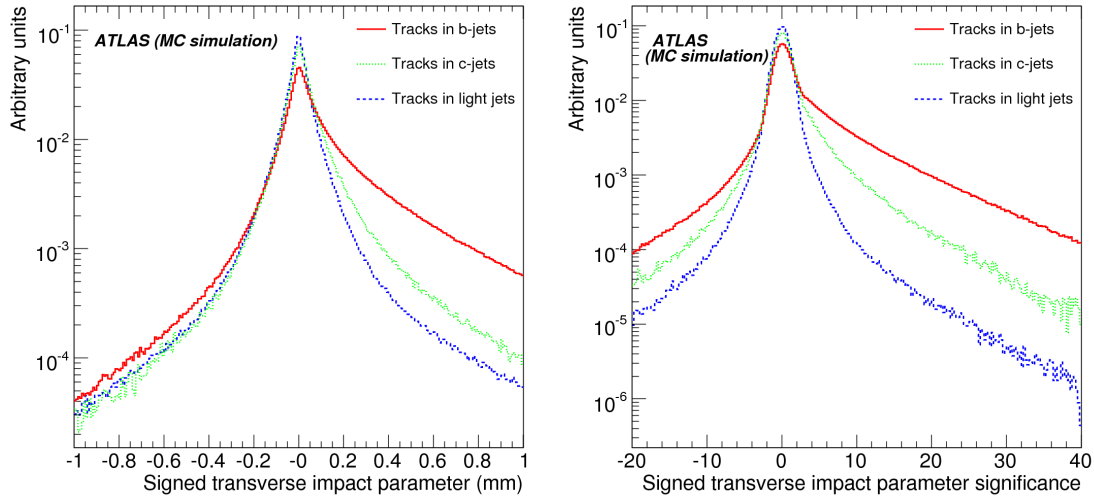
Figure 4.5.: (Left): Signed transverse impact parameter d_0, and (right): Significance of the impact parameter (d_0 / σ_{d_0}) for different types of jets. The Figure shows the separation power for b jets using the impact parameter d_0 as more positively signed impact parameters are expected from heavy jets. Figures are taken from [114].

This JetFitter [115] part of the algorithm uses a Kalman filter to find the primary vertex and fit the complete decay of b hadrons. This fit is an inclusive secondary vertex tagger as opposed to the impact parameter tagger. The algorithm exploits the decay structure of b hadrons inside of the jet. The combination of the two algorithms is done by a neural network (NN).

The performance of the combination algorithm is shown in Figure 4.6. Both the impact parameter and jet fitter components contribute to the total performance of the algorithm. The combination shows a much improved performance when compared to each individual component separately. Given the 70% efficiency working point of the algorithm, the expected rejection of light quarks in a $t\bar{t}$ sample is 99. A rejection of 99 means that for every 99 light jets, one is tagged incorrectly as a b jet.
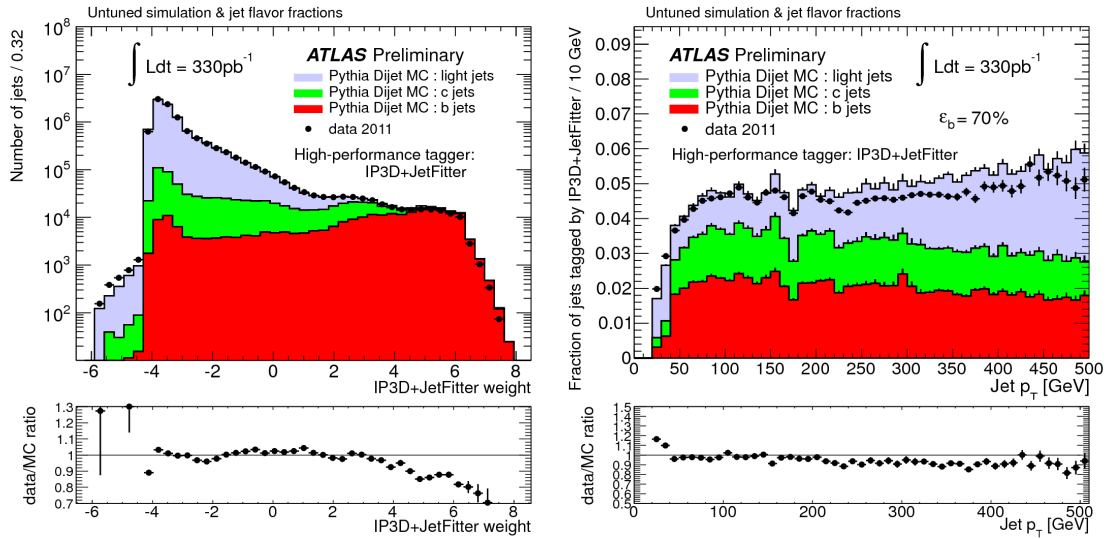
Figure 4.6.: (Left): Jet weight given by the Combination IP3D+JetFitter Algorithm in data and MC. Highlighted are the different types of jets. Heavy jets, specifically *b* jets, have a larger *b*-tagging weight than light jets, which have a predominantly low weight. This weight output per jet is the discriminant when choosing *b*-tagged jets. (Right): Fraction of jets tagged using the combination *b*-tagging algorithm. Figures are taken from [116].

4.1.4. Jet Selection

Jets are required to be high p_T jets, as they are expected to come from the $t\bar{t}$ decay. Jets are required to have at least a p_T of 25 GeV. Jets are also only chosen as physics objects if they lie within the calorimeter acceptance range of $|\eta| < 2.5$. As stated previously, the anti-k_T algorithm is used to reconstruct jets, a topological cluster algorithm with EM+JES calibration. For harder jets, the shape of the cone is very round whereas for softer jets, the cone shape is expected to be much more complex by description of the anti-k_T algorithm. The size of the cone in the algorithm is taken as 0.4. Since jets and electrons are reconstructed in the calorimeter in similar fashion, every electron is reconstructed as a jet. To avoid the double counting, jets must not lie within a $\Delta R < 0.2$ of an electron, or the jet is rejected.

A scale factor for b-tagging is also applied to all jets based on the performance of the b-tagger. The scale factor is determined from MC to data comparisons and corrects the MC for the differences in tagging rates. The scale factor is given as:

$$SF_{btag} = \frac{P_{data}}{P_{MC}}. \qquad (4.3)$$

Each jet is given a flavour (*b*, *c*, or *l*) based on its truth origin in MC. The jet is then checked if it is b-tagged or not. If a jet is b-tagged, it is given a scale factor. In the case where the jet is not b-tagged, it is given an inefficiency scale factor. The inefficiency scale factor is given as:

$$\omega_{jet} = \frac{1 - SF \times P_{MC}}{1 - P_{MC}}, \qquad (4.4)$$

which is dependent on the p$_T$, $|\eta|$, and flavour of the jet. The weights of all jets in the event are then multiplied together to give an overall event b-tag weight.

4.1.5. Electrons

Electrons are reconstructed objects which have energy deposited in the electromagnetic calorimeter. A cluster of energy which is above the 2.5 GeV threshold is matched with a charged track in the inner detector, which has p$_T$ > 0.5 GeV [117–119]. A fixed cone algorithm searches over all calorimeter cells, choosing the one with the highest energy above the threshold as the cluster position. The track match is required since the electron is charged and created hits within the inner detector. This electron must not fall within the crack region of the calorimeter, $1.37 < |\eta| < 1.52$, where the calorimeter objects are difficult to describe. This section of the detector is the transition region, between barrel and end-cap with a non-uniform magnetic field. Electrons must also be allocated as *tight* and isolated from other objects, especially jets, and have a hit in the b layer of the inner detector. The b layer is the inner most part of the tracking section and allows the distinction of electrons from uncharged photons which have a similar signature in the electromagnetic calorimeter.

Reconstructed electrons using the aforementioned criteria, are then calibrated by plotting the Z mass peak in both data and MC. Opposite sign electron pairs which have a combined mass in the range of [80,110] GeV are plotted and a fit is made to both data and MC. Afterwards, a correction factor is applied to MC based on the difference in resolution and peak position. The factor, which accounts for the difference in resolution and peak position between MC and data, is less than 1% in both the end-cap and barrel regions of the calorimeter, and is shown in Figure 4.7.
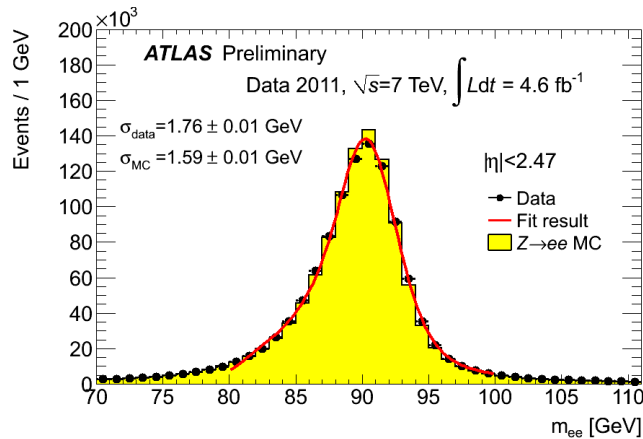
Figure 4.7.: $Z \to e^+e^-$ mass peak in data and MC for selected opposite signed candidate electrons from a Z boson. A correction factor based on the resolution and peak is applied to MC, whereas the central value shift is applied to data. Figure taken from [120].

4.1.6. Electron Selection

Electrons from the W boson are expected to have a large E_T. Therefore, the requirement for electrons used in the analysis is at least an $E_T > 25$ GeV. The variable E_T is calculated using the cluster energy ($E_{cluster}$) and η position of the track:

$$E_T = \frac{E_{cluster}}{\cosh(\eta_{\text{ track}})}. \tag{4.5}$$

Electrons are expected to lie within the detector acceptance of $|\eta| < 2.47$, excluding the crack region of the detector. Electrons must also satisfy the status word: *tight* and contain a match to the reconstructed track in the inner detector. The electron must also be isolated. The isolation requirement for electrons is given by the amount of energy deposited in the vicinity of the reconstructed electron. The isolation check is performed using a cone algorithm, which uses a cylinder shaped measurement of the amount of energy or momentum deposited around the object (in cone size $\Delta R = 0.2$ or 0.3 depending on whether cone20 or cone30, respectively, is used). The energy of the original object is subtracted using an inner cone radius given as $\Delta R = 0.05$. For the electrons used in this analysis, a p_T corrected $E_T^{cone20} < 3.5$ GeV is required.

A scale factor is also applied to MC, based on the performance of MC compared to data. The scale factor is determined for the reconstruction and identification efficiencies of electrons [121] based on the cluster η, ϕ, and E_T.

4.1.7. Electron Trigger

In the e + jets channel, the electron is required to fire the trigger. The trigger menu used for this analysis is given in Table 4.2.

Run Period	EF	L2	L1
D-H4	e20 Medium	e20 Medium	EM18

Table 4.2.: The electron trigger menu used for this analysis. For the entire data-taking period in question, only the single e20 Medium trigger is used.

To calculate the efficiencies of the trigger, the tag and probe method is again used on data and MC. The method is applied on $Z \to e^+e^-$. The efficiencies are based on several different η regions. The reconstructed electron is also required to have fired the trigger. This is checked via a trigger matching algorithm.

4.1.8. Muons

Muons are reconstructed objects from both the muon spectrometer and the inner detector. Since muons are charged, they will leave a track in both the inner detector and the outer muon spectrometer. Muons reach the muon spectrometer, unlike electrons or jets, because they are minimum ionizing particles. This means at the energy range of typical muons from $t\bar{t}$ decays, 10 - 200 GeV, they deposit only a small amount of their energy in the calorimeter. This makes muons simpler to identify because they hit in the muon

spectrometer and can be traced back to the interaction point with the help of the trigger and inner detector.

Muons are reconstructed by the Muɪd algorithm. The Muɪd algorithm uses a combined fit of both the inner detector and muon spectrometer. A global χ^2 fit is performed over both detectors and the individual tracks from each segment are refit to give the new global positioning of the muon. The performance of the algorithm in both data and MC is shown in Figure 4.8. Here the full selection is made using combined muon tracks, with the additional selection for the $Z \to \mu^+\mu^-$ events. This additional selection includes the mass window and oppositely signed muons. The performance shows a slightly worse resolution in data than in Pythia MC. This difference is taken into account by smearing the muon resolution in MC to match that of data.
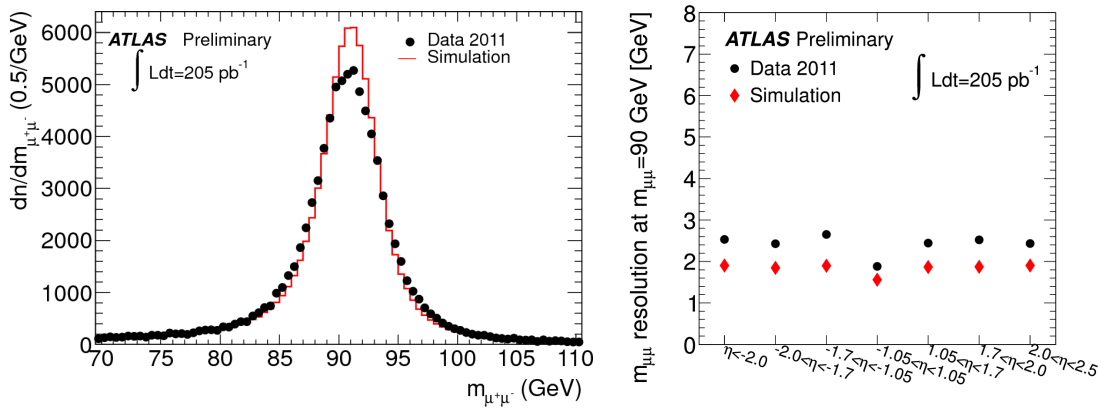
Figure 4.8.: Resolution of the combined muon algorithm for both data and MC for Muɪd muons. (Left): The $Z \to \mu^+\mu^-$ mass peak is plotted in both cases using the combined oppositely signed muons. The data show a slightly worse resolution than Pythia MC, resulting in a slightly broader Z mass peak. (Right): Resolution for both data and MC for several different η regions. Figures are taken from [122].

Since the combined muon algorithm requires both tracks in the inner detector and muon spectrometer, the performance of the reconstructed muon depends on both sub-detectors. For muons from the typical range of muons from $t\bar{t}$ decays, the muon resolution is both the product of the performance for the inner detector and the muon spectrometer. At low muon momenta, the inner detector performance describes solely the muon resolution. At high muon p_T, the combined resolution term is completely dominated by the performance of the muon spectrometer. This can be seen in the expected muon resolution for both standalone (muon spectrometer only) and combined performance shown in Figure 4.9.

4.1.9. Muon Selection

Muons are required to have a $p_T > 20$ GeV and lie within the detector acceptance $|\eta| < 2.5$. Muons are also required to be combined muons, reconstructed using both the inner detector and the muon spectrometer, from the Muɪd *family*. Similarly, in comparison with electrons, muons are required to be isolated. This is important for muons since in
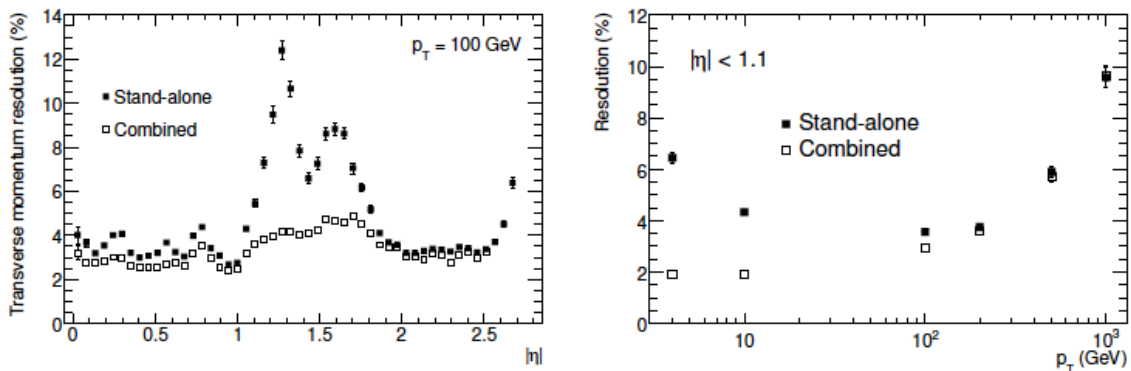
Figure 4.9.: Expected muon p_T resolution for combined and standalone algorithms. (Left): Resolution is shown as a function of η at $p_T = 100$ GeV and (right): as a function of p_T. It can be clearly seen that high p_T muon resolution is based solely on the standalone algorithm performance of the muon spectrometer. Figures are taken from [93].

some cases, a heavy b jet will decay semi-leptonically, leaving a muon inside the jet. Therefore, to veto such non-prompt muons, the muons are required to be isolated as they should be from W decays. The isolation criteria involves both energy and momentum cone algorithms: $E_T^{cone30} < 4$ GeV and $p_T^{cone30} < 4$ GeV. Furthermore, any muon which is found in the vicinity ($\Delta R < 0.4$) of a jet is removed. In addition to the isolation requirement, a series of inner detector hits are needed. At least one b-layer hit, several pixel, SCT and TRT hits are also required.

In the same manner as the $e + $ jets channel, a reconstruction and identification scale factor is applied to MC muons, based on the data to MC description. The scale factor is again determined by the tag and probe method, and is based on the muon p_T, η and ϕ positioning. However, unlike the $e + $ jets channel, the muon trigger is not applied in MC due to a problem in the trigger description. The muon trigger applied to data is found in Table 4.3. As a result, muon trigger efficiencies are directly applied to MC. In addition, the scale factor is also applied to MC. The trigger matching algorithm used to match the selected muon to the trigger firing lepton is not applied in data or MC. The matching efficiency is applied directly afterwards. Due to the known differences in data to MC, there is a resulting 4 % discrepancy in the number of expected muons compared to the number of observed muons in data.

Run Period	EF	L2	L1
D-H4	mu18	mu18	MU10

Table 4.3.: The muon trigger menu used for this analysis. For the entire data-taking period in question, only the single mu18 trigger is used on data. The trigger is not applied to MC.

4.1.10. Missing Transverse Energy ($\not{E}_T$)

Due to the neutrino from the single lepton decay of the $t\bar{t}$ pair, a significant amount of missing transverse energy is expected ($\not{E}_T$). $\not{E}_T$ uses the energy of all cells in the calorimeter and the calculated muon energy in order to check for an imbalance of energy in the transverse direction of the detector. The original energy in the transverse direction is assumed to be zero as the protons are colliding in the longitudinal direction. All of the reconstructed objects' energies are directionally summed into one quantity and the opposite value dictates the size and transverse position of the missing energy. The energy in cells which do not contribute to reconstructed objects are also added to the $\not{E}_T$.

The $\not{E}_T$ variable used for this analysis is a rescaled energy using the same jet energy calibration for consistency. The tight object definition is required for all objects. The understanding of the detector performance is essential to understand the $\not{E}_T$ as all cells in the working detector are used for its calculation. The performance of the $\not{E}_T$ algorithm is shown in the W decay due to the large $\not{E}_T$ component from the escaping neutrino. Using the W decay selection in both the μ and e channels, the MC to data comparison is shown in Figure 4.10, which was performed on $\sqrt{s} = 7$ TeV collision data [123].
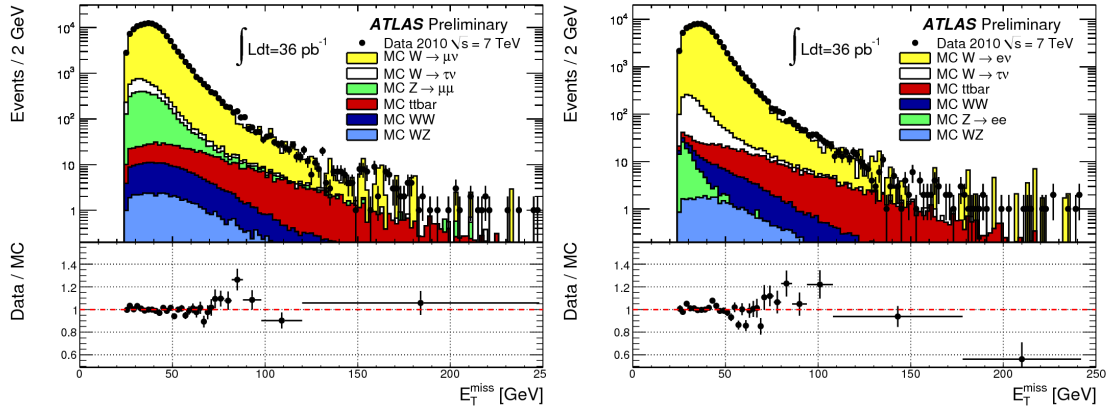
Figure 4.10.: (Left): $W \to \mu\nu$, and (right): $W \to e\nu$ $\not{E}_T$ distributions. Both channels show a very good agreement between MC and data. The figures are taken from $\sqrt{s} = 7$ TeV collision data [123].

The $\not{E}_T$ is calculated in the (x,y)-plane. It is constructed using all of the physics objects (muon, electrons, and jets) as well as the reconstructed jets with p_T less than 20 GeV and clusters which are not associated to any objects. The formula is written as:

$$E_{x,y}^{\text{miss}} = -(E_{x,y}^{\text{muons}} + E_{x,y}^{\text{electrons}} + E_{x,y}^{\text{jets}} + E_{x,y}^{\text{soft jet}} + E_{x,y}^{\text{cell out}}),\tag{4.6}$$

where the $\not{E}_T$ is calculated by the sum in quadrature of the (x,y) components.

$$\not{E}_T = \sqrt{(E_x^{\text{miss}})^2 + (E_y^{\text{miss}})^2}.\tag{4.7}$$

4.2. Event Selection

The following event selection is used to improve the signal over background (S/B) ratio in the lepton + jets channel. The event selection is made to limit the largest portion of

the background contributions while keeping a relatively large amount of signal. The event cuts can be broken into several sections:

Rejection of Collision Background

To reject pile-up and other background events such as cosmic events, a primary vertex with at least four tracks associated to it is required in each event.

Lepton Requirements

Exactly one signal lepton (either electron or muon) is required. The lepton is also required to fire the trigger. This trigger requirement is only applied in the e + jets channel for both data and MC. A trigger matching algorithm is applied to match the selected lepton with the trigger firing lepton. In the μ + jets channel, the data is only required to fire the trigger. In data, a trigger matching algorithm is also applied. However, in MC the trigger and trigger matching efficiencies are directly applied to match the expected performance. Furthermore, there are required to be no electron or muon overlaps in the inner detector.

$\not{E}_T$ Requirements

Since $t\bar{t}$ decays in the single lepton channel to one W boson which decays into a charged lepton and neutrino, there is expected to be a significant amount of $\not{E}_T$. Therefore a basic $\not{E}_T$ requirement of $\not{E}_T > 20$ GeV is required in every event. Since, however, there is still a large amount of background due to QCD multijets, an additional selection is applied to each channel separately. In the μ + jets channel, a triangular cut of $\not{E}_T$ + W transverse mass (m_W^T) > 60 GeV is required. In the e + jets channel, a higher $\not{E}_T$ threshold is required, $\not{E}_T > 35$ GeV, along with a $m_W^T > 25$ GeV. The m_W^T is defined as:

$$m_W^T = \sqrt{2p_T^l \cdot p_T^\nu [1 - \cos(\phi^l - \phi^\nu)]}. \tag{4.8}$$

Jet Requirements

At least four jets are required per event. It is expected from tree-level $t\bar{t}$ decay into the single lepton channel that there are four jets in the final state. To reject a large amount of QCD multijets, at least one of these jets must be b-tagged using the JetFitterCombNN algorithm. The b-tagging weight must be > 0.35. This cut corresponds to the 70 % efficiency working point of the tagger. The light quark rejection is 99 at this working point.

Bad Jets

Using jet quality cuts, jets defined as *bad* with $p_T > 20$ GeV are not used. Not only are these jets not used, but events which contain at least one such jet are also discarded. Sources of bad jets include noise in certain calorimeter sections, as well as energy spikes in the hadronic end-cap.

LAr Dead FEBs

At event level any LAr bursts are removed in data. Also in data, some objects were lost due to dead LAr FEBs present for some of the data taking period (E-H), corresponding to about 80 % of the data-taking period. Therefore, an appropriate number of MC events are scaled to be lost in this region to match the hole present during some of the data-taking. This hole effects the calorimeter performance and can be seen in the electron and jet reconstruction.

Good Runs List

To ensure the detector is performing properly, a Good Runs List (GRL) is used. When the full detector is functioning as it should, a good run list calculates the selected luminosity blocks (LBs) which are used for physics analyses. The GRL is defined for the entire physics group at ATLAS.

Pileup Re-weighting

In 2011 data-taking, pileup uncertainties due to out-of-time pileup from bunch trains constitute a large difference in MC to data modelling. As a result, this cannot be ignored and needs to be taken into account. The MC which is used to measure the top quark mass was created before data taking in 2011 began. The MC primary vertex distribution is therefore only a *best-guess* scenario. For the first part of data-taking period, the bunch separation is 50 ns. With such small separation time, overlapping signals can cause problems when reconstructing objects in the detector. To deal with this out-of-time as well as in-time pileup, re-weighting is performed on MC to match that of the data periods which are used for the 1.04 fb^{-1}. In-time pileup is the result of many reconstructed vertices in the same event due to multiple interactions at high instantaneous luminosities.

5. Modelling of Signal and Background Processes

5.1. Signal Monte Carlo

Monte Carlo (MC) simulations are used to model the physics processes, with the exception of QCD, to measure the top quark mass. For the simulation of the signal $t\bar{t}$ and single top production, the MC generator HERWIG [124] is used. The hard scattering is described using a NLO addition to HERWIG known as MC@NLO [125]. The underlying event for signal events is modeled by an extension to HERWIG: JIMMY [126, 127]. JIMMY describes the underlying event, which takes into account all remnants of the incoming protons. JIMMY has been tuned with first ATLAS data in 2010 [128].

The parton momenta are obtained from the parton density functions (PDFs) given by CTEQ6L [40]. The PDFs are described in Section 2.3. The parton showering is governed by the DGLAP equations [129–132]. The equations describe the evolution of a single parton splitting into two separate partons. The tuning of MC can allow parton splitting to occur more or less likely and both before or after the hard scattering process. These variations are taken into account when modeling initial and final state radiation systematics.

Once the energy of the parton reaches sufficiently low levels, the fragmentation begins. This regions is described by non-perturbative QCD. The fragmentation model used by HERWIG is cluster fragmentation. This process must be tuned to the dataset used because various models may not represent the effects seen in data. The cluster fragmentation used allows gluon splitting to $q\bar{q}$ pairs. From these pairs, clusters of quarks are formed based on colour.

For the consideration of different $t\bar{t}$ signal models, the NLO POWHEG generator [133] is used. Different fragmentation models are also used: PYTHIA [134] instead of JIMMY are interfaced with the POWHEG generator. This is elaborated in the context of the systematic uncertainties of the top mass measurement.

PYTHIA is different from HERWIG since it utilizes the string-fragmentation model for showering and matching. String fragmentation models can be visualized as strings between $q\bar{q}$ pairs to represent the potential energy between these two quarks. As the string expands, so too does the potential energy. Thus, as the energy reaches a threshold limit, the string breaks and a new $q\bar{q}$ pair is created.

5.2. Background Monte Carlo

The simulation of background processes was done using LO event generation and parton showering. The background processes which are described by MC are W/Z + jets and

diboson production of WW, ZZ and WZ. The W + jets and Z + jets samples are produced using ALPGEN [135] + HERWIG and the JIMMY extension. ALPGEN uses an MLM-Matching [136]; where each exclusive jet bin is produced separately. They are separated into the three lepton flavours (e, μ, and τ) and jet parton multiplicity. The jet multiplicities run from 0 to 5. Since they are ALPGEN samples, the MLM-Matching is used with a cluster transverse momentum parameter of radius 0.2 for the cone. The MLM-Matching technique matches the parton shower of the LO event. Double counting of events is checked when matching the hard process to the showering and overlapping events are discarded between different parton multiplicity bins. This overlap primarily occurs at high p_T or wide-angled emissions of partons.

In MC production, the mass of the emitted quark must also be considered. So far, the mass of the b and c quark have not been taken into account, however their mass is significantly higher than that of the light quarks (u, d and s). Therefore, in addition to the W + jets and Z + jets samples, additional samples with massive b and c quarks in the final state are also produced. In both W + jets and Z + jets, $b\bar{b}$, $c\bar{c}$, along with single c final state samples in the W + jets case only are produced. The sample generation and showering is the same as the light samples except for a change in phase space. Since these samples are complimentary and not completely orthogonal to the light jet samples, overlapping events were removed from the light W/Z + jets samples. The overlap is primarily the result of b quarks originating from gluon splitting in the light jet samples. In such scenarios, the events are considered in the heavy flavour samples only.

The diboson samples are produced with ALPGEN and HERWIG. For all background samples, the NLO cross section is applied to the overall scale of each sample (separated in some cases by parton multiplicity).

5.3. Event Generation

All event generation uses the GEANT4 [137] framework to simulate the effects of the produced MC on the ATLAS detector. The event information is passed to the GEANT4 simulation where the energy and position of the objects are modeled by interaction models of the detector materials. All remnants from the original pp collision are considered and simulated until the event is fully reconstructed in the detector. The ATLAS detector itself is described by over 25 million volumes in total. All detector response is considered and passed to the ATHENA framework [138] in a similar manner as data. The trigger and offline object reconstruction are then performed to obtain the reconstructed objects from the simulated event.

5.4. Data Driven Methods

In addition to the background MC, two background processes are modeled from auxiliary measurements. One is the measurement of QCD multijets in data. Since multijet production is very difficult to model with MC, the measurement needed is made on data. To estimate the QCD multijet background, two separate methods are used: matrix method [139] and so-called anti-electron model. The matrix method is used in both the e + jets and μ + jets channel as the default estimation. The anti-electron method is

used as a cross-check QCD estimation in the e + jets channel and used to estimate the systematic uncertainty based on QCD modelling. The second data driven estimation is of the normalization level of the W + jets background, the most significant background in the l + jets channel.

5.4.1. QCD Multijets Estimation from the Matrix Method

The first method used to measure the QCD multijet production is known as the Matrix Method. The procedure uses the efficiency of tight and loose leptons in order to estimate weights for each lepton in data. This is the default method used to estimate the QCD multijets for this analysis. Events from QCD multijets are events which are assumed to contain fake leptons either from improperly isolated leptons from semi-leptonic b decays, mis-reconstructed jets or in the electron case, photon conversions.

For each of the two channels, a separate event selection is made. In the first case, the original event selection is performed. The first case uses the *tight* definition of the lepton. The second event selection uses a loose definition of the lepton. In both cases an event weight is given to the data. The weight corresponds to whether the event contains a loose or tight definition of the lepton. When adding all of the weights for a given sample, the total yield and corresponding shape can be obtained for QCD multijets background.

The definitions for tight leptons are given by the nominal event and object selections found in Section 4.2. The loose definitions are the same as the tight definitions except for the following modifications:

- muon: no isolation requirement (both p_T^{cone} and E_T^{cone} are not used),

- electron: a looser isolation requirement from the p_T corrected $E_T^{cone} < 6$ GeV (instead of 3.5 GeV), a type *medium* electron with an additional requirement of a reconstructed track with a b-layer hit in the inner detector, and the use of medium missing transverse energy requirement at the event level (instead of tight $\not{E}_T$).

The number of events in the two separate samples are given by:

$$N^{loose} = N_{real}^{loose} + N_{fake}^{loose}, \tag{5.1}$$
$$N^{tight} = \epsilon_{real}N_{real}^{loose} + \epsilon_{fake}N_{fake}^{loose}, \tag{5.2}$$

where the ϵ_{fake} and ϵ_{real} are the two efficiencies for fake and real QCD events. They are defined by:

$$\epsilon_{fake/real} = \frac{N_{fake/real}^{tight}}{N_{fake/real}^{loose}}. \tag{5.3}$$

The fake efficiency is calculated from an enriched QCD sample obtained when using a low transverse mass m_W^T region in the μ + jets channel, which contains a significant amount of QCD events. m_W^T is defined in Equation 4.8.

The resulting distribution for inclusive 1 jet events can be seen in Figure 5.1, where an abundance of QCD events is visible in the low transverse W mass (m_W^T) region.
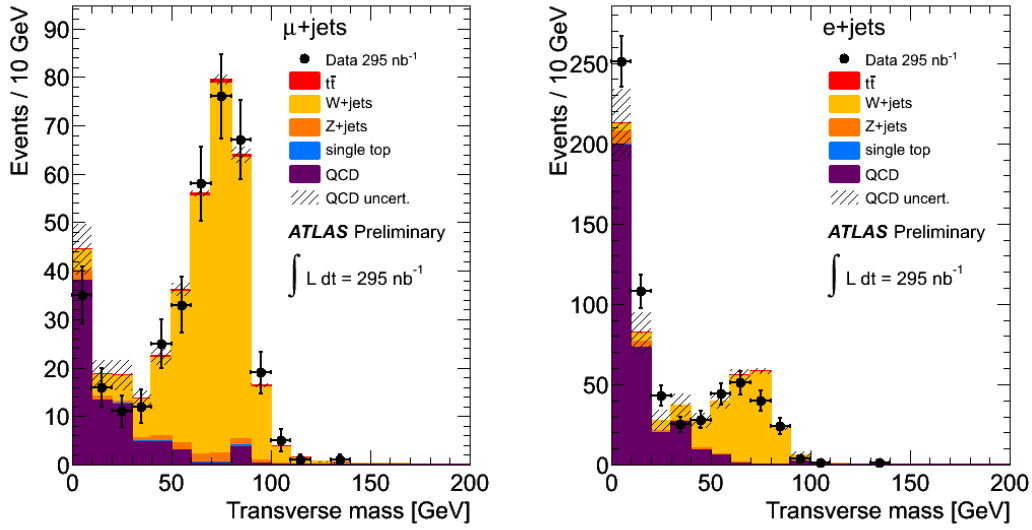
Figure 5.1.: Control regions of the low m_W^T region in both (left): $\mu + $ jets and (right): $e + $ jets for the matrix method background estimation for QCD multijets production. The abundance of QCD events can be seen in this region. Figures taken from [140].

In the $e + $ jets channel, the fake efficiencies were determined from the low $\not{E}_T$ control region ($5 < \not{E}_T < 20$ GeV).

The real efficiency is calculated with the tag and probe method in a sample of $Z \to \mu^+\mu^-$ or $Z \to e^+e^-$ events, similarly to the trigger and identification efficiencies for lepton objects. The tag and probe method uses an identified lepton ("tag") and searches for the second lepton from the Z decay ("probe").

The resulting weights applied to the data are given to events where the loose lepton also fulfills the tight requirements:

$$w_{MM}^{tight} = \frac{\varepsilon_{real} \cdot \varepsilon_{fake}}{\varepsilon_{real} - \varepsilon_{fake}} \tag{5.4}$$

and when the loose electron fails the tight requirements:

$$w_{MM}^{loose} = \frac{(\varepsilon_{real} - 1) \cdot \varepsilon_{fake}}{\varepsilon_{real} - \varepsilon_{fake}} \tag{5.5}$$

The total number of events which contain at least a loose lepton receive a weight. The loose leptons obtain a small negative weight, whereas events which contain a lepton which satisfies both tight and loose definitions, obtain a positive weight. By adding all of these events, the total shape and normalization of the QCD multijets background is estimated.

5.4.2. QCD Multijets Estimation from the Anti-Electron Model

In the electron channel, the so-called "anti-electron model"[1] is employed to estimate the QCD multijets shape uncertainty which is accounted for in the total systematics uncertainty of this method. The model uses the same selection as the electron, except inverts the tight isolation, resulting in an "anti-electron". As a result, the sample is completely orthogonal to the dataset used for the analysis. The resulting fit to data, along with the other MC processes determines the overall normalization of the sample. From this fit, an extrapolation of the shape is made into the signal region, giving the shape and normalization for QCD multijets in data.

5.4.3. W + Jets Normalization

The second data driven estimate made for the modelling of background processes is the estimation of the normalization of W + jets. The MC is used to model the shape and the data is used to normalize the overall contribution of W + jets in background. The normalization estimation is performed using the W charge asymmetry measurement [141]. The asymmetry arises from W bosons which are created charge asymmetrically (more W^+ than W^-) at the LHC since they are produced by $q\bar{q}$ annihilation. The W boson then decays leptonically leaving a charged lepton which can be identified. As a result, the charge imbalance is measured giving the overall normalization of the W + jets events.

Using the assumption that all other physics processes produce symmetrically charged leptons, the number of W^+ and W^- can be determined using the formula:

$$N_{W+} + N_{W-} = \left(\frac{r_{MC}+1}{r_{MC}-1}\right)(D^+ - D^-), \tag{5.6}$$

where D^+ and D^- are the number of events in data which pass the full event selection before b-tagging with a positively charged or negatively charged lepton respectively. The variable r_{MC} is the cross section ratio of W^+ production divided by W^- production determined in MC. The results of this measurement are applied to the overall normalization of W + jets background in the 4 inclusive jet channel. The resulting SF determined in the 4 jet inclusive jet bin is found in Table 5.1. The largest uncertainties of the method arise from uncertainties in the parton density functions, jet energy scale, and heavy flavour fraction in W + jets events.

N_{jets}	μ + jets pretag	μ + jets tagged	e + jets pretag	e + jets tagged
≥ 4	0.80 ± 0.11	0.79 ± 0.18	0.96 ± 0.14	0.89 ± 0.20

Table 5.1.: Normalization factor applied to W + jets events in MC. The numbers are obtained from the W charge asymmetry measurement made at ATLAS.

---

[1]explained in further detail in Ref. [44]

5.4.4. W + Jets Heavy-to-light Normalization

To account for the proper heavy-to-light ratio in W + jets events, studies were performed on data to check the proper fraction of b, c and light events. The study is performed using the $W + 1$ and $W + 2$ jet bins. Using three numbers: the number of tagged events in $W + 1$ and $W + 2$ jet bins and the number of $W + 2$ events before b-tagging, a relationship between tagged and un-tagged events for $b\bar{b}$, $c\bar{c}$ and Wc scenarios can be established in data. The resulting scale factors are found to be:

$$SF_{Wb\bar{b}/Wc\bar{c}} = 1.63 \pm 0.76 \tag{5.7}$$

and for the fraction of Wc events:

$$SF_{Wc} = 1.11 \pm 0.35 \tag{5.8}$$

compared to the original ALPGEN MC. To keep the overall normalization, W + light jet samples are rescaled down to keep the total number of events the same.

6. Model to Data Comparison

6.1. Dataset

The dataset used to measure the top quark mass is a subset of the 2011 LHC data collected at the ATLAS detector. During the 2011 run, 5.25 fb^{-1} of data were collected by ATLAS from 5.81 fb^{-1} of data delivered by the LHC. The overall data-taking efficiency is 93.5 %, a significant achievement for the LHC and the ATLAS detector running. For this analysis, the first 1.04 fb^{-1} of this data is used. This run period corresponds to the early part of the year, with a lower instantaneous luminosity and number of protons per bunch than with the full 5.81 fb^{-1}. The determination of the ATLAS luminosity can be found at Ref. [142]. Both the cumulative and instantaneous luminosity are shown in Figure 6.1.
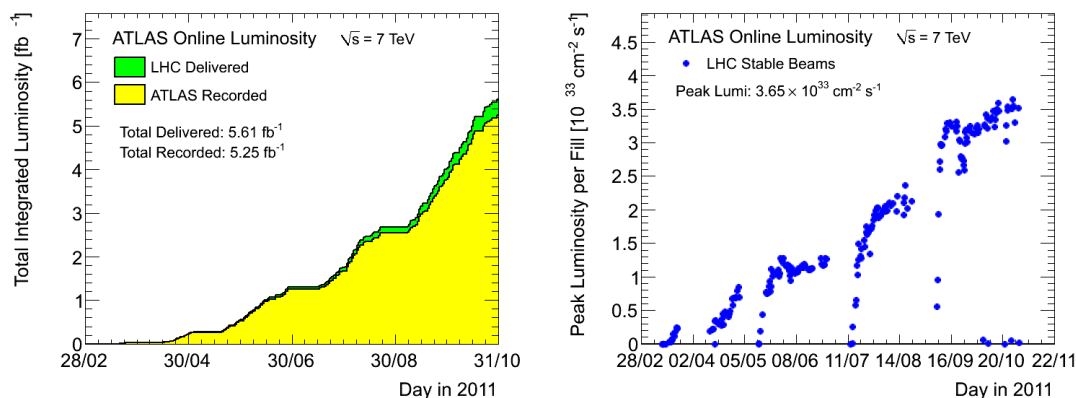
Figure 6.1.: 2011 ATLAS collected luminosity. (Left): Shown are both the delivered and collected luminosity. The performance of the ATLAS detector was very efficient, having a 93.5 % overall efficient data taking status for the year 2011. (Right): Peak luminosity during stable beam running collected over the 2011 run year. Figures taken from [143].

6.2. Pretag Control Plots and Event Yields

The total event yields for the various contributions of signal and background MC, as well as the Matrix Method data driven QCD estimate and W + jets normalization are found in Table 6.1 before b-tagging is applied. These event yields correspond to the luminosity of 1.04 fb^{-1}. Control plots in both Figures 6.2 and 6.3 are made for various event observables and kinematics for the μ + jets and e + jets channels respectively.

Channel with $\int L\,dt = 1.04\ \text{fb}^{-1}$	μ + jets	e + jets
$t\bar{t}$ (m$_{top}$ = 172.5 GeV)	7100 ± 250	4800 ± 180
Single top (m$_{top}$ = 172.5 GeV)	460 ± 18	320 ± 13
W + jets	8600 ± 380	5000 ± 240
Z + jets	970 ± 53	770 ± 42
Diboson	130 ± 6	80 ± 4
QCD Multijets	1640 ± 1640	910 ± 910
Signal + background	18900 ± 1850	11900 ± 1070
Data	19599	12023

Table 6.1.: Observed numbers of events in data compared to the expected numbers of MC signal and different background channels without the b-tag requirement. The QCD multijts in both channels is estimated using the Matrix Method. The QCD multijets uncertainty is taken as 100%. Not only is the QCD multijets background estimate data-driven, but also the total normalization of W + jets taken from data-driven estimates. The uncertainties include the scale factor uncertainties, MC statistics and data-driven QCD multijets and W + jets uncertainties.

The overall MC to data agreement is very good in both channels. It can be seen that there is an excess of data in the μ + jets channel. In comparison, the e + jets channel has almost perfect agreement between MC and data. The excess in data events, which is still covered by the expected MC uncertainty, is the result of not applying the trigger or trigger matching in MC. The efficiencies of both are applied to the MC afterwards, however there is still a difference in the high H_T (sum of the jet p$_T$) region. In this region, more data events are observed than MC.

There is also a difference in the number of events between the e + jets and μ + jets channels. In the e + jets channel, only about 2/3 of the total number of events in the μ + jets channel is observed. The reason for such a difference in the two channels is due to the tighter event selection requirements in the e + jets channel to limit the QCD multijets levels, specifically from the $\not{E}_T$ and transverse W mass requirement. Not only is the $\not{E}_T$ requirement at a higher threshold in comparison to the μ + jets channel, but also the lepton p$_T$ cut for the electron is higher (25 GeV instead of 20 GeV).

The data period is also broken into several segments due to a FEB failure during some of this period. As a result, approximately 80 % of the data is missing a small segment of the calorimeter. This can be directly seen in the control plots, where the jet ϕ is missing a segment and is not flat as expected. To compensate for this effect, a random number of events is given a smaller weight comparable to the fraction of luminosity which contain the problem.

The pretag control plots show a background dominated region to evaluate the performance of the two data-driven background estimates. It is seen that the overall agreement in the pretag samples is very good.
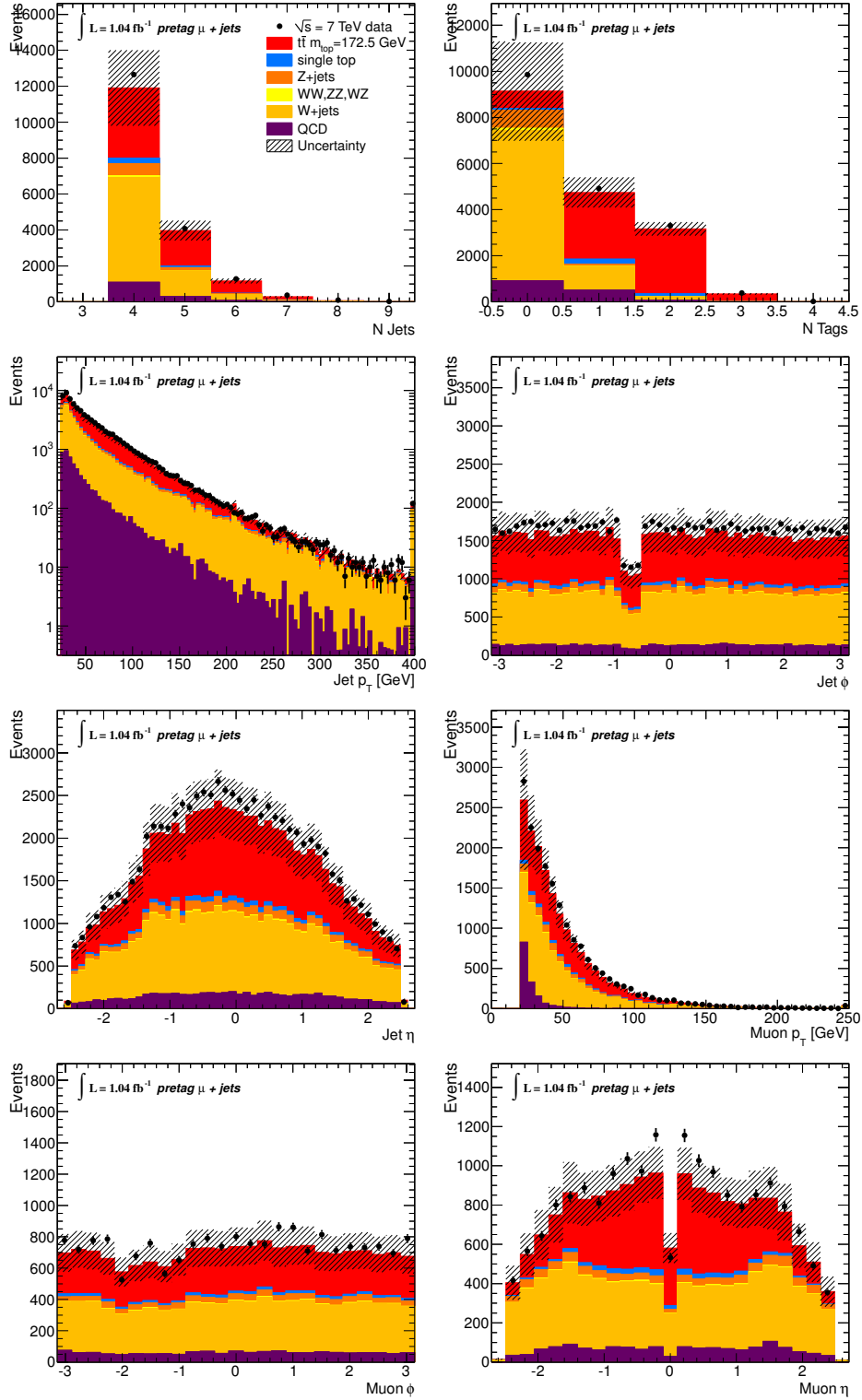
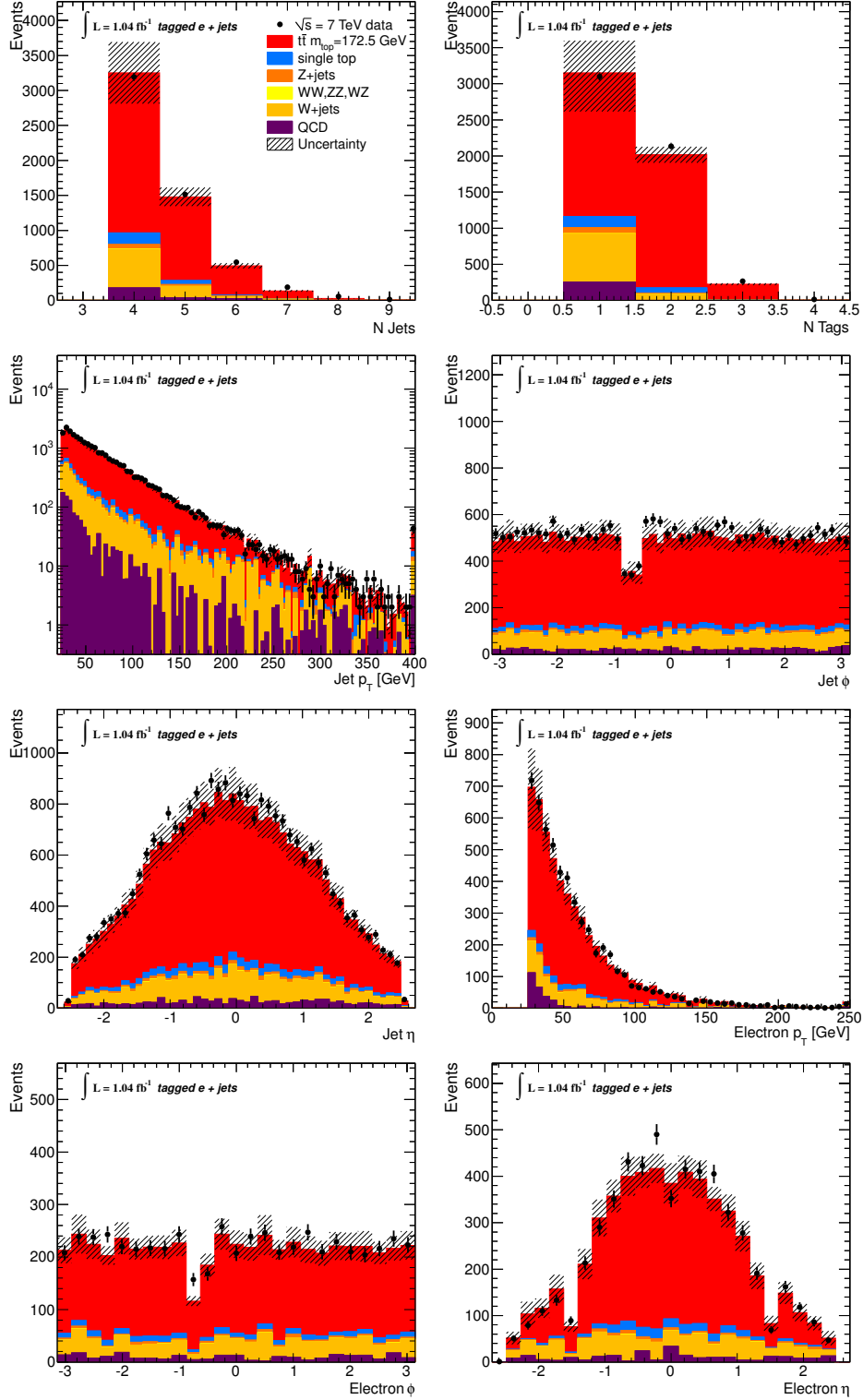***Figure 6.2.:*** Pretag μ + jets channel control plots. They include the number of jets and b-tags along with kinematics (p_T, η and ϕ) of the jets and muons. The uncertainties on the MC are the combined uncertainties from MC statistics, scale factors and data-driven estimate uncertainties.
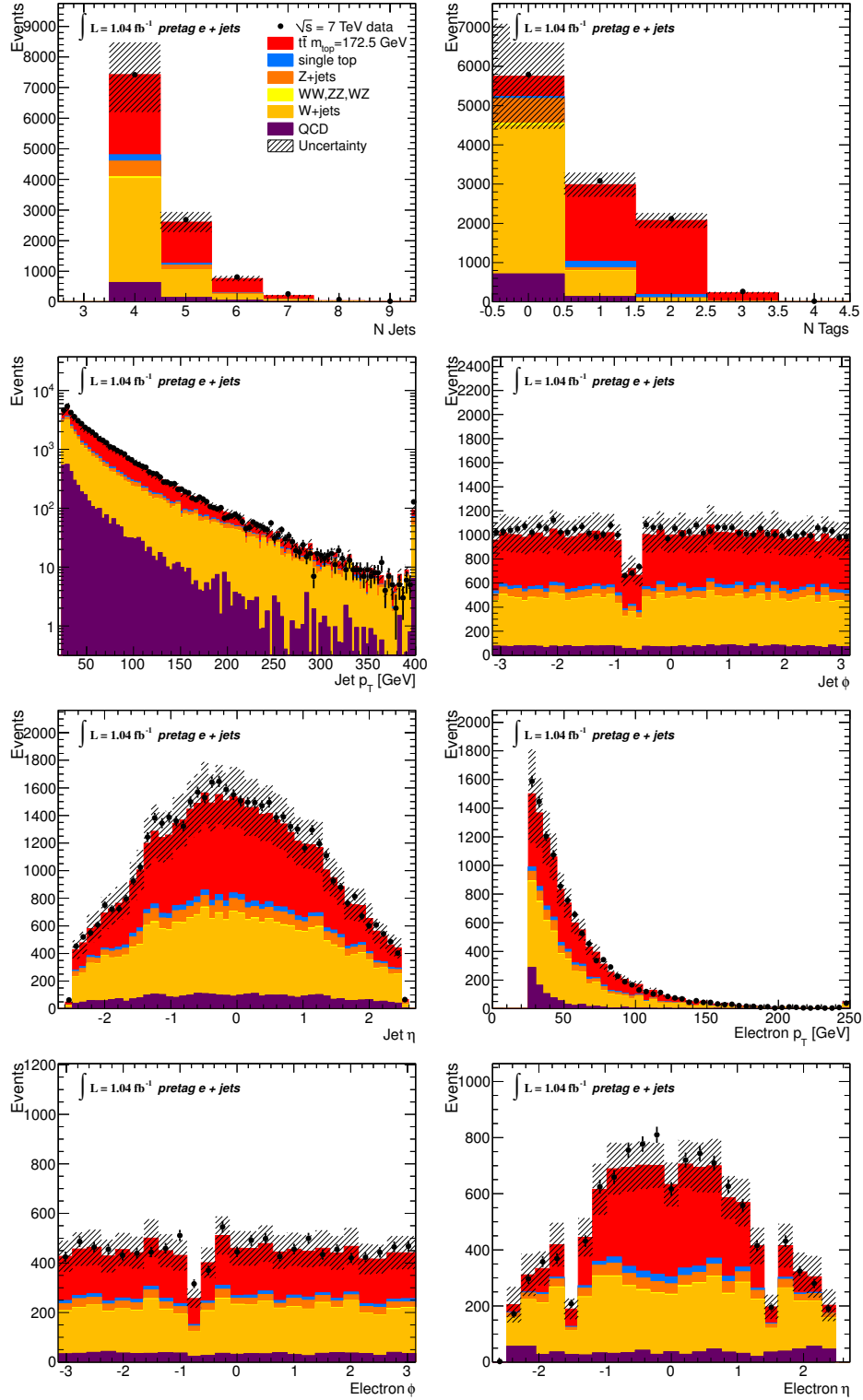
Figure 6.3.: Pretag e + jets channel control plots. They include the number of jets and b-tags along with the kinematics (p_T, η and ϕ) of the jets and electrons. The uncertainties on the MC statistics, scale factors and data-driven estimate uncertainties.

6.3. Tagged Control Plots and Event Yields

The final number of events for both MC and data in both the e + jets and μ + jets channels after the event selection are found in Table 6.2. Control plots in Figure 6.4 and Figure 6.5 show the MC to data comparison after event selection. Several object properties are plotted including p_T, η and ϕ of the objects. Also included are the number of jets and number of b-tagged jets in each event. The uncertainties on MC expectation include the MC statistical uncertainty, 100 % QCD estimation uncertainty and systematical uncertainties from the b-tagging scale factor uncertainties along with the scale factor uncertainties from reconstruction, trigger and identification of the leptons. These scale factors are applied to the MC, and as a result, their uncertainties are included in the MC expectation. In the case of the μ + jets, the trigger was not applied directly to MC, instead the trigger efficiency was applied to objects based on p_T and η of the muon. The overall W + jets normalization is obtained from data. The overall agreement of MC to data is very good, however in both channels, the MC expectation is lower than the observed data.

The signal over background (S/B) for this event selection is found to be 2.6 ± 1.2 in the μ + jets channel and 2.8 ± 1.2 in the e + jets channel when considering only the $t\bar{t}$ as signal. Since the single top event yield is dependent on the top mass, it is also used as signal in the templates. The S/B in this case is 3.3 ± 1.8 in the μ + jets channel and 3.6 ± 1.9 in the e + jets channel.

Channel with $\int$ L dt = 1.04 fb^{-1}	μ + jets	e + jets
$t\bar{t}$ (m_{top} = 172.5 GeV)	6300 ± 230	4250 ± 160
Single top (m_{top} = 172.5 GeV)	360 ± 14	260 ± 10
W + jets	1300 ± 920	840 ± 590
Z + jets	140 ± 17	110 ± 13
Diboson	22 ± 2	14 ± 1
QCD Multijets	520 ± 520	270 ± 270
Signal + background	8600 ± 1100	5700 ± 700
Data	9114	5832

Table 6.2.: Observed numbers of events in data compared to the expected numbers of MC signal and different background channels for only the object selection cuts listed beforehand. The tighter object definition in the e + jets channel lowers the number of events in comparison to the μ + jets channel. The QCD multijets backgroundin both channels is estimated using the Matrix Method. Errors for MC yields include the MC statistics and b-tagging event weight scale factor uncertainties. The data-driven estimates are obtained from the estimate itself, including 100 % for QCD multijets.

The overall agreement for object kinematics between model and data is very good. The inclusive jet p_T spectrum, which is of importance for top quark mass measurements is well described by the MC and data-driven estimates in both channels. Both the hard and soft ends of the p_T spectrum are well described in MC when compared to the observed data. The missing segment of the calorimeter for some of the data taking period is also well modeled in both the jet ϕ and electron ϕ. The overall normalization agrees in both channels.
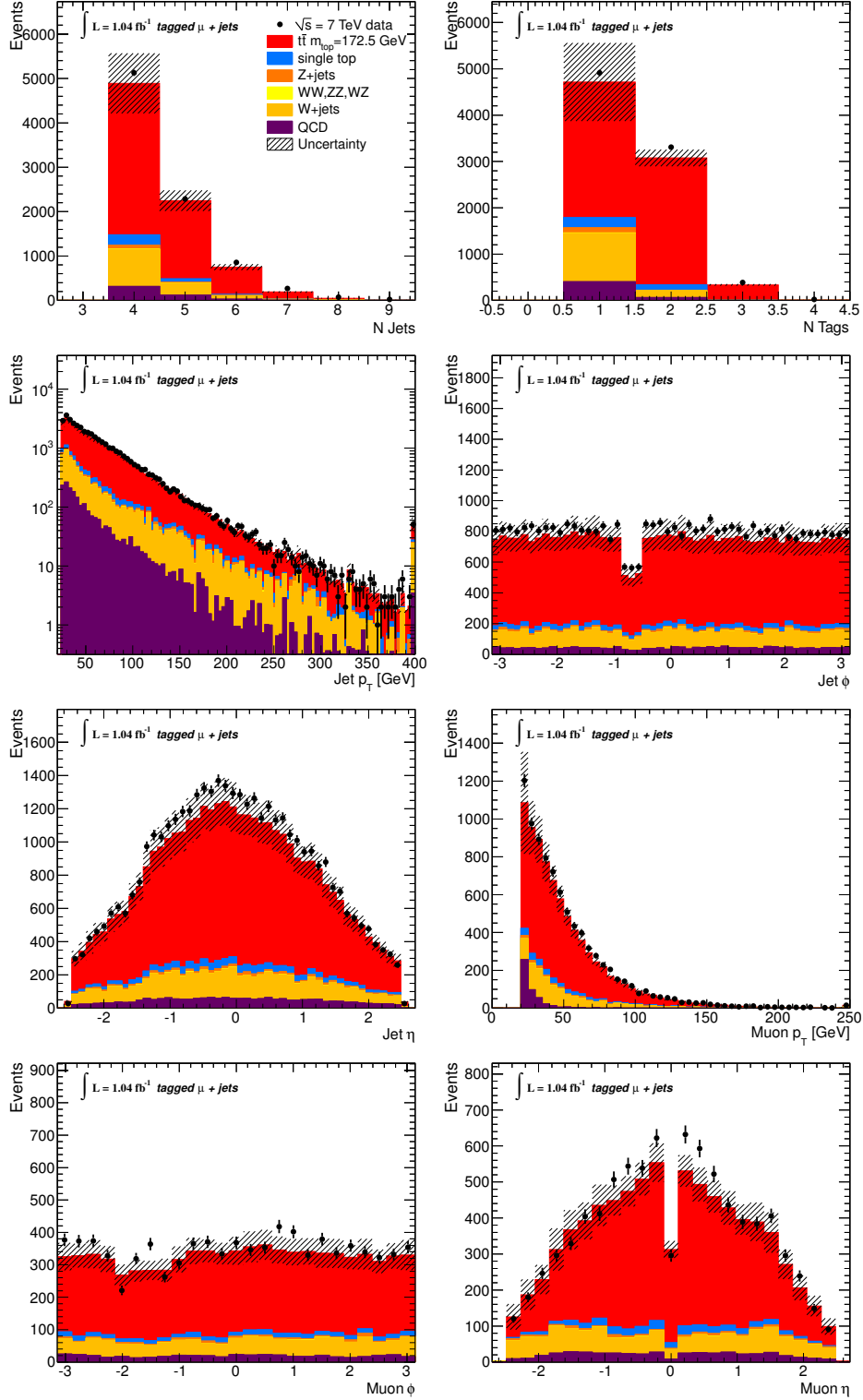
Figure 6.4.: μ + jets channel control plots. They include the number of jets, number of b-tags along with kinematics (p_T, η and ϕ) of the jets and muons. The uncertainties include the MC statistics, scale factors and data-driven estimate uncertainties.

Figure 6.5.: e + jets channel control plots. They include the number of jets and b-tags along with the kinematics (p_T, η and ϕ) of the jets and electrons. The uncertainties include the MC statistics, scale factors and data-driven estimate uncertainties.

The leading jet is expected to come on average from the hard process, containing the highest p_T jet. As a result, it is expected that the p_T and η of the leading jet must have a good agreement in the model when compared to data. The leading jet p_T and η spectrums for data are found in the subsequent Figure 6.6 and show an overall agreement of the model expectation.
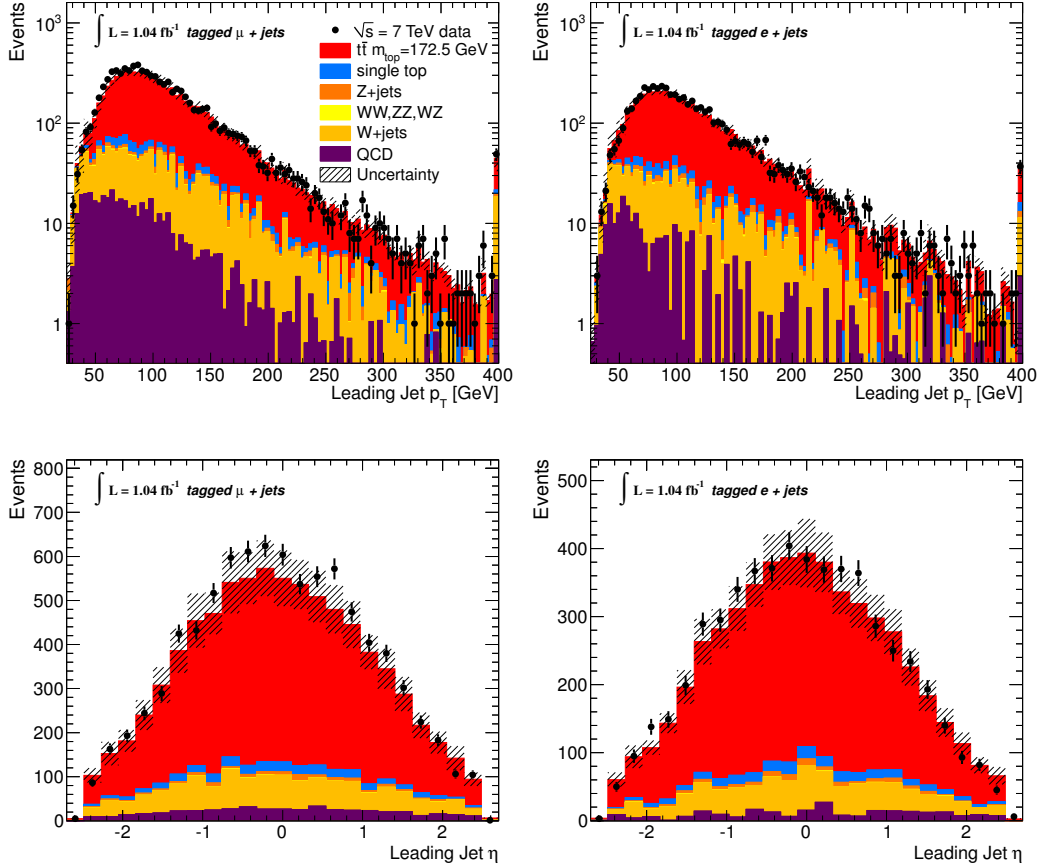
Figure 6.6.: (Top left): Leading Jet p_T spectrum for μ + jets and (top right): e + jets channels. (Bottom left): Leading Jet η spectrum for μ + jets and (bottom right): e + jets channels. The agreement for both channels is very good showing a good description of the data by the MC used.

6.3.1. Pileup

All MC is re-weighted based on the difference of pileup in MC and data. Since the MC number of primary vertices does not match that of data, a re-weighting is necessary in MC. To check the output of this re-weighting, the number of primary vertices is plotted for both MC and data in Figure 6.7. The overall agreement is very good. The agreement of number of primary vertices is required as a first step to verify the effects of pileup are modeled properly in the MC. The top quark mass as a function of the number of primary vertices or position in the bunch train is checked in the systematics of the measurement

and an appropriate error is associated to the outcome of this reweighting procedure.
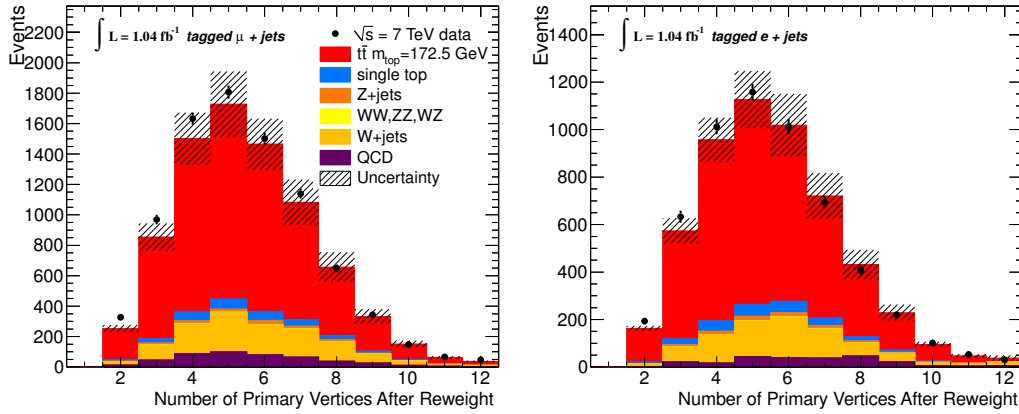
Figure 6.7.: (Left): μ + jets channel and (right): e + jets channel plotted number of primary vertices in data and the reweighted number of primary vertices in MC. The reweighted MC shows very good agreement with the data period used for this analysis.

6.3.2. b-Tagging

The weight of the JetFitterCombNN on inclusive 4-jet events (after event selection with and without including at least one b-tag in this selection) is found in Figure 6.8. The large amount of events contain jets with a weight < 0. A significant portion of these events are jets from background events. It can be clearly seen that after the b-tag requirement, a significant portion of the background events are discarded. Not only are a large amount of background events eliminated by the b-tag requirement, but also there are few background events remaining with large jet weights. Most of the events which contain at least one jet above the jet weight cut of 0.35 are signal. This can also be seen in Figure 6.4 and 6.5, in the top right corner where number of b-tags is shown. In the events with 1 b-tag, the majority of events are signal, however a large number of background events still remain. For a much more pure signal sample, one could require 2 b-tags. The 2 b-tag requirement however, is not necessary in the lepton + jets channel since the background sample is also fit when making the data measurement and does not constitute a large uncertainty.
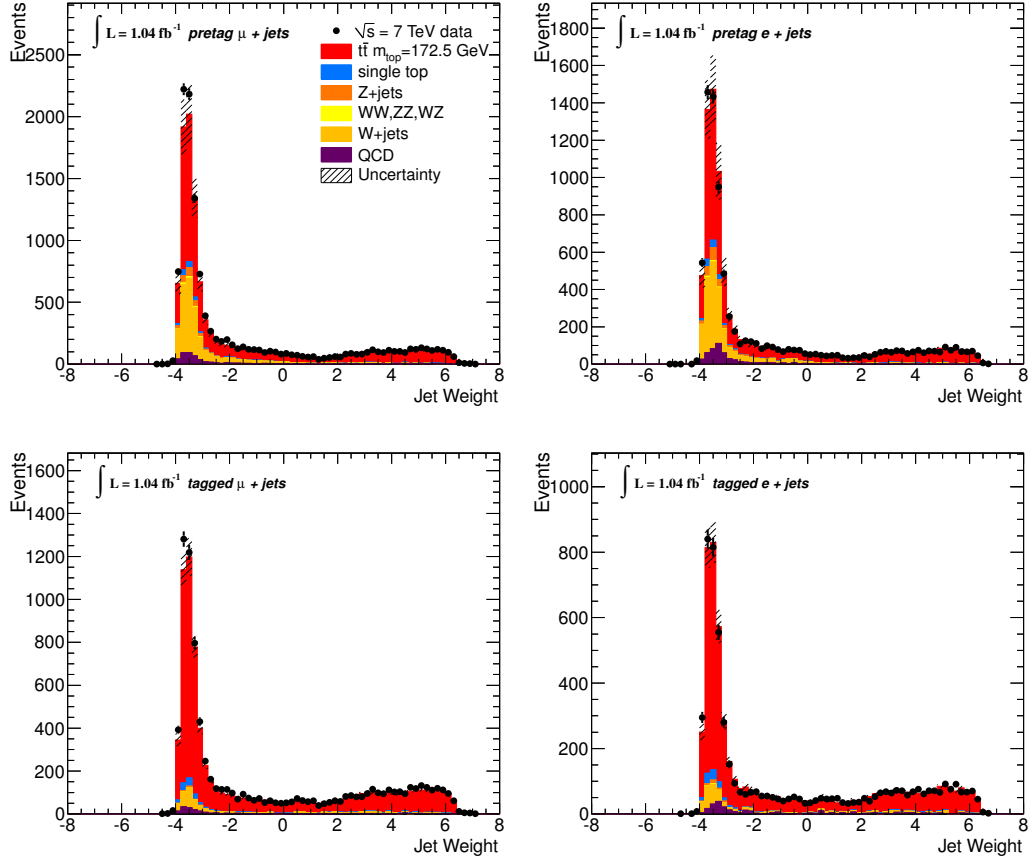
Figure 6.8.: (Left plots): μ + jets channel and (right plots): e + jets channel for the jet weight from the JetFitterCombNN tagger. The top plots show the jet weight of all jets after the event selection (without b-tagging). It can be seen that a very large portion of jets from background processes, such as W + jets, have a low Jet Weight. The cut at 0.35 diminishes this amount, as seen in the bottom two plots after it is required that at least one jet per event has a weight greater than 0.35.

7. Reconstruction of Top Quark Pairs

7.1. Kinematic Likelihood Fitter

The Kinematic Likelihood Fitter (KLFitter), is a reconstruction technique developed to reconstruct $t\bar{t}$ decays from pp collisions at ATLAS. It exploits the known decay topology of the top quark in the single lepton channel described previously in Chapter 2 in order to properly associate jets to the quarks in the final state of the decay process. In the single lepton decay of the $t\bar{t}$ system, the resulting tree level situation contains two b quarks and two light quarks.

One of the largest contributions to the uncertainty on the top mass is the combinatorial background, which results in a larger width of the top mass estimator. The combinatorial background is the result of placing signal jets with the improper quarks form the $t\bar{t}$ decay. As a result, the top mass value is, on average, expected to be further away from the true top mass value. Therefore, the top mass distribution is wider than the distribution obtained from the properly reconstructed events. The reduction in the mis-identification of jets reduces the width of the reconstructed peak of the estimator. Subsequently, the resolution on the top mass is improved with a better reconstruction efficiency.

A likelihood is used to properly assign these four jets to the true decay quarks. The LO scenario is assumed, giving rise to four jets in the final $t\bar{t}$ decay topology, two of which are b jets. Three of the jets in the decay are associated to the hadronic top decay, whereas a final fourth jet along with the charged lepton and neutrino build the leptonic top; one jet in each hemisphere is a b jet. To build this decay topology, the four highest p_T reconstructed jets in an event are used. The leading p_T jets are expected to come from the hard scattering event, whereas the possible extra jets in the event are assumed to be the result of soft jet radiation.

Taking only the four leading p_T jets in the event limits the total number of possible jet orderings (permutations) in the event, as well as reducing the computation time required to process additional permutations. In the single lepton channel, four jets can be permuted a total number of times equal to $4! = 24$. However, the light jets resulting from the hadronic W decay are indistinguishable. This reduces the possible number of permutations to 12.

7.2. Likelihood

The likelihood outputs a value for every combination of jet ordering based on the kinematic information of the reconstructed objects. The likelihood distinguishes the possible permutations per event. The best output likelihood, given by the largest log-likelihood value permutation is chosen to the "best" permutation and used as the jet ordering for the event.

The likelihood comprises of Breit-Wigner functions and transfer functions of individual reconstructed objects. The likelihood is written as:

$$
\begin{aligned}
\mathrm{L_{kin}} \;=\; & \mathrm{BW}\left\{\mathrm{m}(\mathrm{q_1 q_2}) \mid \mathrm{m_W}, \Gamma_\mathrm{W}\right\} \cdot \mathrm{BW}\left\{\mathrm{m}(\mathrm{l}\nu) \mid \mathrm{m_W}, \Gamma_\mathrm{W}\right\} \cdot \\
& \mathrm{BW}\left\{\mathrm{m}(\mathrm{q_1 q_2 b_{had}}) \mid \mathrm{m_{top}}, \Gamma_\mathrm{top}\right\} \cdot \mathrm{BW}\left\{\mathrm{m}(\mathrm{l}\nu \mathrm{b_{lep}}) \mid \mathrm{m_{top}}, \Gamma_\mathrm{top}\right\} \cdot \\
& \mathrm{W}\left(\tilde{\mathrm{E}}_{\mathrm{jet_1}} \mid \mathrm{E_{b_{had}}}\right) \cdot \mathrm{W}\left(\tilde{\mathrm{E}}_{\mathrm{jet_2}} \mid \mathrm{E_{b_{lep}}}\right) \cdot \mathrm{W}\left(\tilde{\mathrm{E}}_{\mathrm{jet_3}} \mid \mathrm{E_{q_1}}\right) \cdot \\
& \mathrm{W}\left(\tilde{\mathrm{E}}_{\mathrm{jet_4}} \mid \mathrm{E_{q_2}}\right) \cdot \mathrm{W}\left(\tilde{\mathrm{E}}_\mathrm{x}^{\mathrm{miss}} \mid \mathrm{p_{x,\nu}}\right) \cdot \mathrm{W}\left(\tilde{\mathrm{E}}_\mathrm{y}^{\mathrm{miss}} \mid \mathrm{p_{y,\nu}}\right) \cdot \\
& \left.\begin{cases} \mathrm{W}\left(\tilde{\mathrm{E}}_\mathrm{l} \mid \mathrm{E_l}\right), & \text{single electron channel} \\ \mathrm{W}\left(\tilde{p}_{\mathrm{T,l}} \mid \mathrm{p_{T,l}}\right), & \text{single muon channel} \end{cases}\right\} \cdot \mathrm{w_{btag}},
\end{aligned}
\tag{7.1}
$$

The likelihood is broken down into three sections:

Breit-Wigner functions representing the mass of the two W bosons and two t quarks. The hadronic W is comprised of the mass of the two light quarks $(\mathrm{m}(\mathrm{q_1 q_2}))$ compared to the expected mass and width of the W boson $(\mathrm{BW}\{\mathrm{m}(\mathrm{q_1 q_2}) \mid \mathrm{m_W}, \Gamma_\mathrm{W}\})$. The leptonic W is built from the charged lepton and neutrino $(\mathrm{m}(\mathrm{l}\nu))$, constructing a BW comparing the expected W mass to the reconstructed leptonic constituents $(\mathrm{BW}\{\mathrm{m}(\mathrm{l}\nu) \mid \mathrm{m_W}, \Gamma_\mathrm{W}\})$. The two W bosons, leptonic and hadronic are constrained by an equal mass constraint equal to 80.4 GeV, and a width of 2.1 GeV [15]. That means, the expected hadronic and leptonic W masses and widths are required to be equal and remain constant in the fit.

The second set of Breit-Wigner functions are used to reconstruct the two top hemispheres. Using the reconstructed mass of the two light jets from the hadronic W boson decay and the b quark, the fit is compared to a free top mass value m_{top} and mass dependent width Γ_{top} $(\mathrm{BW}\{\mathrm{m}(\mathrm{q_1 q_2 b_{had}}) \mid \mathrm{m_{top}}, \Gamma_\mathrm{top}\})$. The same is done in the leptonic hemisphere using the remaining b jet and charged lepton and neutrino $(\mathrm{BW}\{\mathrm{m}(\mathrm{l}\nu \mathrm{b_{lep}}) \mid \mathrm{m_{top}}, \Gamma_\mathrm{top}\})$. The top mass value in the fit is free floating, however is required to be equal in both hemispheres, resulting in an additional equal mass constraint.

Transfer functions account for the difference in reconstructed object energy after the calibration back to the parton level. For the reconstructed energy each jet object $(\tilde{E}_{\mathrm{jet}_i})$ is compared to the parton energy $(E_{\mathrm{q_i}})$. The transfer functions are used for all jet objects according to their p_T and η $(\mathrm{W}\left(\tilde{\mathrm{E}}_{\mathrm{jet_i}} \mid \mathrm{E_{q_i}}\right))$. The same is true for the missing energy in the x- and y-components $(\tilde{E}_{\mathrm{x},y}^{\mathrm{miss}})$ compared to the momentum in the same direction of the neutrino $(p_{x,y,\nu})$. Finally, a transfer function is used for the energy of the electron $(\tilde{E}_\mathrm{l})$ or p_T of the muon $(\tilde{p}_{\mathrm{T,l}})$ based on the channel. Further description of the transfer functions is found in Section 7.3.

b-tagging weight is used to assist in the assigning of the proper jet ordering through the use of the b-tagging information. The likelihood thus far only uses the event kinematic information. Jets are designated b or light with the use of a b-tagger. This information is used in addition for the kinematics through a weight $(\mathrm{w_{btag}})$ based on the b-tagging efficiency and rejection. Further details are found in Section 7.4.

For each event, the one permutation which maximizes the log likelihood compared to the other eleven permutations is chosen as the proper jet ordering for this event. The jets in the event are then assigned by the jet ordering in this permutation.

7.3. Transfer Functions

The transfer functions account for the energy difference between the reconstructed objects and their original parton energy in a LO picture. The transfer functions are parametrized by a double-Gaussian. This function accounts for tails in the energy difference between reconstructed and parton level. The transfer functions are defined by:

$$
W\left(\tilde{E}_{\mathrm{jet}} \mid E_{\mathrm{q}}\right) = \frac{1}{2\pi(\mathrm{p}_2 + \mathrm{p}_3\mathrm{p}_5)} \cdot \left[e^{-\frac{(\Delta E - \mathrm{p}_1)^2}{2\mathrm{p}_2^2}} + \mathrm{p}_3 \cdot e^{-\frac{(\Delta E - \mathrm{p}_4)^2}{2\mathrm{p}_5^2}} \right],
\tag{7.2}
$$

where $\tilde{E}_{\mathrm{jet}}$ is the energy of the measured jet and E_q is the original particle energy. The ΔE is given as:

$$
\Delta E = \frac{E_{\mathrm{truth}} - E_{\mathrm{reco}}}{E_{\mathrm{truth}}}.
\tag{7.3}
$$

In each object, there are five fit parameters which are determined from MC. They are all functions of the parton energy. The five fit parameters for light jets and electrons are:

$$
\begin{aligned}
p_1 &= a_1 + b_1 E; \\
p_2 &= a_2/\sqrt{E} + b_2; \\
p_3 &= a_3 + b_3 E; \\
p_4 &= a_4 + b_4 E; \\
p_5 &= a_5 + b_5 E.
\end{aligned}
$$

The parameters a_i and b_i are fit and assumed to be continuous for the jet energy range up to 700 GeV. Beyond this energy, the transfer functions are extrapolated using the same fit. For muons, all five fit parameters are linearly dependent on the parton energy. For b jets, parameters p_1 and p_3 are given as: $p_i = a_i/\sqrt{E} + b_i E$, whereas the remaining parameters are identical to the light jet parameters. The transfer functions are normalized to one for a given truth energy, such that:

$$
\int dE_{\mathrm{reco}} \, W(E_{\mathrm{reco}}|E_{\mathrm{truth}}) = 1.
\tag{7.4}
$$

Not only is the fit divided into ranges of energy (or p_T for the muons) but also for different detector regions in $|\eta|$. The four different regions are given as: $0 < |\eta| < 0.8$, $0 < |\eta| < 1.37$, $1.37 < |\eta| < 1.52$, and $1.52 < |\eta| < 2.5$. For muons, the detector regions are not based on calorimeter sections; therefore, the division in $|\eta|$ is given by three sections: $0 < |\eta| < 1.11$, $1.11 < |\eta| < 1.25$, $1.25 < |\eta| < 2.5$. An example of the transfer function double Gaussian fit for a given energy range in the barrel section of the detector is found in Figure 7.1.
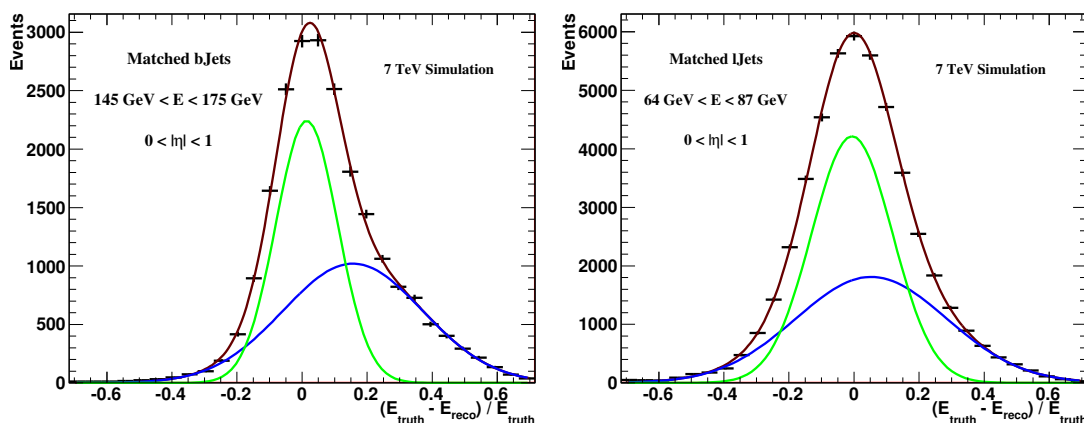
Figure 7.1.: (Left): b jet transfer function in the central detector region ($|\eta| < 1$) and parton energy $145 < E < 175$ GeV. (Right): Light jet transfer function in the central detector region ($|\eta| < 1$) and parton energy $64 < E < 87$ GeV. In both cases, the shape of the double Gaussian is presented by the two curves, plus the combination.

The transfer functions are derived using a sample of signal MC only at a top mass equal to ($m_{top} = 172.5$ GeV/c^2). Reconstructed jets are matched with the truth quarks using the criteria:

$$\Delta R(\text{reco}, \text{truth}) < 0.3. \tag{7.5}$$

If an event contains a jet which is matched to multiple quarks or a quark which is matched to multiple jets, the event is not used in the calculation of the transfer functions. It is also required that the event contain at least four matched jets. The four matched jets must be the jets from the leading four p_T jets. The additional jets in the events are disregarded. Therefore, transfer functions are constructed in very clean sub-samples of the total number of events. The sub-sample from which the performance of the kinematic fitter is tested accounts for about only 27 % of the original sample size. The same transfer functions derived on signal are used for background as well.

Examples of the evolution of the light and b jet transfer functions for several different parton energies is given in Figure 7.2. The evolution shows the change in width and shape as the jet in question has higher energies. The transfer functions are validated up to jet energies of about 700 GeV. Comparing the transfer functions of the jets and leptons, the transfer functions for jets are much wider than for the leptons.
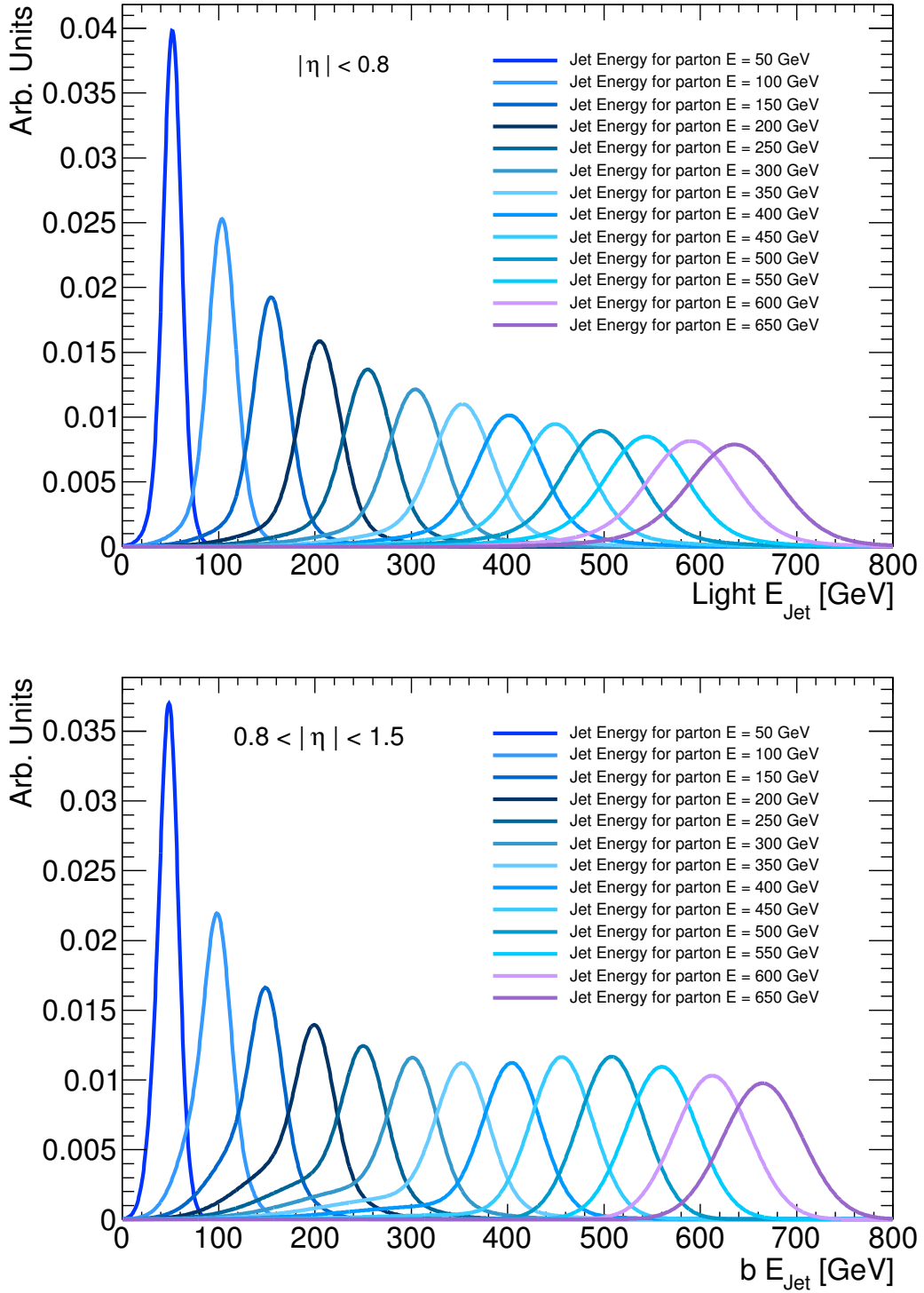
Figure 7.2.: Evolution of the transfer functions for the entire fitted parton energy range. (Top): Light jet transfer functions for the central $|\eta|$ region. (Bottom): b jet transfer functions for the middle $|\eta|$ range with the calorimeter gap removed. All transfer functions are normalized to 1.

7.4. b-Tagging

To improve the reconstruction efficiency of the fitter, the b-tagging information is also used in the likelihood. Each jet is given a b-tagging weight, and it is required that at least one jet has a weight over the 70 % efficiency working point in each event. Therefore an additional term is added to the end of the likelihood expression in Formula 7.1, (w_{btag}), given by:

$$
w_{\text{btag}} = \left\{ \begin{array}{l} \varepsilon \text{ , } b_{\text{had}} \text{ has b-tag} \\ (1 - \varepsilon) \text{ , } b_{\text{had}} \text{ has no b-tag} \end{array} \right\} \cdot \left\{ \begin{array}{l} \varepsilon \text{ , } b_{\text{lep}} \text{ has b-tag} \\ (1 - \varepsilon) \text{ , } b_{\text{lep}} \text{ has no b-tag} \end{array} \right\} \cdot
$$
$$
\left\{ \begin{array}{l} \frac{1}{R} \text{ , } q_1 \text{ has b-tag} \\ (1 - \frac{1}{R}) \text{ , } q_1 \text{ has no b-tag} \end{array} \right\} \cdot \left\{ \begin{array}{l} \frac{1}{R} \text{ , } q_2 \text{ has b-tag} \\ (1 - \frac{1}{R}) \text{ , } q_2 \text{ has no b-tag} \end{array} \right\}, \qquad (7.6)
$$

where ε is the efficiency and R the rejection factor of light jets. The working point of the tagger contains a 70 % efficiency of selecting true b jets and a rejection of 99. Therefore, the additional likelihood expression for b-tagging gives 0.7 for a b-tagged jet in the b quark position, 0.3 for a non b-tagged jet in the same position, and 1/99 for a b-tagged jet in the light quark position and 1 - 1/99 for a non b-tagged jet in the light quark position.

The likelihood thus favours the permutation for which a b-tagged jet is placed in the leptonic or hadronic b quark position and where the non b-tagged jets are placed as light quarks from the W decay. This information complements the kinematic likelihood part of the likelihood.

7.5. Performance

To test the performance of the KLFitter with the current setup, it is run with events containing reconstructed jets which are matched to the truth decay products. Using the same matching criteria as for the construction of the transfer functions, the results from the efficiency study are found in Figure 7.3. The overall reconstruction efficiency of the full $t\bar{t}$ decay is found to be about 70 %. The reconstruction efficiency is slightly higher in the e + jets channel, however within the statistical uncertainty of the sample. This efficiency is significantly higher than the efficiency one would obtain by choosing randomly positioned jets in one of the four jet permutations. For the entire $t\bar{t}$ decay, the probability of randomly selecting the proper jet ordering is 1/12.

The large gain in efficiency is due to the likelihood itself and the addition of the b-tagging information. Firstly, the kinematic likelihood reconstruction using only the kinematic information of the event has a reconstructed efficiency of about 52 % on its own[1]. When combined with the b-tagging weight used in this analysis, the efficiency is improved to about 70 % for total $t\bar{t}$ reconstruction.

The reconstruction efficiency of individual objects is also studied. In the $t\bar{t}$ hadronic hemisphere decay, the W boson is reconstructed properly in about 83 % of the events. This means that only 17 % of the time a light quark will be interchanged with a b quark. For the hadronic b quark, it is properly reconstructed just over 70 % of the time. The leptonic

---

[1]This study was performed for the top mass measurement made using the fitted top mass value for the Moriond 2011 Conference. It is a part of the first ever publicly presented top mass measurement made at ATLAS [144].
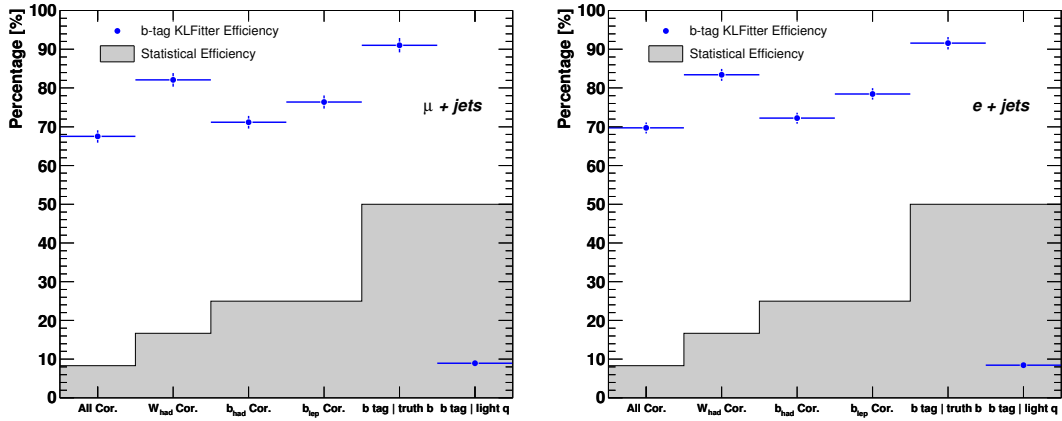
Figure 7.3.: (Left): μ + jets channel and (right): e + jets channel reconstruction efficiency for several physical objects from the $t\bar{t}$ decay. The full efficiency for reconstructing all four jets from both leptonic and hadronic hemispheres of the $t\bar{t}$ decay is about 70 % in both channels, slightly higher in the e + jets channel. The shadowed region shows the expectation when randomly positioning the jets in any order.

b quark has a slightly higher reconstruction efficiency of about 75 %. It is expected that the leptonic b would be less likely to be identified as a light quark compared to the b from the hadronic side since the three jets from the hadronic top would be boosted into the same direction when the top quark has a high enough p_T. As a result, it would be more likely to mis-identify one of the light jets from the W decay as the hadronic b. The fitted p_T of the $t\bar{t}$ system can be seen in Appendix A, Figure A.2 and Figure A.4. The $t\bar{t}$ system is not expected to be at rest when created at the LHC, and this is what can be observed from these figures.

The final reconstructed efficiencies presented are the b quark reconstruction efficiencies. Using the 70 % efficiency of the b-tagger, it is expected that 70 % of the b quarks will be b-tagged. Using this information along with the kinematic information of the $t\bar{t}$ decay, it is found that more than 90 % of b jets are properly reconstructed from the available true b quarks.

7.6. Fitted Kinematics

To check the description of the model to data, and to verify that the kinematic reconstruction works in both data and MC, several fitted quantities are checked. The fitted variables of the KLFitter represent the estimated quantities for the objects from the $t\bar{t}$ decay. The fitted variables are built based on the reconstructed quantities with the help of the transfer functions which account for detector effects. Control plots in both μ + jets and e + jets channels are shown in Figure 7.4 and Figure 7.5. The overall description of the model is in perfect agreement with data. This is important to help verify the entire KLFitter model. Additional control plots can be found in Appendix A: Figures A.2 - A.5.
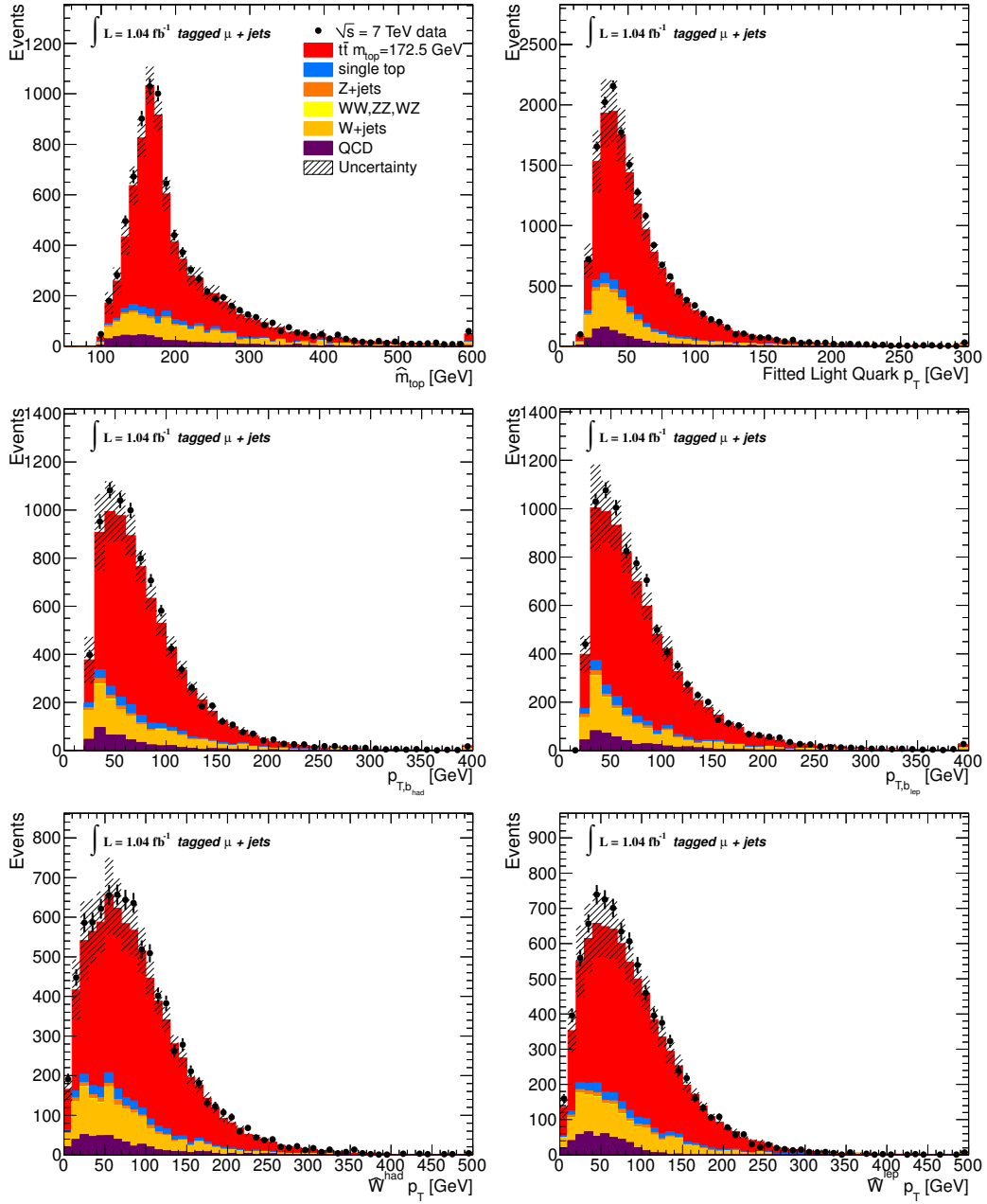
Figure 7.4.: μ + jets control plots for fitted quantities derived from the KLFitter. (Top left): Fitted top quark mass using both hemispheres, which are required to be equal. (Top right): Light quark p_T from the two jets resulting from the hadronic W decay. (Middle left): p_T of the hadronic hemisphere b quark. (Middle right): p_T of the leptonic hemisphere b quark. (Bottom left): p_T of the hadronically decaying W boson. (Bottom right): p_T of the leptonically decaying W. All control plots show good agreement with data. The uncertainties are derived from the MC and data-driven background estimates as in Chapter 6.

Figure 7.5.: e + jets control plots for fitted quantities derived from the KLFitter. (Top left): Fitted top quark mass using both hemispheres, which are required to be equal. (Top right): Light quark p_T from the two jets resulting from the hadronic W decay. (Middle left): p_T of the hadronic hemisphere b quark. (Middle right): p_T of the leptonic hemisphere b quark. (Bottom left): p_T of the hadronically decaying W boson. (Bottom right): p_T of the leptonically decaying W. All control plots show good agreement with data. The uncertainties are derived from the MC and data-driven background estimates as in Chapter 6.

7.7. Likelihood Discriminant

For each jet-ordering permutation, an output likelihood value is calculated. The value serves as a discriminant between the twelve permutations. The higher the log likelihood output, the better the kinematic and b-tagging information of the event is presumed to describe the $t\bar{t}$ decay. Shown in Figure 7.6 are the shapes of the likelihood output based on the Nth permutation. The first permutation shows the most favourable jet ordering based on the event kinematics. The last permutation, which is the twelfth permutation, shows the worst jet ordering possible in the given event. The first permutation is the jet ordering used for the event.
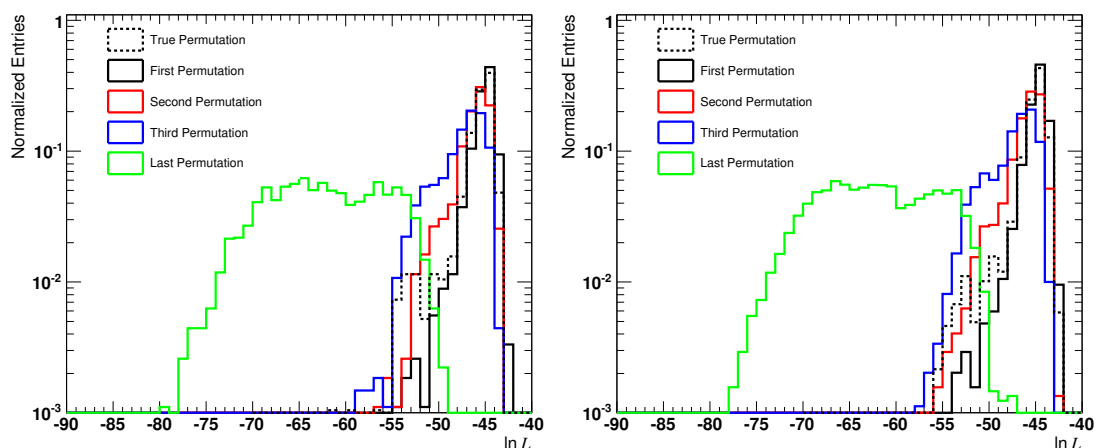
Figure 7.6.: (Left): μ + jets and (right): e + jets channel likelihood output from the kinematic likelihood fitter. The different colours show the difference in likelihood shapes starting with the best (first) permutation, which represents the highest log likelihood output per event to the last (twelfth) permutation which represents the lowest log likelihood, or least favourable kinematic jet ordering. The true jet ordering likelihood is also plotted for comparison.

Figure 7.6 shows that the best permutation has a similar likelihood in signal events; the log likelihood output for best permutation is a very sharply peaked distribution. The best permutation per event is found to have a log likelihood output of about -45. The difference in log likelihood output for each successive permutation can also be seen from this plot. The mean and median of the peaks are shifted to lower log likelihood values with each successive permutation. The permutation probability ($\mathcal{P}_{P_i}$), which is calculated by taking the likelihood value and dividing it by the total sum of all likelihood values in the event:

$$\mathcal{P}_{P_i} = \frac{\mathcal{L}_i}{\sum_j \mathcal{L}_j}, \tag{7.7}$$

is shown in Figure 7.7. The different permutations gradually shift from best permutation mostly at a permutation probability of 1, to the last permutation which is almost always exclusively 0.

Finally, the likelihood output is checked for comparisons between MC and data. This is important to verify the entire KLFitter model as a whole. If there is a discrepancy in any of these MC modelled variables, it will result in a discrepancy in the likelihood output shape. In Figure 7.8, the model to data comparison of the log likelihood is shown. It can be seen that there is a very good model agreement to data for the likelihood output, and thus, the transfer functions and kinematic quantities are properly modelled in the MC, up to the precision of the statistics in data.
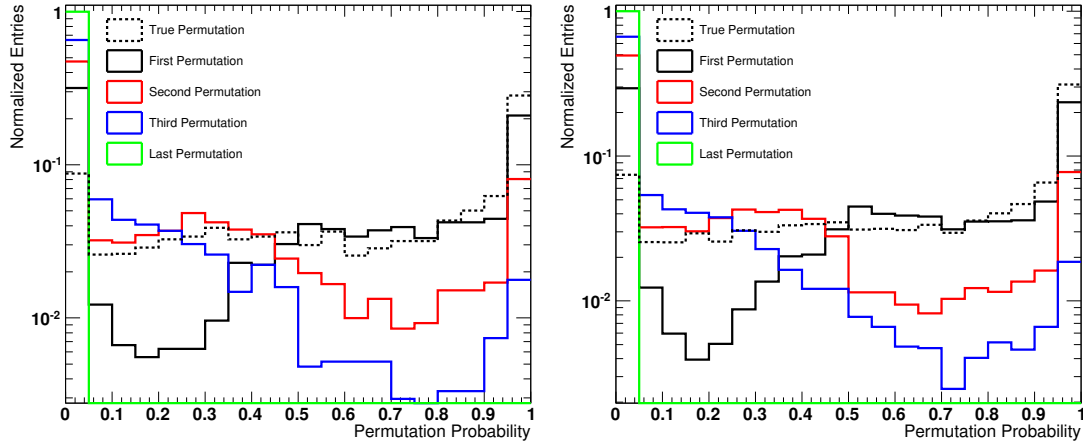
Figure 7.7.: (Left): μ + jets and (right): e + jets channel permutation probability. The permutation probability shows the separation power per each successive permutation. The true jet probability is also plotted for comparison.
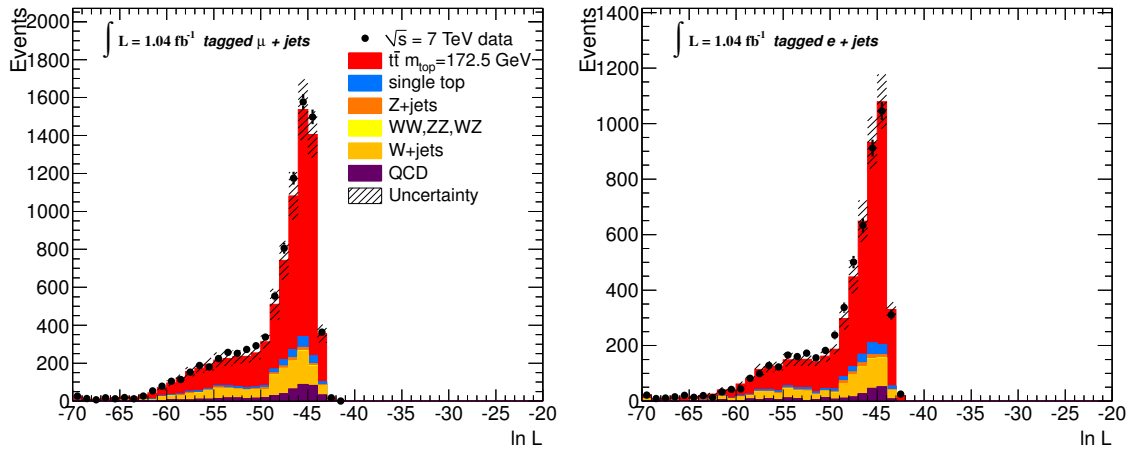
Figure 7.8.: (Left): μ + jets and (right): e + jets channel likelihood output for data and MC. The agreement of the MC with data is very good. This is important to verify the transfer functions and the fitter performance is similar in both data and the model. The uncertainties are derived from the MC and data-driven background estimates as in Chapter 6.

8. Estimator Optimization

8.1. Stabilized R_{32} Variable

A top mass sensitive variable is needed to measure the top mass from a template distribution. The simplest and most straight forward method is to measure the top quark mass directly from the reconstructed top mass. Taking it one step further than just using the reconstructed four-vectors, the top mass can be reconstructed using the KLFitter and the event-by-event top mass estimator from the fitted mass in both $t\bar{t}$ decay hemispheres. This estimated top mass has the advantage of using the transfer functions to improve the resolution of the jet energy. The improved resolution of the b jets can be directly seen in the Appendix under Figure A.1. The improved resolution corresponds to an improved statistical precision of the measured top quark mass. The improved top mass resolution is compared to that from the detector resolution in Figure 8.1. In the same figure, the MC to data comparison of the top mass estimator using the KLFitter with 35 pb^{-1} of data in the 2010 ATLAS run is shown. This estimator was used to measure the top mass in the first data-taking period in 2010.
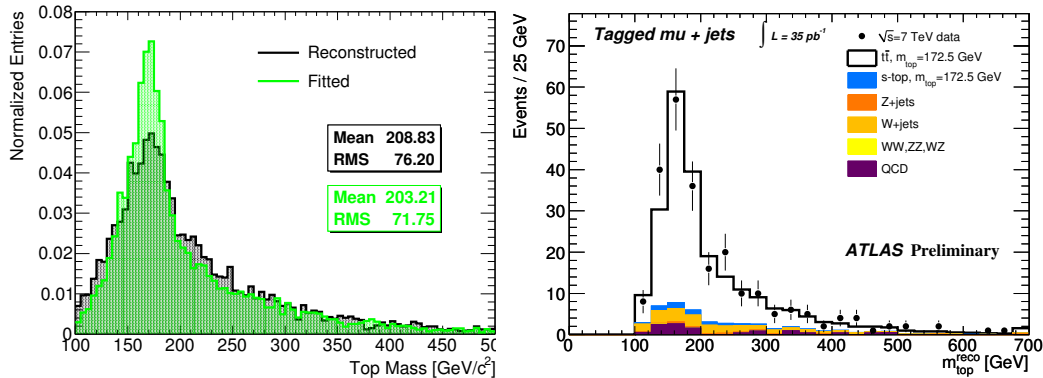
Figure 8.1.: (Left): Reconstructed (black) and Fitted (blue) top mass. The Fitted top mass has a much narrower peak compared to reconstructed top mass due to the improvements in jet resolution with the help of the transfer functions used in the KLFitter. The result is a smaller statistical uncertainty on the top mass measurement. (Right): MC to data comparison in the μ + jets channel for the top mass measurement made on 2010 data at ATLAS.

This method was performed using 2010 data, achieving the best statistical precision of the three methods performed at ATLAS [144]:

$$m_{\text{top}} = 174.8 \pm 2.7 \text{ (stat.)} \pm 7.5 \text{ (syst.) GeV/c}^2. \tag{8.1}$$

The method however had no handle on the JES uncertainty, the largest uncertainty on the estimated top mass, dominating in the systematic uncertainty[1]. As a result, the stability against the shifts in the JES needs to be established to achieve a much more precise estimator. The simplest and most robust method to achieve stability against the JES is to make an in-situ calibration per event. To do this, the hadronic W mass of the event is used to calibrate out the JES. The in-situ calibration method used in this analysis is the R_{32}. The R_{32} is composed of the ratio of the invariant mass of the jets that make up the hadronic top quark over the invariant mass of the jets associated to the hadronic W. This stabilized variable is defined as, and used in ATLAS [145, 146]:

$$R_{32} \quad \equiv \quad \frac{m_{\text{top}}^{\text{reco}}}{m_{\text{W}}^{\text{reco}}}.$$ (8.2)

In this scenario, a tendency for a large shift in the JES will result in a larger top mass, but also a larger W mass. As a result, the R_{32} will be stabilized and minimally effected by this shift. The same is true for a shift downward in the JES. The relative shift in peak position of the R_{32} and reconstructed top mass can be seen in Figure 8.2. For a uniform shift in the JES, the R_{32} peak position remains relatively constant whereas the top mass peak shifts largely.
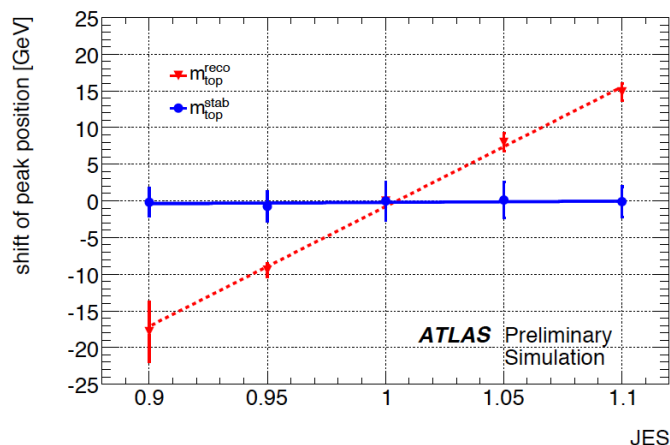
Figure 8.2.: Relative shift in the peak position for the stabilized mass ($m_{\text{top}}^{\text{stab}}$ is defined as $R_{32} \times W$ mass) compared to that of the top mass from reconstructed four-vectors. There is little to no stability against the JES from the four-vector reconstructed top mass. The R_{32} peak position barely shifts due to a uniform shift in JES. Figure taken from [147].

The shift in Figure 8.2 corresponds to a relatively uniform shift in JES, relative to jet p_T. As a result, the JES shift factor can be taken out of the R_{32}, and the resulting estimator remains unchanged:

$$R_{32} = \frac{\text{JES} \times m_{\text{top}}^{\text{reco}}}{\text{JES} \times m_{\text{W}}^{\text{reco}}}.$$ (8.3)

In reality, the JES is not uniform in p_T nor η. As a result, the JES cannot be completely factored out of the R_{32}, and some small fluctuations remain. Using the 2010 JES uncer-

---

[1]JES accounts for 6.6 GeV of the total 7.5 GeV systematic uncertainty for this measurement.

tainty[2], the relative shift up and down in the JES is shown in Figure 8.3 for both the reconstructed top mass and the R_{32}.
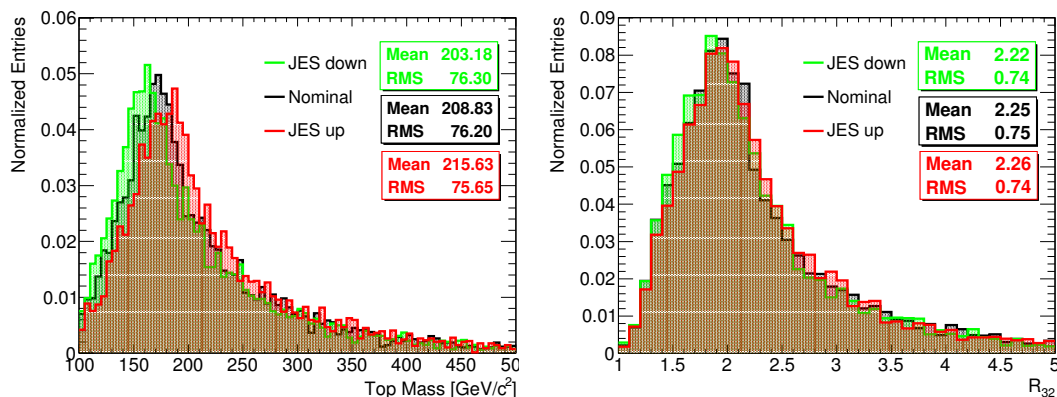
Figure 8.3.: (Left:) Top mass distributions for the nominal 172.5 GeV MC and the shifted $\pm 1\sigma$ JES. The shift in JES corresponds to the 2010 JES prescription. The overall shift in the mass is significant and can be seen in both the peak and shape of the distribution. (Right:) R_{32} nominal and shifted JES histograms. The shift is not as dominant as for the top mass. However, the variations correspond to a mean shift of about 2 GeV.

The figure shows a minor shift in R_{32} variations from a scale of $\pm 1\sigma$ in JES. The top mass shifts significantly, where the mean of the distribution changes up and down from the nominal by ≈ 6 GeV. The R_{32} peak position stays almost identical for the up/down variations in comparison to the nominal; however there are small shifts in the shape which result in a minor shift in the distribution mean. The relative shift in the R_{32} distribution corresponds to about 2 GeV. In the same 2010 data analysis, the total systematic uncertainty of R_{32} analysis[3] was 4.9 GeV, of which about 2.0 GeV was from the JES.

8.2. Optimization Against JES

Since the 2010 analysis, the JES has increased due to additional pile-up uncertainties. The upper boundary of the JES is about 8 % of the jet p_T. Since the JES is significantly larger in the 2011 data, a further selection on the estimator needs to be applied in order to reduce the largest uncertainties, including the JES.

The largest uncertainties on the top mass measurement are the JES, the bJES and initial and final state radiation (ISR/FSR). The JES, as previously explained, contains a relative uncertainty of 2.5 % to 8 % of the jet p_T based on the p_T and η of the jet. The largest uncertainty comes from jets with low p_T and forward η regions. The bJES, an independent additional JES uncertainty only applied to b quark decays, is also p_T dependent. The bJES comes from the additional dead material and b-jet hadronization to

---

[2]2010 JES uncertainty corresponds to shifts in the JES from 2.5 % to 6 % in jet p_T.
[3]No kinematic reconstruction was performed to build the R_{32} estimator in this analysis.

the decay of b hadrons in the calorimeter which is not covered by the JES. The bJES also has its largest uncertainty for low p_T jets similar to the total JES.

The remaining large systematic uncertainty arises due to ISR and FSR, where a gluon is radiated resulting in a loss of energy in the $t\bar{t}$ decay reconstruction. Since QCD is collinear and infrared divergent, a simple ΔR cut may help reduce the uncertainty. Therefore, an optimization in both the μ + jets and e + jets channels is made on the estimator based on a higher p_T cut and a ΔR cut between jets. The optimization for the μ + jets channel is found in Figure 8.4 and for the e + jets channel in Figure 8.5.
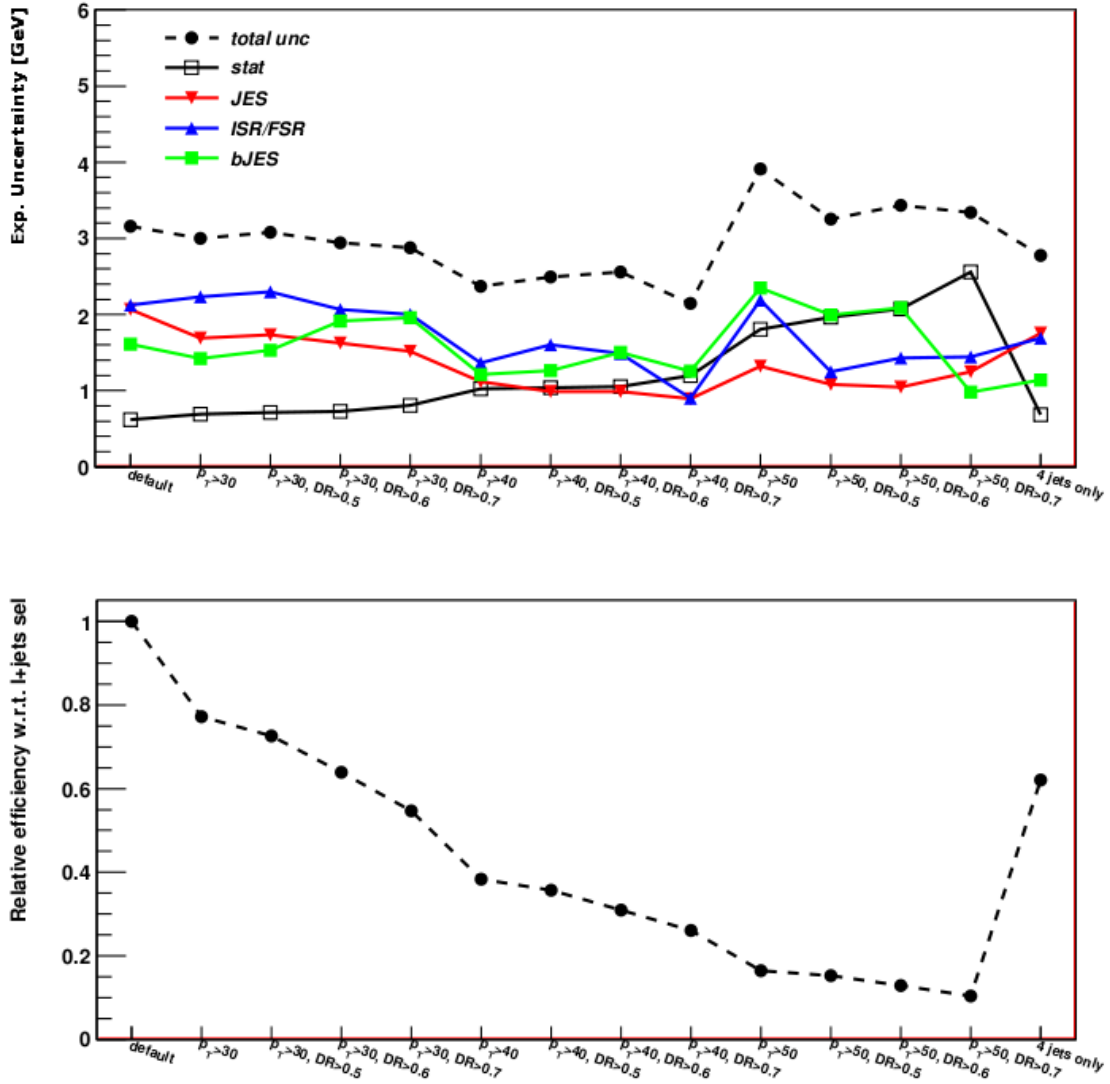
Figure 8.4.: Optimization for different estimators in the μ + jets channel. The estimators include cuts on the p_T for jets used in the hadronic top triplet. The Top plot shows the combination of the largest uncertainties associated with the top mass measurement along with the statistical uncertainty. The bottom plots shows the decrease in statistics with each successive cut.
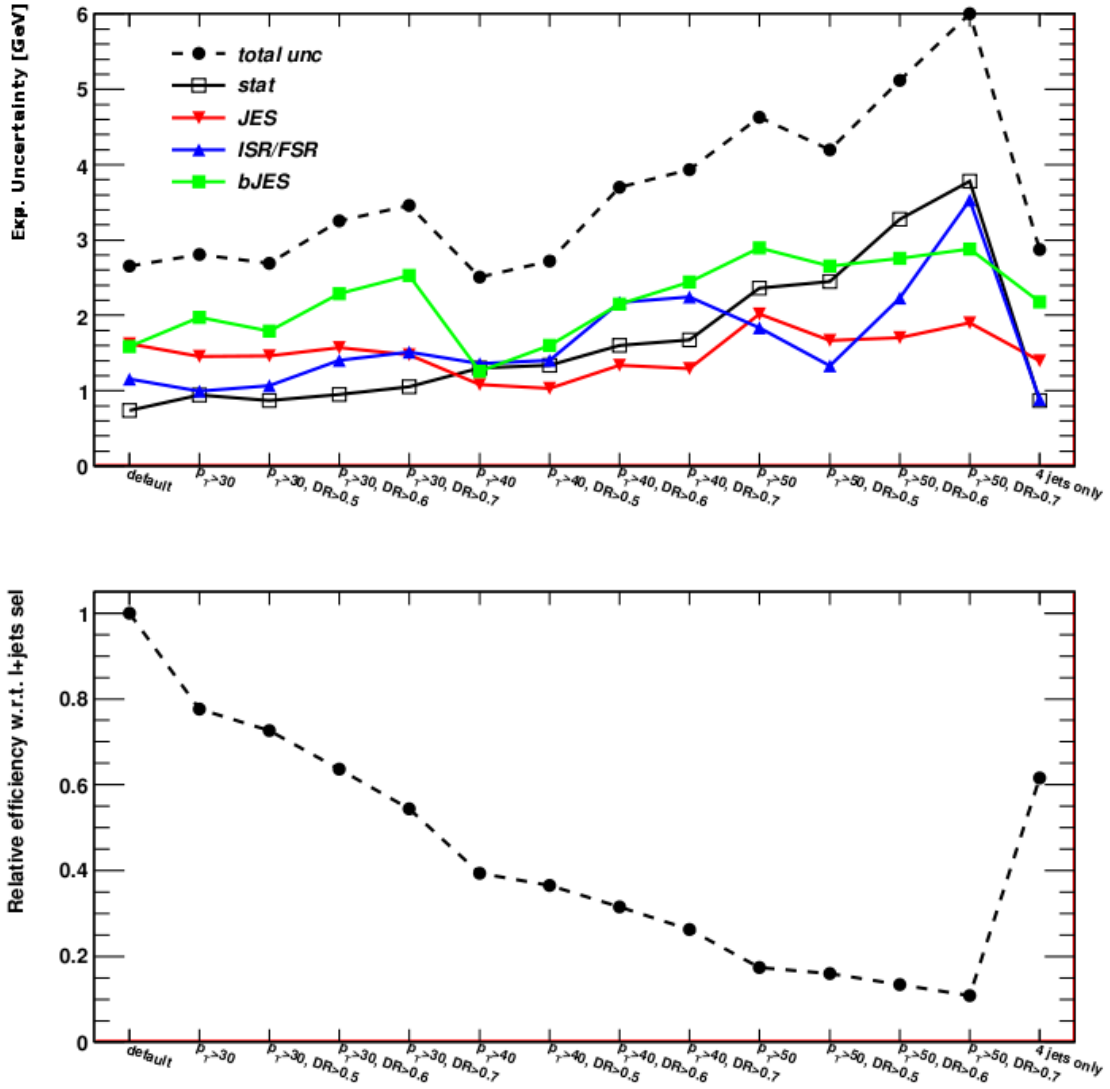
Figure 8.5.: Optimization for different estimators in the e + jets channel. The estimators include cuts on the p_T for jets used in the hadronic top triplet. The top plot shows the combination of the largest uncertainties associated with the top mass measurement along with the statistical uncertainty. The bottom plots shows the decrease in statistics with each successive cut.

The two additional requirements are an increase in the jet p_T used for the hadronic hemisphere of the $t\bar{t}$ decay and a minimum ΔR cut between jets. Using the signal templates only, an un-binned likelihood is performed to determine the overall minimum χ^2 for each scenario. The overall error is determined by taking the difference in fit values from the shifted systematic to the nominal. The statistical error of the nominal sample is also included and added to the total systematic error in quadrature. This is done separately for both μ and e + jets channels and combined using a statistical combination. The overall best point which gives the most precise top mass measurement is chosen.

From the optimization it can be seen that the bJES is a large uncertainty for this measurement because the R_{32} is sensitive to shifts in the bJES. The bJES dependence is mostly only found in the m_{top} term, as it contains the b jet from the top decay. The bJES is applied to true b hadron decays, thus if the efficiency of the KLFitter is very good, which it is, the bJES uncertainty will only appear in the numerator of the R_{32}. For this reason, the bJES can be seen in both optimization figures to be the largest in almost every bin, even with a much smaller relative shift compared to the JES.

The successive p_T cuts have an effect on both the JES and bJES, by lowering the uncertainty from these systematics. This is expected due to the p_T dependence of the uncertainty. The ΔR cuts have a very minimal effect on the total uncertainty and fail to limit the ISR/FSR uncertainty. As a result of the optimization, an additional requirement is imposed on the three jets out of which the R_{32} is built. The three jets are required to all have a p_T of at least 40 GeV. This is an increase of 15 GeV from the standard selection imposed on all jets in the analysis.

8.3. Likelihood Optimization and W Mass Window

8.3.1. Likelihood Optimization

Building on the likelihood discriminant discussed in Section 7.7, the top mass estimator can furthermore be improved. The likelihood can be used as a discriminant to evaluate the kinematics of the event. After applying the jet p_T cut requirement on the estimator jets from the hadronic hemisphere of the $t\bar{t}$ decay, the likelihood has the shape shown in Figure 8.6 for data.
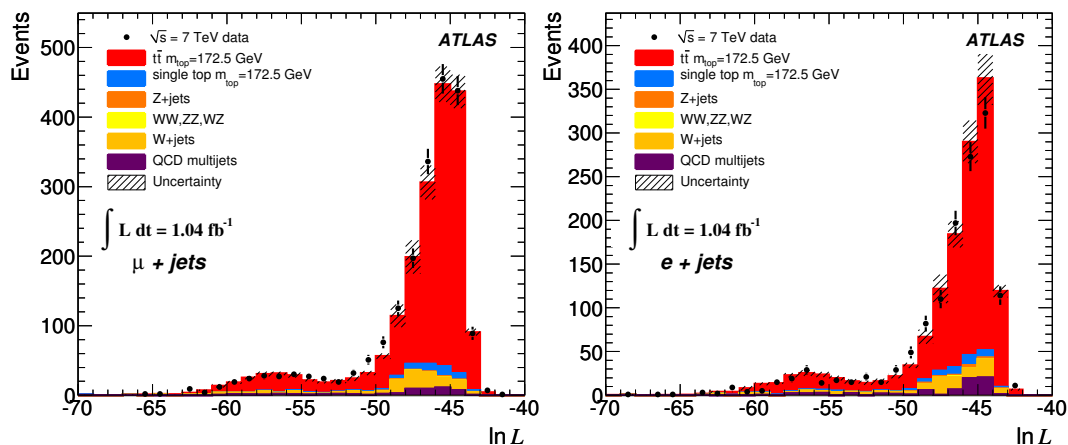
Figure 8.6.: (Left): μ + jets channel and (right): e + jets channel distributions of the KLFitter likelihood output. The shape contains a very sharp peak at about -45 and a much smaller and broader peak at -58. The agreement between data and MC in both channels is very good.

The shape of the likelihood is much narrower when compared with the one before the jet p_T optimization. Furthermore, there are two distinct shapes which can be seen: one very large peak at about -45 and one much broader and smaller peak at -58. To understand the origin of these peaks, several different scenarios are plotted in Figure 8.7.
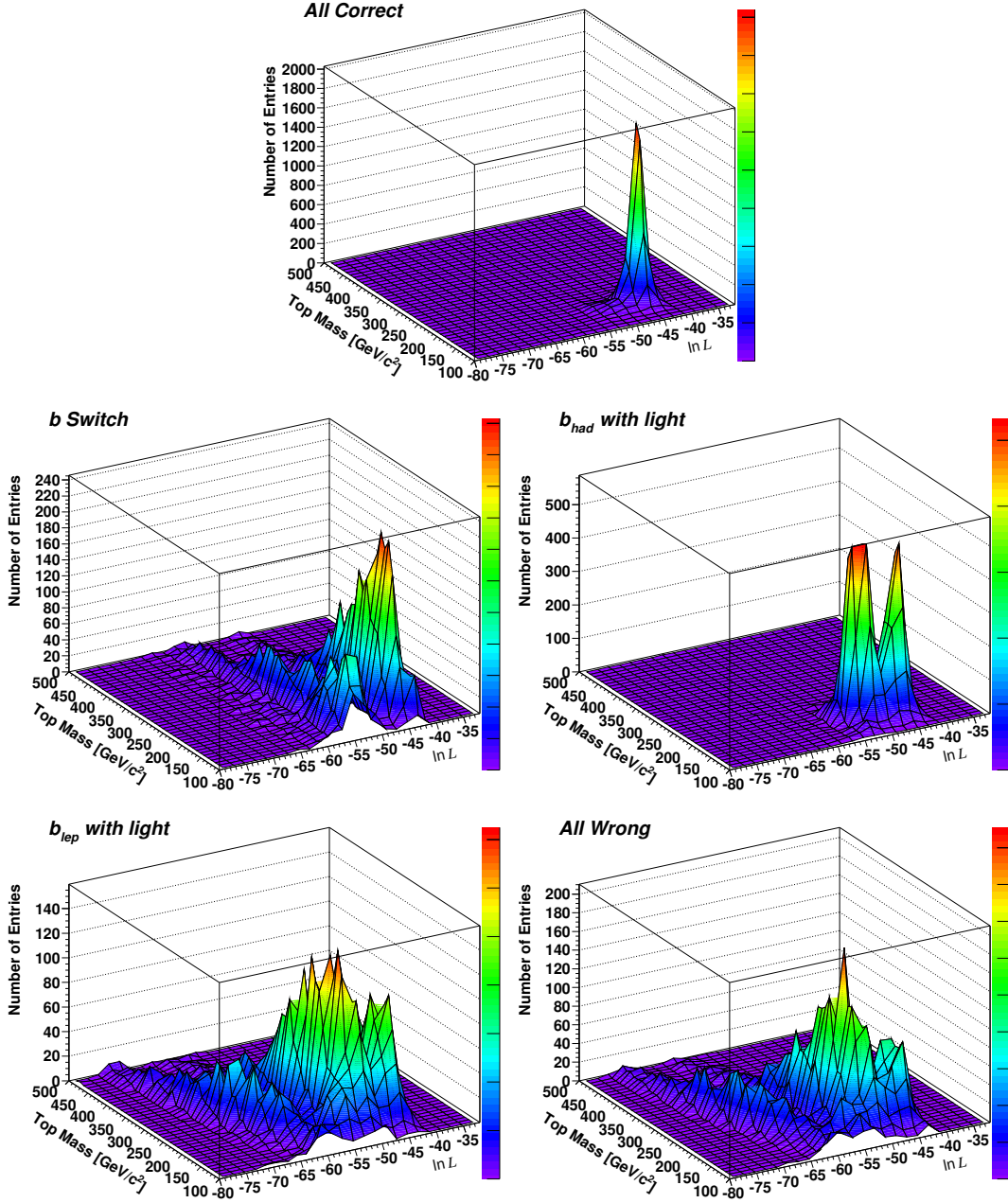
Figure 8.7.: Correlation between top mass and log likelihood for different reconstructed scenarios. (Top:) Events which have all jets correctly assigned. The likelihood and top mass form a peak corresponding to a likelihood output of -45 and top mass value which is very close to the true top mass value in MC: 172.5 GeV. (Middle left:) Events which have the b jets switched. (Middle right:) Hadronic b jet is switched with a light jet, causing two peaks. (Bottom left:) Leptonic b jet is switched with a light jet (Bottom right:) All incorrectly identified. The resulting likelihood has lost the peak at -45 and contains a wave structure which is present in the misidentifications due to the swapping of event kinematics which show discrete likelihood outputs.

In this figure, different scenarios representing either the proper ordering of jets or different types of mis-reconstructed events are displayed showing the dependence on both the mass and likelihood output in 2-d histograms. From the 2-d top mass and likelihood plots, the second hump structure can easily be explained by the mis-identification of the event kinematics. The projection of the output log likelihood values onto a 1-d surface is shown in Figure 8.8.
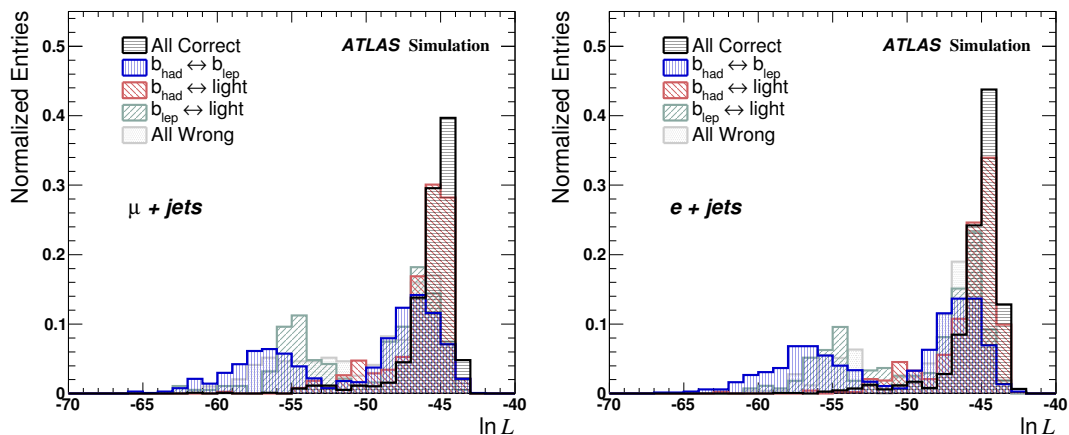
Figure 8.8.: (Left): μ + jets channel and (right): e + jets channel likelihood output for the several reconstruction scenarios. For the *All Correct* scenario, the likelihood is limited to the peak at -45. Due to the mis-identification of certain event kinematics, the second peak at about -58 appears.

It is therefore useful to place an additional cut on the estimator due to the output likelihood from the KLFitter. To improve the reconstruction efficiency and thus, improve the overall precision of the estimator, a kinematic reconstruction log likelihood of the event is required to be > -50. This eliminates a significant portion of the mis-reconstructed events. Since it is expected that the correctly reconstructed events contain a likelihood output larger than -50. The corresponding top mass distribution is thus expected to be much narrower. This can be directly seen in the top 2-d plot for all correct events in Figure 8.7. This behaviour is shown directly in the top mass plot in Figure 8.10 in the following section.

8.3.2. W Mass Window

A further optimization made on the estimator is the use of the W mass window. The hadronic top decay contains two light jets from the decay of the W boson. By limiting the mass window of these two reconstructed jets, the precision on the top mass can be improved. A mass window of $60 < m_W^{\mathrm{reco}} < 100$ GeV is taken. The reconstructed W mass is found in Figure 8.9.

The overall improvement to the reconstructed top mass and R_{32} estimator due to these two optimization requirements is shown in Figure 8.10. Starting with the original estimator in black, the additional likelihood requirement is applied followed by the W mass window in a two-step procedure. The likelihood requirement significantly reduces the width of the top mass and R_{32}. The tail of the top mass is also decreased. This is expected due to
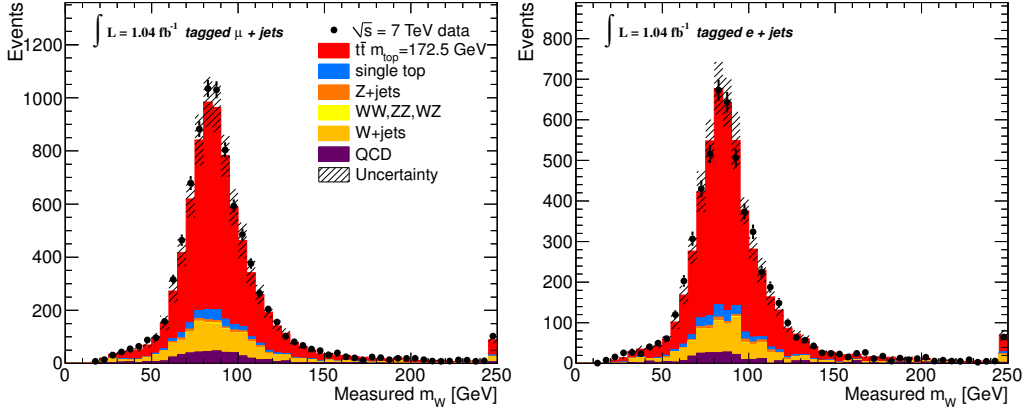
Figure 8.9.: (Left): μ + jets channel and (right): e + jets channel W mass output. The reconstructed W mass is taken from the reconstructed mass of the two jets designated to be from the W decay by the KLFitter.

the relationship between top mass and likelihood, where lower likelihood outputs result in larger tails in the top mass distribution. This is visible from the mis-reconstructed plots in Figure 8.7. The W mass window also reduces large W mass reconstruction values. As a result, the top mass distribution also looses more of its tail, however the most significant effect is to the R_{32}, where low R_{32} values are suppressed. With high W mass values, the R_{32} is expected to be lower. This loss in large W mass values results in a drop in the width of the R_{32} distribution by almost 11%. The resulting estimator after the optimization is highlighted by the red section in Figure 8.10. The total improvement in width by the two optimization requirements is found to be over 21%.
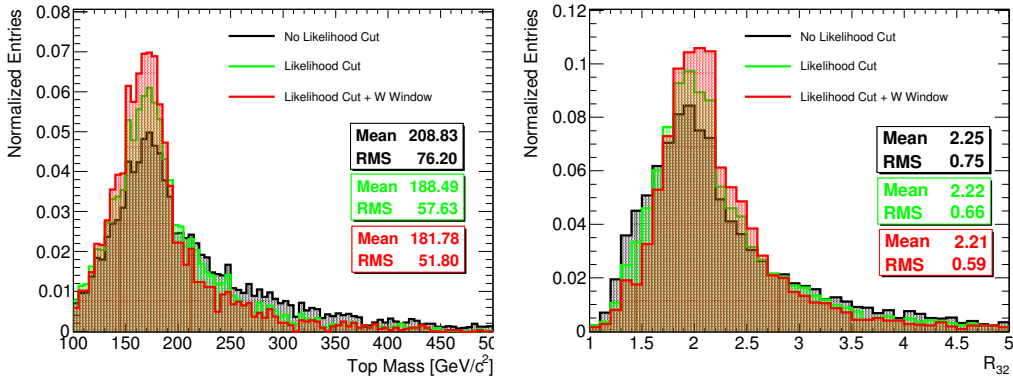
Figure 8.10.: (Left): Reconstructed top mass and (right): R_{32} after event and object selection along with $p_T > 40$ GeV requirement in black. The blue region highlights the same variables after the likelihood requirement is fulfilled in the event ($\ln L > -50$). The output estimators are much narrower, largely decreasing the top mass tail region. In red, the final optimized error including the W mass window requirement ($60 < m_W < 100$ GeV). This mass window reduces significantly the low R_{32} region. The overall improvement in resolution is more than 21%.

In every event, the KLFitter is also required to converge. If the convergence is not obtained, the event is rejected and discarded. The convergence of KLFitter is > 99%.

To check the model to data, the p_T of the assigned hadronic b jet is plotted. This p_T is the fitted transverse momentum of the jet using the KLFitter. The agreement after the mass estimator optimization is very good and no discrepancy in the modeling can be seen.
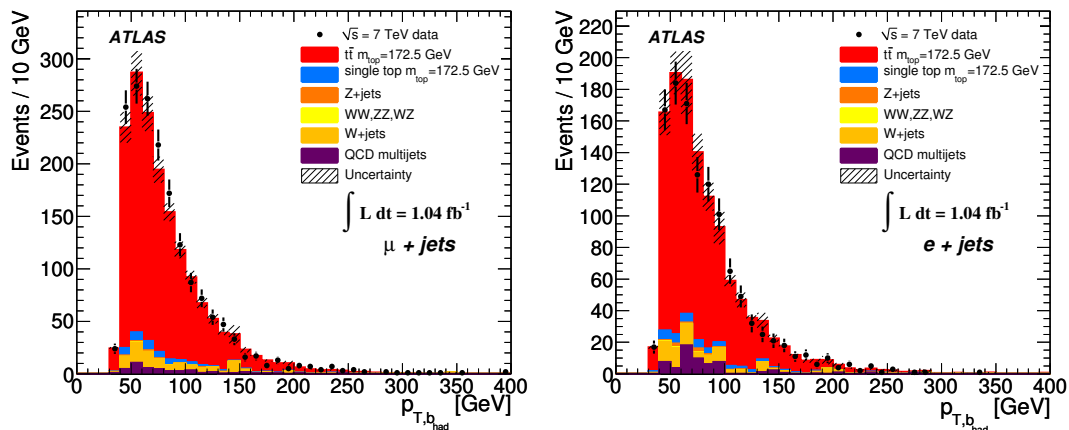
Figure 8.11.: (Left): μ + jets channel and (right): e + jets channel p_T of the fitted hadronic b jet. The check is made after the mass estimator optimization to compare the fitted variables obtained from the KLFitter model. The agreement in both channels is very good.

8.4. Top Mass Estimator

The optimized R_{32} estimator includes the additional selection cuts:

- p_T of three jets which build the R_{32} must be greater than 40 GeV,

- W mass window between $60 < m_W < 100$ GeV,

- likelihood reconstruction veto from the KLFitter > -50 to separate poorly reconstructed events, and

- Minuit convergence in the fit procedure.

The resulting statistics is reduced to only 23 % of the original number after event and object selection. The resulting number of events in the both e + jets and μ + jets channels are found in Table 8.1. The S/B has increased significantly from the previous values to 9.8 ± 5.4 in the μ + jets channel and 7.0 ± 3.6 in the e + jets channel. The large increase in S/B is achieved through the extra p_T cut on the hadronic triplet. Since the largest background contribution comes from jets with low p_T, requiring a larger p_T threshold limits the number of background events.

The resulting measured m_W and m_{top} are shown in Figure 8.12. The agreement for both variables when compared to data is very good. The variables are plotted after all the optimization has been completed. The R_{32} after optimization is shown for both channels in Figure 8.13.

Channel with $\int L\ dt = 1.04\ \text{fb}^{-1}$	μ + jets	e + jets
$t\bar{t}$ (m$_{top}$ = 172.5 GeV)	1450 ± 50	990 ± 40
Single top (m$_{top}$ = 172.5 GeV)	53 ± 3	43 ± 2
W + jets	100 ± 70	80 ± 60
Z + jets	8 ± 3	12 ± 3
Diboson	2 ± 1	2 ± 1
QCD Multijets	40 ± 40	50 ± 50
Signal + background	1650 ± 80	1180 ± 80
Data	1724	1151

Table 8.1.: Observed numbers of events in data compared to the expected numbers of MC signal and different background channels after both the object selection cuts and the estimator optimization. The errors are derived from the modeling uncertainties, both MC and data-driven, and the scale factors.
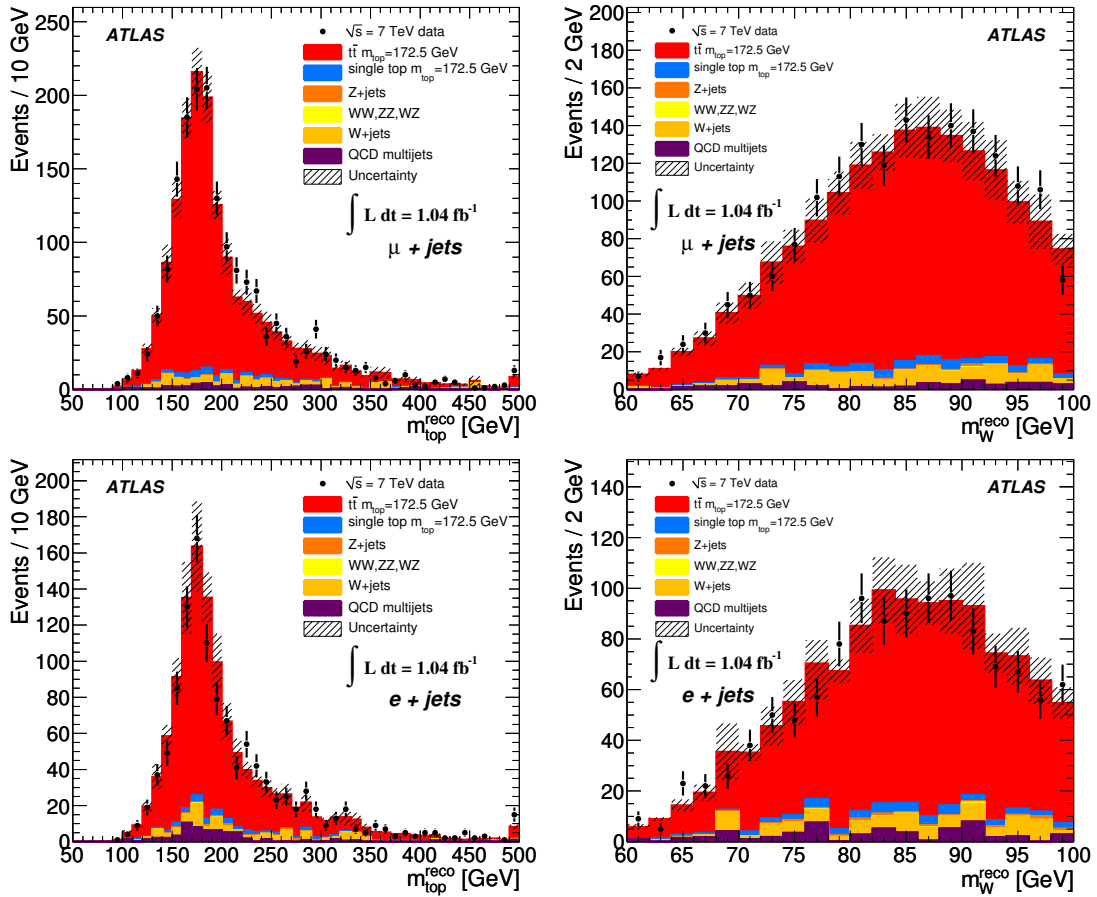
Figure 8.12.: Measured quantities for both the reconstructed top and W masses. The top row shows the μ + jets channel while the bottom row shows the e + jets channel. In all four plots, the agreement with data is very good. The dominating errors are still the W + jets and QCD background uncertainties as well as the b-tagging scale factor.
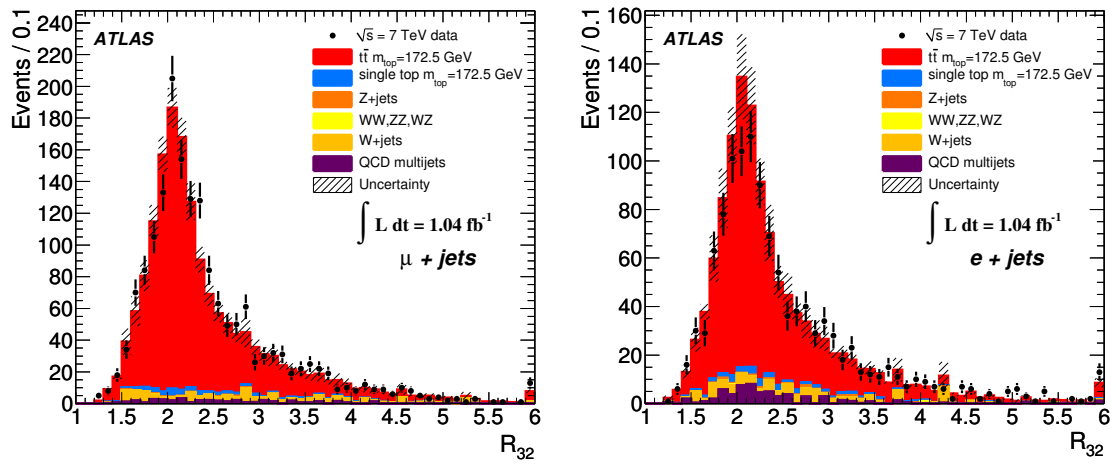
Figure 8.13.: (Left): μ + jets channel and (right): e + jets channel R_{32} estimator for the top mass after the optimization cuts are applied. The agreement with data is very good.

9. Template Method

Using the R_{32} distribution, templates are built from samples generated with different top mass values. The dependence of the R_{32} on the top mass is exploited for the measurement. Using the templates, a parametrization is described to create a continuous dependence between the templates. This parametrization is then fit to the data to extract a top mass value. This is known as the template method. It is by definition unbiased since the measurement only uses a predetermined dependence on the mass. Mass dependent templates are created for the signal model and a mass independent background is described.

9.1. Signal Parameterization

Signal templates are derived from the contributions of $t\bar{t}$ and single top R_{32} distributions; both of which are dependent on the top mass. Though single top and $t\bar{t}$ do not have similar R_{32} shapes, the single top contribution is significant enough that it must be considered. The single top is summed with the $t\bar{t}$ decay contributions to model the signal mass dependent distribution. For the signal contribution, only MC is used for the modeling.

For signal, there are six mass variation samples, they include 160, 170, 172.5, 175, 180, and 190 GeV/c^2. For each of these samples an R_{32} distribution is created. From this point, it is possible to measure the top mass using a binned expectation of each distribution compared to the one with data. However, since there are only six mass points, the method can be improved to create a continuous expectation based on the parametrization of the R_{32} against mass.

To parameterize the R_{32}, a function is chosen which describes the distribution itself. The function chosen is the combination of two different distributions which describe the peak and tail of R_{32}. Their linear combination is used to describe the entire distribution. This function includes the addition of the Hinkley[1] and Landau functions.

The Hinkley function is used since it describes the ratio of two correlated normal variables, X_1 and X_2, with means θ_i and variances σ_i^2. This ratio is appropriate because the R_{32} variable is made of the ratio of the top and W mass, which are indeed correlated. The ratio is given as $W = X_1/X_2$. The correlation of the X_1 and X_2 is denoted by ρ. The density of the ratio, $f(w)$ is given as:

$$f(w) = \frac{b(w)d(w)}{\sqrt{2\pi}\sigma_1\sigma_2 a^3(w)} \cdot \mathrm{erf}\left(\frac{b(w)}{\sqrt{1-\rho^2}a(w)}\right) + \frac{\sqrt{1-\rho^2}}{\pi\sigma_1\sigma_2 a^2(w)} \cdot \exp\left[\frac{-c}{2(1-\rho^2)}\right], \quad (9.1)$$

---

[1]Originally derived by D. V. Hinkley to account for the ratio of two correlated normal variables [148].

where:

$$a(w) = \sqrt{\frac{w^2}{\sigma_1^2} - 2\frac{\rho w}{\sigma_1 \sigma_2} + \frac{1}{\sigma_2^2}},\tag{9.2}$$

$$b(w) = \frac{\theta_1 w}{\sigma_1^2} - \frac{\rho(\sigma_1 + \sigma_2 w)}{\sigma_1 \sigma_2} + \frac{\theta_2}{\sigma_2^2},\tag{9.3}$$

$$c = \frac{\theta_1^2}{\sigma_1^2} - 2\frac{\rho \theta_1 \theta_2}{\sigma_1 \sigma_2} + \frac{\theta_2^2}{\sigma_2^2},\tag{9.4}$$

$$d(w) = \exp\left[\frac{b^2(w) - ca^2(w)}{2(1 - \rho^2)a^2(w)}\right].\tag{9.5}$$

$$\tag{9.6}$$

The Hinkley function has five independent parameters: $\theta_1, \theta_2, \sigma_1, \sigma_2$, and ρ. For the fit of the R_{32} distribution, the correlation is chosen to be held constant at $\rho \equiv 0.5$, reducing the number of degrees of freedom by one. The Hinkley function is combined with the Landau function in a linear combination, such that there are eight independent parameters:

$$P = \text{Hinkley}(p_0, ..., p_4) + \text{Landau}(p_5, ..., p_7).\tag{9.7}$$

Five of the parameters are from the Hinkley function and three are from the Landau function. Each parameter is assumed to be linearly dependent on the top mass:

$$p_i = y_i + m_{top} \cdot x_i\tag{9.8}$$

Since each parameter is mass dependent, the fit is performed over the phase-space determined by the combination of all parameters. The phase-space is continuous for the entire mass range [160,190] GeV/c^2 through interpolation of the linear fits. Outside of this mass range, the linear fits are extrapolated from the linear interpolation.

The fit of the signal R_{32} distribution is constrained to the range [1.3,3.8] which corresponds to a top mass range of [104.5,305.5] GeV/c^2. For each of the six mass templates, a fit is made using the function to each individual mass point. At the same time, a combined fit of all six mass points is made simultaneously to obtain a global minimum in each channel. The combined fits have a global χ^2/dof as follows:

- μ + jets channel χ^2/dof = 166.5/173 = 0.96; Probability = 0.62.

- e + jets channel χ^2/dof = 166.9/172 = 0.97; Probability = 0.60.

Both channels show very good agreement between the fit and the template. Each individual fit can be found in Figure 9.1. The individual fits are highlighted by the solid black line. This fit is the linear combination of the two functions highlighted in red for the Hinkley and blue for the Landau functions. The global fit is shown at each mass point by the yellow region. The difference between the combined global fit and each individual fit is marginal, which shows very good agreement for the chosen function.

In Figure 9.2, the linear assumption of the parameters is shown. The linear fits show very good agreement with the global fit in both channels.
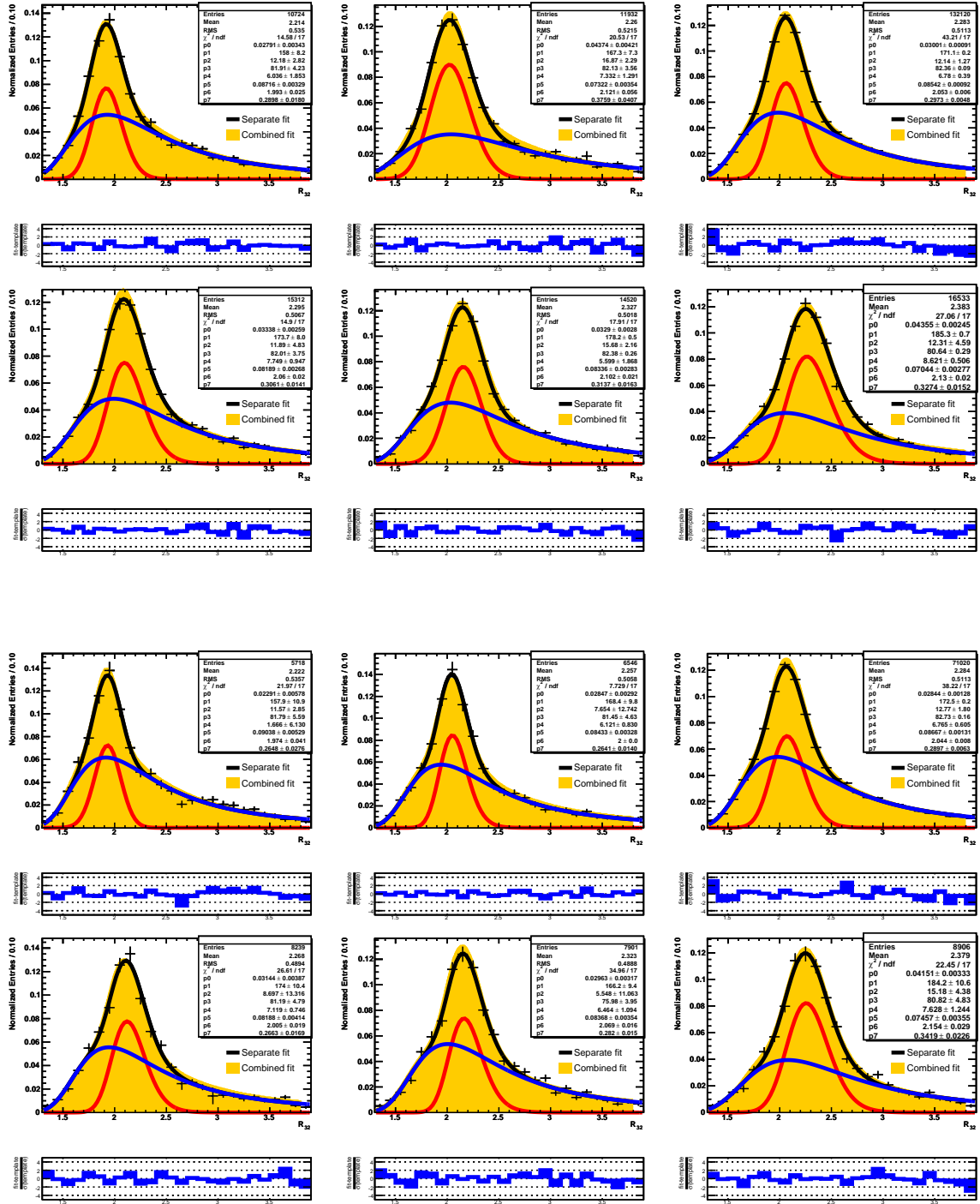
Figure 9.1.: Templates for the different top mass point for the μ + jets channel (top) and e + jets channel (bottom). The yellow region shows the combined overall fit from every mass point, whereas the black line shows the individual mass point fit. The individual mass points which are shown from top left to bottom right are 160, 170, 172.5, 175, 180 and 190 GeV mass points. The overall agreement in both channels is very good when comparing the combined and separate mass point fits.
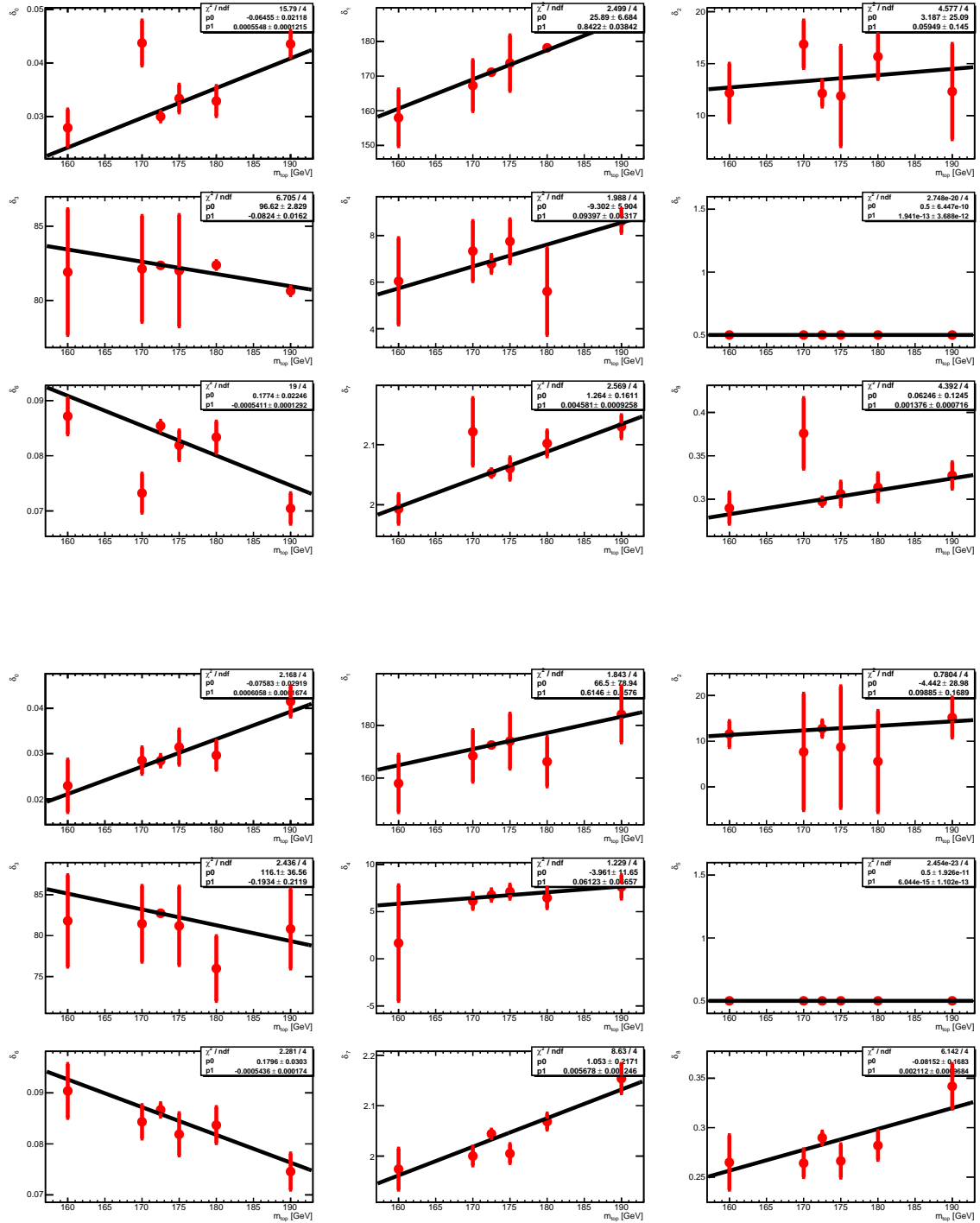
Figure 9.2.: (Top): μ + jets channel and (bottom): e + jets channel linear fits of the parameters from the Hinkley + Landau function fit at different mass points. The linear fit shows good agreement with the parameters and verifies the assumption of the parameterization against mass. δ_5 represents the correlation between the two Gauss functions and is held constant at 0.5.

The combined fits analyzed at the four equidistant mass points of: 160, 170, 180, and 190 GeV/c^2 are overlaid along with the R_{32} distributions at the given mass points in Figure 9.3. The agreement between the combined fit and the model distributions is very good in both the peak and tail regions. The separation power of the R_{32} distribution is also noticeable between the four mass points.
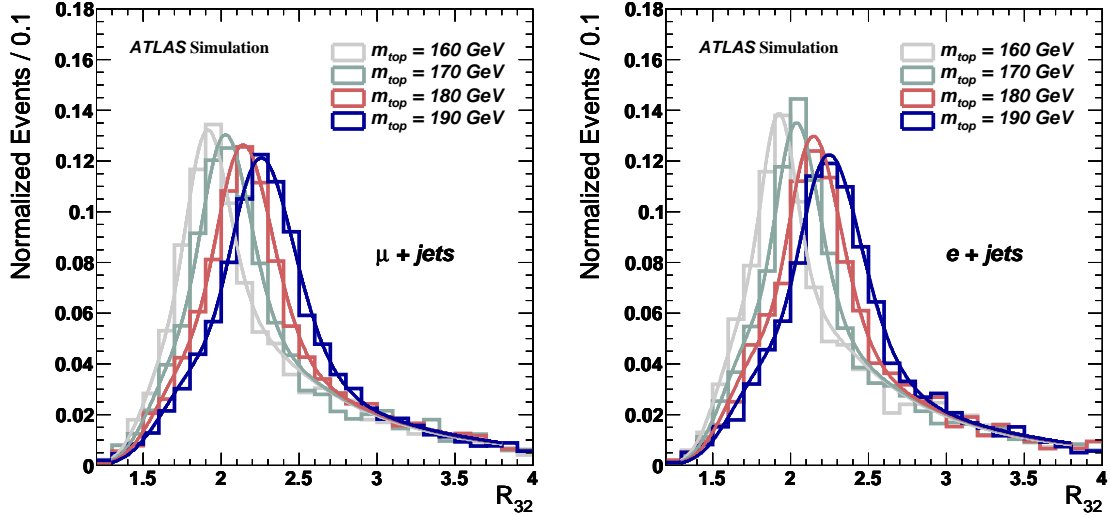
Figure 9.3.: (Left): μ jets channel and (right): e + jets channel overlaid distributions of the four equidistant mass points. The combined fit is analyzed at each of the given mass points (solid line) and compared with the distribution. For all the mass points, the functions agree very well with the distributions. The fit of the distribution is fixed to the range [1.3,3.8].

The difference between the distribution and the fit are accounted for in the modeling uncertainties as systematic uncertainties of the method.

9.2. Background Parameterization

The background R_{32} distribution contains the combination of W + jets, Z + jets, diboson, and QCD multijets contributions. These four contributions are mass independent, and thus the background model is mass independent. A single distribution is created and fit with a Landau function.

The background distribution is limited by statistics in the MC, as well as the uncertainties of the data-driven estimates in both W + jets and QCD modelling. The uncertainties in the W + jets data-driven estimate account for about 70 % the total number of events. For QCD multijets, the uncertainty is 100 % the total number of events. The fit of the distributions in both the μ + jets and e + jets channels are found in Figure 9.4. The agreement between the distribution and the Landau function model is very good in both channels. The fit is again made for the same R_{32} range [1.3,3.8] as for the signal distributions.
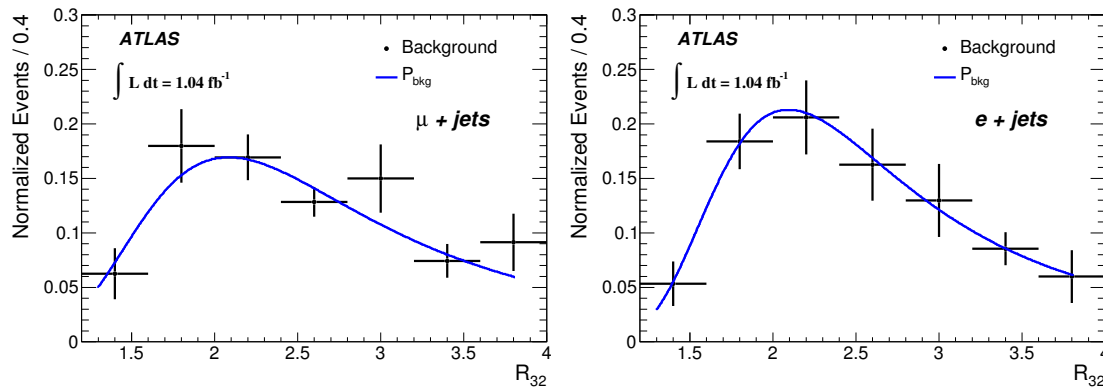
Figure 9.4.: (:eft): μ + jets channel and (right): e + jets channel background distribu-
tion along with the Landau function fit (blue solid line). The function is
mass independent and only the single parametrization is used for the entire
mass range. The uncertainty includes the MC statistics as well as the nor-
malization of W + jets and QCD multijets modelling which account for 70
% and 100 % of the specific number of events, respectively.

9.3. Binned Likelihood Fit

To perform the measurement, a binned likelihood method is used. A likelihood is
constructed which uses the expectation value in each bin based on the expected number of
events given by the signal and background R_{32} distributions. The expectation, λ_j, given
by:

$$\lambda_j = f_s \cdot N_{s,j}(m_{top}) + (1 - f_s) \cdot N_{b,j}. \tag{9.9}$$

λ_j is dependent on the number of expected signal events $N_{s,j}(m_{top})$ and the number of
background events $N_{b,j}$. It is also dependent on the relative signal fraction compared to
the total number of events f_s.

The $N_{s,j}(m_{top})$ is calculated using the parametrization of the signal distributions at a
given mass value. Therefore, not only is the shape used in the maximization, but also the
total number of events per bin given by the signal and background number of events.

The likelihood is constructed in two independent parts:

$$\mathcal{L}(R_{32}|m_{top}) = \mathcal{L}_{shape}(R_{32}|m_{top}) \times \mathcal{L}_{bkg}(R_{32}). \tag{9.10}$$

where the separate parts are defined as:

$$\mathcal{L}_{shape} = \prod_j^{N_{bins}} \left(\frac{\lambda_j^{N_{obs,j}}}{N_{obs,j}!} \right) \cdot e^{-\lambda_j}, \tag{9.11}$$

$$\mathcal{L}_{bkg} = \exp\left[\frac{(N_{b,obs} - N_{b,exp})^2}{2\sigma_b^2} \right]. \tag{9.12}$$

The first term represents a Poisson probability of observing $N_{obs,j}$ events in bin j given the λ_j expected events. Since λ_j is dependent on the top mass, the likelihood is maximized with respect to the top mass. The first term is also the only part of the likelihood which is sensitive to the top mass.

The latter term of the likelihood is a Gaussian function representing the expected level of background, which is allowed to float with any cross-section above 0. The expected number of background $N_{b,exp}$ and error σ_b are obtained by the model expectation given by the MC and data-driven estimates along with their uncertainties. This nuisance term biases the likelihood towards a background expectation which is given by the model background expectation, using the total number of background events expected in the model along with the associated uncertainty. The expected mean and error are taken from the background MC and data-driven estimates and their associated uncertainties found in Table 8.1.

10. Method Validation

Studies were performed to validate the properties of the template method using ensemble tests. The study is performed to certify that no bias has been introduced when constructing the likelihood or in the creation of the templates. Since a linear parametrization is used in the construction of the templates, the assumption must be validated through these checks. The verification of the method using ensemble tests checks both the output mass and its associated statistical uncertainty.

10.1. Ensemble Tests and Pull Evaluation

Ensemble tests are performed to study the stability of the template method. The resulting output mass is verified with the known input mass. Along with the estimated mass, the estimated statistical uncertainty is obtained from the likelihood. Both of the properties are verified using the so-called "pull". The resulting pull evaluation determines the stability of the method.

Ensembles of pseudo-data are created from the MC at each of the six given mass points: 160, 170, 172.5, 175, 180 and 190 GeV/c^2, which are the same MC events used for the creation of the templates. Ensembles are created using the MC events from signal and background event pools. An expected number of signal and background events are pulled from the two MC pools, corresponding to the luminosity of 1.04 fb^{-1} achieved in data. In this single case, the pseudo-data are analyzed using the binned likelihood, and the estimated mass and statistical uncertainty are measured. This procedure is repeated 5000 times. In each of the 5000 pseudo-data sets, the number of signal and background events are varied based on a Poissonian expectation of the expected total number of events given by Table 8.1.

After the 5000 datasets are analyzed, the distribution of measured top mass values and uncertainties are obtained. The output top mass is compared with the input top mass, and the estimated uncertainties are compared with the standard deviation of the output - input distributions using the pull. The pull formula is:

$$\text{pull} = \frac{\text{output mass} - \text{input mass}}{\text{estimated uncertainty}}. \tag{10.1}$$

The expectation value of the pull if the method has no bias is 0. The expected width of the pull distribution is 1, if the fluctuation of the estimator is the same as the estimated statistical uncertainty. If the width of the pull distribution is smaller than unity, the statistical uncertainty is over-estimated; if the width of the pull distribution is larger than unity, the statistical uncertainty is under-estimated since the fluctuation in the measured top mass is larger than the estimated uncertainty.

10.2. Treatment of Correlations

Since the MC statistics are limited, more pseudo-data samples are created than independent statistics allow. The sizes of the MC signal samples correspond to a luminosity of 15 fb^{-1}. In each ensemble, there must be a total of 1.04 fb^{-1}. Therefore, the limited number of events will only allow for approximately 15 independent ensembles. This number of samples is not enough to properly measure the stability of the method. As a result, instead of creating a small number of independent samples, re-sampling of events is used. For each ensemble, the pool N contains the total number of original events, regardless of which events have been sampled previously. This of course results in correlations between ensembles which must be accounted for.

The full derivation of the correlation factor where over-sampling is used is documented in Ref. [149], however the results are highlighted as follows. The mean of the distribution is not affected due to correlations as a result of over-sampling. The mean does not deviate from the expected mass and remains unaltered regardless of the number of correlated samples used, however, the uncertainty on the estimator is proportionally under-estimated based on the correlation among the samples.

The statistical uncertainty of the estimator is corrected from the obtained uncertainty:

$$\sigma_{\text{corrected}} \;\;=\;\; \sigma \cdot \sqrt{\frac{1}{N_{\text{samples}}} + \rho}, \tag{10.2}$$

where σ is the expected uncertainty of a single fit with the given luminosity and N_{samples} is the number of samples produced in the ensemble. The ρ is the additional factor given by the correlation between the samples. For independent, non-correlated ensembles, the corrected uncertainty is given as: $\sigma/\sqrt{N_{\text{samples}}}$, where $\rho = 0$. In the case of independent ensembles, one can decrease the error by just using more ensembles. However, when the samples are correlated, a saturation is reached based on the correlation factor.

The probability that the same event is chosen in multiple ensembles is therefore:

$$\rho = 1 - e^{-n/N}, \tag{10.3}$$

where n is the number of events pulled from a pool of N events. This is also the expression of correlation between samples. As a result, the corrected uncertainty for ensemble testing is given by the expression:

$$\sigma_{\text{corrected}} \;\;=\;\; \sigma \cdot \sqrt{\frac{1}{N_{\text{samples}}} + (1 - e^{-n/N})}. \tag{10.4}$$

This expression is applied to the expected uncertainty of one event to correct for correlated ensembles, decreasing the error by the factor given. One can see from the formula that the limiting factor to which the uncertainty can be decreased occurs when $1 - e^{-n/N}$ = 1/N$_{\text{samples}}$. At this point, there is not much to gain by increasing the N$_{\text{samples}}$ used for ensemble testing. The uncertainty does not decrease any further due to the correlation. 5000 ensembles are used in the ensemble testing and at this point, the limiting factor has been reached and more ensembles do not improve the uncertainty by a significant factor.

10.3. Ensemble Test Results

For each of the six mass points, ensemble tests are done to verify the stability of the method. The resulting measured mass, measured number of events and measured background fraction are obtained. Using the distributions of the measured mass and uncertainty, the pull mean and width of the mass are estimated at each of the six MC mass points. The output top mass against the input top mass, the difference in output and input top mass, as well as the pull mean and width for the separate channels are shown in Figure 10.1.

In both channels, the output mass is compatible with that of the input within one standard deviation. The pull mean and width also are statistically compatible with the expected behaviour. The pull width and output top mass error have been corrected by a factor representing the over-sampling of MC. This correction can be seen in the relative uncertainties of the top mass in the various mass points. For the nominal 172.5 GeV, the over-sampling is much smaller than for the other five mass points, and as a result, the uncertainty on this point is smaller in comparison. The difference between the linear fit of the pull mean and zero is taken as a source of systematic uncertainty due to the method itself. The linear fit parameters are shown in the plots of the pull mean in both channels.

Since the likelihood fit also determines the number of events and the background fraction, ensemble tests are also done to test if the output values agree with input. Using the same set of ensembles, the expected number of events and background fractions were estimated. In the μ + jets channel, the total number of events from MC is expected to be 1654. The background fraction is 9 %. In the e + jets channel, the number of events from MC is expected to be 1188 with a background fraction of 12.4 %. The measured output distribution of these variables from the 5000 ensembles are found in Figure 10.2 for the nominal 172.5 GeV mass point.

From the Figure 10.2, it is important to note that due to the Gaussian prior in the likelihood in Equation 9.10, there is a requirement that the cross section be above zero in the observed background fraction and thus can have no negative background fraction contribution to the total number of events. This has no effect on the observed background fraction since the width of the distribution is improved due to the prior. The prior decreases the uncertainty on the estimated background. For the μ + jets channel, the input to the prior is a total background fraction of 9 % with an uncertainty on that fraction of 54 %. In the fit, the output estimated background fraction yields a background fraction of 9 % with an uncertainty of 22 %. This is a considerable improvement on the background estimation. The same is visible in the e + jets channel, where the expected background fraction is 13 % with an uncertainty of 56 %. The observed background fraction from the ensemble tests yields a background fraction of 12 % with an uncertainty of 25 %. The prior reduces the overall uncertainty of the likelihood.
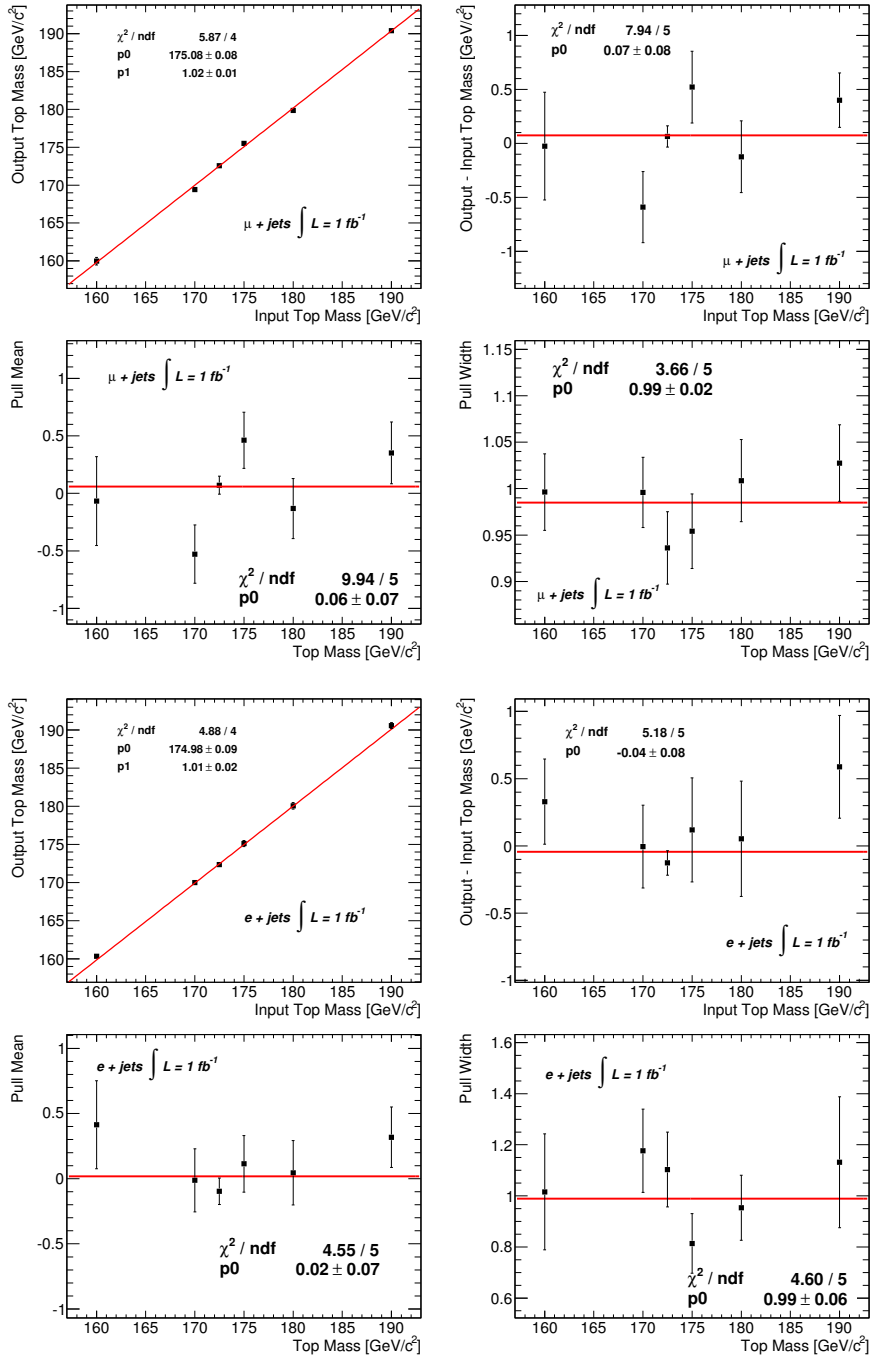
Figure 10.1.: Calibration curves for the top mass measurement using ensemble tests for different mass points in the (top four plots): μ + jets channel and (bottom four plots): e + jets channel. In both channels, (top left): The output against input top mass value found after the likelihood fit. (Top right): The residual top mass value. (Bottom left): Pull mean and (bottom right): pull width values are shown. The complete closure tests show all measured values are comparable with the expected values within the uncertainty.
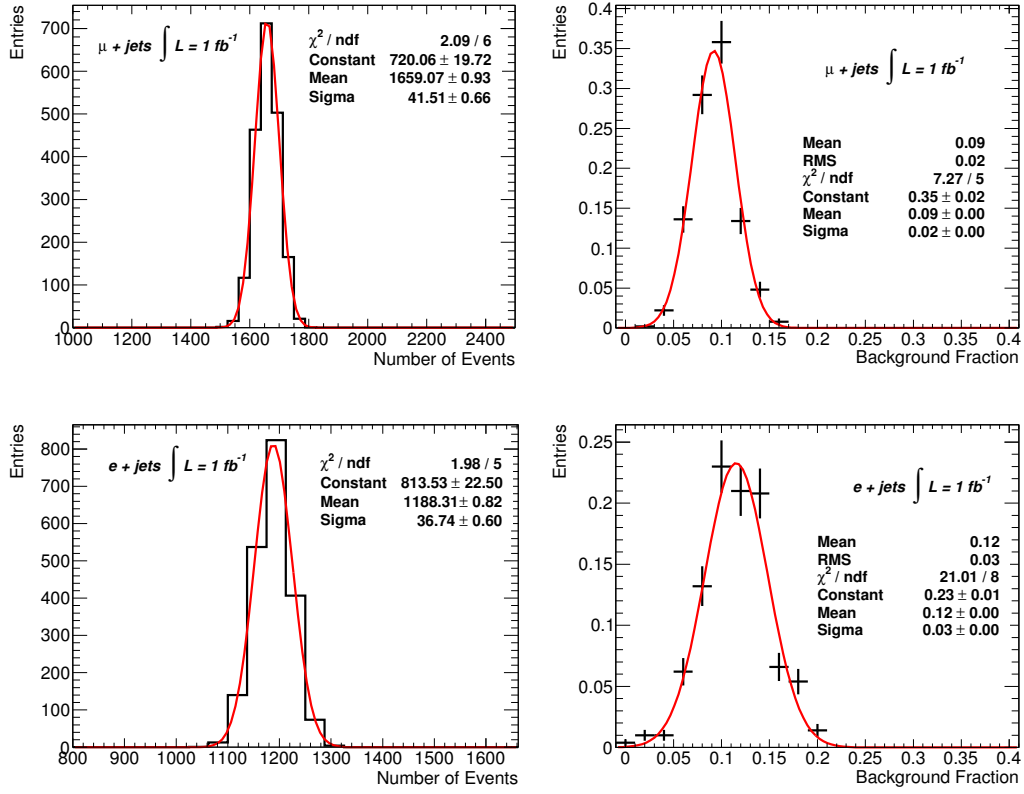
Figure 10.2.: (Top left): Output number of events from ensemble testing in the μ + jets channel. (Top right): Output background fraction in the μ + jets channel. (Bottom left): Output number of events from ensemble testing in the e + jets channel. (Bottom right): Output background fraction in the e + jets channel. In all four cases, the output value is statistically compatible with the input expectation. For the background fraction, the reduction in uncertainty is significant due to the prior used in the likelihood.

10.4. Expected Statistical Uncertainties

The expected statistical uncertainty of the method is obtained through ensemble tests. The statistical uncertainty is determined from the likelihood for each individual fit. To obtain the statistical uncertainty on the top mass, the three dimensional probability density function is projected, or marginalized, onto the top mass axis. As a result, a one dimensional probability is drawn against the mass. The statistical uncertainty is denoted by the boundaries of the central 68 percentile of the distribution. By design, the probability density does not have to be symmetric and as such, the uncertainties on either side are also not symmetric by nature. To obtain the expected statistical error, the average of the up and down statistical uncertainty per event is taken.

After the fit of all the pseudo-data ensembles, the statistical uncertainties are plotted to form the expected statistical uncertainty distribution. For the two separate channels, the distribution of statistical uncertainty on the measurement is plotted in Figure 10.3.
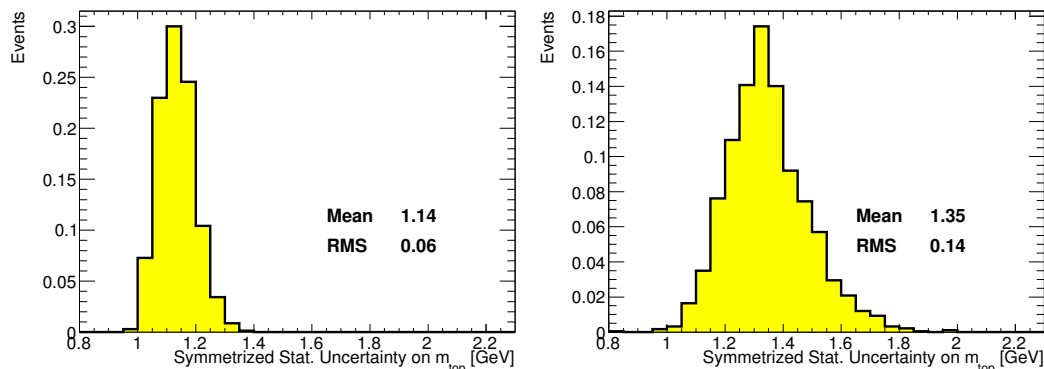
Figure 10.3.: (Left): μ + jets and (right): e + jets channel statistical uncertainty on the top mass measurement from 5000 ensembles. The expected statistical uncertainty is larger in the e + jets channel due to the reduction in the number of events between the two channels.

The expected statistical uncertainty for the two channels are:

- μ + **jets**: 1.14 ± 0.06 GeV;
- e + **jets**: 1.35 ± 0.14 GeV.

The μ + jets channel has a smaller expected statistical uncertainty than for the e + jets channel. This is expected due to the larger number of events in this channel. The difference in number of expected events is about 2:3 between e + jets and μ + jets channels. The size difference in expected statistical uncertainty between the two channels can thus be expressed using the expression for uncorrelated errors:

$$\sigma_e = \sigma_\mu \cdot \sqrt{2/3} \approx 0.82 \tag{10.5}$$

When comparing the two numbers: 1.14 GeV and 1.35 GeV, given by the ensemble tests, the factor difference is 0.84, as expected.

11. Systematic Uncertainties

Systematic uncertainties play a significant role in the estimation of the top quark mass. There are many different sources of systematic uncertainties which need to be understood and the resulting impact quantified. To calculate systematic uncertainties, pseudo-experiments using systematically modified ensembles are performed. The modified ensembles are measured using the nominal parametrization derived in Chapter 9. A systematic uncertainty is quantified by performing ensemble tests using the modified samples and creating a measured top mass distribution. From the output top mass distribution, the mean top mass from the modified sample compared to the mean of the nominal MC sample at 172.5 GeV/c^2; or in some cases with another modified ensemble. The difference in the two means of the top mass distributions is taken as the systematic uncertainty.

11.1. Systematic Uncertainties due to the Method

The first set of sources of systematic uncertainty are related to the model employed in the top mass measurement. These include the template parametrization derived previously in Chapter 9. The method uncertainties are also the result of the MC used, both the generation and showering in the creation of the signal templates. This set of systematics is quantified using modified signal templates only.

Method Calibration The parametrization of the templates and the linearity of the assumptions are analyzed. In the ensemble tests performed in Section 10.1, the output - the input top mass is plotted in Figure 10.1. A linear function is fitted over the six measured top mass values. The difference in the linear fit compared to zero, quantified from the y-axis intercept, is taken as the systematic uncertainty due to the calibration of the method.

Signal MC The effect of different MC generators is analyzed. MC@NLO is compared with another NLO MC generator known as POWHEG (Positive Weight Hardest Emission Generator). In the MC@NLO generator, soft and collinear radiation is simulated to all orders using a LO parton shower. POWHEG simulates the hardest emissions at NLO level and ignores the rest. The difference in the two generators, which have identical cross-sections at NLO, arises in the differential distributions which are affected by higher order corrections. The uncertainty due to the generators is found to be quite significant.

Hadronization Different hadronization models in MC are compared within the POWHEG generator. The showering model of PYTHIA is compared with that interpreted in HERWIG (Hadron Emission Reactions with Interfering Gluons). In the HERWIG model of shower generators, a cluster fragmentation is used. All gluons split into $q\bar{q}$ pairs after the parton showering. Clusters are formed using colour singlet objects made from the available quarks and anti-quarks. In the PYTHIA modeling of shower generators, a string fragmentation model for showering and matching is used. Further

information is found in Section 5.1. The systematic uncertainty from this difference is found to be significant, however not as large as the generator exchange.

11.2. Systematic Uncertainties Measured in Data

The only systematic uncertainty measured on data is the estimated pileup uncertainty which is a result of the high instantaneous luminosity at the LHC. At high instantaneous luminosity, many interactions occur in the same event. The LHC runs with an in-train bunch separation of only 50ns. This results in many vertices per event which need to be untangled. This is known as in-time pileup. It is also possible to have overlapping signals in the detector from the neighbouring bunch crossings, known as out-of-time pileup. Pileup also causes a reduction in the b-tagging efficiency since some of the primary vertices may appear as secondary or vise-versa. An event with twenty reconstructed primary vertices is shown in Figure 11.1, where the vertices are highlighted by different coloured ovals. The two brightly coloured tracks in the last event are two electrons resulting from a candidate Z decay. The estimation of the systematic is done by splitting the data into several periods and looking for a significant dependence of the top mass due to the two forms of pileup.
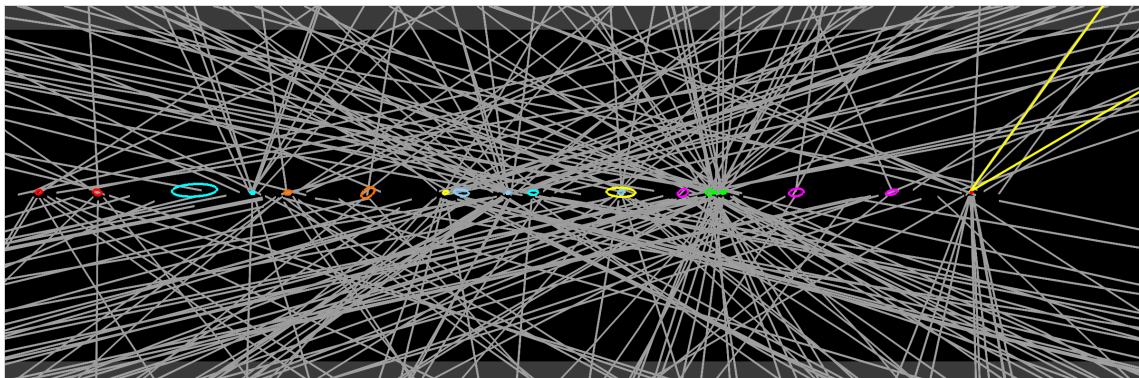
Figure 11.1.: Candidate $Z \to ee$ event during the 2011 Run which shows a high level of pileup, including twenty reconstructed vertices in the single event. Pileup due to the number of reconstructed vertices is referred to as in-time pileup. Figure taken from [150].

Pileup To estimate the effect of in-time pileup and out-of-time pileup on the top mass, the data is separated based on the number of primary vertices per event and average number of pileup interactions in a given data luminosty block, denoted by <mu>. The results of the data fit according to number of primary vertices are shown in Figure 11.2. While there is a slight trend for higher top mass values at higher number of vertices, the results are well within the statistical uncertainty of the linear fit. To quantify out-of-time pileup, data is placed into three bins denoting the average number of pileup interactions per event. A horizontal line is plotted and the χ^2 test shows agreement with the horizontal line, inferring no need to place a linear dependence of <mu> on the top mass. The fitted top mass based on the position in the bunch train is shown in Figure 11.3.
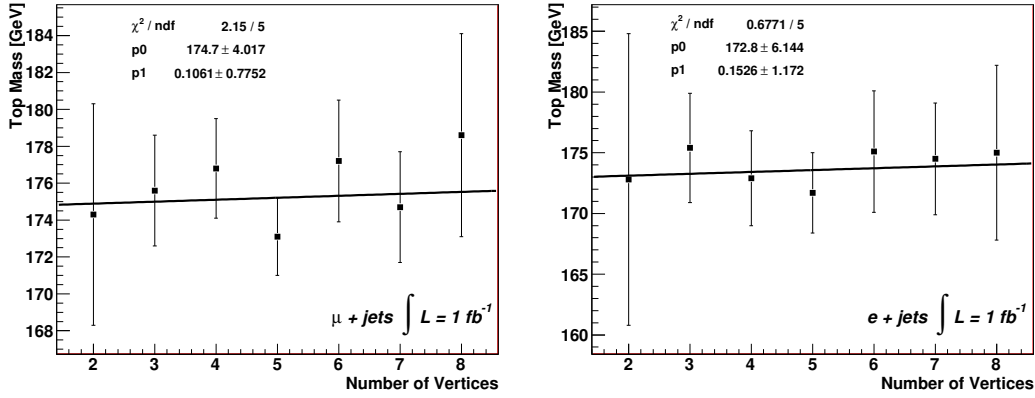
Figure 11.2.: (Left): μ + jets channel and (right): e + jets channel quantification of the in-time pileup comparing the measured top mass to the number of reconstructed primary vertices in the event. No visible dependence is seen. To quantify this uncertainty, a weighted sum of the fitted top mass values for each of the number of vertices is taken.
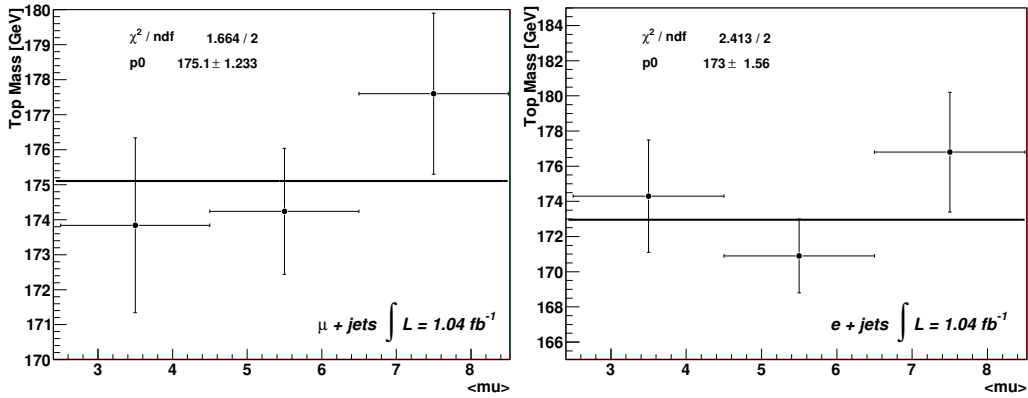
Figure 11.3.: (Left): μ + jets channel and (right): e + jets channel quantification of the out-of-time pileup comparing the measured top mass to the average number of pileup interactions. Again, no visible dependence is seen as the horizontal line χ^2/ndf is very close to 1 in both channels.

There is no significant dependence in measured top mass as a function of the number of primary vertices or average number of pileup interactions. As a result of the two tests, the top mass dependence on pileup is determined to be minimal. To quantify the uncertainty, a weighted sum of the fitted top mass values for the different number of vertices is taken.

11.3. Systematic Uncertainties Applied to Signal Only Templates

The following list of systematic uncertainties are only modeled in the signal templates. The background templates are unaltered in the ensemble testing. The signal only modified templates are compared with the nominal mass templates to quantify the systematic uncertainty. These uncertainties are related to the modeling parameters within the MC used to model the signal templates. This includes the initial and final state tuning, underlying event parameters, colour reconnection within the samples and the PDF uncertainty.

Initial and Final State Radiation Initial and final state radiation of additional gluons is described by QCD. Its strength can be modified in the MC, resulting in more or less soft jets. This change in ISR and/or FSR has two direct effects on the method. Firstly, the reconstruction efficiency is directly affected by the addition or loss of soft jets, which may have a higher p_T than the four hard jets from the $t\bar{t}$ decay. Secondly, the reconstructed energy of the resulting jets is altered by radiation of gluons. This effect is studied using pseudo-experiments with varying ISR and FSR up and down. In total, six signal samples are produced: ISR up, ISR down, FSR up, FSR down and both ISR and FSR up and down. The variation is done in the parameters determining ISR and FSR in PYTHIA. The MC samples are created using ACERMC [151–153] and PYTHIA. The ACERMC generator is a LO generator with ALPGEN showering. To compute the uncertainty, the largest difference in measured top mass from two of the six variation samples is halved.

Underlying Event The underlying event is modified within the ACERMC and PYTHIA MC; modified tunes can be seen in Ref. [154]. Since the MC is LO as in the ISR/FSR variations, the systematic is quantified by taking the difference in top mass from the UE MC and the average mass from the largest ISR/FSR deviations.

Colour Reconnection MC samples with different colour reconnection settings are compared. The different tunes are explained in detail in Refs. [155–157]. Two samples with differing CR activity using the Perugia2010 tune as well as using the TuneAPro tune are compared. The maximum difference between the resulting top masses from the two sample variations is taken as the systematic uncertainty due to colour reconnection.

PDF Uncertainty The PDF uncertainty takes into account the uncertainties due to the parton distribution functions which are used in generating the samples. The signal samples are generated using the CTEQ6.6 pdf sets [158]. The uncertainty is calculated using the additional 22 pairs of pdf sets provided by the CTEQ group. The signal sample events are re-weighted based on the pdf event weight. The 22 sets of templates are used to measure the top mass using ensemble testing. The uncertainty due to the pdf set is calculated using the quadratic sum of the measured mass differences of the 22 sets:

$$\sigma_{\text{PDF}} = \frac{1}{2} \sqrt{\sum_{i=1}^{22} \left(m_{\text{up}}^i - m_{\text{down}}^i \right)^2} \tag{11.1}$$

11.4. Systematic Uncertainties due to Background Modelling

The following list of sources of systematic uncertainty pertain to the modelling of the background. This includes the data driven models of the $W +$ jets and QCD multijets contributions to the background, both the shape and normalization of these backgrounds. To determine these systematic uncertainties, the signal template remains the nominal mass signal template while the background template is modified and compared to the nominal background template using ensemble testing.

W Background Normalization The background from $W +$ jets production is normalized using a data driven method described in Section 5.4.3. The uncertainty due to the normalization is conservatively estimated to be ±70 %. Background templates are re-created with the adjusting of the normalization of the $W +$ jets contribution. The largest measured deviation between the up and down modified background samples is taken as the systematic uncertainty.

W Background Shape To quantify the $W +$ jets shape determined by ALPGEN MC, differences in the re-weighting algorithm are used. Several MC model parameters are modified within ALPGEN. Further information can be found in Ref. [44]. Several of the modified parameters include the renormalization scale and the functional form of the factorization scale. Truth-level parameters are varied using the re-weighting algorithm and several observed kinematics are affected. The resulting templates are substituted with the nominal background template and the largest variation with the nominal template is taken as the systematic.

QCD Multijets Background Normalization The QCD multijets background is modelled using the matrix method data driven estimate. The method used is described in Section 5.4.1. The background estimate uncertainty is taken to be a conservative ±100 %. Background templates with modified amounts of the QCD mutijets normalization are created and the largest difference, either up or down, is taken to be the systematic uncertainty.

QCD Multijets Background Shape Instead of using the matrix method to estimate the QCD multijets background, a second method, the anti-electron method is employed to estimate the QCD multijets background from data in the $e +$ jets channel, described in Section 5.4.2. In the $\mu +$ jets channel, a second matrix method estimation is used. The difference between in the fitted top mass found from the shifted background template and the nominal one is taken as the systematic uncertainty.

11.5. Systematic Uncertainties Applied to Jets

The subsequent list of systematic uncertainties are due to the jet energy and resolution obtained by the ATLAS detector. The understanding of jet properties plays a central role in top mass measurements due to the relation between the energy of the jets and the resulting top mass estimate. The jet energy scale is the largest source of uncertainty of early measurements. These jet uncertainties are applied to signal and background samples in a similar fashion. The object and event selection are redone. This includes the creation of new templates. The studied systematic uncertainties include the jet energy resolution, reconstruction efficiency, energy scale and b jet specific energy scale.

Jet Energy Resolution The uncertainty of the jet energy resolution is quantified by smearing the jet energy in both signal and background MC to match that of data [111]. The jet energy is smeared by a Gaussian function, where the width is described by the resolution of the detector. The shifted systematics correspond to a loss of about 5 % in the resolution of the jet energy. The templates are recreated after event selection using the smeared jet energy and compared to the nominal jet energy resolution.

Jet Reconstruction Efficiency In MC, the jet reconstruction efficiency is compared to that of data in Ref. [111]. The agreement between data and MC is found to be within an accuracy of 2 %. To estimate the systematic uncertainty, jets with a given p_T and η are removed randomly from MC before event and object selection to match the reconstruction efficiency in data.

Jet Energy Scale The largest uncertainty to the top mass measurement is the jet energy scale. Since the top mass depends directly on the energy of the jet measured in the calorimeter, it is important the response be properly understood.

The JES is comprised of several components which are assumed to be uncorrelated with one another. A detailed description of the total JES and the correlations between the various JES components can be found in Refs. [111, 159]. The validation of the JES was performed using the 2010 dataset. A full list of the JES components is found in Section 4.1.2.

The signal and background components of the JES are treated differently due to the jet composition difference in $t\bar{t}$ and W + jets. In the background samples, the jet composition is assumed to have a 50/50 quark-gluon fraction, raising the uncertainty for low p_T jets due to gluon response. In $t\bar{t}$ the composition is mostly quarks and thus the resulting uncertainty is less than that of W + jets.

In total, a JES uncertainty between 2.5 % and 8 % is expected. This is an increase from 2010 data due to the increase in pileup uncertainty. An energy uncertainty of 8 % roughly correlates to an uncertainty of $\mathcal{O}(8\%)$ on the top mass. Therefore the R_{32} with additional constraints on low jet p_T reduces the total uncertainty due to JES to less than $\mathcal{O}(1\%)$, a significant improvement in the precision of the top mass.

b jet Energy Scale In addition to the JES, an additional uncertainty is placed on the jet energy scale due to b jets. The b jet energy scale is the result of the decay of the heavy b jet in the calorimeter. The shower shape is expected to be larger than ones from light jets and requires an additional response uncertainty. b-jets are expected to have a secondary vertex shifting the axis of the jet, resulting in a broader cluster in the calorimeter. Energy is also lost in semi-leptonically decaying b-jets which contain an escaping neutrino. Such decays include neutrinos which result in missing energy in the reconstructed jet. The b-jet energy scale uncertainty ranges from 0.8 % at very high jet p_T to 2.5 % at low jet p_T. The evolution of the bJES can be seen in Table 11.1, which highlights the various different uncertainties associated to b jets. The bJES uncertainty is only applied to jets which are true b jets; that is to say they are associated with a true b quark in the $t\bar{t}$ decay chain. The uncertainty due to the bJES is added as an uncorrelated JES term.

The validation of the bJES has been performed in 2010 data. The validation was performed through the comparison of the jet p_T measured in the calorimeter to that of the total track p_T associated to the jet. The calorimeter aspect is measured

p_T Range [GeV]	Uncertainty [%]
$p_T < 40$	2.5 %
$40 < p_T < 80$	2.0 %
$80 < p_T < 210$	1.7 %
$210 < p_T < 600$	1.1 %
$p_T > 600$	0.8 %

Table 11.1.: b jet energy scale uncertainty applied to true b jets associated to a b quark in MC as a function of its p_T. The largest uncertainty is associated to low p_T jets. The bJES is diminished by the optimization performed on the R_{32} estimator [146].

through single hadron response in the calorimeter [159]. The variation of MC generators were also used to model differences in b quark fragmentation, hadronization and the underlying soft radiation.

Again, as in the case of JES, the largest uncertainties are associated to low p_T jets. This effectively is diminished by the estimator optimization performed on the R_{32}. The bJES is a large uncertainty to the top mass, especially in the R_{32} since there is no handle on the systematic shift of the b jet. If the b jet is properly reconstructed in the KLFitter, the shift in the bJES cannot be diminished by the R_{32} and is directly shifting the R_{32} and top mass estimation. The only improvement in top mass precision results from the p_T threshold requiring higher p_T jets. Effectively, it eliminates the largest bJES uncertainty of 2.5 % for jets below 40 GeV. As a result of the inability to stabilize the bJES, it is one of the largest uncertainties on the top mass.

11.6. Additional Check of the Correlations of the JES Calorimeter Response

In addition to the nominal JES shift of 1 σ, an additional check based on the separation of JES components is performed. It is not expected that the calorimeter response of the detector is 100 % correlated to the other JES components. This assumption may lead to an underestimation of the JES. In fact, the correlation of the calorimeter response has been measured in 2010 data [159]. The results of the correlation are found in Figure 11.4.

Since it can be seen that not all bins are correlated to the calorimeter response, an additional check is performed where the 100 % correlation assumption is not used. Instead of assuming a 100 % correlation of the JES calorimeter response term, the term is separated into three separate terms. Firstly, the calorimeter response is taken as 50 % correlated to the other JES components. Independently, the other 50 % is split into a linearly increasing JES calorimeter response (from 0 % to 50 %) and one decreasing in exactly the opposite fashion. As a result, the net effect is the same, however the calorimeter response term is not assumed to be 100 % correlated. The results of this test are shown in Table 11.2.

It can be seen that there is not an underestimation of the JES uncertainty due to the assumption that the calorimeter response component of the JES is 100 % correlated with the other components. As a result, no additional uncertainty is applied to the JES.
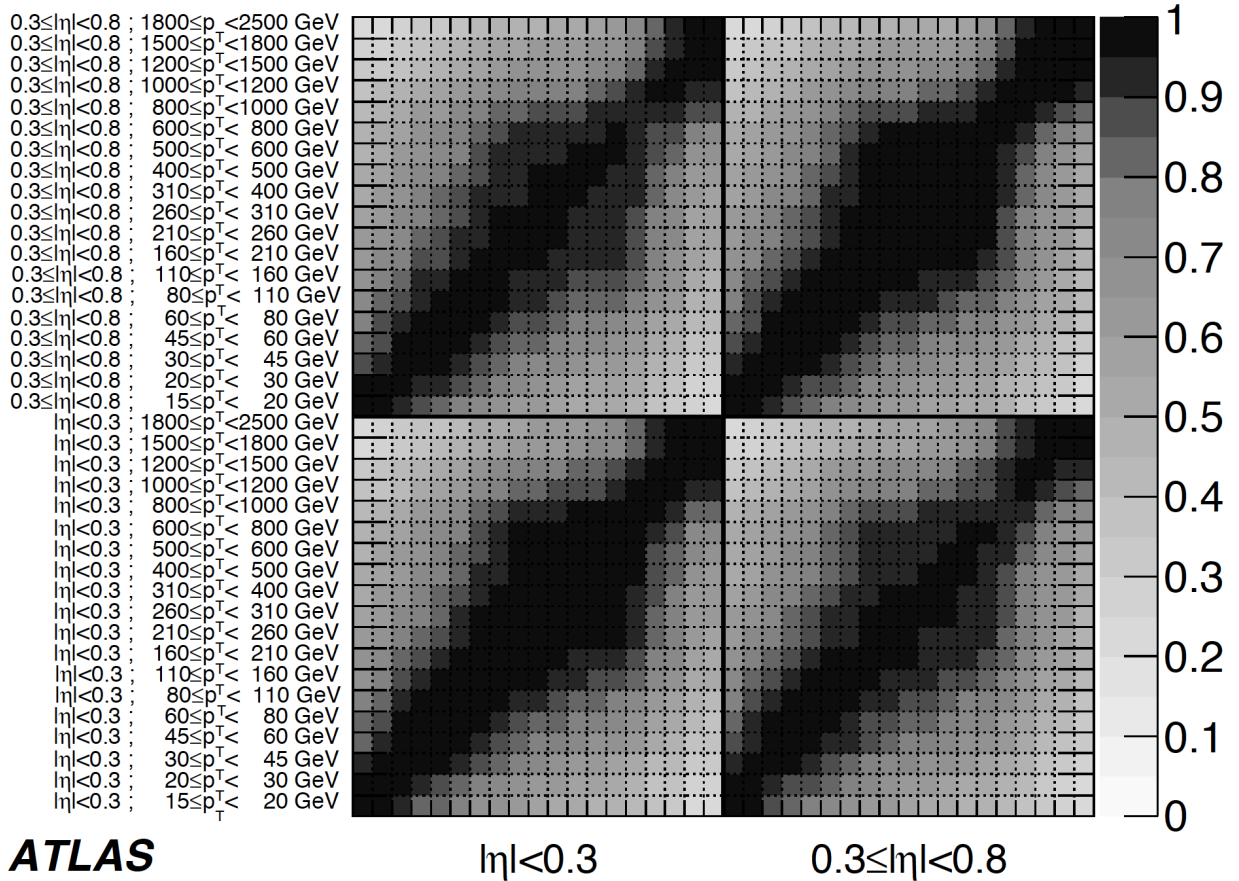
Figure 11.4.: Correlation coefficient of the total uncertainty on the calorimeter jet response for reconstructed jets. The dark area shows the highest correlation. Nearby bins are highly correlated, however bins further apart are only loosely correlated. Figure taken from [159].

Uncertainty [GeV]	e + jets	μ + jets
1 σ up	**1.21**	**1.25**
JEScalo + $\rho = .5$ others	0.9	1.1
JEScalo lin increasing	0.3	0.4
JEScalo lin decreasing	0.6	0.6
Sum	**1.12**	**1.32**

Table 11.2.: Check of the decorrelation of the JES calorimeter response component. In the 1 σ up nominal JES term, the calorimeter response is assumed to have a 100 % correlation with the other terms. To check there is no underestimation of the JES uncertainty, the calorimeter response term is split into three components. Firstly, 50 % is taken as correlated with the other components, secondly, a term linearly rises from 0 % to 50 % and thirdly a term decreases from 50 % to 0 %. The three terms are added independently and compared to the 1 σ. The decorrelation of the components shows no underestimation of the JES.

11.7. Systematic Uncertainties Applied to the Leptons, Scale Factors and Corrections to the $\not{E}_T$

The final set of systematic uncertainties are those applied to the leptons, $\not{E}_T$, and b-tagging scale factors. The lepton resolution in MC is smeared to match that of data as previously stated in Section 4.1.5 and Section 4.1.8. The uncertainty on the lepton smearing is quantified as a source of systematic uncertainty. The next uncertainty is due to the scale factors applied to the b-tagging weight. The efficiency and rejection of the b-tagger contain an uncertainty. The last uncertainty is due to out-of cone corrections coming from energy depositions which are not located inside the reconstructed cone. These uncertainties are expected to have a minimal effect on the top mass estimation.

Lepton Smearing To match the resolution of the lepton p_T (E_T) in the μ + jets (e + jets) channels, the lepton is smeared in MC to match the resolution found in 2010 data. The overview of the resolution smearing is further explained in Section 4.1.5 and Section 4.1.8. In the electron case, the energy is smeared by about 3-4 %, with the largest uncertainty for low energy electrons, whereas for the muon it is the p_T components of the combined algorithm, including the inner detector and muon spectrometer. The full muon resolution for different detector components used to determine the smearing can be found in [160]. The resulting systematic uncertainty is minimal since the lepton is not used to estimate the top quark mass.

Lepton Energy Scale In addition to the smearing, the lepton energy offset in the e + jets channel is measured from 2010 data in the $Z \rightarrow ee$ peak [120]. The scale factors are less than 2 % within $|\eta| < 2.5$. The offset error is used to estimate the uncertainty due to the lepton energy scale. The systematic uncertainty has no visible effect on the top quark mass estimation.

b-tag Scale Factors b-tagging scale factors are applied to MC to accommodate for the difference in the b-tagging efficiency and mistag rates when compared to data. A scale-factor is given to each jet, along with its associated error. The scale factor depends on jet p_T, η, and flavour [161]. The b-tagging scale factor uncertainty is estimated by shifting in the uncertainty up and down in each jet, resulting in an event weight which is systematically shifted up or down. The combination of all event weights shifted up and down are combined into shifted systematic templates. The largest difference, either up or down, in each channel is taken as the systematic uncertainty.

Out-of-Cone $\not{E}_T$ Corrections Uncertainties due to the $\not{E}_T$ arise from the corrections in the $\not{E}_T$. Soft jets with $7 < p_T < 20$ GeV are used for the calculation of the $\not{E}_T$, however they are not used as physics objects. They are 100 % correlated with the uncertainty from the energy in the calorimeter not associated to objects used for the analysis. As a result, the systematic uncertainty is the addition of shifted soft jets and unassociated cells, defined as a cell out term, fluctuated up and down. The maximum difference to the nominal template is taken as the systematic. Both signal and background are fluctuated for this systematic. Since again the $\not{E}_T$ is not used to estimate the top mass, its effect is minimal.

The results of the measurement on data as well as the quantified systematic uncertainties are found in the following chapter.

12. Top Mass Measurement Results

12.1. Mass Measurement on Data

Using the partial 2011 ATLAS dataset with an integrated luminosity of 1.04 fb^{-1}, the top mass measurement is performed. In the exact same manner as for the ensemble tests, the dataset is fit once using the likelihood in each channel separately. The fit results for the μ + jets channel and e + jets channel are found in Figures 12.1 and 12.2.
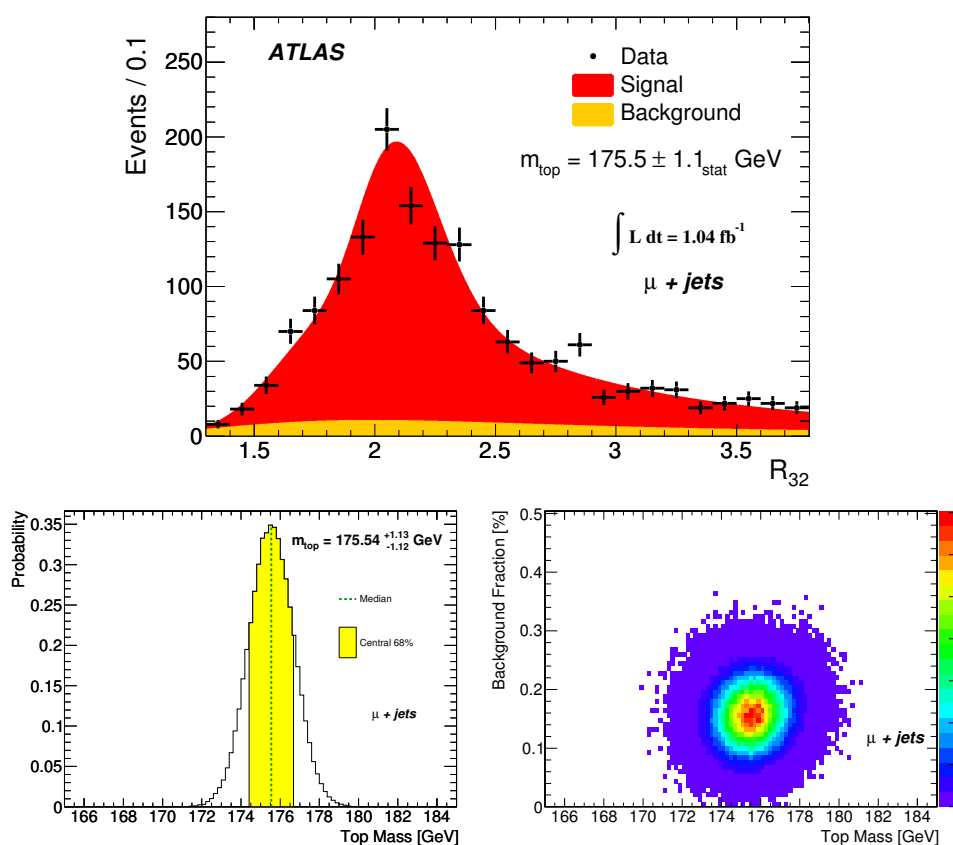
Figure 12.1.: Results of the fit of the top mass measurement in the μ + jets channel. (Top): Stacked signal and background templates created using the fit parameters. They are compared to the collected data. The fitted top mass corresponds to a value and statistical uncertainty of $175.54 \, {}^{+\,1.13}_{-\,1.12}$ GeV/c^2. (Bottom left): Marginalized probability distribution onto the top mass axis. The probability density is shown to be almost symmetric along with the 68 central percentile highlighted. (Bottom right): 2-d probability density of the fitted top mass and background distribution.
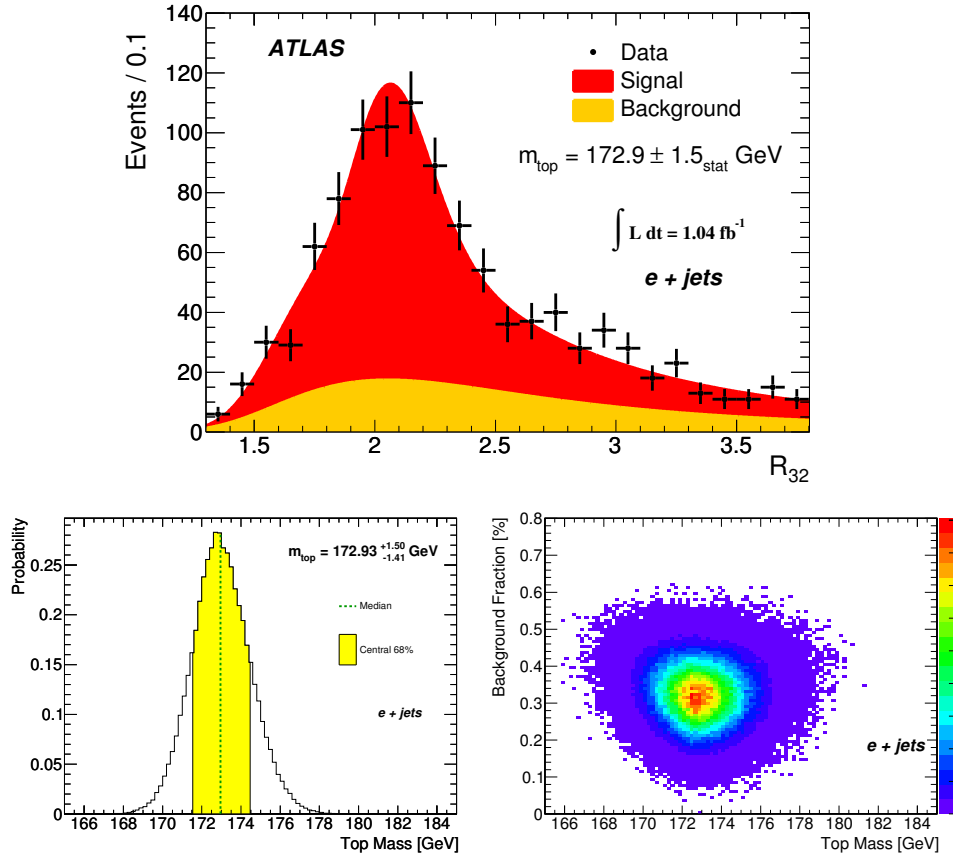
Figure 12.2.: Results of the fit of the top mass measurement in the e + jets channel. (Top): Stacked signal and background templates created using the fit parameters. They are compared to the collected data. The fitted top mass corresponds to a value and statistical uncertainty of $172.93 \, ^{+ \, 1.50}_{- \, 1.41}$ GeV/c^2. (Bottom left): Marginalized probability distribution onto the top mass axis. The probability density is shown to be almost symmetric along with the 68 central percentile highlighted. (Bottom right): 2-d probability density of the fitted top mass and background distribution.

The fits to data in both channels show results similar to those expected from the ensemble tests. In the μ + jets channel, the observed statistical uncertainty corresponds identically to the expected statistical uncertainty. The observed background fraction is within 1 σ of expectation and the fit yields a top mass of $175.5 \pm 1.1_{\text{stat}}$ GeV/c^2, containing a symmetric top mass probability density.

In the e + jets channel, the fit on data is also very close to the expected values predicted by the ensemble tests. The median observed statistical uncertainty is 1.46 GeV/c^2, compared to the expected 1.35 ± 0.14 GeV/c^2; within the 1 σ expectation. The data fit is however slightly on the higher statistical uncertainty side of the distribution. The expected background fraction fit is also higher than expected, highlighted in the bottom right of Figure 12.2. The observed background is slightly over 2 σ from the expected. The top mass probability distribution is less symmetric than the μ + jets channel, with a slightly higher uncertainty in the upwards direction than in the downwards direction:

$+1.50$ GeV/c^2 and -1.41 GeV/c^2.

The stacked templates for signal and background compared to data in both channels contain a χ^2/N which is close to 1. The χ^2/N is interpreted as the goodness-of-fit of the stacked MC histograms compared with data, with an expectation close to 1. In the $\mu +$ jets channel the χ^2/N $= 1.5$; in the $e +$ jets channel the χ^2/N $= 0.8$.

12.2. Observed Statistical Uncertainties

The top mass fits including the expected statistical error in the $\mu +$ jets and $e +$ jets channels are found to be, respectively:

- $\mathrm{m}_{\mathrm{top}}^{\mu+\mathrm{jets}} = 175.54 \, {}^{+ \, 1.13}_{- \, 1.12}$ GeV/c^2 (expected stat. error $= 1.14 \pm 0.06$ GeV/c^2)

- $\mathrm{m}_{\mathrm{top}}^{e+\mathrm{jets}} = 172.93 \, {}^{+ \, 1.50}_{- \, 1.41}$ GeV/c^2 (expected stat. error $= 1.35 \pm 0.14$ GeV/c^2)

The observed statistical uncertainty along with the expected statistical uncertainty distributions show how the data fit compares with the expected fits. Figure 12.3 shows the comparison between the statistical uncertainties.
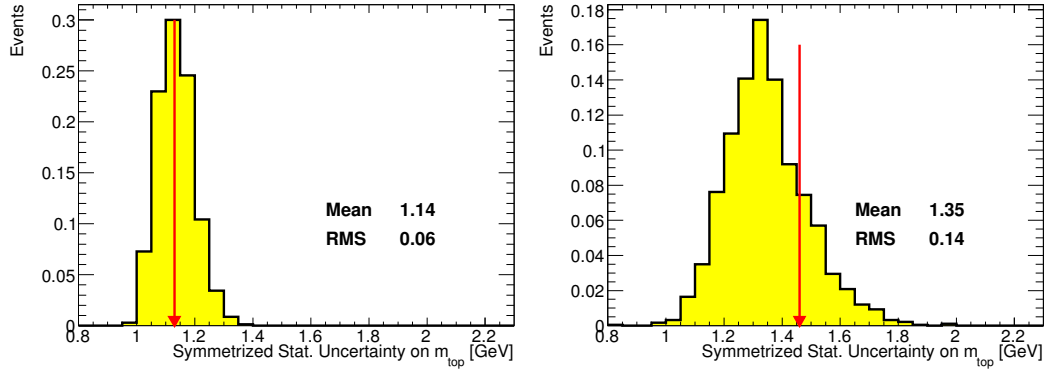
Figure 12.3.: (Left): $\mu +$ jets channel and (right): $e +$ jets channel expected statistical uncertainty distributions with the mean and width of the density. The red arrow highlights the observed statistical uncertainty in each channel on the fitted data. In both channels the fit is within 1 σ of the expected top mass uncertainty. In the $e +$ jets channel, the fit of the top mass results in a slightly higher observed statistical uncertainty than the expected mean of the distribution obtained from the ensemble tests.

The error in both channels is within 1 σ of the expected statistical precision. The observed statistical uncertainty in the $\mu +$ jets is closer to the expected mean, whereas the $e +$ jets observed statistical uncertainty is slightly less than 1 σ higher than expected. In the $e +$ jets channel, the measurement is not as precise as the $\mu +$ jets channel due to 2/3 the limited statistics. The measured top mass difference between the two channels is found to be $2.6 \pm 1.9_{\mathrm{stat}}$ GeV/c^2, slightly larger than 1 σ in difference.

12.3. Measured Systematic Uncertainties

The systematic uncertainties which have been measured are listed in Table 12.1. The quantified systematics are measured in each channel separately and are listed along with the correlation of the systematic uncertainty between channels. This is used for the combination of the two channels.

	Systematic Uncertainty [GeV]		
	e + jets	μ + jets	Correlation
Expected Statistical Uncertainty	1.4	1.1	0
Method Calibration	0.1	< 0.1	0
Signal MC (powheg vs. mcnlo)	0.8	0.7	1
Hadronization (pythia vs. herwig)	0.3	0.5	1
Pileup	< 0.1	< 0.1	1
ISR and FSR (signal only LO)	1.5	1.4	1
Underlying Event (LO)	0.1	0.1	1
Colour Reconnection	0.5	0.7	1
PDF Uncertainty	0.2	0.1	1
W Bkg. Normalization	0.2	0.2	1
W Background Shape	0.1	0.2	1
QCD Bkg. Normalization ($\pm100\%$)	0.1	< 0.1	0
QCD Background Shape	0.1	0.1	0
Jet Energy Resolution	0.3	0.4	1
Jet Reconstruction Efficiency	0.1	0.1	1
Jet Energy Scale	1.2	1.3	1
b-jet Energy Scale for True b-jets	1.1	1.2	1
Lepton Smearing	< 0.1	0.1	0
Lepton Energy Scale	0.1	< 0.1	0
b-tag Scale Factors	0.2	0.1	1
Out-of-Cone $\not{E}_T$ Corrections	< 0.1	< 0.1	1
Total Systematic Uncertainty	2.5	2.6	

Table 12.1.: List of all systematic uncertainties studied for the 1-d R_{32} Top Mass measurement. The systematic uncertainties are calculated using ensemble testing on MC shifted samples. In each case, 5000 ensembles are analyzed per fit and as a result the statistical precision on the fit is ≈ 0.1 GeV for large systematic samples and 0.3 GeV for the smaller samples. The correlation highlights the estimated correlation of the systematic between the channels. It is used for the combination of the two channels.

The largest systematic uncertainties for the top mass arise form the JES, bJES and initial and final state radiation. These three systematic uncertainties account for about 90 % of the total systematic uncertainty of the top mass measurement. The first two are expected to be the largest systematic uncertainties of the analysis. They have been minimized by the R_{32} estimator choice and the optimization of the estimator itself. The initial and final state radiation uncertainty is a very conservative estimate resulting from

tuning the PYTHIA generator to early LHC data. The largest shift comes from final state radiation, where the kinematic fitter is largely unable to properly associate the proper jet ordering. The soft jet radiates energy from the $t\bar{t}$ system and the leading order likelihood is unable to properly reconstruct the $t\bar{t}$ decay products.

It is also clear from the total uncertainty on the top mass estimate that the largest portion of the uncertainty is due to the systematic component, approximately double the statistical uncertainty in both channels. Even using only one fifth of the total 2011 dataset, the uncertainty is limited by systematics. In addition, the statistical uncertainty is worsened when taking the R_{32} ratio as opposed to measuring the top quark mass directly.

12.4. Mass Measurement Combination

The two channel measurements are combined into a single lepton + jets measurement. The combination is a linear combination of the two numbers, taking into account the correlations between the measurements and their systematics. This is achieved through the use of the BLUE method [162, 163]. The Best Linear Unbiased Estimator Method allows for the combination of multiple measurements assuming the correlation between the numbers is known. In this scenario, the correlations between the statistics are zero, since each measurement is independent of the other. The systematic uncertainties are mostly 100 % correlated, as the effect of the systematic shift is expected to be similar in both channels. This is true for systematics such as the JES or bJES, where shifts in jet energy disregard the flavour of the lepton in the $t\bar{t}$ decay. Taking 100 % correlation is the most conservative approach. Some of the systematic uncertainties are not correlated between channels, such as the background shape in the two channels, where the QCD estimation for the given channels is different. The same is true for the lepton systematics, which are completely channel independent.

The separate measurements of the top mass in the two individual channels are:

$$
\begin{aligned}
m_{\text{top}}^{\mu+\text{jets}} &= 175.5 \pm 1.1 \ (\text{stat.}) \ \pm 2.6 \ (\text{syst.}) \ \text{GeV/c}^2 \\
m_{\text{top}}^{e+\text{jets}} &= 172.9 \ ^{+\ 1.5}_{-\ 1.4} \ (\text{stat.}) \ \pm 2.5 \ (\text{syst.}) \ \text{GeV/c}^2
\end{aligned}
$$

The total uncertainty in each separate channel is given as:

$$
\begin{aligned}
m_{\text{top}}^{\mu+\text{jets}} &= 175.5 \pm 2.8 \ \text{GeV/c}^2 \\
m_{\text{top}}^{e+\text{jets}} &= 172.9 \pm 2.9 \ \text{GeV/c}^2
\end{aligned}
$$

The μ + jets is slightly more precise, by roughly 2 %. To perform the combination, the numbers from the systematics table (Table 12.1) along with the correlations are used. The combination using the BLUE method gives a lepton + jets top mass measurement of:

$$
m_{\text{top}}^{e+\text{jets}} = 174.4 \pm 0.9 \ (\text{stat.}) \pm 2.5 \ (\text{syst.}) \ \text{GeV/c}^2
$$

The relative contribution of each channel in the combined fit is 54 % in the μ + jets channel and 46 % in the e + jets channel. Since the relative uncertainties of the two

channels are very similar, the combined fit uses information from both channels almost equally, slightly favouring the μ + jets channel. MINUIT converges with a $\chi^2/N = 1.9 \; / \; 1$, which corresponds to a 17 % probability. The χ^2/N is represented by the difference of the two measurements and the given uncertainties, including correlations. The two N degrees of freedom are the two mass measurements. A high χ^2/N represents the combination of two numbers which are far apart relative to their uncertainties. The χ^2/N is slightly higher than 1 since the two channel fit results are about 1.5 σ from one another. Since the systematics are largely 100 % correlated this difference manifests itself directly in the large χ^2/N in the combination. Further information is given in Appendix B.1. The total uncertainty on the top mass measurement is 2.7 GeV or a relative uncertainty of 1.5 %.

As a final representation of the very well understood detector understanding and modelling of the R_{32} for the top mass measurement, the combined channels are represented together in a single model to data distribution. The combined distribution shows almost perfect agreement between the model and data in the complete lepton + jets channel. The distribution of the R_{32} in the lepton + jets channel is found in Figure 12.4.
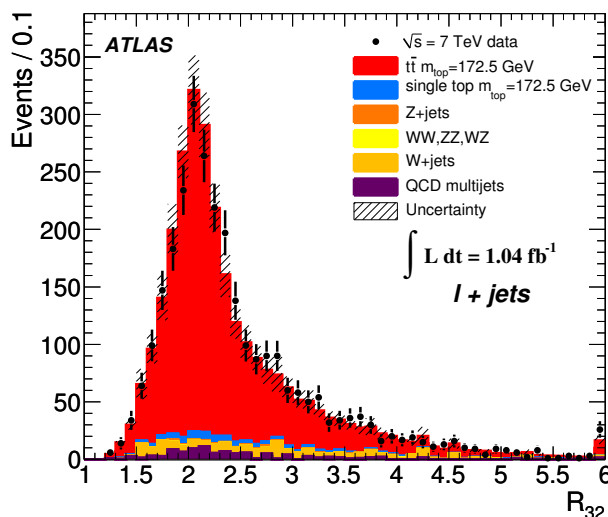
Figure 12.4.: Combination R_{32} distribution, combining both the μ + jets and e + jets channels into one lepton + jets channel R_{32} distribution. The overall agreement is in almost perfect with the data. The distribution is not fit in the measurement, but used for visual confirmation of the agreement in the lepton + jets channel.

13. Conclusion

A top mass measurement has been performed in the lepton + jets channel with the ATLAS experiment using the first 1.04 fb^{-1} of data collected during 2011. The analysis was based on a template fit using the R_{32} variable, which is built from the ratio of the hadronically decaying masses of the top quark and W boson. Using this variable, the jet energy scale, the largest source of systematic uncertainty of the top mass estimator, is significantly limited.

To improve the reconstruction efficiency, a kinematic likelihood known as the KLFitter is employed. The fitter uses a likelihood approach to properly assign the observed jets to the partons of a $t\bar{t}$ decay topology in the lepton + jets channel. The reconstruction efficiency has been shown to be about 70 % in both the μ + jets and e + jets channels.

With additional stringent estimator requirements, including an increased p$_T$ threshold, W mass window, and a requirement on the likelihood, the top mass is measured as:

$$m_{top}^{l+jets} = 174.4 \pm 0.9 \text{ (stat.)} \pm 2.5 \text{ (syst.) GeV/c}^2.$$

The measurement has a relative 1.5 % uncertainty on the top mass. This already shows a significant understanding of early data. Since the top mass measurement involves a very good understanding of the detector and the encountered physics processes, this is a significant achievement for the ATLAS collaboration in the first years of data taking.

13.1. Top Mass Average Within the ATLAS Collaboration

Two top quark mass measurements have been performed at ATLAS using 1.04 fb^{-1} of data [146] of which one has been described here. The second method, denoted by "2-d" in the following, fits both the reconstructed top quark and W boson mass. A χ^2-reconstruction algorithm is used for the three jets from the hadronic top and the two jets from the W boson to properly assign the jet ordering.

The fit of the W boson is a measure of the JES in data, significantly limiting its effect on the top mass estimation. The four measurements estimate the top mass as:

$$m_{top}^{1-d\ \mu+jets} = 175.5 \pm 1.1 \pm 2.6 \text{ GeV/c}^2, \tag{13.1}$$
$$m_{top}^{1-d\ e+jets} = 172.9 \pm 1.5 \pm 2.5 \text{ GeV/c}^2, \tag{13.2}$$
$$m_{top}^{2-d\ \mu+jets} = 175.0 \pm 0.7 \pm 2.6 \text{ GeV/c}^2, \tag{13.3}$$
$$m_{top}^{2-d\ e+jets} = 174.3 \pm 0.8 \pm 2.3 \text{ GeV/c}^2. \tag{13.4}$$

The four numbers are consistent with one another and lie within an interval of 2.9 GeV/c^2. For both methods, the top quark mass estimate in the μ + jets channel is slightly larger than that in the e + jets channel. The four individual top mass measurements

are shown in Figure 13.1 along with the combination of the 2-d measurement, denoted "l+jets", most precise single measurement made at CDF in the lepton + jets channel and the combination of the Tevatron results dating from September 2011.
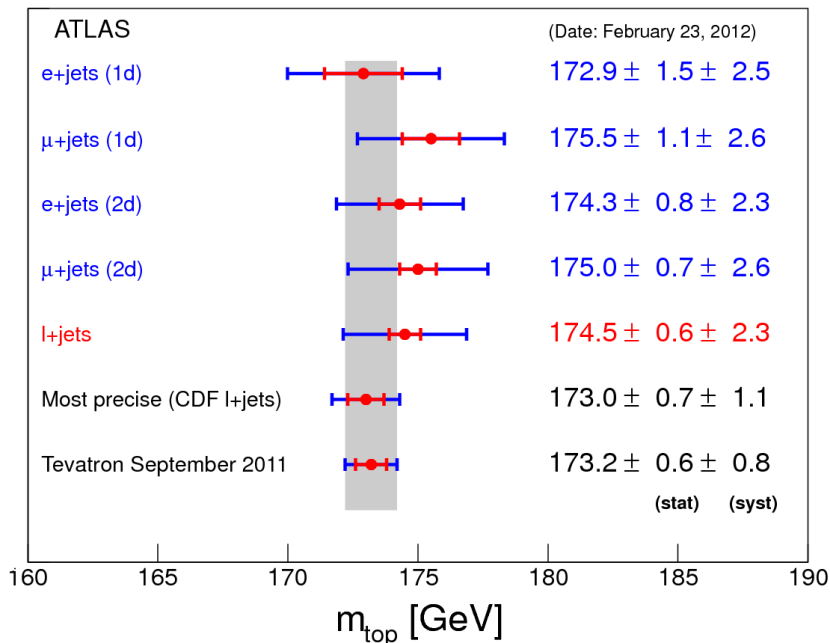
Figure 13.1.: Results from the measurements performed by the ATLAS collaboration using 1.04 fb^{-1} of data. Two methods were used, 1-d and 2-d, in the μ + jets and the e + jets channels. The numbers are all consistent with one another, and agree well with the Tevatron combination. Figure taken from [146].

Of the four ATLAS measurements, the most precise one is the 2-d measurement in the e + jets channel. To combine the four measurements using the BLUE method, the correlations between the statistical uncertainties and the systematic uncertainties is measured.

To measure the statistical correlation of the estimators, the four measurements were repeated on identical 500 pseudo-data sets in each channel. The correlation is determined to be 0.16 (0.15) in the μ + jets (e + jets) channel. The correlation between channels in the same measurement is zero. This very small correlation highlights the difference in the top mass estimators. The maximum statistical correlation due to the additional estimator requirements on the 1-d analysis is only about 55 %. This would only be the case if after the estimator optimization, all events would be identical between the two estimators. In addition, the two estimators apply completely different reconstruction algorithms, resulting in different jets which are used for the measurement. As a result, the statistical correlation is very small between measurements and results in almost two independent estimators.

The systematic uncertainties are almost fully correlated with one another in both channels and measurements. The correlations between the two channels in the same measurement are found in Table 12.1. The correlation between each measurement in the same

channel is identically 1 for all systematics listed in the table. The only non fully correlated uncertainties are the measured statistical uncertainties and method calibration systematic uncertainty. In the 2-d analysis, the JES is measured simultaneously in the likelihood fit. As a result, the statistical error contains also a component due to the JES uncertainty. Therefore the jet scale factor (JSF) uncertainty determined from the 2-d likelihood fit is estimated using ensemble tests and is removed from the statistical uncertainty component and placed as an additional systematic uncertainty for the 2-d analysis only. The JSF is not correlated with the 1-d analysis. The full correlation between the measurements is determined to be between 0.64 and 0.79. The correlation is much higher than the statistical correlation alone because the dominant uncertainties are systematic uncertainties, which are fully correlated. Using the full correlations, the combined estimate of the top quark mass is:

$$m_{top}^{l+jets} = 174.4 \pm 0.6 \text{ (stat.)} \pm 2.3 \text{ (syst.) GeV/c}^2, \qquad (13.5)$$

a total uncertainty of 2.4 GeV/c^2, or 1.4 %. This number is found to be almost identical to that of the combined 2-d top mass measurement.

The 1-d estimator adds about 30 % of the information to the combination whereas the 2-d adds 70 %. The χ^2 of the combination is $\chi^2/N = 2.1/3$, corresponding to a χ^2 probability of 56 %. In this case, all four measurements add significant amounts of information to the top mass estimate. The reason for such a large influence on the top mass estimate due to the 1-d estimator comes from the bJES uncertainty, which is smaller in the 1-d case than the 2-d case. The four bJES uncertainties are found in Table 13.1.

Measurement	bJES [GeV/c^2]
1-d μ + jets	1.2
1-d e + jets	1.1
2-d μ + jets	1.5
2-d e + jets	1.6

Table 13.1.: bJES uncertainty in the four different ATLAS top mass measurements. In both channels, the 1-d analysis is significantly less effected by the bJES.

It can be clearly seen that the 1-d analysis is significantly less effected by the bJES. This is the result of the increase in p$_T$ cuts used in the construction of the R_{32} estimator. This significantly reduces the correlation between the two measurements and increases the 1-d weight in the ATLAS combination. The full information of the combination is located in Appendix B.2.

The result of the work done in improving the 1-d R_{32} estimator and reduction of the JES and bJES through additional p$_T$ cuts and other requirements has significantly improved the 1-d measurement. Using the reconstruction power of the KLFitter, which reconstructs proper $t\bar{t}$ events with roughly 70 % efficiency, the R_{32} top mass estimator has a significant improvement in precision compared to using a χ^2 reconstruction algorithm. The weight of the 1-d measurement is significant in the ATLAS combination. The estimator has been shown to be very stable and robust on early data, providing a measurement which is compatible with a 2-d measurement using the same luminosity and a very large overall JES uncertainty.

13.2. Comparison with Other Top Mass Measurements

The 1-d R_{32} method is the first measurement of its kind and was developed by the ATLAS collaboration. Though there have been several top mass measurements using a form of "in-situ" calibration, none have measured the top mass through the stabilized variable. Adding the additional strength of the KLFitter reconstruction algorithm, the measurement used on first data collected at ATLAS has been shown to be very powerful to measure the top mass in the lepton + jets channel with very large reduction in uncertainties.

The measurements at the Tevatron have measured the top mass to a relative uncertainty of only 0.5 %. Using detector understanding and data collected from over twenty years, the work has made it the most precisely measured quark mass. After one year of running and data collecting at ATLAS, the precision is already of the order 1.5 % and the statistical uncertainty is of the same order as those obtained at the Tevatron. An increase of statistics will not reduce the uncertainty on the top quark mass significantly. The total uncertainty is dominated by systematic effects. To compete with the Tevatron top quark mass, work needs to be done to further understand detector uncertainties and modeling of the MC simulation.

The reduction in the large systematics, JES, bJES and ISR/FSR, can be done by further work on the understanding of the ATLAS detector. From the analysis standpoint, further dimensional measurements can be performed. Either to measure the JES by a W mass measurement to estimate the JES in data. A third dimension may be added as well for the bJES or ISR/FSR, which all can be measured on data.

Performing additional data-driven estimates of the uncertainties increases the statistical error on the top mass, however the LHC produces a significant amount of data and a loss in statistical precision in the method can be recovered by adding the full 5 fb^{-1} of data collected in 2011. This is especially significant since the three largest systematics do not significantly decrease with additional data.

13.3. Analysis Prospects

The stabilized 1-d R_{32} method was developed to perform an early top mass measurement which is stabile against the largest perceived uncertainty, the JES. For early data, this is exactly the scenario which played itself out; the JES was the largest uncertainty and due to lack of statistics, a 2-d method was not a viable solution because the statistical uncertainty was too large. For the measurement of the 35 pb^{-1} dataset collected in fall 2010, the most precise measurement was obtained using the R_{32}. However, from the measurements using the 1.04 fb^{-1}, the statistical uncertainty was no longer an issue for any top mass measurement made in the lepton + jets channel. At this stage, the 2-d method had a much improved precision. As a result, the addition of the KLFitter and estimator cuts were required. Since the largest uncertainties due to JES and bJES occur at low p$_T$, the use of higher p$_T$ jets only at the cost of statistical precision was the best option with the 1-d R_{32} method.

To obtain a more precise top mass measurement with the R_{32} is very difficult without adding an extra dimension to the fit. The additional statistics (1 fb^{-1} to 5 fb^{-1}) should

reduce the statistical uncertainty from 0.9 GeV to about 0.4 GeV. If the systematic uncertainties do not reduce, which is the case by applying the same method to the full 2011 dataset, the total uncertainty on the top mass is improved by only about 0.1 GeV. Therefore there is no reason to apply this identical method to the full 2011 dataset.

Stricter p_T cuts could improve the larger uncertainties, but the JES calorimeter response eventually is worsened at larger p_T of jets (See Figure 4.3). The cuts will also significantly reduce the statistical precision of the method. Requiring two b-tags is also an option, however the improvement will be significantly limited to reconstruction of the $t\bar{t}$ decay. The background will be reduced to almost zero, however the background uncertainties are almost zero in the current method since the background is fit using the binned likelihood and modelling uncertainties are minimal compared to the largest systematic uncertainties. The only viable option is to perform data-driven estimates of the largest backgrounds by fitting them simultaneously with the top mass. The JES can be reduced by measuring the hadronic W boson simultaneously with the top quark. This is what is done in the 2-d method. The same can be done for bJES with a sensitive variable.

As a result, it is clear that the R_{32} method has been fully exhausted and performed a significant measurement of the top quark mass. Using the kinematic likelihood fitter, the KLFitter, with a 70 % reconstruction efficiency and additional estimator requirements, the precision of the top mass estimate has significantly improved from the ATLAS runs of fall 2010 to summer 2011. The relative uncertainty obtained during the first running year at ATLAS is already only 1.5 %. The top mass measurement using the 1-d stabilized R_{32} method has been determined to be:

$$m_{top}^{l+jets} = 174.4 \pm 0.9 \text{ (stat.)} \pm 2.5 \text{ (syst.)} \text{ GeV/c}^2,$$

which is a significant achievement for the ATLAS collaboration during its first years of running and has added significant information to the understanding of the top quark mass from a new experiment in high energy physics.

A. KLFitter Fitted Kinematics

A.1. Resolution of the Fitter

The KLFitter employs transfer functions to improve the resolution of the reconstructed objects. The transfer functions account for the difference in energy from particle level to the reconstruction and calibration level.

The difference in resolution of the matched hadronic b quark and leptonic b quark are shown in Figure A.1. The resolution for the true objects, best fitted object and the measured objects are shown. The plots highlight the improvement in resolution when using the fitter and its transfer functions. The resolution is improved for the fitted objects in the direction of the true objects by a considerable amount. The improved energy resolution results in improved object reconstruction when using the fitted parameters determined by the fitter. The improved resolution increases the precision of the top mass estimator.
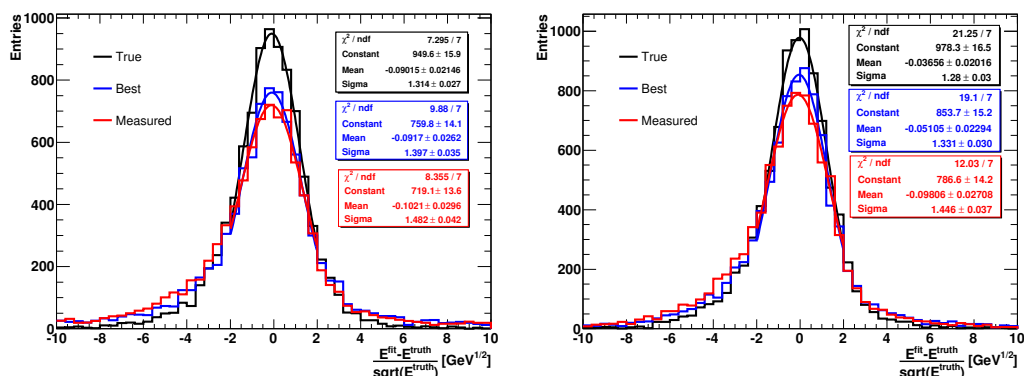
Figure A.1.: Improvement in energy resolution for (left): the matched hadronic b quark and (right): the matched leptonic b quark. Highlighted are the energy resolution for the true quark, the resolution of the measured object from detector resolution and the improved resolution of the fitted best object. The improved resolution is the result of the transfer functions in the fitting procedure.

A.2. Object and Event Kinematics

Several of the object fitted kinematics from the KLFitter. In addition to Figures 7.4 and 7.5, more fitted objects are produced. These fitted objects highlight more complex reconstructed objects from the two top quarks and W bosons as well as η and ϕ distributions of the b quark, light quarks and lepton. the overall agreement is excellent between model and data.
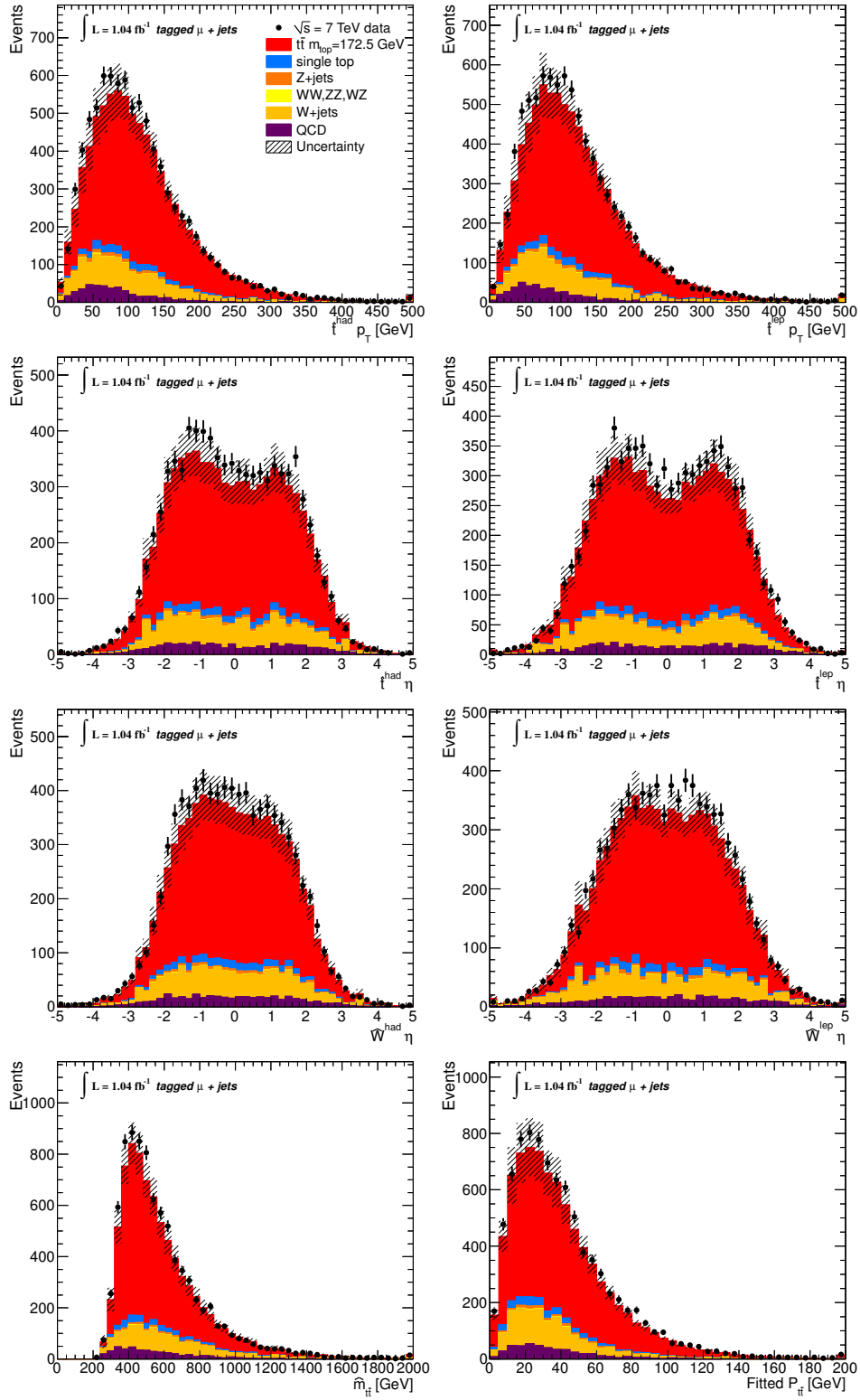
Figure A.2.: Fitted quantities such as the top quark η and ϕ in hadronic and leptonic hemispheres and the W η. Finally the combined $t\bar{t}$ mass and p_T are shown for the μ + jets channel.
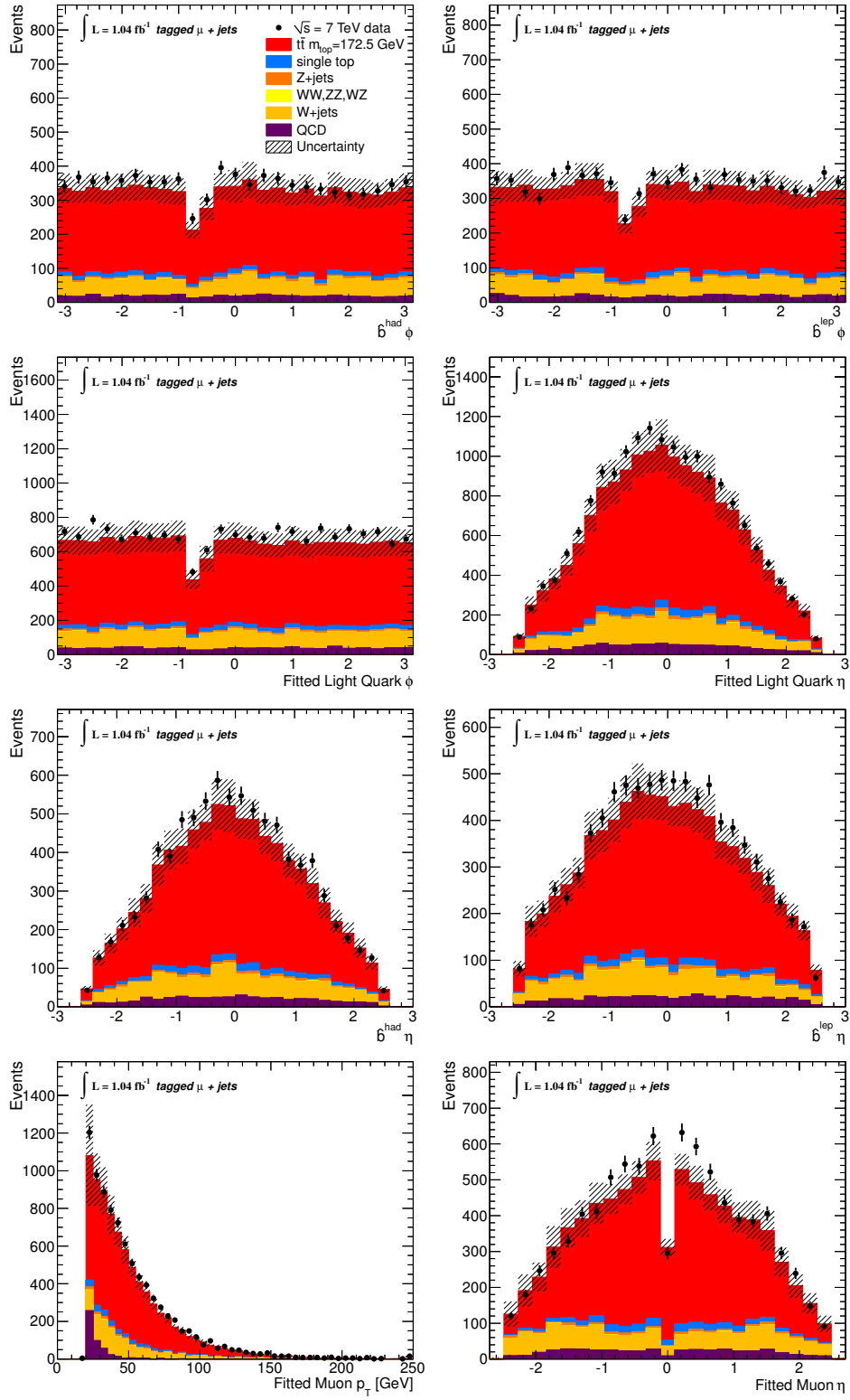
Figure A.3.: Fitted quantities in the μ + jets channel such as the b, both hadronic and leptonic, and light quark η and ϕ distributions. Finally the fitted muon p_T and η are shown.
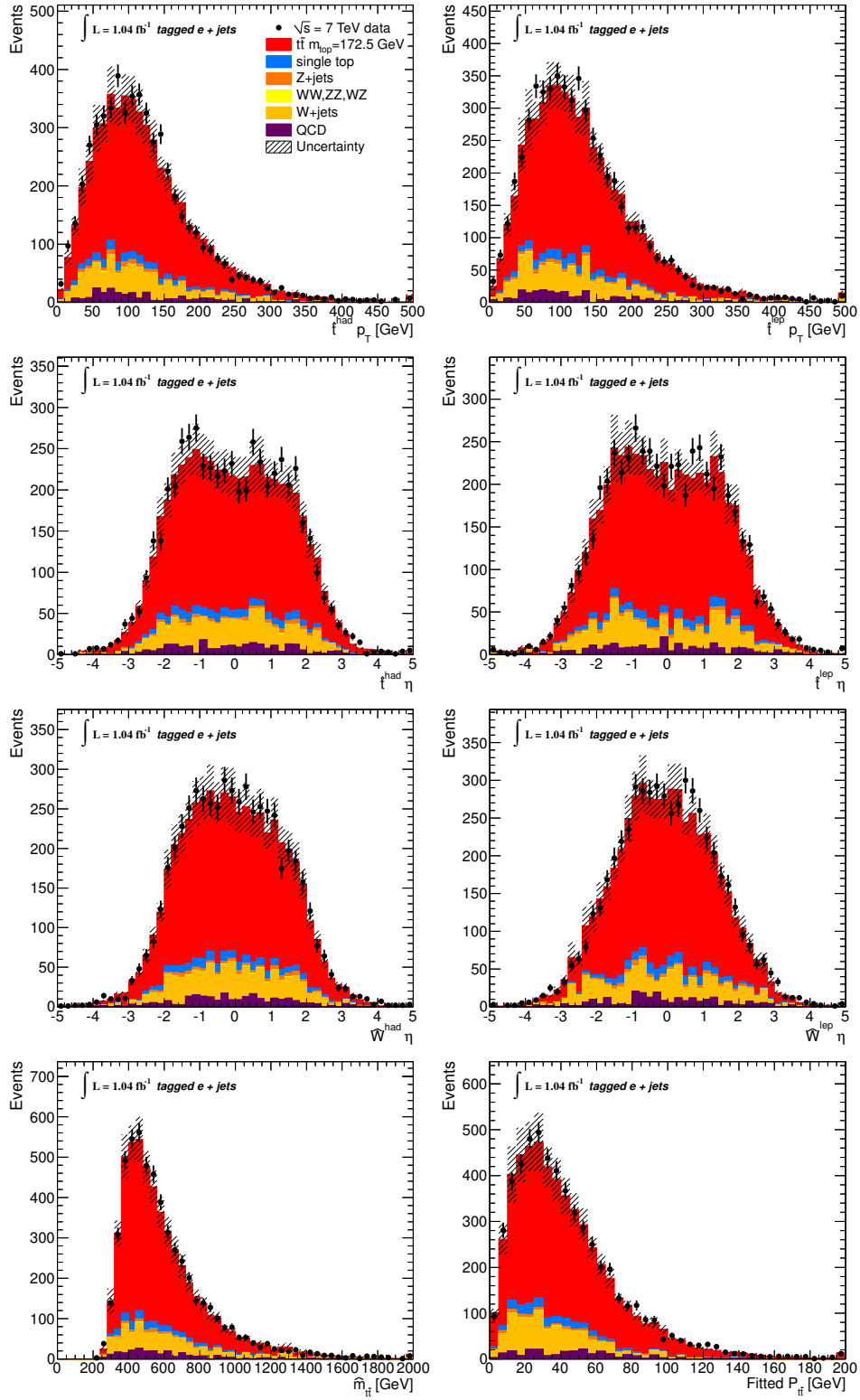
Figure A.4.: Fitted quantities such as the top quark η and ϕ in hadronic and leptonic hemispheres and the W η. Finally the combined $t\bar{t}$ mass and p_T are shown for the e + jets channel.
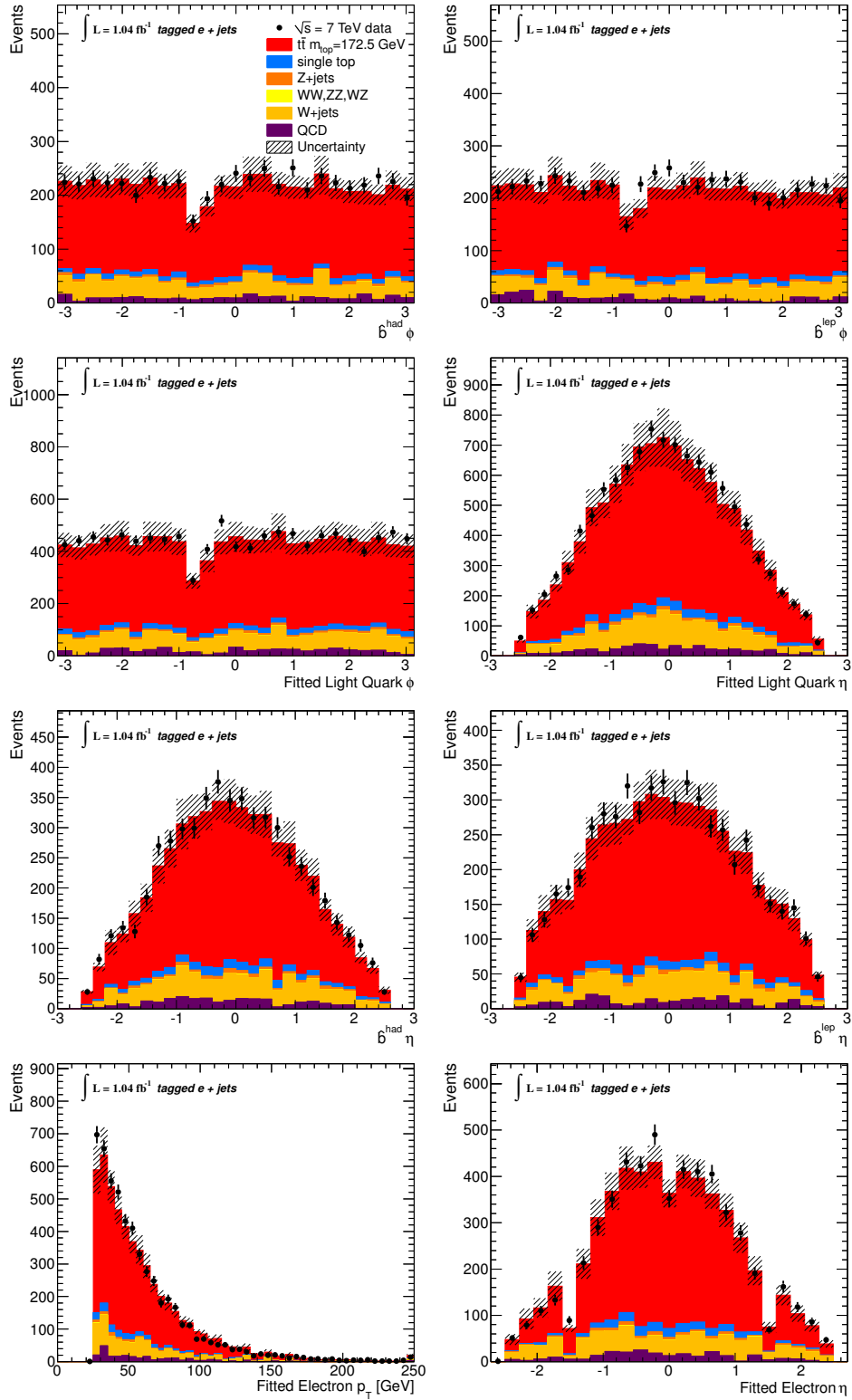
Figure A.5.: Fitted quantities in the e + jets channel such as the b, both hadronic and leptonic, and light quark η and ϕ distributions. Finally the fitted electron p_T and η are shown.

B. BLUE Combination

The BLUE method is employed to combine several correlated results. A correlation matrix is obtained for the measurements and their uncertainties, both statistical and systematical. The combination between the μ + jets channel and e + jets channel is demonstrated along with the four channel combination within the ATLAS experiment from the 1-d and 2-d methods.

B.1. Combination of Channels

The combination of the μ + jets and e + jets channel is performed assuming statistical correlations of 0 and systematic correlations shown in Table 12.1. The resulting combination gives a correlation matrix between the two channels:

$$\begin{pmatrix} 1.00 & 0.77 \\ 0.77 & 1.00 \end{pmatrix}$$

The result shows a high correlation between the two channels, given that the statistic uncertainties are uncorrelated. In this case, the large systematic uncertainties are fully correlated, resulting in the large cross channel correlation.

Since the channels are correlated with one another by a factor of 0.77, the improvement in the systematic uncertainty is limited. The resulting top mass is given as:

$$m_{top}^{l+jets} = 174.4 \pm 0.9 \text{ (stat.)} \pm 2.5 \text{ (syst.) GeV/c}^2$$

The statistical precision improvement is significant, however the combined systematic uncertainty does not improve do to almost fully correlated systematic uncertainties between channels. The fit gives a top mass which is almost the median value of the two channels, combined using 54 % from the μ + jets channel and 46 % from the e + jets channel. The overall $\chi^2/N = 1.9/1$ or 17 %. The large χ^2/N is the result of the large difference in the measured top mass values. The mass difference is found to be 2.6 ± 1.9 GeV/c^2.

B.2. Combination Within ATLAS

The combination of measurements can also be performed within the context of the ATLAS lepton + jets channel. The four measurements [146] performed at ATLAS in the μ + jets and e + jets channel have been done using two separate measurements with a luminosity of 1.04 fb^{-1}. The combination comprises of the two 1-d channels with two 2-d channels. The statistical correlations have been measured using ensemble testing and are shown in the following array. The array goes from left to right, up to down, from the 1-d μ + jets, 1-d e + jets, 2-d μ + jets and 2-d e + jets channels.

$$\begin{pmatrix} 1.00 & 0.00 & 0.16 & 0.00 \\ & 1.00 & 0.00 & 0.15 \\ & & 1.00 & 0.00 \\ & & & 1.00 \end{pmatrix}$$

The statistical correlation has been measured using identical pseudo-datasets in ensemble tests. the resulting statistical correlation is found to be very small between the two measurements. The total statistical correlation is 0.16 (0.15) in the μ + jets and e + jets channel respectively.

The systematic uncertainties are correlated as in 12.1 between μ + jets and e + jets in each measurement. All systematic uncertainties in the table are fully correlated with one another in each channel between measurements, with the obvious exception of the method calibration. In addition, the 2-d contains a systematic uncertainty due to the jet scale factor, which is measured simultaneously to the top mass in the measurement. The jet scale factor has been measured to be:

Measurement	JSF Uncertainty [GeV/c^2]
2-d μ + jets	0.5
2-d e + jets	0.6

Table B.1.: Additional JSF systematic uncertainty applied to the two 2-d channels. This additional uncertainty is removed from the total statistical uncertainty since it is determined by the simultaneous measurement of the top and W boson.

This additional systematic uncertainty is only added to the 2-d measurement, and is uncorrelated between measurements. The full correlation matrix between the four measurements is determined to be:

$$\begin{pmatrix} 1.00 & 0.79 & 0.74 & 0.71 \\ & 1.00 & 0.64 & 0.71 \\ & & 1.00 & 0.74 \\ & & & 1.00 \end{pmatrix}$$

The four measurements are again highly correlated as a result of the large systematic correlation. The correlation between channels is the highest in each measurement 0.79 (0.74) in the 1-d (2-d) measurements respectively. The smallest correlation is found to be between the 1-d e + jets channel and the 2-d μ + jets channel (0.64).

The resulting top mass is measured to be:

$$m_{top}^{l+jets} = 174.4 \pm 0.6 \text{ (stat.)} \pm 2.3 \text{ (syst.)} \text{ GeV/c}^2$$

The total uncertainty on the top mass is 2.4 GeV/c^2, or 1.4 %. The overall $\chi^2/N = 2.1/3$, which corresponds to a chi^2 probability of 55.7 %. The overall fit is consistent and contains a small χ^2/N since the four measurements are all very close to one another. In both measurements the μ + jets channel contains a slightly larger mass than the e + jets channel.

The contribution of each measurement to the total combined measurement is shown in Table B.2.

Measurement	Relative Weight [%]
1-d μ + jets	9.2
1-d e + jets	18.3
2-d μ + jets	27.6
2-d e + jets	46.9

Table B.2.: Relative weight of each of the four measurements towards the combination in the ATLAS lepton + jets channel. Due to highly correlated systematics, the two smallest uncertainty measurements, 2-d μ + jets and 2-d e + jets are the largest contributing measurements. The 1-d analysis contributed 27.5 % towards the final combination.

It can be seen from Table B.2 that the highest contributing measurements are the 2-d μ + jets and 2d e + jets channel. Since the largest systematics are fully correlated, the combination does not improve significantly from either of the 1-d or 2-d analyses. The relative uncertainty on the top mass is reduced by only 12 % from the 1-d analysis, and the final top mass value is identical to less than $\mathcal{O}(0.1 \text{ GeV/c}^2)$.

The four measurements are consistent and all give weight to the total combination. The final number is not reflected by the relative weights since the four measurements are all consistent. The 1-d analysis gives a significant total weight of 27.5 % to the ATLAS combination.

List of Figures

List of Tables

Bibliography

[1] Abachi, S., et al. (DØ), *Observation of the Top Quark*, Phys. Rev. Lett **74** (1995) , `hep-ex/9503003`.

[2] Abe, F., et al. (CDF), *Observation of Top Quark Production in $p\bar{p}$ Collisions*, Phys. Rev. Lett **74** (1995) , `hep-ex/9503002`.

[3] The CDF and DØ Collaborations and the Tevatron Electroweak Working Group, *Combination of CDF and DØ Results on the Mass of the Top Quark using up to 5.8 fb^{-1} of data*, `arxiv:1107.5255 (2011)`.

[4] Noether, E, *Invariante Variationsprobleme*, Nachr. D. Koenig. Gesellsch. D. Wiss. Zu Goettingen, Math-phys. Klasse (1918) .

[5] Gell-Mann, M, *A Schematic Model of Baryons and Mesons*, Phys. Lett. **8** (1964) .

[6] Glashow, S.L., *Partial Symmetries of Weak Interactions*, Nucl. Phys. **22** (1961) 579.

[7] Weinberg, S., *A Model of Leptons*, Nucl. Phys. **19** (1967) .

[8] Salam, A., *Weak and Electromagnetic Interactions*, exert from: W. Svartholm, editor, *Elementary Particle Theory*. Stockholm (1968) 367.

[9] Aubert, J. J., et al. (E598), *Experimental Observation of a Heavy Particle J*, Phys. Rev. Lett. **33** (1974) .

[10] Augistin, J. E., et al., *Discovery of a Narrow Resonance in e+ e- Annihilation*, Phys. Rev. Lett. **33** (1974) .

[11] Perl, M. L., et al., *Evidence for Anomalous Lepton Production in e+ e- Annihilation*, Phys. Rev. Lett. **35** (1975) .

[12] Herb, S. W., et al., *Observation of a Dimuon Resonance at 9.5-GeV in 400-GeV Proton Nucleus Collisions*, Phys. Rev. Lett. **39** (1977) .

[13] Innes, W. R.; et al., *Observation of Structure in the Υ Region*, Phys. Rev. Lett. **359** (1977) 1240.

[14] Kodama K., et al (DONUT Collaboration), *Observation of tau Neutrino Interactions*, Phys. Lett. B **504 (3)** (2000) 218, `arXiv:hep-ex/0012035`.

[15] The Particle Data Group, Amsler C. et al., *Review of particle physics*, Phys. Lett. **B667** (2008) 1.

[16] Arnison, G., at al. (UA1), *Experimental observation of isolated large transverse energy electrons with associated missing energy at $\sqrt{s} = 540$ GeV*, Phys. Lett. B **122** (1983) 103–116.

[17] Banner, M., et al. (UA2), *Observation of single isolated electrons of high transverse momentum in events with missing transverse energy at the CERN anti-p p collider*, Phys. Lett. B **122** (1983) 476–485.

[18] Arnison, G., at al. (UA1), *Experimental observation of lepton pairs of invariant mass around 95 GeV/c² at the CERN SPS collider.*, Phys. Lett. B **126** (1983) 398–410.

[19] Bagnaia, P., et al. (UA2), *Evidence for Z0 → e+ e- at the CERN anti-p p collider*, Phys. Lett. B **129** (1983) 130–140.

[20] Kobayashi, M. and Maskawa, T., *CP Violation in the Renomarlizable Theory of Weak Interaction*, Prog. Theor. Phys. **49** (1973) 652–657.

[21] Cabibbo, N., *Unitary Symmetry and Leptonic Decays*, Phys.Rev.Lett. **10** (1963) 531–533.

[22] Higgs, P. W., *Broken Symmetries, Massless Particles and Gauge Fields*, Phys. Lett **12** (1964) .

[23] Englert, F. and Brout, R., *Broken Symmetry and the Mass of Gauge Vector Mesons*, Phys. Rev. Lett. **13** (1964) .

[24] Guralnik, G. S., Hagen, C. R. and Kibble, T. W. B., *Global Conservation Laws and Massless Particles*, Phys. Rev. Lett. **13(20)** (1964) 585.

[25] Djouadi, A., *The Anatomy of Electro-Weak Symmetry Breaking*, Phys. Rept. **457** (2008) , `hep-ph/0503172`.

[26] LEP Working Group for Higgs Boson Searches, *Search for the Standard Model Higgs Boson at LEP*, Phys. Lett. **B565** (2003) 61–75.

[27] The CDF and DØ Collaborations, *Combined CDF and D0 Upper Limits on Standard Model Higgs Boson Production with up to 8.2 fb-1 of Data*, `arXiv: 1107.5518`.

[28] The ATLAS Collaboration, *Combination of Higgs Boson Searches with up to 4.9 fb⁻¹ of pp Collisions Data Taken at a center-of-mass energy of 7 TeV with the ATLAS Experiment at the LHC*, ATLAS-CONF-2011-163 (2011) .

[29] The CMS Collaboration, *Combination of SM Higgs Searches*, CMS-PAS-HIG-11-032 .

[30] Kane, G, *The Dawn of Physics Beyond the Standard Model*, Scientific American (2003) .

[31] Fritzsch, H., Gell-Mann, M., and Leutwyler H. Phys. Lett. B **47** (1973) 365.

[32] Gross, D.J. and Wilczek, F., *Ultraviolet Behavior of Non-Abelian Gauge Theories*, Phys.Rev.Lett **30** (1973) 1343–1346.

[33] Politzer, H.D., *Reliable Perturbative Results for Strong Interactions*, Phys.Rev.Lett **30** (1973) 1346–1349.

[34] R. Brandelik et al. (TASSO collaboration), *Evidence for Planar Events in e+e- Annihilation at High Energies*, Phys. Lett. B **86** (1979) 243–249.

[35] Schmelling, M., *Status of the Strong Coupling Constant*, `arXiv:hep-ex/9701002`.

[36] Albajar, C., et al. (UA1), *Search for New Heavy Quarks at the CERN Proton - anti-Proton Collider*, Z. Phys. C **37** (1988) 505–525.

[37] Altarelli, G., et al.(UA2), *Total Cross-Sections for Heavy Flavor Production in Hadronic Collisions and QCD*, Nucl. Phys. B **308** (1988) 724.

[38] The ATLAS Collaboration, *Measurement of the top quark-pair production cross section with ATLAS in pp collisions at $\sqrt{s} = 7$ TeV*, `arxiv:1012.1792v2`.

[39] Fiedler, F., *Precision Measurements of the Top Quark Mass*, `arXiv:1003.0521v1`.

[40] Pumplin, J.,Stump, D.R.,Huston, J.,Lai, H.L.,Nadolsky, P., and Tung W.K., *New Generation of Parton Distributions with Uncertainties from Global QCD Analysis*, `arXiv:hep-ph/0201195`.

[41] `http://projects.hepforge.org/mstwpdf/plots/plots.html`.

[42] Kidonakis, N., *Next-to-next-to-leading Soft-gluon Corrections for the Top Quark Cross Section and Transverse Momentum Distribution*, Phys. Rev. D **82** (2010) 114030.

[43] Martin, A.D. and Stirling, W.J. and Thorne, R.S. and Watt, G., *Parton Distributions for the LHC*, Eur. Phys. J. **C63** (2009) 189–285.

[44] The ATLAS Collaboration, *Measurement of the top quark pair production cross-section with ATLAS in the single lepton channel*, `arXiv:1201.1889`.

[45] The DØ Collaboration, *Observation of Single Top-Quark Production*, Phys. Rev. Lett **103** (2009) 092001.

[46] The CDF Collaboration, *Observation of Electroweak Single Top-Quark Production*, Phys. Rev. Lett **103** (2009) 092002.

[47] The ATLAS Collaboration, *Search for s-channel Single Top-Quark Production in pp Collisions at $\sqrt{s} = 7$ TeV*, `ATLAS-CONF-2011-118`.

[48] Kidonakis, N., *Two-loop Soft Anomalous Dimensions for Single Top Quark Associated Production with a W- or H-*, Phys. Rev. D **82** (2010) 054018.

[49] Kidonakis, N., *Next-to-next-to-leading-order Collinear and Soft Gluon Corrections for t-Channel Single Top Quark Production*, Phys. Rev. D **83** (2011) 091503.

[50] Kidonakis, N., *NNLL Resummation for s-Channel Single Top Quark Production*, Phys. Rev. D **81** (2010) 054028.

[51] The ATLAS Collaboration, *Observation of t Channel Single Top-Quark Production in pp Collisions at $\sqrt{s} = 7$ TeV with the ATLAS detector*, `ATLAS-CONF-2011-088`.

[52] The ATLAS Collaboration, *Measurement of the t-channel Single Top-Quark Production Cross Section in 0.70 fb^{-1} of pp Collisions at $\sqrt{s} = 7$ TeV with the ATLAS detector*, `ATLAS-CONF-2011-101`.

[53] Quadt, A., *Top quark physics at hadron colliders*, Eur. Phys. J. C **48** (2006) .

[54] Jezabek, M., Kuhn, J. H., *QCD Corrections to Semileptonic Decays of Heavy Quarks*, Nucl. Phys. B **314** (1989) 1.

[55] `http://www-d0.fnal.gov/Run2Physics/top/top_public_web_pages/`.

[56] Guindon, S. for The ATLAS Collaboration, *Measurement of Top Quark Properties at ATLAS*, `ATL-PHYS-SLIDE-2011-109`.

[57] The ATLAS Collaboration, *Measurement of the top quark charge in pp collisions at $\sqrt{s} = 7$ TeV in the ATLAS experiment*, `ATLAS-CONF-2011-141`.

[58] The ATLAS Collaboration, *Measurement of the W boson polarisation in top quark decays with the ATLAS detector*, JHEP **1206** (2012) 088.

[59] The DØ Collaboration, *Direct measurement of the mass difference between top and antitop quarks*, `arXiv:1106.2063`.

[60] The ATLAS Collaboration, *Measurement of spin correlation in $t\bar{t}$ production from pp collisions at $\sqrt{s} = 7$ TeV using the ATLAS detector*, `ATLAS-CONF-2011-117`.

[61] The ALEPH Collaboration, The DELPHI Collaboration, The L3 Collaboration, The OPAL Collaboration, The SLD Collaboration, The LEP Electroweak Working Group, and The SLD Electroweak Heavy Flavour Groups, *Precision electroweak measurements on the Z resonance*, Phys. Rep. **427** (2006) 257.

[62] Timo van Ritbergen, T., and Stuart, R. G., *Complete 2-loop quantum electrodynamic contributions to the muon lifetime in the fermi model*, Phys. Rev. Lett. **82** (1999) 488.

[63] Bai, J. Z., *Measurements of the Cross Section for e+e- $\rightarrow$ Hadrons at Center-of-Mass Energies from 2 to 5 GeV*, Phys. Rev. Lett. **88** (2002) 101802.

[64] Sirlin, A., *Radiative corrections in the $SU(2)_L \times U(1)$ theory: A simple renormalization framework*, Phys. Rev. D **22** (1980) 971.

[65] The LEP Collaborations (ALEPH, DELPHI, L3 and OPAL), the LEP Electroweak Working Group and the SLD Heavy Flavour Group `http://lepewwg.web.cern.ch/LEPEWWG/`.

[66] Veltman, M,., *The Infrared - Ultraviolet Connection*, Acta Phys. Polon. B **12** (1981) 437.

[67] Langenfeld U, Moch S, and Uwer P, *Measuring the running top-quark mass*, Phys. Rev. **80** (2009) 054009.

[68] Hoang, A. H., and Stewart, I. W., *Top Mass Measurements from Jets and the Tevatron Top-Quark Mass*, Nuclear Phys. Proc. Suppl. **185** (2008) 220.

[69] Fleming, S., Hoang, A. H., Mantry, S., and Stewart, I. W., *Jets from massive unstable particles: Top mass determination*, Physical Review D **77** (2008) 074010.

[70] Galtieri, A. B., Margaroli, F., Volobouev, I., *Precision measurements of the top quark mass from the Tevatron in the pre-LHC era*, `FERMILAB-PUB-11-458`.

[71] Buckley A et al, *General-purpose event generators for LHC physics*, (2011) , `arXiv:1101.2599v1`.

[72] The CDF Collaboration, *Measurement of the top quark mass with in situ jet energy scale calibration in the all-hadronic channel using the Template Method with 5.8 fb^{-1}*, (2011) , `CDF note 10456`.

[73] The DØ Collaboration, *Measurement of the top quark mass in the lepton+jets channel using the ideogram method*, Phys. Rev. D **75** (2007) 092001.

[74] The DØ Collaboration, *Direct measurement of the top quark mass at DØ*, Phys. Rev. D **58** (1998) 052001, `arXiv:hep-ex/9801025`.

[75] *Measurement of the top quark mass in the muon+jets channel*, `CMS-PAS-TOP-11-015`.

[76] The DØ Collaboration, *Measurement of the top quark mass in $p\bar{p}$ collisions using events with two leptons*, `arXiv:1201:5172`.

[77] The DØ Collaboration, *A precision measurement of the mass of the top quark*, Nature **429** (2004) 638–642.

[78] The CDF Collaboration, *Top Quark Mass Measurement in the Lepton + Jets Channel Using a Matrix Element Method and in situ Jet Energy Calibration*, Phys. Rev. Lett. **105** (2010) 252001.

[79] The DØ Collaboration, *Precise measurement of the top-quark mass from lepton+jets events at DØ*, Phys. Rev. D **84** (2011) 032004.

[80] The DØ Collaboration Phys. Lett. B. **703** (2011) 422.

[81] The CDF Collaboration, *Combination of CDF top quark pair production cross section measurements with up to 4.6 fb^{-1}*, (2009) , `Conf. Note 9913`.

[82] The ATLAS Collaboration, *Determination of the top-quark mass from the ttbar cross section measurement in pp collisions at $\sqrt{s} = 7$ TeV with the ATLAS detector*, `ATLAS-CONF-2011-054`.

[83] The ATLAS Collaboration, *Measurement of the Top-Quark Mass from 2011 ATLAS Data using the Template Method*, `ATLAS-CONF-2011-120`.

[84] The CMS Collaboration, *Measurement of the top quark mass in the l+jets channel*, `CMS-PAS-TOP-10-009`.

[85] The LHC Machine Group reported by G. Brianti at the XVth Interm. conf. on High Energy Accelerators, Hamburg, Germany, *Status report on the CERN Large Hadron Collider (LHC)*, (1992) , `CERN/AC-DI/92-03 (LHC)`.

[86] The ATLAS Collaboration, *ATLAS Detector and Physics Performance Technical Design Report, Volume I*, (1999) .

[87] The CMS Collaboration, *CMS Physics Technical Design Report, Volume I*, (2006) .

[88] The ALICE Collaboration, *Technical Proposal for A Large Ion Collider Experiment at the CERN LHC*, (1995) .

[89] The LHCb Collaboration, *LHCb Technical Proposal*, (1998) .

[90] `http://cdsweb.cern.ch/record/1165534/files/CERN-Brochure-2009-003-Eng.pdf`.

[91] The TOTEM Collaboration, *The TOTEM Experiment at the CERN Large Hadron Collider*, Journal of Instrumentation **3** (2008) .

[92] The LHCf Collaboration, *The LHCf detector at the CERN Large Hadron Collider*, Journal of Instrumentation **3** (2008) .

[93] The ATLAS Collaboration, *The ATLAS Experiment at the CERN Large Hadron Collider*, Journal of Instrumentation **3** (2008) 8003.

[94] The ATLAS Collaboration, *ATLAS Inner Detector Technical Design Report*, (2007) .

[95] The ATLAS Collaboration, *Charged-particle multiplicities in pp interactions measured with the ATLAS detector at the LHC*, (2010) , `arXiv:1012.5104`.

[96] The ATLAS Collaboration, *Liquid Argon Calorimeter Technical Design Report*, (1996) .

[97] Oliveira Damazio, Denis on behalf of the ATLAS Collaboration, *ATLAS LAr Calorimeter: Construction, Integration, Commissioning*, Journal of Physics: Conference Series: **110** (2008) 092007.

[98] Varanda, M. J. on behalf of the Tilecal/ATLAS Collaboration., *The Tile Hadronic Calorimeter for the ATLAS Experiment*, LIP, Lisbon, Portugal .

[99] The ATLAS Collaboration, *ATLAS Muon Spectrometer Technical Design Report*, (1997) .

[100] The ATLAS Collaboration, *Determination of the muon reconstruction efficiency in ATLAS at the Z resonance in proton-proton collisions at sqrt(s)=7 TeV*, `ATLAS-CONF-2011-008`.

[101] The ATLAS Collaboration, *Muon Combined Performance*, `ATLAS-CONF-2011-1504`.

[102] Elsing, M., Schörner-Sadenius, T. on behalf of The ATLAS Collaboration, *Configuration of the ATLAS Trigger System*, (2003) , `physics/0306046`.

[103] Weber, P., *ATLAS Calorimetry: Trigger, Simulation and Jet Calibration*, Dissertation , `HD-KIP 08-03`.

[104] Catani, S.,Dokshitzer, Y. L., Seymour, M. H., and Webber, B. R., *Longitudinally-invariant k_T-clustering algorithms for hadron-hadron collisions*, Nucl. Phys. B **406** (1993) 187.

[105] Ellis, S. D. and Soper, D. E.,, *Successive Combination Jet Algorithm For Hadron Collisions*, Phys. Rev. D **48** (1993) 3160.

[106] The ATLAS collaboration, *Performance of Jet Algorithms in the ATLAS Detector*, `ATL-PHYS-INT-2010-129`.

[107] Soyez, G, *The SISCone and anti-kt jet algorithms*, `arXiv:0807.0021`.

[108] The ATLAS collaboration, *Jet selection for Top Physics*, (2010) , `ATL-COM-PHYS-2010-835`.

[109] The ATLAS collaboration, *A Simple p_T- and η-Dependent Monte Carlo-Based Jet Calibration*, (2009) , `ATL-COM-PHYS-2009-076`.

[110] The ATLAS Collaboration, *Close-by Jet Effects on Jet Energy Scale Calibration in pp Collisions at $\sqrt{s} = 7$ TeV with the ATLAS Detector.*, `ATLAS-CONF-2011-062`.

[111] The ATLAS Collaboration, *Jet energy measurement with the ATLAS detector in proton-proton collisions at sqrt(s) = 7 TeV*, `arXiv:1112.6426`.

[112] The DØ Collaboration `http://www-d0.fnal.gov/Run2Physics/top/singletop_observation/`.

[113] The ATLAS Collaboration, *Expected performance of the ATLAS Detector, Trigger and Physics*, `arXiv:0901.0512`.

[114] The ATLAS Collaboration, *Performance of Impact Parameter-Based b-tagging Algorithms with the ATLAS Detector using Proton-Proton Collisions at sqrt(s) = 7 TeV*, `ATLAS-CONF-2010-091`.

[115] Piacquadio, G., Weiser, C., *A new inclusive secondary vertex algorithm for b-jet tagging in ATLAS*, J.Phys.Conf.Ser. **119** (2008) 032032.

[116] The ATLAS Collaboration, *Commissioning of the ATLAS high-performance b-tagging algorithms in the sqrt(s) = 7 TeV collision data*, (2011) , `ATLAS-CONF-2011-102`.

[117] The ATLAS Collaboration, *Measurement of the $W \to l\nu$ and $Z \to ll$ production cross sections in proton-proton collisions at sqrt(s) = 7 TeV with the ATLAS detector*, Journal of High Energy Physics **12** (2010) .

[118] The ATLAS Collaboration, *Electron and photon reconstruction and identification in ATLAS: expected performance at high energy and results at 900 GeV*, (2010) , `ATLAS-CONF-2010-005`.

[119] The ATLAS Collaboration, *Electron performance in the ATLAS experiment*, (2010) , `ATL-COM-PHYS-2010-208`.

[120] The ATLAS Collaboration, *Calibrated $Z \to ee$ mass with 2011 data*, 2011. `ATL-COM-PHYS-2011-1637`.

[121] The ATLAS Collaboration, *Electron Performance Measurements with the ATLAS Detector Using the 2010 LHC Proton-Proton Collision Data*, 2011. `hep-ex/1110.3174`.

[122] The ATLAS Collaboration , *Di-muon invariant mass resolution in $Z \to \mu\mu$ decays at 7 TeV*, 2011. `https://twiki.cern.ch/twiki/bin/view/AtlasPublic/MuonPerformancePublicPlots`.

[123] The ATLAS Collaboration, *Reconstruction and Calibration of Missing Transverse Energy and Performance in Z and W events in ATLAS Proton-Proton Collisions at $\sqrt{s}$=7 TeV*, 2011. `ATLAS-CONF-2011-080`.

[124] Corcella, G., et al., *HERWIG 6.5: An Event Generator for Hadron Emission Reactions With Interfering Gluons (Including Supersymmetric Processes)*, JHEP **0101** (2001) 010.

[125] Frixione, S. and Webber, B.R., *Matching NLO QCD Computations and Parton Shower Simulations*, JHEP **0206** (2022) 029.

[126] Butterworth, J.M., Forshaw, J.R., and Seymour, M.H., *Multiparton Interactions in Photoproduction at HERA*, Z. Phys. C **72** (1996) 637–646.

[127] `http://projects.hepforge.org/jimmy/`.

[128] The ATLAS Collaboration, *First Tuning of HERWIG/JIMMY to ATLAS Data*, Atl-phys-pub-2010-014, 2010.

[129] G. Altarelli and G. Parisi, *Asymptotic freedom in parton language*, Nuclear Physics B **126(2)** (1977) 298.

[130] G. V. N. and L. L. N., *Deep inelastic e p scattering in perturbation theory*, Sov. J. Nucl. Phys. **15** (1972) 438.

[131] L. M. Lipatov, *The parton model and perturbation theory*, Sov. J. Nucl. Phys. **20** (1975) 94.

[132] Y. Dokshitzer, *Calculation of the Structure Functions for Deep Inelastic Scattering and e+ e- Annihilation by Perturbation Theory in Quantum Chromodynamics*, Sov. Phys. JETP **46** (1977) 641.

[133] Frixione, S., Nason, P., and Oleari, C., *Matching NLO QCD Computations with Parton Shower Simulations: the POWHEG Method*, Hep-ph/0709.2092, 2007.

[134] Sjostrand T et al Comput. Phys. Commun. **135** (2001) 238.

[135] Mangano, M.L., Moretti, M., Piccinini, F., Pittau, R., and Polosa, A.D., *ALPGEN, a Generator for Hard Multiparton Processes in Hadronic Collisions*, JHEP **0307** (2003) 001.

[136] Hoeche, S., Krauss, F., Lavesson, L., Lonnblad, L., Mangano, M., Schaelicke, A., and Schumann, S., *Matching Parton Showers and Matrix Elements*, `arXiv:hepph/0602031`.

[137] Agostinelli, S. et al., *GEANT4 - A Simulation Toolkit*, Nucl. Instr. and Meth. **A506** (2003) 250.

[138] Aad, G., et al., (The ATLAS Collaboration), *The ATLAS Simulation Infrastructure*, European Physical Journal C **70** (2010) 823.

[139] Abasov V. M. et al. (DØ Collaboration) Phys. Rev. D **76** (2007) .

[140] The ATLAS Collaboration, *Background studies for top-pair production in lepton plus jets final states in sqrt(s)=7 TeV ATLAS data*, `ATLAS-CONF-2010-087`.

[141] The ATLAS Collaboration, *Measurement of the Charge Asymmetry in Top Quark Pair Production in pp Collisions at $\sqrt{s} = 7$ TeV Using the ATLAS Detector*, 2012.

[142] *Luminosity Determination in pp Collisions at sqrt(s) = 7 TeV using the ATLAS Detector in 2011*, `ATLAS-CONF-2011-116`.

[143] The ATLAS Collaboration `https://twiki.cern.ch/twiki/bin/view/AtlasPublic/` `LuminosityPublicResults`.

[144] The ATLAS Collaboration, *Measurement of the Top-Quark Mass using the Template Method in pp Collisions at sqrt(s)=7 TeV with the ATLAS detector*, `ATLAS-CONF-2011-033`.

[145] The ATLAS Collaboration, *Measurement of the Top-Quark Mass from 2011 ATLAS Data using the Template Method*, `ATLAS-CONF-2011-120`.

[146] The ATLAS Collaboration, *Measurement of the top quark mass with the template method in the top antitop $\rightarrow$ lepton + jets channel using ATLAS data*, 2012. Eur. Phys. J. C **72** (2012) 2046.

[147] The ATLAS Collaboration, *Prospects for the Measurement of the Top-Quark Mass using the Template Method with early ATLAS Data*, `ATL-PHYS-PUB-2010-004`.

[148] D. V. Hinkley, *On the Ratio of Two Correlated Normal Random Variables*, Biometrika **56(3)** (1969) 635–639.

[149] Barlow R., *Application of the Bootstrap Re- sampling Technique to Particle Physics Ex- periments*, Preprint MAN-HEP-99-4 (2000) , `www.hep.manchester.ac.uk/preprints/archive.html`.

[150] The ATLAS Collaboration, *ATLAS Event Displays from 2010 and 2011 Collision Data*, `https://twiki.cern.ch/twiki/bin/view/AtlasPublic/` `EventDisplayPublicResults`.

[151] *AcerMC Monte-Carlo Generator*, 2012. `http://borut.home.cern.ch/borut/`.

[152] Kersevan, B.P. and Richter-Was, E., *The Monte Carlo event generator AcerMC version 1.0 with interfaces to PYTHIA 6.2 and HERWIG 6.3*, Comput. Phys.Commun. **149** (2003) 142.

[153] Kersevan, B.P. and Richter-Was, E., *The Monte Carlo event generator AcerMC version 2.0 with interfaces to PYTHIA 6.2 and HERWIG 6.5*, `arXiv:hep-ph/0405247`.

[154] Moraes, A., *Underlying Event Tunes for the LHC in M. G. Albrow et al. [TeV4LHC QCD Working Group], Tevatron-for-LHC report of the QCD working group*, (2006) .

[155] Albrow, M.G., et al. for The TeV4LHC QCD Working Group Collaboration `arXiv:hep-ph/0610012`.

[156] Skands, P.Z., *Tuning Monte Carlo Generators: The Perugia Tunes*, Phys. Rev. D **82** (2010) 074018.

[157] Buckley, A., et al., *Systematic event generator tuning for the LHC*, Eur. Phys. J. C **65** (2010) 331.

[158] Nadolsky, K. et al., *Implications of CTEQ global analysis for collider observables*, Phys. Rev. D **78** (2008) 013004.

[159] The ATLAS Collaboration, *Single hadron response measurement and calorimeter jet energy scale uncertainty with the ATLAS detector at the LHC*, `arXiv:hep-ph/1203.1302v1`.

[160] The ATLAS Collaboration, *ATLAS Muon Momentum Resolution in the First Pass Reconstruction of the 2010 p-p Collision Data at $\sqrt{s} = 7$ TeV*, `ATLAS-CONF-2011-046`.

[161] The ATLAS Collaboration, *Calibrating the b-Tag Efficiency and Mistag Rate in $35\ pb^{-1}$ of Data with the ATLAS Detector*, `ATLAS-CONF-2011-089`.

[162] Lyons L., Gibaut D., and Clifford P., *How to combine correlated estimates of a single physical quantity*, Nucl. Instr. and Meth. **A270** (1988) 110.

[163] Valassi, A., *Combining correlated measurements of several different quantities*, Nucl. Instr. and Meth. **A500** (2003) 391.

Acknowledgements

enough. To my two brothers, Greg and Chad, who have always been there for me, always wondering why I decided to study physics, and never letting me live-down my childhood mishaps.

Finally, to my beautiful wife Lubka, who has lived through every single page of this thesis. You have been there for every moment, both the pleasant ones and the difficult ones. I would not be here today without you, with every single moment of your encouragement and amazing soul, you helped me realize my dreams. I cannot begin to thank you for everything you have done. D'akujem velmi pekne.

STEFAN GUINDON - Curriculum Vitae

Marienstrasse 3
Göttingen 37073
Germany

<u>phone</u>: +49 (0) 551 39 7672
<u>email</u>: stefan.guindon@cern.ch

PERSONAL INFORMATION

Current Academic Title: Diplom-Physiker, B.Sc.
Sex: Male
Citizenship: Canadian
Date and Place of Birth: July 11, 1986, Cornwall, Ontario, Canada

EDUCATION

GEORG-AUGUST-UNIVERSITÄT GÖTTINGEN, Göttingen, Germany
Dr. rer. nat. Candidate, High Energy Physics
November 2008 - Present

- Top Quark Mass Measurement at the ATLAS Experiment at CERN
- Year-long stay at CERN (European Organization for Nuclear Research), Geneva, Switzerland
- DAAD (German Academic Exchange Service) Young Researcher's Grant

GEORG-AUGUST-UNIVERSITÄT GÖTTINGEN, Göttingen, Germany
Diplom-Physik, Physics
May 2008 - November 2008

- Simulation and modelling of physics detectors using Garfield and GEANT4 simulation code
- Experimental detector studies of detector setup for GERDA Collaboration located at Labratori Nationali del Gran Sasso, Italy

UNIVERSITY OF OTTAWA, Ottawa, Ontario, Canada
Bachelor's of Science with Honours in Physics, *Magna cum Laude*
September 2004 - May 2008

- Entrance and Merit scholarship recipient
- Dean's Honour Roll 2006 - 2008
- Honours thesis on theoretical description and modelling of a quantum dot system for quantum computing

ST. JOSEPH'S SECONDARY SCHOOL, Cornwall, Ontario, Canada
Ontario High School Diploma
September 2000 - May 2004

- Honour Roll Student and Class of 2004 Valedictorian
- Ontario Scholar

INTERNSHIPS

CERN, Geneva, Switzerland
January 2011 - January 2012

- Year-long stay at CERN to pursue studies for Doctoral research
- On-site research and work towards publication of analysis

CERN, Geneva, Switzerland
INSTITUTE OF PARTICLE PHYSICS CANADA (COLLABORATION)
June 2008 - September 2008

- Grant from NSERC (Natural Science and Engineering Research Council of Canada) to study as a CERN Summer Student from Non-Member State.
- Research on GEANT4 model simulations of gaseous detectors. Programming of first model for gaseous detector simulations within GEANT4.
- Attended CERN summer school lectures

NATIONAL RESEARCH COUNCIL OF CANADA, MICROSTRUCTURAL INSTITUTE, Ottawa, Canada
October 2007 - April 2008

- Work towards a Bachelor's Thesis on theoretical quantum dot system to be used for quantum computing
- Theoretical modelling and programming models for a triple quantum dot

MAX-PLANCK-INSTITUTE FOR PHYSICS, Munich, Germany
May 2006 - August 2006

- DAAD Rise Scholarship Recipient
- Experimental work on detector response and setup for the GERDA Collaboration at LNGS
- Hands-on experience in the laboratory and work with radioactive materials

PUBLICATIONS AND PUBLIC PAPERS

- First ATLAS Top Mass Measurement,
  published in the European Physics Journal C: Eur.Phys.J. C72 (2012) 2046
- Conference Note for Moriond 2011 Winter Conference, at:
  https://cdsweb.cern.ch/record/1337783/files/ATLAS-CONF-2011-033.pdf
- LHC experiments Committee (LHCC) Poster Session, at:
  https://cdsweb.cern.ch/record/1340980/files/ATL-PHYS-SLIDE-2011-109.pdf

CONFERENCE PRESENTATIONS

- Presentations at the German Physical Society yearly meetings (2009-2012),
- 2010 ATLAS Germany Workshop Presentation on Top Mass Measurement efforts within Germany

TEACHING

SUPERVISION OF DIPLOM AND BACHELOR STUDENTS

- Oversight of thesis and student preparing for a Bachelor's degree in High Energy Physics

STATISTICS FOR PHYSICAL SCIENCES

- Teaching Assistant in charge of problem solving sessions and 1-on-1 assistance

DATA ANALYSIS FROM LEP EXPERIMENT

- Small working group lab course with a large amount of interaction with students over several semesters

OUTREACH

- Helped at several scientific LHC outreach events within Germany, specifically the *Weltmaschine* exhibition. Spoke with public and student groups of the science studied at CERN
- Poster for the Scottish Universities LHC Summer School in 2009
- *Rent-a-Scientist* outreach program for high school level students

SCIENTIFIC SCHOOLS

- Helmholtz Alliance School on Advanced Statistical Methods (Teaching Assistant), Karlsruhe, Germany, October, 2009
- Scottish Universities LHC Summer School, St. Andrew's, Scotland, August, 2009
- ISAPP (International School on Astroparticle Physics), Munich, Germany, May 2006

SPOKEN LANGUAGES

- ENGLISH - Mother Tongue
- FRENCH - Mostly Fluent (Level C)
- GERMAN - Studying (Level B)
- SLOVAK - Beginner

Datum: 01.07.2012